DISSERTATION

MARINE ICE NUCLEATING PARTICLES: SOURCES, COMPOSITION, EMISSIONS, AND MODEL PARAMETERIZATIONS

Submitted by

Kathryn A. Moore

Department of Atmospheric Science

In partial fulfillment of the requirements

For the Degree of Doctor of Philosophy

Colorado State University

Fort Collins, Colorado

Fall 2023

Doctoral Committee:

Advisor: Sonia M. Kreidenweis
Co-Advisor: Paul J. DeMott

Delphine K. Farmer
Jeffrey R. Pierce
Susan C. van den Heever

ABSTRACT

MARINE ICE NUCLEATING PARTICLES: SOURCES, COMPOSITION, EMISSIONS, AND MODEL PARAMETERIZATIONS

Sea spray aerosol has received increasing attention over the last decade as a source of ice nucleating particles (INPs) to the atmosphere. Sparse measurements in remote marine regions indicate both marine INP concentrations and ice nucleating efficiency are several orders of magnitude lower than those of mineral or soil dusts, which dominate the INP budget on a global scale. The Southern Ocean (SO) surrounding Antarctica is thought to be the only region where marine INPs are the predominant INP type due to its remoteness from continental and anthropogenic aerosol sources and persistent strong westerlies that help isolate the region, although several recent studies have suggested this may also be true of the high Arctic seasonally or intermittently. INPs are critical for initiating cloud glaciation at temperatures warmer than ~-36 °C and can thus have an outsize effect on cloud phase and related climate feedbacks due to their relative scarcity. This is particularly true over the polar oceans, where low and mid-level mixed phase and supercooled clouds are ubiquitous and especially sensitive to aerosols due to the generally low background particle concentrations.

The research presented here aimed to improve our understanding of the factors influencing marine INP emissions and the sources and composition of INPs in remote marine regions, as well as to evaluate and improve current INP model parameterizations. This was accomplished using observations made in the Southern Ocean, one of the few remaining pristine aerosol environments, during the Southern Ocean Cloud Radiation Aerosol Transport Experimental Study (SOCRATES) aircraft campaign on the NSF/NCAR G-V, and the second Clouds, Aerosols, Precipitation, Radiation and atmospherIc Composition Over the southeRN ocean (CAPRICORN-2) ship campaign on the R/V *Investigator* in 2018. Ambient observations were supplemented by measurements from the CHaracterizing Atmosphere-Ocean parameters in SOARS mesocosm

experiment (CHAOS) in the new Scripps Ocean-Atmosphere Research Simulator (SOARS) wind-wave channel. CHAOS measurements allowed for isolation of the role of wind speed in marine INP production, which had not previously been characterized through controlled experiments.

SOCRATES and CAPRICORN-2 are notable for collecting the first vertically resolved INP measurements over the Southern Ocean, including the first in situ observations in and above cloud in the region. Both aerosol and INP concentrations showed excellent agreement between G-V and R/V *Investigator* observations during overflights of the ship, supporting the use of such a multi-platform measurement approach for future campaigns interested in aerosol and INP vertical profiles. New techniques for estimating marine aerosol surface area and the number of particles >0.5 μm, key quantities often used in INP parameterizations, were developed based on lidar and nephelometer measurements. A new parameterization for marine INPs is proposed, which uses both wind speed and activation temperature, and reduces bias compared to the existing parameterization based solely on temperature. Marine boundary layer (MBL) and above cloud INP concentrations from the same SOCRATES flight support the hypothesis suggested by several modeling studies that marine INPs dominate at low altitudes, and mineral dust becomes increasingly important with height. Unexpectedly, enhanced INP and aerosol iron concentrations, but low iron solubilities, were observed for samples collected south of 60 °S during CAPRICORN-2. Antarctica is suggested as a potential source of both biological and inorganic INPs to the Southern Ocean marine boundary layer through the emission of mineral and soil dusts from ice-free areas. Similar high latitude dust sources in Iceland and Svalbard have been observed to contribute to INPs in the Arctic atmosphere, and are anticipated to increase in importance as the climate warms.

ACKNOWLEDGEMENTS

I would like to thank the SOCRATES and CAPRICORN-2 science teams for the excellent planning, operations, and post-campaign discussions, especially PIs Jay Mace, Alain Protat, and Greg McFarquhar. The assistance and support of Cory Wolff and Pavel Romashkin, NCAR project managers for the SOCRATES project, as well as the G-V crew, are greatly appreciated. I am especially grateful to Mike Reeves and Jorgen Jensen of NCAR for calibration, measurements, and analysis of GNI and UHSAS data from SOCRATES. The support of the CSIRO Marine National Facility (MNF) in the form of sea time on the RV Investigator, support personnel, scientific equipment, and data management during CAPRICORN-2 is gratefully acknowledged. In particular, I wish to thank Ian McRobert (CSIRO Technical Services Officer) for assistance with the RV Investigator's electrical and data management systems during and after CAPRICORN-2, and to Ruhi Humphries (CSIRO Senior Research Scientist), Jason Ward (formerly CSIRO Senior Experimental Scientist) and Melita Keywood (CSIRO Research Director, Earth Systems) for their work maintaining aerosol equipment on board the RV Investigator. Thanks also to Roy Geiss at the Colorado State University Electron Microscopy Lab for performing STEM analytical measurements on the CAPRICORN-2 and SOCRATES samples. And a final thanks to Raymond J. Leibensperger III, M. Dale Stokes, Grant Deane, and Chris Lee for coordination and planning of the CHAOS mesocosm campaign.

The material in this dissertation is based upon work supported by the National Center for Atmospheric Research, which is a major facility sponsored by the National Science Foundation under Cooperative Agreement 1852977 (Chapters 2, 3, 5). The data collected during SOCRATES used NSF's Lower Atmosphere Observing Facilities, which are managed and operated by NCAR's Earth Observing Laboratory. I also acknowledge the NOAA Air Resources Laboratory (ARL) for the provision of the HYSPLIT transport and dispersion model (https://www.ready.noaa.gov). Chapters 2, 3, and 5 were primarily supported by the National Science Foundation (NSF) by Grant AGS-1660486 and by the United States Department of Energy (DOE) through Grants DE-

SC0018929 and DE-SC0021116. Chapters 3, 4, and 5 were additionally supported by the NSF Center for Aerosol Impacts on Chemistry of the Environment (NSF CHE-1801971). I also wish to acknowledge support by an NSF Graduate Research Fellowship under Grant 006784 and an American Meteorological Society Graduate Fellowship.

TABLE OF CONTENTS

LIST OF TABLES

LIST OF FIGURES

1. Introduction

Sea spray aerosols (SSA), along with mineral and soil dusts, represent the largest sources of natural aerosols, and play important roles in the climate system through direct interactions with radiation, as well as indirect effects through aerosol-cloud interactions (e.g. Lewis and Schwartz 2004; O'Dowd and de Leeuw 2007; Andreae 2007; Grythe et al. 2014; de Leeuw et al. 2011; Carslaw et al. 2017; Cochran et al. 2017; Ginoux et al. 2012; Kok et al. 2023). SSA are produced through two main mechanisms: 1) primary marine aerosol (PMA) is generated from sea spray and bubble bursting at the ocean surface and 2) secondary marine biogenic particles are formed through condensation of reaction products from gas-phase precursors such as dimethyl sulfide (DMS) (e.g. Lewis and Schwartz 2004; O'Dowd and de Leeuw 2007; Quinn et al. 2017; Sanchez et al. 2021b; Twohy et al. 2021). Inorganic sea salt dominates PMA mass, whereas secondary marine aerosols include sulfur and carbonaceous components (Cochran et al. 2017; Quinn et al. 2017). Mineral dust aerosols are solid, inorganic particles derived from the weathering of rocks, and are typically aerosolized through mechanical means (Kok et al. 2012; 2023). Dust composition varies depending on the mineralogy of the source region, but include species such as illite, kaolinite, quartz, carbonates, feldspar, and metals such as iron oxides (Perlwitz et al. 2015; Kok et al. 2023). Agricultural and soil dusts can contribute up to 25% of the global dust loading, and additionally contain organic species (Ginoux et al. 2012).

Aerosols contribute the largest uncertainty to global radiative forcing estimates, with natural aerosols responsible for a significant portion of this (Forster et al. 2021; Carslaw et al. 2013; Andreae 2007). As the natural (pre-industrial) aerosol burden and its effects are largely unknown, our ability to constrain and predict the influence of anthropogenic aerosols on climate sensitivity (Kiehl 2007), radiative forcing, and cloud processes (Andreae 2007) has been hindered (Carslaw et al. 2013). Uncertainties in pre-industrial aerosol loadings and composition manifest in uncertainties in baseline simulations needed to assess future climatic changes (Carslaw et al. 2013; 2017). As a result, regions such as the Southern Ocean (SO), which earth system models

suggest have experienced only weak influences of anthropogenic aerosols, serve as important proxies for pre-industrial aerosol conditions (Hamilton et al. 2014), and a good location to test aerosol-cloud interactions in models.

The Southern Ocean is a vast band of water surrounding Antarctica and separating it from other Southern Hemisphere landmasses. Its remoteness from continental and anthropogenic aerosol sources and persistent strong westerlies help isolate the region, and both in situ observations (e.g. Quinn et al. 2017; Mace et al. 2020; Humphries et al. 2021; Uetake et al. 2020) and modeling studies (e.g. McCoy et al. 2015a; Hamilton et al. 2014) have indicated the predominant aerosol sources are local. The SO influences oceanic and atmospheric circulation and heat transport on both local and global scales (Rintoul 2007; Hwang and Frierson 2013). In addition, improving our understanding and simulations of Southern Ocean clouds has emerged as a critical piece of representing the overall climate system (e.g. Trenberth and Fasullo 2010; Kay et al. 2016b; Tan et al. 2016; Bodas-Salcedo et al. 2013; 2016; Frey and Kay 2017; Gettelman et al. 2020; McFarquhar et al. 2021). Following Trenberth and Fasullo's (2010) initial demonstration of systematic positive biases in CMIP3 model estimates of absorbed shortwave radiation poleward of 55°S, many studies have focused on cloud and radiation measurements, simulations, and reanalyses in this region. This radiation bias induces subsequent warm biases in sea surface temperature (SST) year-round, and leads to associated errors and uncertainties in predicting other model outcomes, such as the position of the Southern Hemisphere jet (Ceppi et al. 2012; 2014) and climate sensitivity (Trenberth and Fasullo 2010; Tan et al. 2016).

In polar regions, low-level clouds exert an important influence on surface radiative fluxes, the sign and magnitude of which depends on the incoming solar flux, surface albedo, and cloud phase (Kay et al. 2016a). Over the Southern Ocean, the cloud shortwave effect dominates and cloud radiative forcing is generally negative (Kay et al. 2016a; Bodas-Salcedo et al. 2013). The SO is one of the cloudiest regions on Earth, with low cloud cover (<3 km) approaching or exceeding 80% year round (Mace et al. 2009). Low and midlevel clouds are particularly important for the radiative budget of the SO, but have historically been poorly represented in earth system models

and reanalyses (Bodas-Salcedo et al. 2013; 2016; Kay et al. 2016b; Naud et al. 2014). Infrequent and limited in situ observations, uncertainties in satellite cloud retrievals at high latitudes, and the inability of some satellite retrievals (e.g. CloudSat) to observe very low and thin clouds has made rectifying this problem difficult (McFarquhar et al. 2021; Mace et al. 2020; Alexander and Protat 2018). Spurred by these issues, a suite of field campaigns were conducted in the SO over the last 5 years, and also prompted updates to cloud processes in individual CMIP6 (Coupled Model Intercomparison Project Phase 6) models relative to their CMIP5 (Phase 5) counterparts. These improvements have increased predictions of supercooled liquid water (SLW) and reduced radiation biases in the region, improving agreement with observations (Bodas-Salcedo et al. 2019; Gettelman et al. 2020), although are likely also responsible for the higher equilibrium climate sensitivities (ECS) observed in many CMIP6 models relative to CMIP5 (Zelinka et al. 2020). Future ECS is predicted to strongly depend on the cloud phase feedback over the Southern Ocean, so improving our understanding of processes that influence cloud phase in this region is critical (Bjordal et al. 2020).

If total condensate in a cloud is fixed, liquid drops tend to have a smaller diameter but be more numerous than ice crystals (Tan et al. 2016; Korolev et al. 2017). As a result, supercooled liquid or mixed phase clouds are optically thicker and have a higher albedo than fully glaciated clouds. In addition to the direct radiative differences, the development of precipitation and thus cloud lifetime depends strongly on ice phase processes (Korolev et al. 2017). One such process is ice nucleation, or the initiation of ice particle formation in clouds, and will be the focus of this dissertation. Ice nucleation in the atmosphere occurs through two main pathways: 1) homogeneous freezing of cloud drops below ~-36°C, and 2) heterogeneous ice nucleation, which occurs when an ice nucleating particle lowers the activation energy to form a critical ice embryo (Kanji et al. 2017). Heterogeneous ice nucleation at temperatures warmer than -35°C is the most relevant for glaciation of mixed phase clouds. Several pathways, including immersion freezing, deposition, and contact freezing, are known to occur in the atmosphere,

with immersion freezing (freezing initiated by an INP inside a liquid drop) the most important for mixed phase clouds (Kanji et al. 2017), such as are common over the SO.

In the immersion freezing mode, mineral and soil dusts are the dominant INP types globally, due to their high ice nucleation activity (Hoose and Möhler 2012; Testa et al. 2021) and large emission rates (Ginoux et al. 2012). Biological ice nucleators (pollen, fungal spores, some bacteria) can be important at temperatures warmer than -10°C in some regions (Garcia et al. 2012; Pummer et al. 2015; Wilson et al. 2015; Kanji et al. 2017). More recently, marine INPs have been identified as a distinct category (see DeMott et al. 2016), and shown to include marine diatoms and their exudates (Wilson et al. 2015; Rosinski et al. 1987), as well as marine macromolecules (McCluskey et al. 2018b). Marine INP concentrations are generally 1-2 orders of magnitude or more lower than continental measurements at equivalent temperatures (DeMott et al. 2016), with SO measurements (McCluskey et al. 2018c; Schmale et al. 2019; McCluskey et al. 2023) at the lower bound of those reported from other ocean regions (DeMott et al. 2016; Welti et al. 2020). Observed low INP numbers, its remote location, and modeling studies (Burrows et al. 2013; Vergara-Temprado et al. 2017; McCluskey et al. 2019) support the idea that the SO INP population is dominated by marine SSA and distinct from that found in the northern hemisphere, though direct field confirmation is still needed. Recent observations that mineral dust dominates over locally-sourced marine INPs in the Canadian Arctic (Irish et al. 2019) means measurements of pristine marine aerosols (Hamilton et al. 2014) from the Southern Ocean are invaluable in understanding the role of marine INPs in mixed phase cloud processes. The unusually high proportion of supercooled liquid water in SO clouds (Morrison et al. 2011; Chubb et al. 2013; McFarquhar et al. 2021) is consistent with low numbers of INPs in this region and indicates that INP concentrations and composition may strongly control cloud phase and precipitation formation over the SO, as also suggested by recent modeling studies (Vergara-Temprado et al. 2018). Modern INP observations over the Southern Ocean are limited in extent (McCluskey et al. 2018c; Schmale et al. 2019; Welti et al. 2020; Tatzelt et al. 2022; Kremser et al. 2021; McFar-

quhar et al. 2021; Miyakawa et al. 2023) and data from recent campaigns will greatly enhance our ability to understand the role they play in SO clouds.

The following chapters of this dissertation aim to 1) contribute to knowledge of SSA emissions, abundance, size distributions, and vertical profiles in marine environments, 2) assess the properties, sources, and role of marine INPs in cloud formation over the Southern Ocean, and 3) improve and evaluate current INP model parameterizations. To address these areas, 4 key questions will be explored:

1. Can marine aerosol surface area be accurately estimated with remote sensing measurements?

2. What factors (seawater temperature, wind speed) influence the emission of marine INPs?

3. How can marine INPs be best parameterized in models?

4. What are the sources of INPs in the Southern Ocean marine boundary layer, and what are the implications for clouds?

Chapter 2 focuses on measurements of marine aerosols, and evaluates how marine aerosol surface area can be best estimated with remote sensing measurements of bulk optical properties. Aerosol surface area is used in many models' INP parameterizations, as well as influencing particle light scattering, hygroscopic growth, and reactivity. Chapter 3 presents measurements of INPs from simultaneous aircraft and ship campaigns conducted over the SO in Austral summer 2018, which include the first in situ observations in and above cloud in the region. Vertical INP profiles provide information about variation in particle sources with altitude, as well as supplying the first measurements to validate existing INP model simulations. Chapter 4 summarizes results from a 2022 mesocosm study in a breaking-wave simulator, which aimed to isolate individual factors (seawater temperature, wind speed) that may influence marine INP emissions. Chapter 5 builds on results from Chapter 3, utilizing INP composition measurements and back trajectories to assess sources of INPs over the SO and implications for changes under future climates. Chapter 2 (Moore et al. 2022) is published in the Journal of Geophysical Research:

Atmospheres, and Chapter 3 is in review in the same journal; they are both reproduced here without changes to the published and submitted versions, respectively. Chapters 4 and 5 are in preparation for submission following submission of this dissertation.

2. Estimation of Sea Spray Aerosol Surface Area over the Southern Ocean Using Scattering Measurements

2.1 INTRODUCTION

The Southern Ocean (SO) is a vast region of water surrounding Antarctica, separating it from the other Southern Hemisphere landmasses. Its remoteness from continental and anthropogenic aerosol sources and persistent strong westerlies help isolate the region, and both in situ observations (Humphries et al. 2021; Mace et al. 2020; Quinn et al. 2017) and modeling studies (Hamilton et al. 2014; McCoy et al. 2015a) have indicated that the predominant aerosol sources in the boundary layer are local. As a result, the SO may serve as a proxy for pre-industrial marine aerosol conditions (Hamilton et al. 2014) and is a good location to test aerosol-cloud interactions in models. Aerosols directly influence atmospheric radiative forcing through scattering and absorption of solar radiation, as well as indirectly through aerosol-cloud interactions such as nucleation of cloud droplets and ice crystals. They contribute the largest uncertainty to global radiative forcing estimates, with natural aerosols responsible for a significant portion of this, making observations in areas free of anthropogenic influences, such as the SO, critical (Andreae 2007; Carslaw et al. 2013; Kiehl 2007). However, difficulty in reaching the SO, coupled with frequent storms and high winds, have led to a paucity of direct aerosol, cloud, and precipitation observations relative to other regions (McFarquhar et al. 2021).

Aerosols in the SO marine boundary layer (MBL) are primarily of marine origin, and of two types: 1) primary marine aerosol (PMA) generated from sea spray and bubble bursting at the ocean surface and 2) marine biogenic particles that form through condensation of reaction products from gas-phase precursors such as dimethyl sulfide (DMS) (Lewis and Schwartz 2004; Quinn et al. 2017; Sanchez et al. 2021b; Twohy et al. 2010). PMA, which is dominated by sea salt, is thought to control the optical properties and direct aerosol radiative forcing in the Southern Ocean (Quinn et al. 1998). Secondary marine biogenic aerosols, which can include sulfur and

carbonaceous components, frequently dominate the cloud condensation nuclei (CCN) budget in the SO MBL, although PMA also contributes significantly to CCN concentrations, particularly under high wind conditions (Fossum et al. 2018; Humphries et al. 2021; Quinn et al. 2017; Sanchez et al. 2021b; Twohy et al. 2010). The ice nucleating particle (INP) budget for the SO is not as well constrained as that of CCN, although growing evidence suggests it is also dominated by local marine aerosols (Burrows et al. 2013; McCluskey et al. 2018c; McFarquhar et al. 2021; Vergara-Temprado et al. 2017). Low level marine clouds are particularly sensitive to changes in aerosol loading, size, and composition, due to their generally low droplet concentrations. The SO is one of the cloudiest regions on Earth, with low cloud cover (<3 km) approaching or exceeding 80% year round (Mace et al. 2020), and SO clouds are more likely to be supercooled than those at similar temperatures in the Northern Hemisphere (Alexander and Protat 2018; Chubb et al. 2013; Huang et al. 2012). Despite their prevalence, global climate models (GCMs) struggle to simulate cloud coverage and cloud phase in the region (Kay et al. 2016a; McFarquhar et al. 2021). A variety of methods have been used to parametrize ice nucleation in both global and cloud-resolving models, and to compare the relative efficiencies of particle types at nucleating ice. One of the most common methods involves normalizing INP concentrations with a more frequently measured value, such as particle surface area or number (DeMott et al. 2010; 2015; Hoose and Möhler 2012; Kanji et al. 2017; McCluskey et al. 2018a; Niemand et al. 2012; Ullrich et al. 2017). In addition to use in INP parameterizations, aerosol surface area is an important observational quantity, influencing light scattering, hygroscopic growth, and reactivity (Lewis and Schwartz 2004; O'Dowd and de Leeuw 2007).

The need for observations of particle number and surface area concentrations, both to directly compare to modeled values, as well as to evaluate and improve marine INP parameterizations, was the primary motivation for this study. Particularly over the SO, measurements of aerosol size distributions are infrequent and limited in spatial and temporal extent. Estimating aerosol properties using light scattering observations from nephelometers and lidars is appealing because of their autonomous operation and higher availability of measurements. Two

techniques for retrieving marine aerosol surface area from bulk optical measurements will be evaluated here for the Southern Ocean. The first, proposed in DeMott et al. (2016), uses ambient aerosol scattering coefficients from a three-channel nephelometer, and the second utilizes lidar aerosol backscatter profiles (Mamouri and Ansmann 2016), and are described further in Sec. 2.2.3.4 and 2.2.2. To our knowledge, neither of these methods have been previously applied to observations from the Southern Ocean marine boundary layer. Two campaigns that occurred concurrently in 2018, the Southern Ocean Cloud Radiation Aerosol Transport Experimental Study (SOCRATES, hereafter SOC) aircraft campaign and the second Clouds, Aerosols, Precipitation, Radiation and atmospherIc Composition Over the southeRN ocean (CAPRICORN-2, hereafter CAP-2) ship campaign, provide a unique opportunity to assess these techniques with co-located aerosol size distribution measurements that were used to validate proposed conversion parameters (Sec. 2.3.2 and 2.3.3).

2.2 METHODS

2.2.1 Overview of CAPRICORN-2 and SOCRATES Campaigns

The SOC and CAP-2 campaigns occurred simultaneously during January-March 2018 in the Southern Ocean region south of Tasmania with the goal of providing in-situ measurements to improve and validate climate model simulations of marine boundary layer processes, clouds, and aerosols over the Southern Ocean. The SOC campaign used the NSF/NCAR G-V aircraft to make measurements of cloud and aerosol properties in the MBL, within clouds, and above clouds in the region. Complementary MBL measurements were conducted during CAP-2 on the RV *Investigator* (voyage IN2018_V01), an Australian Government research platform operated by the Commonwealth Science and Industrial Research Organisation (CSIRO). Flight tracks for all 15 SOC flights and the ship track for CAP-2 are shown in Figure 2.1. These measurements were made during late austral summer into early austral autumn. Detailed descriptions of the goals, measurements, and preliminary findings for these campaigns are described in (McFarquhar

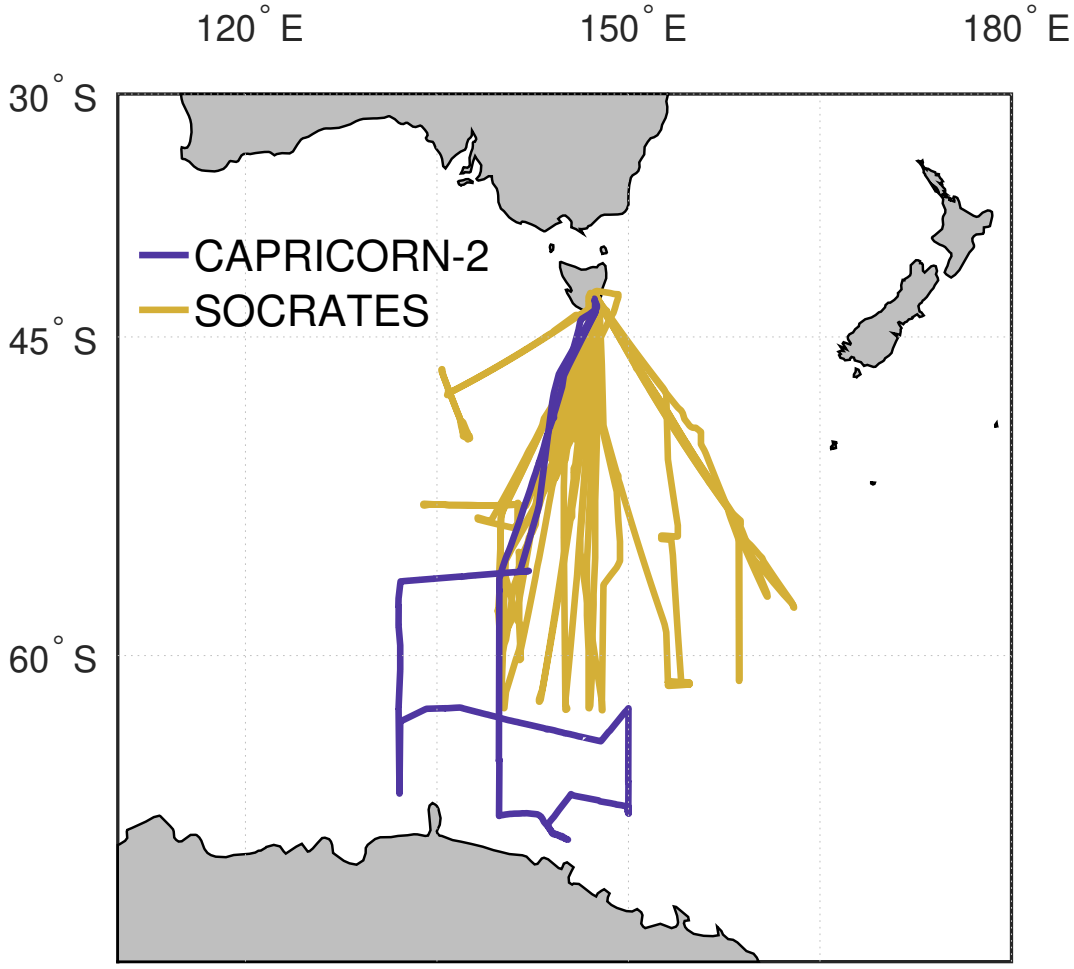

Figure 2.1: Track of the RV *Investigator* (CAP-2) and flight tracks from the NSF/NCAR G-V (SOC) are shown in purple and gold, respectively.

et al. 2021). Coordinated overflights of the ship by the aircraft within the marine boundary layer occurred in a select number of cases, and these will be highlighted in Sec. 2.3.1.

2.2.2 Use of lidar profiles to estimate aerosol surface area and particle number

Mamouri and Ansmann (2015; 2016, hereafter MA) proposed a methodology for deriving vertical profiles of dry aerosol surface area, SA_{dry}, and number, N_{dry}, from lidar backscatter profiles and AERONET (Smirnov et al. 2009) observations. Expected uncertainties are in the range 25%-50%. Throughout this manuscript, all measurements reported as "dry" were made below the efflorescence relative humidity (ERH) of sea salt, which is about 45-48% (Tang et al. 1997), and typically below 30%. We explored the use of the MA parameterizations for estimating aerosol surface areas (SAs) and concentrations of particles larger than 500 nm (N_{500}) during CAP-2. Briefly, their methodology involves using Level 2.0 AERONET inversions and correlating surface areas or number concentrations inferred from the inverted volume size distributions with aerosol optical thickness (AOT) at a particular wavelength. The resulting correlations constitute a relationship between column extinction and column aerosol surface area or number, and were derived for three aerosol types: marine, desert dust, and continental (meaning pollution). Lidar ratios representative of the expected aerosol type are used to calculate vertical particle extinction profiles from backscatter data, which are then converted to aerosol SA or N_{500} profiles using the AERONET-extinction relationship for the relevant aerosol type and desired parameter.

To derive a representation appropriate for marine aerosol, which is most relevant for the present study, MA used AERONET data from Ragged Point, Barbados, from 2007-2015, after screening for $AOT_{500\,nm} < 0.07$ and total Ångström exponent (å; computed for the wavelength pair 440 nm and 870 nm) between 0.25 and 0.6. These criteria removed periods affected by biomass burning emissions and long-range transported dust, which are annual occurrences in the Caribbean region (Corona-Núñez et al. 2020; Prospero et al. 2014). MA derived conversion parameters for three lidar wavelengths: 355 nm, 532 nm, and 1064 nm. A 355-nm lidar was de-

ployed during CAP-2 (Sec. 2.2.3.5) and this wavelength will be the focus here. Since AERONET measures ambient aerosol, the inverted surface areas and number concentrations must be corrected to dry (less than the sea salt ERH) using an assumed diameter growth factor to be fairly compared to the dry, in-situ observations presented here. For this purpose, a growth factor of 2 was used by MA, corresponding to that expected for sea salt at relative humidities (RH) ~80%, assumed representative of a typical nonprecipitating marine boundary layer. Therefore, wet surface areas were scaled by a factor of 4 to arrive at dry surface areas for marine (denoted by subscript m) particles, $SA_{m,dry}$, assuming no vertical variation in RH in the marine boundary layer:

$$SA_{m,dry}(z) = \frac{c_{s,m}}{4} \times \sigma_m(z) \tag{2.1}$$

with $SA_{m,dry}$ in μm^2 cm^{-3}, the conversion factor $c_{s,m}$ in μm^2 cm^{-3} Mm, and lidar extinction profiles $\sigma_m(z)$ at the applicable wavelength in Mm^{-1}. For a wavelength of 355 nm, $c_{s,m}/4$ is reported as 0.52±0.09. To derive dry N_{500}, the AERONET number distributions are integrated for ambient sizes >1000 nm diameter to account for hygroscopic growth:

$$N_{500,m,dry}(z) = c_{1000,m} \times \sigma_m(z) \tag{2.2}$$

with $N_{500,m,dry}$ in cm^{-3} and $C_{1000,m}$ in cm^{-3} Mm; at 355 nm, $C_{1000,m}$=0.05±0.01. These values are summarized in Table A.1.

2.2.3 Aerosol Measurements during CAPRICORN-2

2.2.3.1 RV Investigator Aerosol Inlet

The aerosol laboratory on the RV *Investigator* contained a suite of instruments for measuring aerosol properties. These included sub- and super-micron aerosol size distributions, aerosol scattering, aerosol chemical composition, cloud condensation nuclei number concentration, fluorescent biological particles, and total aerosol number concentration. The RV *Investigator* has a custom-designed aerosol sampling inlet, with the intake located approximately

18.4 m above sea level at the bow of the ship. The whole inlet is stainless steel, with an inner diameter of 16 cm, which tapers to a 4 cm conical intake. Ambient air is sampled into the conical intake section at ~440 L min^{-1}, which is oriented horizontally to limit the amount of precipitation entering the inlet, and automatically adjusts to orient into the wind (forward 180° only). The inlet then travels vertically down the foremast into the aerosol lab, which is located directly underneath the inlet at the bow of the ship, to minimize particle losses. Inside the aerosol lab, approximately 9 m from the intake, is a sample manifold with instrument pickoffs for aerosol sampling. All aerosol instruments considered in this study were located inside the aerosol lab and sampled from the aerosol sampling manifold. Particle transmission efficiency through the aerosol sampling inlet, including dependence on wind speed and ship motion, has not been fully characterized. Theoretical calculations of transmission efficiency for all data presented here (Sec. 2.2.3.3) are shown in Fig. A.1 and utilized the von der Weiden et al. (2009) Particle Loss Calculator and Paul Baron's Aerocalc spreadsheet (Brockmann 2011). These calculations assumed a constant aspiration angle of 0°, and a wind velocity of 10 m s^{-1}, which is the average for the CAP-2 campaign.

2.2.3.2 Ship Exhaust Contamination and Continental Aerosols

The largest sources of particle contamination on board the RV *Investigator* are exhaust from diesel combustion from the engines and waste incineration. These waste streams are emitted from separate but co-located flues approximately 50 m aft of the aerosol intake, and at a similar height to the sampling inlet (Humphries et al. 2019). Following the technique presented in Humphries et al. (2019), a time series of predicted exhaust influence on measurements during the CAP-2 voyage was created and used to exclude periods of likely exhaust influence from all data presented here. Based on Alexander and Protat (2019), all aerosol measurements north of 47°S were also excluded from this analysis, as the region close to Tasmania occasionally has contributions from continental aerosols.

2.2.3.3 Particle Size Distribution Measurements

Submicron and supermicron aerosol size distributions were measured directly using a TSI Scanning Mobility Particle Sizer (TSI, SMPS 3080) for aerosols in the range 15-660 nm and a TSI Aerodynamic Particle Sizer (TSI, APS 3320) for aerosols between 500 nm and 20 μm. A single-jet impactor was located immediately before the SMPS inlet to remove particles larger than the upper scan size. The SMPS size measurements were calibrated before, after, and at two-week intervals during the voyage against polystyrene latex spheres (PSLs) of known sizes. No adjustments were made to the measured electrical mobility sizes, as they agreed with the known PSL sizes to within ±5 nm during each calibration. SMPS distributions with total number concentrations <50 cm^{-3}, as well as all data at sizes <25 nm were removed due to poor counting statistics and increased noise, respectively. The APS was located approximately 1 m from the sampling manifold, and the inlet minimized bends to reduce losses of supermicron particles. The APS aerodynamic size measurements were calibrated against PSLs of known size and density (ρ=1.05 g cm^{-3}) at weekly intervals during the voyage, as well as before and after the campaign. Both aerosol streams were dried with silica gel diffusion driers prior to measurement to below the ERH of sea salt, ~45-48% (Tang et al. 1997). For submicron size distribution measurements using the SMPS, particles were additionally dried within the instrument due to the introduction of dry sheath air at a 10:1 ratio to the sample flow, and so were assumed to represent aerosol physical dry diameters without additional corrections. Distributions suspected to be influenced by ship exhaust contamination (Sec. 2.2.3.2) were removed from further analysis, as were any distributions where the instrument inlet RH exceeded 30%.

The SMPS and APS measurements were merged into continuous size distributions following the removal of ship exhaust and high-RH scans. SMPS distributions were averaged to 30-min resolution to reduce noise, then the SMPS sizes were adjusted for shape factor (χ) following DeCarlo et al. (2004) Eq. 25, using χ_{SMPS}=1.05 for sea salt particles with 0.025nm < D <500 nm (Zieger et al. 2017) and assuming the slip correction factors cancel, since the adjustment is small. The APS distributions were averaged to the same 30-min resolution, then a size-

correction factor was applied to convert the APS sizes from Da to physical dry diameter, accounting for particle density (ρ_p), shape factor, and hygroscopic growth factor (HGF). An APS diameter correction factor of 0.68 was used, which is based on the density of dry sea salt, ρ_p=2.2 g cm^{-3} (Lewis and Schwartz 2004), shape factor measurements of artificial sea salt particles with D>500nm (Zieger et al. 2017, χ=1.03), and HGF~1 for sea spray aerosols (SSA) below the ERH. Next, the SMPS and APS distributions were combined using a smoothing spline in the overlap region, and this merged distribution was interpolated onto an even diameter grid with logarithmically spaced bins. Finally, the merged distributions were corrected for expected inlet losses as described in Sec. 2.2.3.1, and 3-4 lognormal modes were fit to each distribution. All CAP-2 distributions were initially fit with 3 modes, and an additional coarse mode was added if the 3-mode fit did not match the SMPS/APS data within 50% in the region between 2-3 μm, which was found to have the strongest influence on the estimated PMA mode width. Occasionally, some distributions required a fourth Aitken mode instead, which was similarly determined by a mismatch between the initial 3-mode fit and the SMPS/APS data of >50% in the size range 0.03-0.035 μm. If adding an additional mode did not improve the coefficient of determination, the fit was reverted to a 3-mode lognormal to penalize overfitting. Lower weights were applied in the 0.4-0.6 μm range during fitting to de-emphasize instrument uncertainties in the overlap region, and sizes >3 μm were highly weighted during lognormal fitting to capture the coarse mode and retrieve an accurate mode width. Limits were applied to the mode size and geometric width during fitting, based on Quinn et al. (2017) and Modini et al. (2015), and are reported in Table A.2. The sum of the third and fourth (if needed) coarse modes were considered to represent primary marine aerosol, which is further discussed in Sec. 2.3.1 The inlet transmission efficiency applicable to the APS was used, since minimal losses (<5%) are expected for particles in the SMPS size range (Fig. A.1). The merged distributions were cut off at 5 μm dry diameter; above this, the expected transmission efficiency drops below 40%, making the correction highly uncertain (Fig. A.1). In total, merged aerosol size distributions were calculated for 1075 30-min periods during CAP-2; a contour plot of the number distributions is given in Fig. A.2. Particle

surface area and volume distributions were then calculated for each merged number distribution assuming all particles were spherical, as were the number concentrations of particles larger than 500 nm dry diameter (N_{500}).

2.2.3.4 Use of bulk scattering coefficients to estimate aerosol surface area

DeMott et al. (2016, hereafter D16) proposed a method for retrieving dry marine aerosol surface area from ambient bulk aerosol scattering coefficients (b_{sp}), using a three-channel nephelometer. In the absence of available nephelometer data from CAP-2, theoretical Mie calculations based on the merged aerosol size distributions were used to assess this technique for retrieving dry marine aerosol SA. In this study, theoretical scattering distributions and integrated scattering were estimated for each size distribution at wavelengths corresponding to an Ecotech Aurora 4000 Polar Nephelometer (450 nm, 525 nm, 635 nm), assuming spherical particles and using a refractive index of n=1.5 (Tang et al. 1997). Ångström exponents (å) were then calculated for each wavelength pair from the calculated scattering coefficients using:

$$\mathring{a} = \frac{-log\left(b_{sp}^{\lambda_1}/b_{sp}^{\lambda_2}\right)}{log\left(\lambda_1/\lambda_2\right)} \tag{2.3}$$

where λ_1 and λ_2 refer to different measured wavelengths (Seinfeld and Pandis 2016). Following the methodology of D16, the blue/red å was used to assign an effective aerosol scattering efficiency, Q, under the assumption that the particles being measured can be characterized as having a single effective scattering size. D16 utilized a step function for Q, where if the ambient red/blue å>1, Q was assigned as 3 (submicron particles dominate scattering), and if å<1, Q was assigned as 2 (supermicron particles dominate scattering) (Table A.1; DeMott et al. 2016; Mulcahy et al. 2009). The same step function was applied to the dry scattering measurements from CAP-2, which will be discussed further in Sec. 2.3.2. The integrated aerosol surface area can then be estimated from the blue b_{sp} and the calculated scattering efficiency:

$$SA_{scat} = 4\left(\frac{b_{sp}^{450nm}}{Q}\right) \tag{2.4}$$

In D16, the estimated aerosol surface areas were then adjusted for hygroscopic growth using the measured RH and assumed HGF. During CAP-2, the aerosol size distributions were measured dry, all theoretical calculations were performed for 0% RH, and no further adjustments were made. Aerosol surface areas calculated using Mie theory and the D16 estimates of Q were compared to those inferred directly from the number distributions to evaluate this technique for dry marine aerosols in Sec. 2.3.2. Particularly for sea salt, particle nonsphericity is an important consideration that influences optical properties and was not explicitly considered in the Mie calculations presented here. Bi et al. (2018) provide a comprehensive assessment of the influence of RH, assumed particle mixing state, and nonsphericity on sea salt optical properties. For visible wavelengths (and their size distributions), they found a spherical assumption overestimates scattering by a maximum of about 10%, and at 66% RH, the overestimation is a maximum of about 12%. As a result, our Mie scattering calculations may overestimate scattering by up to 10%, and a consequent overestimation of Q by the same amount (Eq. 2.4).

2.2.3.5 Lidar

The MA method of retrieving aerosol surface area and N_{500} from lidar profiles was evaluated for the Southern Ocean using the Leosphere RMAN 510 Raman UV polarization lidar (355 nm) deployed on the RV *Investigator* during CAP-2, which provided profiles of height-resolved backscatter along the voyage track (Alexander and Protat 2019; McFarquhar et al. 2021). The elastic lidar equation was solved using the Rayleigh returns during clear-sky intervals (Fernald 1984). Only profiles retrieved at night were retained, due to the improved signal-to-noise ratio and profile-to-profile stability of the lidar's backscatter signal. Lidar particle linear depolarization ratios were consistently less than 5% throughout CAP-2, indicating hydrated marine aerosols were the primary aerosol type observed (Alexander and Protat 2019). The near-surface mixed layer mean lidar ratio (S=20 sr) observed during CAP-2 and the preceding CAPRICORN-1 voyage (similar region) was used for all profiles to estimate height-resolved aerosol extinction coefficients from the backscatter measurements (Alexander and Protat 2019). These were then converted to dry aerosol surface area and N_{500} profiles using the MA marine aerosol conver-

sion factors, as described in Sec. 2.2.2. Since MA assumed a constant HGF of 2, whereas the ambient RH is variable, the influence of the HGF value used to derive dry aerosol surface areas was explored using RH measurements collected on the foremast of the RV *Investigator*, followed by calculating an expected HGF for SSA using the Extended Aerosol Inorganic Model (E-AIM; Clegg et al. 1998; 2021) for each lidar profile.

To enable comparisons between the lidar-derived aerosol surface area and N_{500} and those from in-situ aerosol instruments (Sec. 2.2.3.3, 2.2.3.4), lidar-derived values at an altitude of 300 m were used, which is the lowest level at which the lidar's overlap function is essentially unity. To minimize differences in the air masses observed by the in-situ and remote-sensing instruments, only lidar profiles where the boundary layer was well-mixed were considered. Formally, the inversion height, identified by radiosondes launched from the ship, was required to be at least 500 m in altitude to ensure lidar data collection within the well-mixed boundary layer. Additionally, the inversion strength of retained profiles was at least 5 K km-1, and the change in potential temperature between the surface and inversion height was <4 K. Adjusting these thresholds had minimal effect on the lidar profiles selected, since a well-mixed near-surface layer and strong temperature inversions at the top of the boundary layer are often present during clear-sky conditions over the Southern Ocean (Alexander and Protat 2019). These thresholds and the other requirements discussed above resulted in the selection of 157 2-minute (approximate averaging time) lidar profiles. Aerosol parameters at 300 m derived from the lidar profiles were averaged to the same 30-min intervals as the merged number distributions (Sec. 2.2.3.3) to facilitate comparisons between the different estimates, resulting in 17 30-min periods.

The impact of particle nonsphericity on backscatter (and hence lidar ratios) can be considerable. Alexander and Protat (2019) have shown the effects of lidar ratio on a dried sea spray (nonspherical) aerosol layer, and found they can be readily detected by the RMAN 510 through shifts in depolarization, in addition to sharp increases in derived lidar ratios (see e.g. Alexander and Protat 2019, Fig. 5). In this manuscript, we limited the analysis to lidar retrievals at 300 m, since Alexander and Protat (2019) showed that nonspherical sea salt layers in this region were

primarily found in dehumidified decoupled layers above the mixed layer, and the lidar observations near the surface were consistent with the presence of spherical particles.

2.2.4 Radiosondes

Radiosondes were launched from the RV *Investigator* every 3-6 hours during CAP-2, for a total of 234 successful releases (Vömel and Brown 2018). Vertical profiles of temperature, humidity, and wind were collected for each launch, up to a median altitude of 17.9 km. We determined the altitude of the temperature inversion at the top of boundary layer as the altitude of the maximum vertical gradient in potential temperature between 250 m and 3000 m (Alexander and Protat 2019). Since radiosondes were launched regularly throughout the campaign, we assume that the thermodynamic profiles sampled by the radiosondes are comparable spatially and temporally with observations made by the lidar directly above the ship.

2.2.5 Microtops II Sun Photometer

A portable Microtops II sun photometer instrument was deployed during CAP-2 as part of the AERONET Maritime Aerosol Network (MAN; Smirnov et al. 2009), and was used to collect Ångström exponent (440-870 nm) and AOT (440, 500, 675, 870 nm) data during clear-sky periods. The AOT measurements at 440 nm were extrapolated to 355 nm to match the lidar wavelength (Sec. 2.2.3.5). As occasionally several measurements were taken sequentially, any measurements collected within 30-min were averaged, to enable comparison with the CAP-2 merged size distributions (Sec. 2.2.3.3). If a radiosonde sounding (Sec. 2.2.4) was available within 6 hours, each Microtops AOT measurement was converted to extinction (Mm^{-1}) using the boundary layer inversion height retrieved from the sonde profiles and assuming particles were well mixed vertically within the MBL. If there was no sounding within 6 hours, the AOT measurement was excluded from further analyses.

2.2.6 Aerosol Measurements during SOCRATES

Aerosol measurements on the G-V (UCAR/NCAR - Earth Observing Laboratory 2005) considered here consisted of optical detection of submicron particles using two ultra-high sensitivity aerosol spectrometer (Droplet Measurement Technologies, UHSAS) instruments (0.06 - 1.0 μm particle diameters), optical detection of supermicron particles up to 50 μm using a wing-mounted cloud droplet probe (Droplet Measurement Technologies, CDP; Lance et al. 2010), and physical collection and sizing of impacted supermicron particles (0.7-16 μm dry diameter) using the Giant Nucleus Impactor (GNI; Jensen et al. 2020). One UHSAS instrument was mounted on the wing of the G-V and one sampled in the cabin via a counterflow virtual impactor inlet that was also operated for isokinetic total air sampling (Hartery et al. 2020). We primarily employed data from the wing mounted UHSAS, CDP, and GNI instruments for this study.

The wing mounted UHSAS data were considered to represent dry particle distributions. As also discussed by Sanchez et al. (2021b), we expected that the use of deicing heaters would lower the relative humidity to which particles were exposed to below 40% in the optical cavity, akin to how the same heaters affected particles in the passive cavity aerosol spectrometer probe (PCASP) measurements discussed by Strapp et al. (1992). Striking in the UHSAS measurements in SOC was an apparent particle mode near 0.6-0.7 μm, as shown in Sec. 2.2. Sanchez et al. (2021b) hypothesized that this feature was a consequence of remnant unevaporated water (a deliquescent mode) on the largest particles sensed by the UHSAS. We have since observed that this mode also appears in the UHSAS distributions measured from the CVI inlet inside the G-V cabin (not shown here), which were also assumed to represent dry measurements by Hartery et al. (2020). This suggests that instead of residual water, the feature is a shattering artifact from the inlets, or, more likely, is related to how marine aerosols are sized by the UHSAS. Recent work (Kupc et al. 2018; Moore et al. 2021) has demonstrated that sea spray aerosols, which are expected to have refractive indices much lower than those of the commonly-used PSL calibration particles, will be undersized by the UHSAS. When combined with lower response sensitivity

at sizes above 500 nm, such unexpected features may appear in the UHSAS distribution. This topic requires further study and is not further considered here.

Data from the CDP and GNI were merged with the UHSAS to generate distributions to dry sizes >10 μm, in order to capture all surface area and volume modes for primary SSA. The first and last three bins of the UHSAS data, and the first two bins of the CDP data, were omitted from these merged distributions since they have low counting efficiencies, and in the case of the CDP, also large variability in Mie scattering. The GNI data reported here represent spherical-equivalent dry sizes of particles collected on slides during flights. The GNI particle sizing procedure, which involves re-humidification of particles to estimate their dry mass on the basis of their wet size and reference to sea salt data from Tang et al. (1997), is fully described in Jensen et al. (2020). Since both the UHSAS and GNI data are reported dry, it was necessary to adjust the CDP data for water uptake. The CDP data were considered to represent humidified aerosol sizes, in equilibrium with ambient RH, since it is an open-path instrument. The CDP bin sizes were first corrected following Lance et al. (2010), and then further decreased in size based on hygroscopic growth factors predicted for proxy sea salt particles using E-AIM (Clegg et al. 1998; 2021). Sea salt will dominate particle mass at dry sizes above 1 μm and influences of organics on water uptake should be small. Data from the VCSEL water vapor sensor (SouthWest Sciences and UCAR/NCAR-Earth Observing Laboratory 2008; Zondlo et al. 2010) on the G-V (cabin top-mounted inlet) were was used to estimate the appropriate HGF for each CDP size distribution based on the ambient relative humidity. We note that the differences between using E-AIM for adjusting the CDP data to dry size versus the reference data in Jensen et al. (2020) could lead to a difference of no more than 5% in dry size between the CDP and GNI.

Thirty-six periods of level G-V flight in the lower marine boundary layer (150 – 300 m MSL) in SOC, covering latitudes from about 49-61°S, were identified for analyses of aerosol distribution data. For each pass, typically 8-10 minutes, relative humidity and horizontal wind speed were averaged, and total CDP concentrations were examined to assure that there was no cloud contamination. Each merged size distribution was then fit with two or three lognormal modes,

using the same criteria as described in Sec. 2.2.3.3 for the CAP-2 distributions, except the Aitken mode was not fit, since the UHSAS does not extend to small enough sizes. The sum of the middle and largest (if needed) modes were considered to represent primary marine aerosol, which is further discussed in Sec. 2.3.1. A gap in data availability was always present between the CDP or GNI data in the supermicron regime and the submicron UHSAS data. For all flights where GNI data were available, it was consistently noted that the CDP and GNI distributions agreed quite closely after adjustments were made to correct the CDP bin sizes.

2.3 RESULTS

2.3.1 Comparison of SOCRATES and CAPRICORN-2 aerosol measurements

An example aerosol number distribution from SOC RF04 on January 24, 2018, is shown in Fig. 2.2a, which includes the average single-mode PMA fit by Sanchez et al. (2021b) using only the G-V wing-mounted UHSAS data, in addition to the PMA fit used in this study. Unlike Sanchez et al. (2021b), the peak of the narrow mode ~0.6-0.7 μm in the UHSAS data was ignored during fitting in this study, as including it artificially decreases the mode width and forces the mode size into that range. While there is reasonable agreement between both studies at sizes up to 1 μm, our results indicate inclusion of the CDP and GNI data are necessary to clearly define the significant coarse mode present, which becomes increasingly important for estimating PMA surface area and volume concentrations. A broader PMA distribution is consistent with those reported in the North Atlantic by Saliba et al. (2019) using a similar fit routine as Sanchez et al. (2021b). It also agrees well with the regional Southern Ocean distributions of Hartery et al. (2020) describing "sea spray particles" (defined as the distribution humidified to 80% RH) that were composed by combining SOC G-V cabin-based UHSAS data with particle measurements from a separate ship voyage south of New Zealand. Fig. 2.2b shows a similar example from CAP-2, during the SOC RF12 overpass of the RV *Investigator* on February 18, 2018, which also has a much broader PMA mode than the Sanchez et al. (2021b) fit, in agreement with the SOC results. In accordance with many recent studies of marine aerosols (Hartery et al. 2020; Lewis

and Schwartz 2004; Modini et al. 2015; Saliba et al. 2019; Sanchez et al. 2021b), the majority of size distributions for both campaigns only required a single PMA mode to achieve a coefficient of determination for the entire lognormal fit >0.9 (86% for CAP-2 and 84% for SOC).

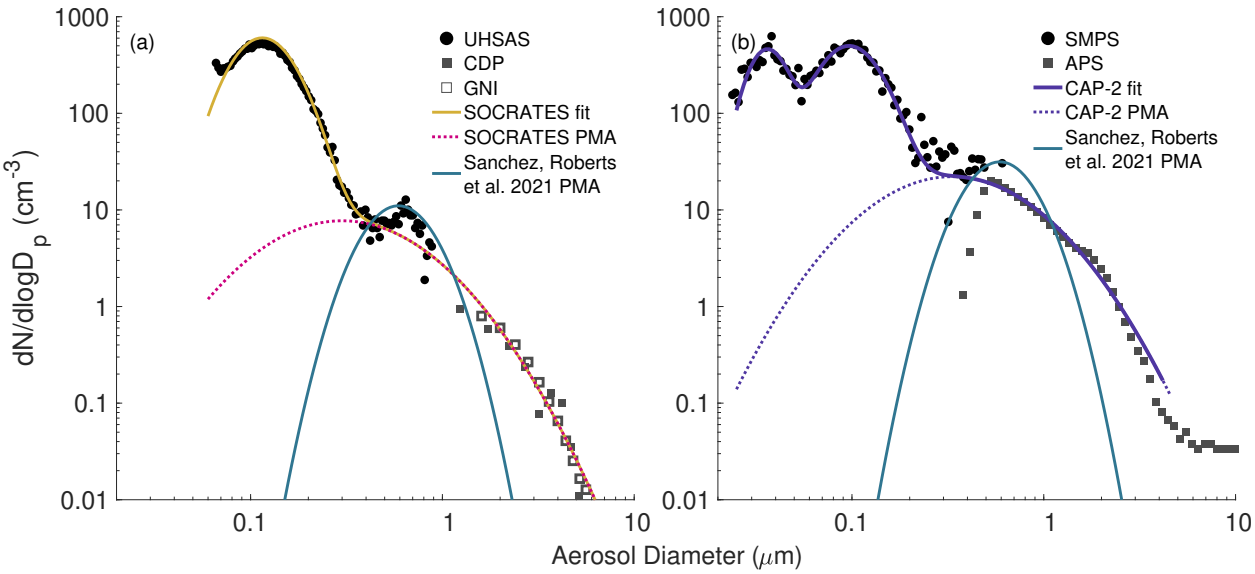

Figure 2.2: Example size distributions from a) SOC RF04 merged aerosol number distribution for a 9-minute marine boundary layer pass at 165 m and b) CAP-2 merged aerosol number distribution during the SOC RF12 overpass. In panel a) UHSAS data are given by filled black circles, CDP data by filled gray squares, and GNI data by open gray squares. The SOC lognormal fit is shown in the solid gold line and PMA estimate in the dashed magenta line. In panel b) SMPS data are given by filled black circles, APS data by filled gray squares, the CAP-2 lognormal fit in the solid purple line, and PMA estimate in the dashed purple line. The average single-mode PMA fit from Sanchez et al. (2021b) is shown in both panels in solid blue for comparison, and has been scaled by the number concentration of each PMA mode.

Direct comparisons between CAP-2 and SOC MBL size distributions were possible on two research flights: RF04 (Jan. 24, 2018) and RF12 (Feb. 18, 2018). Given the large speed difference between the ship and aircraft, as well as the different averaging intervals used for their size distribution measurements, G-V and CAP-2 distributions were counted as overpasses if there was any temporal overlap between their respective averaging intervals. Additionally, the midpoint of the G-V MBL level leg was required to be within 30 km of the average RV *Investigator* position during their respective time windows. G-V distributions represent averages of 8–10-minute level legs in the MBL (Sec. 2.2.6), and CAP-2 distributions are 30-min averages, as described in

Sec. 2.2.3.3. Two G-V overpasses were identified using these criteria, and typically two CAP-2 distributions were identified that overlapped with each G-V overpass. Lognormal fits to G-V and CAP-2 aerosol size distributions during these overpasses are shown in Fig. 2.3. Although the mode positions and shapes differ slightly, good agreement in number concentration is seen in both cases for sizes >0.06 μm, which is the minimum size measured by the UHSAS on the G-V. This suggests the ship-board measurements were representative for the MBL and were not unduly influenced by being close to the ocean surface. For sizes >2 μm, the CAP-2 distributions underpredict particle number, which is likely due to supermicron particle losses not captured by the calculations of inlet transmission efficiencies (Sec. 2.2.3.1), or to spatial mismatch between the ship and aircraft. Comparisons of the total number of particles, surface area, and volume from the G-V, versus those for particles <5 μm (Fig. A.3a,d,g) were used to estimate particle losses unaccounted for in the CAP-2 inlet modeling. Strong linear relationships were found between particle number (R^2=1; Fig. A.3a) and surface area (R^2=0.96; Fig. A.3d) <5 μm and integrated quantities, and a moderate relationship was found between particle volume <5 μm and total volume (R^2=0.37; Fig. A.3g). This exercise indicates the CAP-2 measurements are likely to have accurately captured particle number, underestimated particle surface area by ~15%, and underestimated particle volume by ~60% due to poor inlet transmission of particles >5 μm. Similar trends were seen when particles with 0.5<D<5 μm were correlated with D>0.5 μm (Fig. A.3b,e,h), and when PMA with D<5 μm were correlated with total PMA (Fig. A.3c,f,i). The best-fit linear relationships shown in Fig. A.3 were used to correct the integrated CAP-2 number, surface area, PMA, and volume concentrations to better represent atmospheric concentrations, and these corrected concentrations are used throughout this study for integrated quantities.

Normalized histograms of integrated particle number, surface area, PMA, and volume concentrations for all CAP-2 (following additional loss corrections based on Fig. A.3) and SOC size distributions are shown in Fig. A.4. Ranges of all quantities are similar across the two campaigns, as are the mode positions, with the best agreement for aerosol surface area (Fig. A.4c).

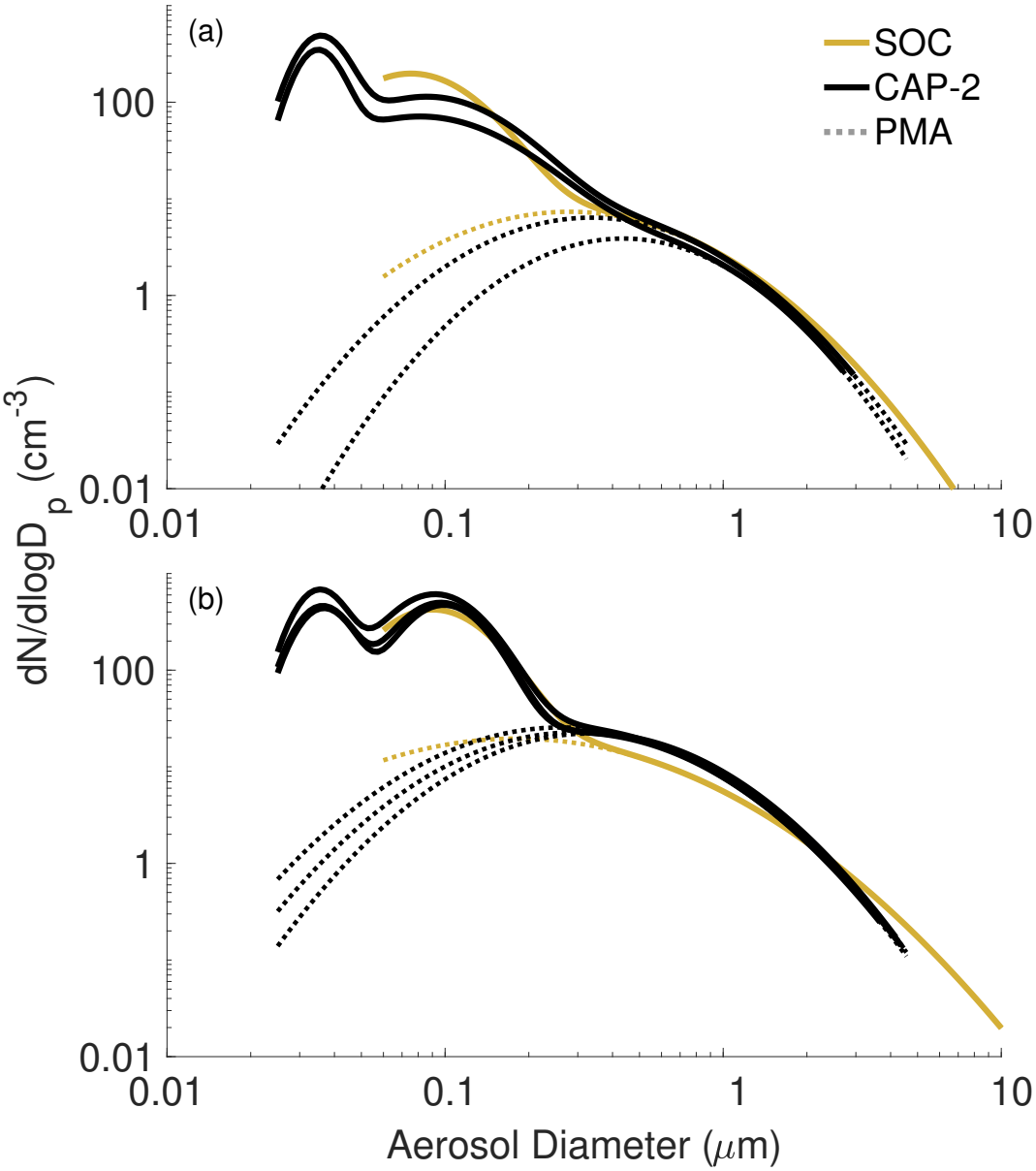

Figure 2.3: Comparisons of SOC and CAP-2 aerosol number distributions during G-V overflights of the RV *Investigator* in the MBL. From SOC flights a) RF04 and b) RF12. CAP-2 data are shown in solid black and SOC MBL data in solid gold lines, with the PMA fits for both campaigns denoted by dashed lines.

For CAP-2, the median surface area concentration is 22.9±11.1 μm^2 cm^{-3}, and for SOC it is 25.9±12.6 μm^2 cm^{-3} (± one standard deviation for each). CAP-2 has a larger median number concentration than SOC (Fig. A.4a; CAP-2: 207±120 cm^{-3}; SOC: 136±80 cm^{-3}) and a greater fraction of distributions with aerosol number >400 cm^{-3}, which is expected due to the SOC instruments being unable to capture the Aitken mode, where a significant fraction of particle number is seen in CAP-2 (Fig. 2.3). SOC, on the other hand, has a larger median volume concentration (Fig. A.4d; CAP-2: 7.0±5.3 μm3 cm^{-3}; SOC: 10.3±6.6 μm3 cm^{-3}) and more distributions with volume concentrations above 15 μm3 cm^{-3}. In addition to differences in instrumentation, some discrepancy in aerosol volume may be due to the different regions and conditions targeted by the SOC flights compared to CAP-2. Overall, the good agreement between CAP-2 and SOC for particle surface area and volume concentrations supports the utility of the corrections presented in Fig. A.3 to account for losses of >5 μm particles within the CAP-2 inlet.

Fig. 2.4 shows total and PMA particle number, surface area, and volume concentrations as a function of wind speed for both field campaigns. Wind speeds shown here are averages during each size-distribution interval from the RV *Investigator* met station on the ship foremast and measurements from the G-V (corrected for air speed) for CAP-2 and SOC, respectively. Following Sanchez et al. (2021b)S, power law relationships were fit to the PMA particle number, SA, and volume concentrations (Fig. 2.4b,d,f) as a function of wind speed, and are reported in Table A.3. PMA concentrations during CAP-2 exhibited a similar correlation with wind speed (Fig. 2.4b; R^2=0.43), as has been seen previously in the Southern Ocean (Sanchez et al. 2021b) and North Atlantic (Saliba et al. 2019). PMA volume concentrations during SOC were more highly correlated (R^2=0.60) with wind speed than during CAP-2 (R^2=0.32), which may be related to different temporal and spatial sampling rates and coverage of the G-V and RV *Investigator*, as well as instrument size restrictions that varied by campaign. The PMA number (Fig. 2.4b) versus wind speed relationships predicted in this study fall between those of Sanchez et al. (2021b) and O'Dowd et al. (1997). Sanchez et al. (2021b) only used SOC UHSAS data to estimate PMA, so it is not surprising that including the coarse mode captured by the GNI and CDP (Fig. 2.2) during

SOC, and by the APS in CAP-2, increases the predicted number concentration of PMA. O'Dowd et al. (1997) used an exponential, rather than power law, model to predict PMA. It agrees well with the relationships derived in this work up to ~10 m s^{-1}, and then rapidly diverges at higher wind speeds. In addition to the differences in functional form, the higher number concentrations predicted by O'Dowd et al. (1997) may be due to their use of particle numbers at 80% RH, rather than the dry distributions used in this work and Sanchez et al. (2021b), as more small particles may grow to large enough sizes to be measured at higher RH. The exponential relationship derived by Saliba et al. (2019) during the NAAMES campaign in the North Atlantic underpredicts PMA from CAP-2 up to wind speeds of ~20 m s^{-1}, particularly around 13-18 m s^{-1} due to the shape of the exponential function.

Saliba et al. (2019) also explored the relationship between PMA mode diameter and atmospheric and oceanic parameters such as wind speed, seawater particle attenuation, and sea surface temperature (SST). Fig. A.5 shows similar relationships for CAP-2 between PMA mode diameter, wind speed, and SST. SST values reported here are measurements from the inlet of the flow-through seawater system on the RV *Investigator*. For the 14% of distributions with 2 PMA modes, the mode diameter representing the mode with the larger number concentration was plotted. In agreement with Saliba et al. (2019), no relationship was found between PMA mode diameter and wind speed (Fig. A.5a), however, there was also no clear relationship between mode diameter and SST for CAP-2 (Fig. A.5b), unlike NAAMES. It should be noted, however, that the majority of SST observations during CAP-2 were at temperatures less than 5 °C, and the SST variation during CAP-2 was driven by latitudinal changes, rather than seasonal variability, as in NAAMES.

PMA number, surface area, and volume concentrations exhibited weak and generally insignificant correlations with latitude (Fig. A.6). Nominally, SOC and CAP-2 have relationships of opposite sign between all aerosol quantities and latitude, although it should be noted the maximum latitude of the G-V was 61 °S, whereas the RV *Investigator* reached the marginal ice zone at 66.5 °S, in addition to there being almost 30 times fewer MBL distributions collected

during SOC. Sanchez et al. (2021b) noted differences between the CCN latitudinal relationships for the SOC and CAP-2 campaigns, and attributed them to differences in sampling strategies and range covered, which is likely also the case here for PMA. The northern and southern transect of CAP-2 had very different PMA number concentrations north of 55 °S, and highly variable concentrations south of 60 °S, which appear to have led to insignificant ($p>0.05$) latitudinal correlations for this campaign. This suggests that meteorological conditions, ocean biogeochemistry, SST, or other factors are more closely related to MBL PMA concentrations over the Southern Ocean than latitude, although further study is needed. Wind speed alone explained up to 60% of PMA concentration variance (Fig. 2.4), supporting this hypothesis. The impact of wind direction, which may reflect differences in warm or cold advection, has not been investigated in this study.

2.3.2 Evaluation of the D16 method for estimating marine aerosol surface area from scattering coefficients

The D16 method for retrieving dry marine aerosol surface area from bulk scattering coefficients (described in Sec. 2.2.3.4) was applied to CAP-2 using Mie calculations based on the merged aerosol size distributions. For data shown in this section only (Figs. 5-7; Fig. A.7-A.9), only the inlet loss corrections presented in Sec. 2.2.3.1 and not the additional corrections derived from Figure S3 were applied, since the Mie calculations require size-resolved aerosol size distributions, and the corrections derived from the G-V data (Fig. A.3) are only applicable to integrated quantities. This is not expected to significantly alter the results presented here, as scattering is dominated by particles smaller than 2 μm, and good agreement in particle number is seen between CAP-2 and SOC below this size (Fig. 2.3).

Normalized frequency distributions of Ångström exponent from the CAP-2 Mie calculations are shown in Fig. A.7. All three å (blue/red, blue/green, green/red) distributions are bimodal, with the largest mode centered around 0-0.25, and ranging from -0.2 to ~0.8. A smaller and very broad mode occurs at larger å values, centered around 1.3 for all wavelength pairs. This bimodal

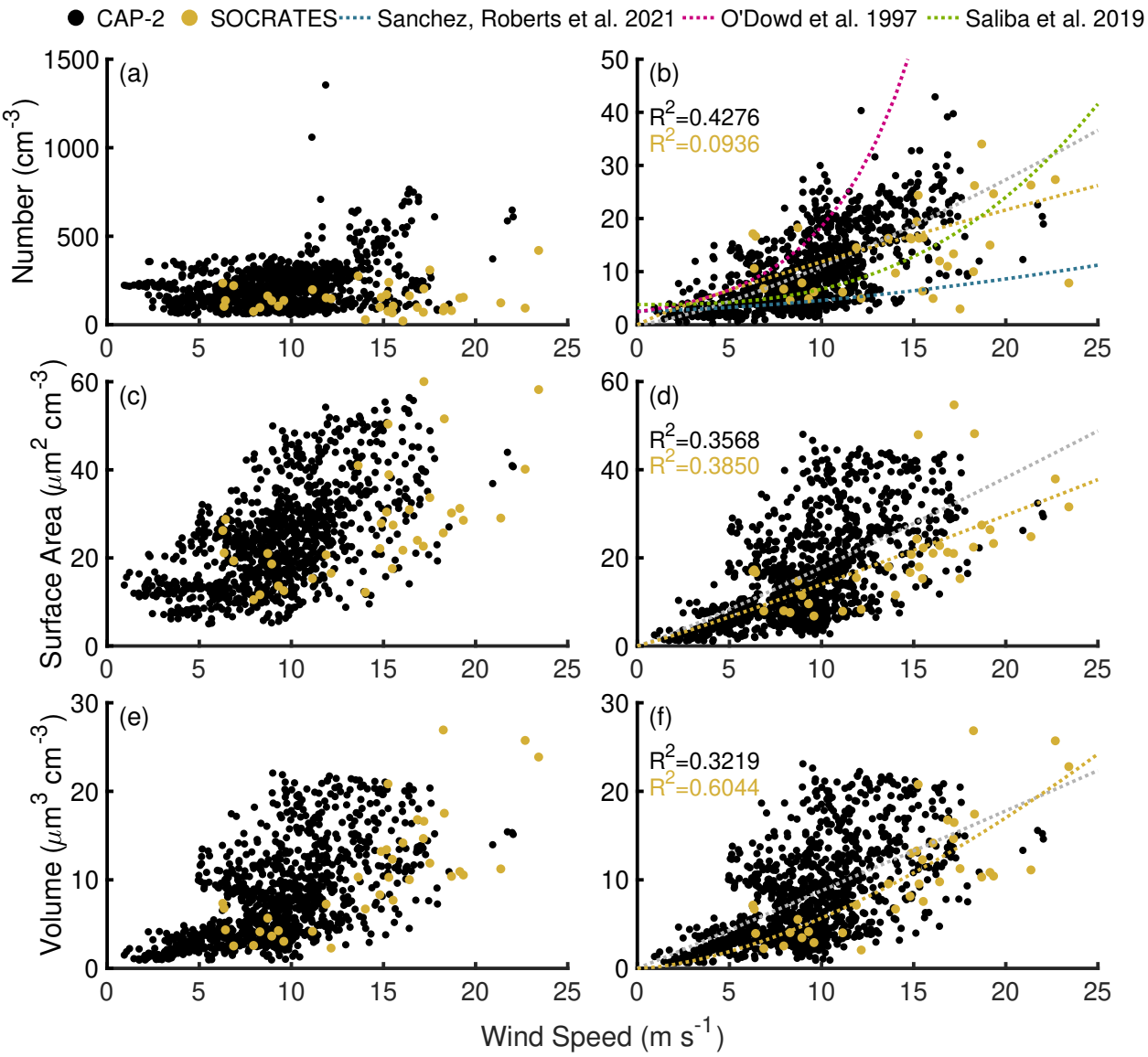

Figure 2.4: Particle a-b) number, c-d) surface area, and e-f) volume concentrations versus wind speed. Panels a,c,e) have total concentrations and b,d,f) show PMA concentrations and best fit power law functions. CAP-2 is in black (power law fits in dashed gray), SOC G-V marine boundary layer passes in gold (power law fits in dashed gold). The blue curve in (b) is the PMA fit from Sanchez et al. (2021b), the magenta curve in (b) is the PMA fit from O'Dowd et al. (1997), and the green curve in (b) is the PMA fit from Saliba et al. (2019).

shape can also be seen in the "clean marine" å frequency distribution reported by Mulcahy et al. (2009) for Northern Hemisphere marine aerosols from Mace Head, Ireland. The smaller mode centered at å=1.3 is more pronounced in the Mace Head data, which may reflect the larger bin size used in their distribution (0.2 vs 0.1 for CAP-2), in addition to differences caused by higher average wind speeds in the Southern Ocean than North Atlantic (Zheng et al. 2016), seasonal variation in sea spray production, or other factors. The CAP-2 Mie å calculations are also in agreement with nephelometer measurements of Ångström exponent from coastal marine sites in NOAA's Federated Aerosol Network (Andrews et al. 2019), as well as ship-based measurements collected near Hawaii during ACE-Asia, which reported å=0.16 ± 0.60 for air masses classified as marine (Carrico et al. 2003).

This dataset provides an opportunity to test whether the simple step function used in D16 to select Q based on å reproduces observed surface area (Eq. 2.4). A comparison between aerosol surface area from the merged CAP-2 size distributions and those estimated using the D16 method applied to Mie calculations based on the same distributions is shown in Fig. 2.5. The points with low å values (<~0.5), which were assigned an effective scattering efficiency of Q=2 based on the D16 criteria, cluster around the 1:1 line, as expected, with a maximum deviation of 25%. Those points with å>1, and assigned Q=3 by D16, underestimate dry aerosol surface area by a factor of 2 or more. To explore the reason for this discrepancy, effective aerosol scattering efficiency was calculated for each size distribution using Eq. 2.4, by replacing SAscat with the measured dry aerosol surface area and solving for Q. The results for each wavelength pair are shown in Fig. 2.6a as a function of the Mie-calculated Ångström exponent. For the majority of the points, which cluster around å=±0.25, Q=2 is a reasonable approximation, which explains the good agreement in Fig. 2.5 for those distributions with å<0.5. However, for distributions with å>1, the calculated Q varies from about 0.5-1.5, rather than the Q=3 that would be assigned by D16.

The bimodal å distribution was investigated further in Fig. 2.6b-c, which again show Q calculated from Mie scattering calculations and the dry aerosol surface area against the Mie

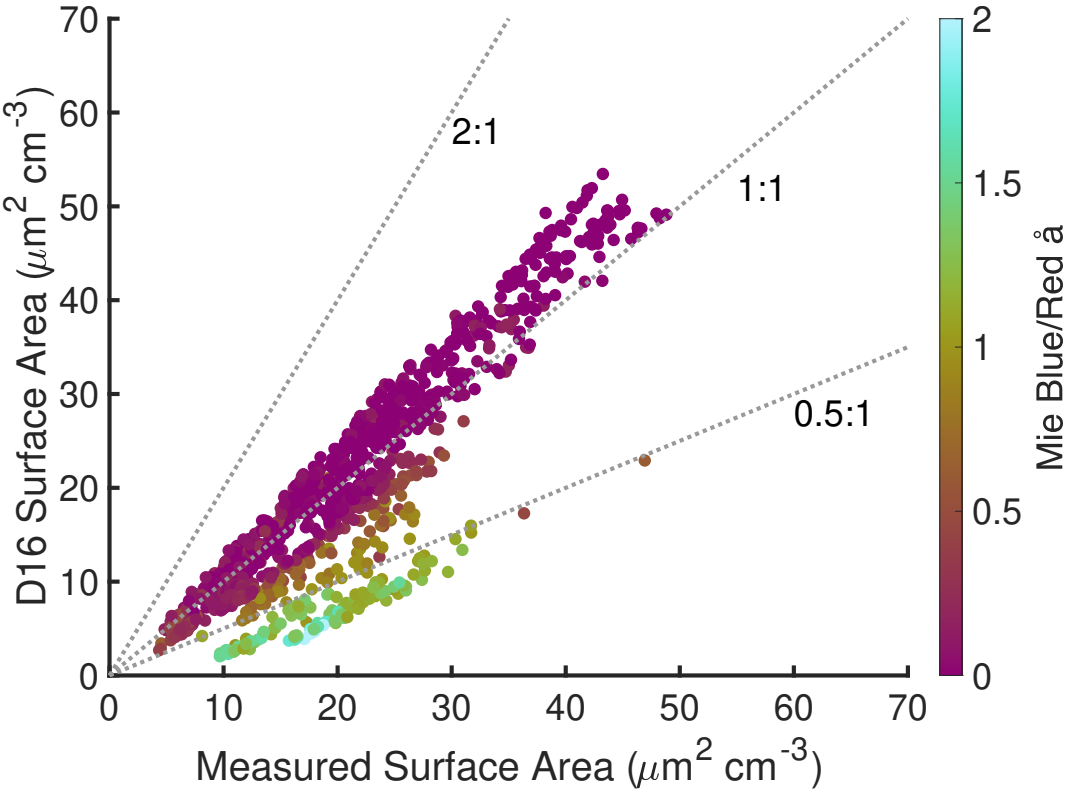

Figure 2.5: Correlation between total aerosol surface areas calculated by integrating the CAP-2 size distributions (x-axis) and those from the D16 method based on Mie calculations (y-axis). Symbols are colored based on the blue/red Ångström exponent from the Mie scattering calculations.

Ångström exponent, although only for the blue/red wavelength pair. Fig. 2.6b is colored by wind speed in 5 m s^{-1} bins, and Fig. 2.6c by latitude of the RV *Investigator* in 5° bins. å=0.8 was selected based on Fig. A.7 to separate the two modes of the Ångström exponent distribution and is indicated by the dashed lines in Fig. A.7 and Fig. 2.6. Distributions with å>0.8 primarily occur at low wind speeds and high southern latitudes. This can be seen even more clearly in Fig. A.8, which shows frequency distributions of wind speed and RV *Investigator* latitude separately for aerosol distributions with blue/red å<=0.8 and å>0.8. Previous work (Saliba et al. 2021; Schmale et al. 2019; Twohy et al. 2021) has demonstrated a large proportion of CCN in the Southern Ocean region are biogenic, and likely derive from the high chlorophyll-a waters present in the marginal ice zone, where enhanced DMS fluxes have been observed (Webb et al. 2019). DMS fluxes peak in mid-summer, the same season as CAP-2, and were estimated by Webb et al. (2019) to be sufficient to nucleate particles in the MBL near the West Antarctic Peninsula 63% of the time. Nucleation of ultrafine particles has been observed in other regions of the Antarctic coastal MBL (e.g. Humphries et al. 2015; Jokinen et al. 2018; Jung et al. 2020; Yu and Luo 2010) in summertime, and biogenic gases are also hypothesized to contribute to condensation and the growth of particles to CCN-sizes (Twohy et al. 2021). Lower wind speeds near the Antarctic continent, in addition to the suppression of sea spray formation around the marginal ice zone (Nilsson et al. 2001) can lead to fewer large primary marine aerosol particles and lower aerosol surface area near Antarctica (Humphries et al. 2015).

Sanchez et al. (2021b) used HYSPLIT (Rolph et al. 2017; Stein et al. 2015) back-trajectories to classify particle regimes during SOC, and found many of the back-trajectories for the "aged" particle type originated near or over the Antarctic coast, coinciding with regions previously shown to have elevated DMS and other phytoplankton-derived VOCs (e.g. Alroe et al. 2020; Humphries et al. 2016). HYSPLIT back-trajectories run using the same method as Sanchez et al. (2021b) provide an evaluation of the degree of marine influence (Sanchez et al. 2021a) of the aerosols measured during CAP-2, defined as the fraction of a 5-day back-trajectory (initialized at 200 m above the location of the RV *Investigator*) that passed over the ocean. Fig. 2.7 shows

the CAP-2 ship track with aerosol Ångström exponent indicated by marker size and the degree of marine influence indicated by marker color. Periods with å>0.8 are concentrated at high latitudes, as also seen in Fig. 2.6 and Fig. A.8. The majority of the periods with marine influence <20% also occur at high Southern latitudes. This supports the findings of Alroe et al. (2020) and Chambers et al. (2018) that air masses with continental influence, either Antarctic or long-range transport, extend a considerable distance from the Antarctic continent and can influence measured aerosol properties. Some of the periods with high å>0.8 have a small degree of marine influence (<20%), but others are predominantly marine (>80% marine influence), indicating a mix of sources in this region. CAP-2 aerosol size distributions exhibited similar influences from submicron particles as å (Fig. A.9). Periods with larger Ångström exponent predominantly have PMA fractions, defined as the fraction of total particle number attributed to PMA, of <5%, indicating a large number of small accumulation/Aitken mode aerosols are present. As also seen in Fig. 2.7, periods with å>0.8 have a wide variety of fractional marine influence, but a higher proportion of periods with marine influence <20% than those periods with å<0.8. Based on these findings, we hypothesize that the distributions with å>0.8 that primarily occur near the Antarctic coast are dominated by submicron biogenic, continental, or long-range transported particles, which control the scattering in this region due to lower PMA formation. This is supported by Humphries et al. (2021), who found the ratio of CCN to total particles increased south of 65 °S, as well as the relative contribution of sulfur to submicron aerosol mass. As a result, we have set å=0.8 as an upper limit for defining distributions which are primarily comprised of PMA throughout this study.

An exponential relationship of the form $Q = a \times e^{b\text{å}}$ was found to best describe the correlation between dry marine aerosol scattering efficiency and Ångström exponent, and the best-fit function between Q_{Green} and blue/red å is shown on all three panels of Fig. 2.6. For those distributions with å<0.8, thought to represent PMA-dominated regimes, the average Q (Q=2.00) agrees exactly with the Q=2 assigned by D16. However, Q ranges from ~1.0-2.7 for these distributions, which induces an uncertainty of ±50% when aerosol surface area is estimated us-

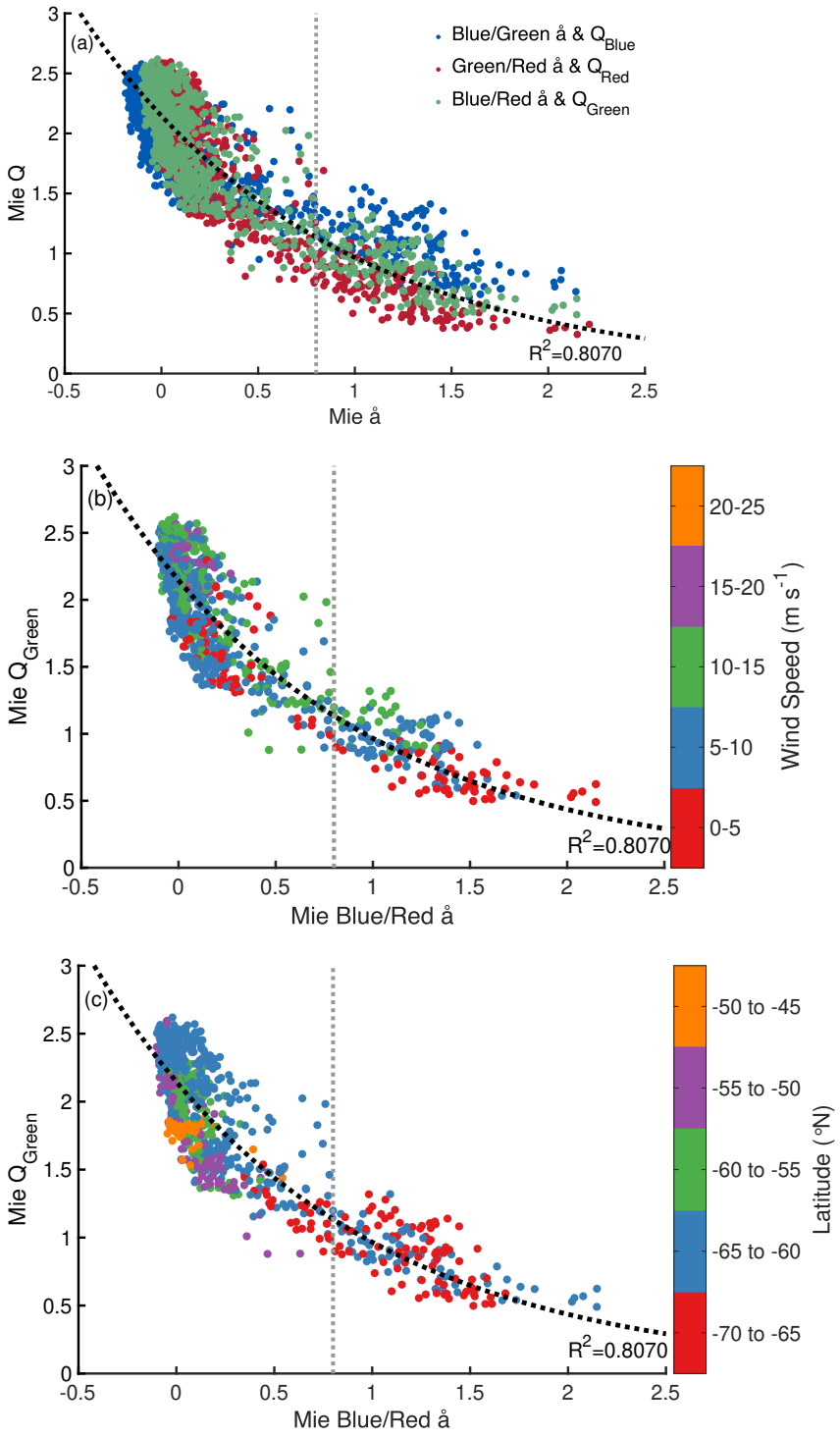

Figure 2.6: Relationship between Ångström exponent and effective dry aerosol scattering efficiency for the CAP-2 size distributions. (a) includes å for all three wavelength pairs and the corresponding Q. (b) and (c) show only Q_{Green} and blue/red å, with symbols colored by wind speed in 5 m s^{-1} bins (b) and latitude of the RV *Investigator* in 5° bins (c). An exponential best-fit relationship between Q_{Green} and the blue/red å is shown on all three panels.

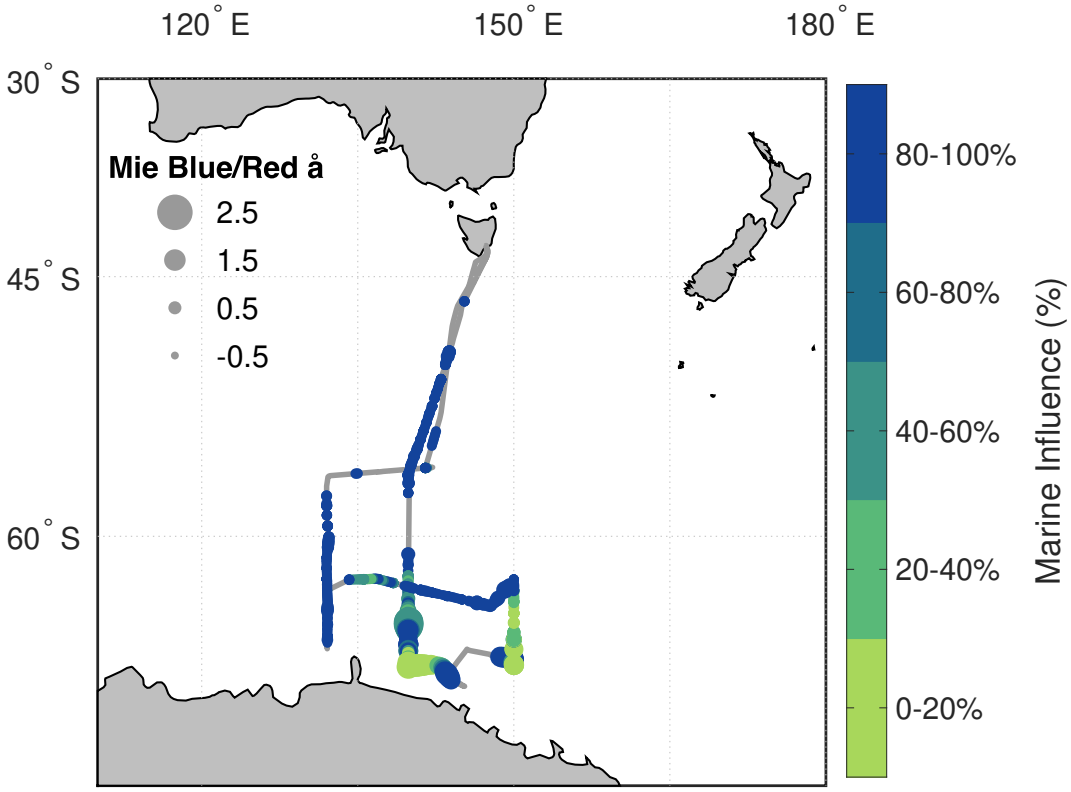

Figure 2.7: Track of the RV *Investigator* (CAP-2; solid gray line) with measurements of aerosol Ångström exponent (å) overlaid and indicated by marker size. Observations of å are colored by the degree of marine influence, defined as the fraction of a 5-day back-trajectory that passed over the ocean (Sanchez et al. 2021b;a).

ing Q=2 for any distribution with å<0.8. Distributions with å>0.8, which would primarily be assigned Q=3 by D16, have Q ranging mostly from 0.5-1.5. Some discrepancy between the D16-assigned Q values and those calculated directly are to be expected, since the å thresholds in D16 correspond to ambient-humidity scattering coefficients, whereas all the CAP-2 data are dry. Because of these differences, we propose that instead of the step function used by D16 to assign scattering efficiency, the exponential relationship shown in Fig. 2.6 $\left(Q_{green} = 2.15 \times e^{-0.80\mathring{a}}\right)$ be used to predict Q from å when estimating marine aerosol surface area from dry scattering measurements. Since this relationship was derived from Mie-calculated scattering coefficients, rather than nephelometer observations, further validation against nephelometer data will be needed. Table A.1 summarizes the differences between the D16 method for estimating marine aerosol surface area and the one proposed here.

2.3.3 Evaluation of the MA method for estimating particle surface area and coarse mode number concentrations using lidar extinction

The Southern Ocean is considered one of the most pristine marine regions on earth, and also has a unique meteorological environment with persistent high winds, high wave heights, and associated high concentrations of sea spray in the boundary layer (e.g. Wang et al. 2015b). Therefore, as a first step, we explored whether MA's existing marine-aerosol parameterization (Sec. 2.2.2) was applicable to this region. We used Level 2.0, Version 3 inversion data from the 2-year deployment of an AERONET CIMEL sun photometer during the Macquarie Island Cloud and Radiation Experiment (MICRE; Marchand 2020; McFarquhar et al. 2021). The frequent cloudiness in the region, however, resulted in only 25 data points, and these were not representative of all seasons: 23 inversions were for data from September-December (Austral spring and early summer). Only 7 of the inversions met the MA criteria (Fig. A.10). However, fourteen of the total points had å < 0.2, suggestive of a dominant coarse mode likely associated with sea spray, despite $AOT_{500\,nm}$ as large as 0.16 (Andrews et al. 2019; Carrico et al. 2003; Mulcahy et al. 2009). In Fig. A.11, we applied the MA methodology to all available MICRE data points

to compute the total wet aerosol surface area and superimposed the MA correlation. MICRE data with low å appear to be reasonably represented by the MA fit at 355 nm, although most of the points meeting the MA criteria are not. Additionally, for points near AOT355 nm = 0.07, it is apparent that surface area varied by a factor of 2 for the same AOT.

A Microtops II sun photometer was present on the RV *Investigator* as part of the AERONET Maritime Aerosol Network (MAN) and provided measurements of Ångström exponent and AOT during CAP-2 (Sec. 2.2.5). Although full AERONET inversions are not available from MAN measurements, the MA technique was further assessed using these open ocean Microtops data, coupled with the aerosol size distributions from CAP-2. Extinction at 355 nm, estimated from Microtops AOT using boundary layer inversion height (BLH) retrieved from radiosondes released from the RV *Investigator* (Sec. 2.2.4), had linear relationships with both aerosol surface area and N_{500} (Fig. 2.8). AOT at 355 nm (Fig. A.12) had a stronger linear correlation with both aerosol surface area and N_{500} than did extinction, which is likely due to variability and uncertainty in estimates of BLH needed to calculate extinction. BLH of radiosondes launched during CAP-2 varied from 0.53-4.98 km, with a median of 2.07 km. The median value is consistent with the M2-M4 and C1-C2 categories discussed in Truong et al. (2020), which includes soundings from the CAP-2 campaign in addition to several others over the Southern Ocean during 2016-2018. As the CAP-2 surface area and N_{500} already represent dry values, no further adjustment to the conversion factors shown in Fig. 2.8 were needed to account for HGF. Notably, the conversion factors between extinction and dry aerosol surface area ($c_{s,m}$,microtops/4=0.106 ± 0.022 μm^2 cm^{-3} Mm) and N_{500} ($C_{1000,m}$,microtops=0.0182 ± 0.0036 cm^{-3} Mm) derived using the Microtops data are a factor of 4.9 and 2.8 smaller, respectively, than those presented in MA for marine aerosols at 355 nm.

Radiosondes up to 6 hours before or after a Microtops measurement were used to convert Microtops AOT to extinction, which introduces additional unaccounted-for uncertainty, since the boundary layer structure may change during that interval. To assess the influence of uncertainty in BLH, the conversion parameters were also derived from Microtops AOT355 nm

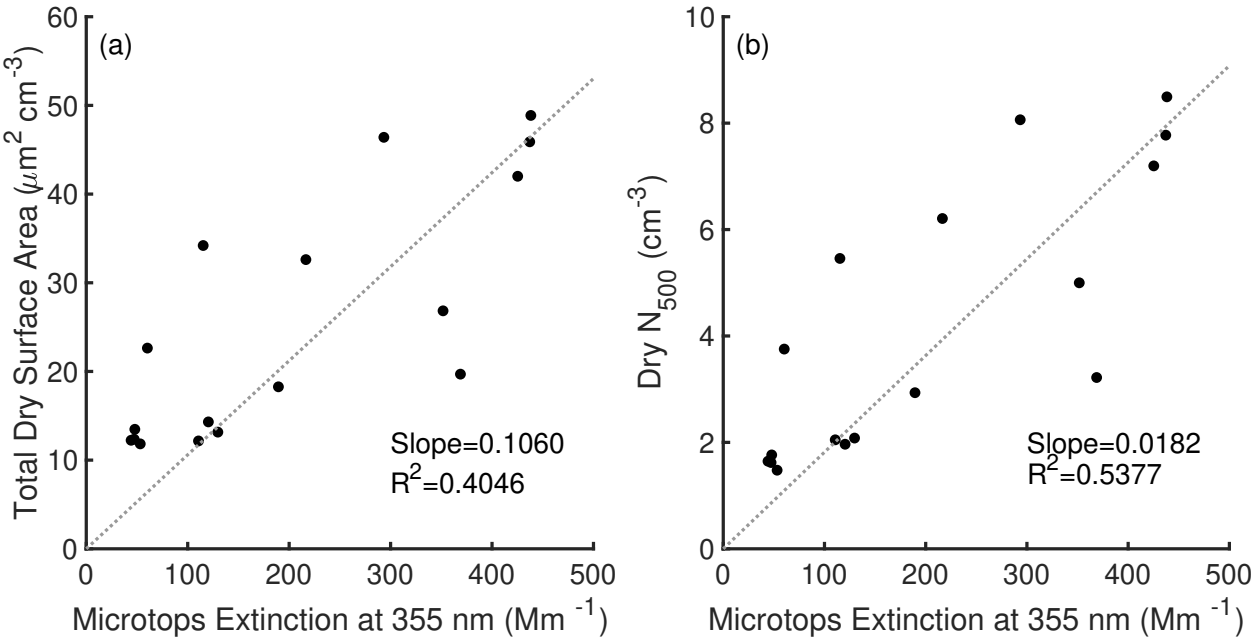

Figure 2.8: Correlations of extinction at 355 nm estimated from the MAN Microtops measurements with (a) total aerosol surface area and (b) N_{500} during CAP-2. Aerosol surface area and N_{500} are from merged aerosol size distributions.

converted to extinction using the median CAP-2 BLH of 2.07 km instead of estimates from individual sondes. This gives an aerosol surface area parameter of 0.173± 0.021 μm^2 cm^{-3} Mm, and an N_{500} parameter of 0.0292 ± 0.0042 cm^{-3} Mm, which, although larger than the Microtops parameters derived from individual sondes, are still significantly smaller than the MA parameters, by factors of 3.0 and 1.7 for aerosol surface area and N_{500}, respectively. In addition to excluding data north of 47 °S (Sec. 2.2.3.2), which can be influenced by continental aerosols, all periods where the CAP-2 Mie-calculated red/blue å>0.8 were removed (Sec. 2.3.2), to isolate periods where PMA is expected to be the dominant aerosol type. The remaining points have $AOT_{500\,nm}$ ranging from 0.036 - 0.127 and å440-870 nm from 0.07 - 0.58. These agree well with other measurements of AOT and å for marine aerosols (Andrews et al. 2019; Carrico et al. 2003; Mulcahy et al. 2009), in addition to Mie calculations based on the CAP-2 size distributions (Sec. 2.3.2). It is possible that since observations including dust are much more common in the MA marine aerosol dataset than over the Southern Ocean, their å (0.25<å<0.6) and AOT ($AOT_{500\,nm}$ <0.07) restrictions may have removed observations with significant coarse mode

marine aerosol, which often has å<0.25, and even å<0, as well as $AOT_{500\,nm}$ >0.1 (e.g. Mulcahy et al. 2009). This could help explain the differences between their conversion parameters and those derived using the CAP-2 Microtops data. The å and AOT values from all the studies mentioned here, as well as this dataset, are summarized in Table A.4.

The MA method was applied to the lidar data from CAP-2 (Sec. 2.2.3.5) using the 1) original MA marine aerosol conversion parameters at 355 nm, 2) MA parameters adjusted to account for ambient surface RH for each measurement (aerosol surface area only), and 3) new parameters derived from the CAP-2 Microtops measurements and aerosol size distributions (Fig. 2.8). For 2), representative HGFs for sea salt were calculated with E-AIM (Clegg et al. 1998; 2021) for each lidar profile using the average surface RH measured from the RV *Investigator* during each period, and used to scale the MA aerosol surface area conversion parameter (Sec. 2.2.2) to reflect the ambient boundary layer RH, rather than assuming an HGF of 2. Table A.1 contains a comparison between all of these methods and their respective conversion parameters. A time series of aerosol surface area at 300 m estimated from lidar extinction using all three conversion parameters is shown in Fig. A.13 for each clear-sky profile. When compared to the SMPS + APS observations, both MA parameters overestimate dry aerosol surface area for most lidar profiles, while the Microtops parameter tracks changes in dry aerosol surface area more closely. This can be seen more clearly in Fig. 2.9, which shows the correlation between lidar-estimated and aerosol size distribution measurements of dry aerosol surface area and N_{500}. The original MA parameters overestimate SA by a factor of ~3-5, and N_{500} by ~1.5-3 times. Adjusting the MA SA conversion parameter based on ambient RH typically increased the estimated dry SA and worsened the agreement by a small amount. The surface RH during CAP-2 was usually less than the 80% assumed in Mamouri and Ansmann (2016), although HGFs up to 2.6 were observed for ambient RH ~90% in a few cases, leading to improved correlations for those periods. The agreement was much better for both aerosol SA and N_{500} using the Microtops-derived parameters, which are distributed close to the 1:1 line in both cases. Since the calculation of extinction from lidar backscatter (Sec. 2.2.3.5) requires an assumed lidar ratio, only periods where the con-

current CAP-2 Mie-calculated red/blue å<0.8 are shown in Fig. 2.9, to isolate PMA-dominated aerosol distributions (Sec. 2.3.2).

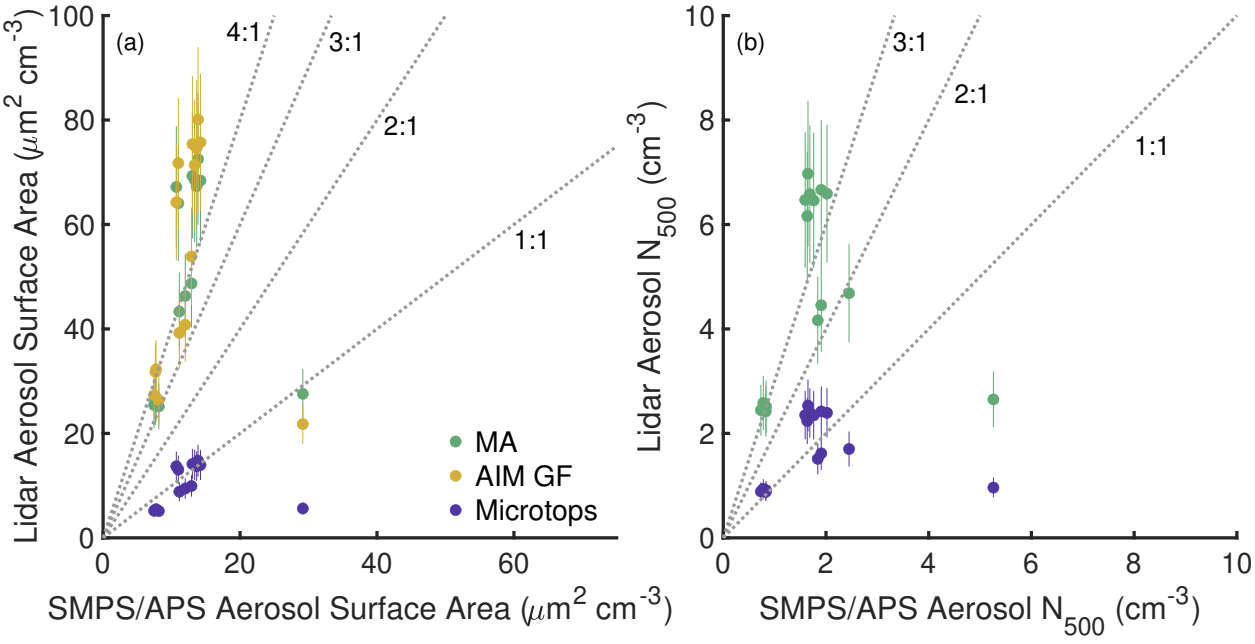

Figure 2.9: Comparison of CAP-2 (a) dry aerosol surface area and (b) N_{500} from the merged size distributions with those estimated from the lidar at 300 m using the MA method. Data using the MA parameters are shown in green, those using MA parameters adjusted for ambient RH in gold, and those using the MA method with conversion parameters derived from the CAP-2 Microtops in purple.

Both the Microtops and lidar datasets are limited to clear-sky conditions, which are infrequent in the predominantly cloudy Southern Ocean, resulting in few data points being available for both deriving the conversion parameters (Fig. 2.8) and testing them (Fig. 2.9). Additionally, the lidar profiles presented here did not cover the full range of wind speeds observed, with a median of 6.1 m s^{-1} and a maximum of 10.0 m s^{-1}. The Microtops observations covered a slightly larger range of wind speeds, with a median of 7.5 m s^{-1} and a maximum of 16.0 m s^{-1}. This effect is clear in Fig. A.14, which shows normalized frequency distributions of lidar-estimated and size distribution measurements of aerosol surface area and N_{500}. The largest SA obtained from the Microtops conversion parameters is 14.8 μm^2 cm^{-3}, whereas for the merged size distributions it is 56.4 μm^2 cm^{-3}. This unfortunately limits the ability to assess the new aerosol SA and N_{500} conversion parameters across the whole range of expected conditions over the Southern Ocean,

although based on this initial analysis, they perform better for this region than those presented in MA.

2.4 CONCLUSIONS

Measurements of aerosol size distributions from the Southern Ocean marine boundary layer were presented from the Southern Ocean Cloud Radiation Aerosol Transport Experimental Study (SOC) aircraft campaign and the second Clouds, Aerosols, Precipitation, Radiation and atmospherIc Composition Over the southeRN ocean (CAP-2) ship campaign, which occurred concurrently in austral summer 2018. Close agreement was seen between size distributions measured on the G-V and RV *Investigator* during overflights for particles up to 2 μm, and corrections were presented to account for large particles not sampled efficiently by the RV *Investigator* aerosol inlet based on wing-mounted instruments from the G-V. Lognormal mode fitting was used to estimate the PMA number concentration for both campaigns, which are broadly consistent with previous measurements of sea spray aerosol in the Southern Ocean (Hartery et al. 2020; Sanchez et al. 2021b) and North Atlantic (Saliba et al. 2019). Wind speed explains up to 60% of the variance in PMA concentrations (Fig. 2.4), whereas latitude had no significant relationship with PMA for either campaign (Fig. A.6).

Aerosol surface area is commonly used to parameterize ice nucleation in models and is also important for light scattering and particle reactivity. Direct measurements are scarce over the SO, and two techniques for inferring dry marine aerosol surface area from light-scattering were evaluated here. The method presented in DeMott et al. (2016), which utilizes ambient scattering coefficients from a three-channel nephelometer, was applied to Mie-theory calculations based on aerosol size distributions measured during CAP-2. The assignment of an effective scattering efficiency Q=2 for distributions with å<1 is a reasonable approximation (within ±50%), although assuming Q=3 for distributions with å>1 leads to an underestimate of dry aerosol surface area by a factor of 2 or more. Instead of the step-function used to assign Q in D16, we suggest a new relationship between dry marine aerosol scattering efficiency and Ångström exponent, which

explains 80% of the variance between Q and å for -0.2<å<2. Additionally, we propose å=0.8 as the cutoff between distributions dominated by PMA (å<0.8) and those dominated by secondary biogenic marine aerosol (å>0.8). The relationships derived here will need to be further assessed with ambient nephelometer data, as these were unavailable for CAP-2 or SOC, and also for regions other than the Southern Ocean.

Lidar backscatter profiles have previously been shown to reproduce aerosol number and surface area concentrations in other environments (Mamouri and Ansmann 2016), and we have evaluated their use for the Southern Ocean with CAP-2 lidar (355 nm) and aerosol measurements. The marine aerosol conversion parameters at 355 nm presented in MA were found to overestimate dry aerosol surface area by a factor of ~3-5, and N_{500} by ~1.5-3 times. Adjusting the MA conversion parameters based on measured RH typically worsened the agreement by a small and insignificant amount. A new set of conversion factors between ambient extinction and dry SA or N_{500} were derived from Microtops AOT measurements during CAP-2. The Microtops parameters improve the estimation of both SA and N_{500} at 355 nm, reducing aerosol SA by 4.9 times and N_{500} by 2.8 times relative to the MA factors. However, the clear-sky lidar profiles available during CAP-2 had a maximum wind speed of 10.0 m s^{-1}, whereas 30-minute average wind speeds of >22 m s^{-1}, and gusts up to 46 m s^{-1}, were observed during the campaign. Based on this initial analysis, the Microtops parameters perform better than the MA parameters for the Southern Ocean region, but they should be evaluated further over a broader range of conditions.

3. Characterizing Ice Nucleating Particles over the Southern Ocean using Simultaneous Aircraft and Ship observations

3.1 INTRODUCTION

The Southern Ocean (SO) surrounding Antarctica is frequently covered by vast tracts of low-level clouds, which have emerged as a key component in simulating regional and global climate, particularly the regional radiative budget (e.g. Bodas-Salcedo et al. 2013; 2016; Frey and Kay 2017; Gettelman et al. 2020; Tan et al. 2016). Satellite retrievals suggest a greater occurrence of mixed-phase clouds containing supercooled liquid water (SLW) over the SO than at equivalent latitudes in the Northern Hemisphere (Chubb et al. 2013; Morrison et al. 2011), and recent in situ observations confirmed the ubiquity of supercooled liquid clouds and lack of ice to -20 °C (McFarquhar et al. 2021). In situ observations, although limited, also indicate more frequent drizzle and less ice over the SO compared to Arctic supercooled and mixed-phase clouds (Chubb et al. 2013). Despite observed differences between SO and Northern Hemisphere clouds, almost all model parameterizations have been developed with Northern Hemisphere data due to the lack of direct observations over the SO (Bromwich et al. 2012).

Until recently, earth system models, including those participating in CMIP5 (Coupled Model Intercomparison Project Phase 5), and reanalysis products overestimated the occurrence of ice and had insufficient liquid cloud cover over the SO, leading to a large shortwave radiation bias in the region (Bodas-Salcedo et al. 2013; Gettelman et al. 2020; Kay et al. 2016a;b; Naud et al. 2014). This imbalance was hypothesized to be due to over-prediction of cloud glaciation and ice precipitation processes (Frey and Kay 2017; Kay et al. 2016a; Mace et al. 2020; McFarquhar et al. 2021; Tan et al. 2016; Vergara-Temprado et al. 2018). Improvements in individual CMIP6 (Coupled Model Intercomparison Project Phase 6) models increased SLW and reduced radiation biases, improving agreement with observations (Bodas-Salcedo et al. 2019; Gettelman et al. 2020). Updated model representations of clouds are also responsible for higher equilibrium cli-

mate sensitivities (ECS) in many CMIP6 models compared to their CMIP5 counterparts due to corresponding changes in shortwave cloud forcing, likely driven by increases in SLW in CMIP6 models (Zelinka et al. 2020). The cloud phase feedback over the Southern Ocean is anticipated to strongly influence simulated future ECS (Bjordal et al. 2020), so understanding processes that affect cloud phase in this region is critical.

Cloud condensation nuclei (CCN) and ice nucleating particle (INP) budgets and sources for the SO are not fully constrained, although the dominant source for CCN is local (Humphries et al. 2021; Quinn et al. 2017; Twohy et al. 2021). The typically small droplet numbers of low marine clouds make them sensitive to changes in aerosol concentration, size, and source. Low INP concentrations, coupled with scavenging and deposition in drizzle, can limit primary ice production and contribute to high supercooling in liquid and mixed phase clouds. This has been observed in several marine regions in the Northern Hemisphere (Rosenfeld et al. 2013), and may also be occurring in the Southern Ocean. Vergara-Temprado et al. (2018) provided support for this hypothesis using the United Kingdom Met Office Global Unified Model, based on modeled INP concentrations. Secondary ice production has been observed in SO clouds >-25 °C, with sometimes large discrepancies between measured ice crystal and INP number concentrations. However, a large proportion of clouds do not contain measurable ice concentrations (Järvinen et al. 2022). These observations indicate INPs may potentially play a large role in SO cloud phase, with downstream effects including cloud lifetime, precipitation, radiation budgets, and even ECS.

Historically, INPs have been thought of as large, insoluble particles with surface structures that have specific sites that promote the freezing of ice (Pruppacher and Klett 2010). These sites, known as active sites, typically scale with particle surface area and so are more numerous in larger particles (see Kanji et al. 2017). This approach has been used to derive model parameterizations for ice nucleation as a function of activation temperature by normalizing INP concentrations with a more commonly measured value, such as particle surface area or number concentration (DeMott et al. 2010; 2015; Hoose and Möhler 2012; Kanji et al. 2017; McCluskey

et al. 2018a; Niemand et al. 2012; Ullrich et al. 2017). This approach requires the aerosol type or mixture to be known, since INP efficiency varies widely among particles of differing composition (e.g. Kanji et al. 2017). Strong relationships between INP concentrations and particles >0.5 μm have been observed for mineral dust (DeMott et al. 2015), which is supported by the dominant supermicron mode of mineral and soil dust size distributions (Maring et al. 2003). Increasing awareness and study of additional categories of INPs, such as biological ice nucleators, which can be soluble and/or as small as ~10 nm, has challenged these assumptions about INP prerequisites (e.g. Kanji et al. 2017; Pummer et al. 2015; Wilson et al. 2015).

On a global scale, mineral and soil dusts are the dominant heterogeneous INP types in the immersion freezing mode due to their efficient ice nucleating ability (Hoose and Möhler 2012; Testa et al. 2021) and high emission rates (Ginoux et al. 2012). Marine INPs have been identified as a distinct category (see DeMott et al. 2016), and shown to include marine diatoms and their exudates (Rosinski et al. 1987; Wilson et al. 2015), as well as marine macromolecules (McCluskey et al. 2018b). Very recent laboratory studies indicate supermicron aerosol may be an important marine INP (Mitts et al. 2021), however, no assessment of the atmospheric transport of such particles was conducted and ambient observations have yet to confirm this. Marine INP number concentrations are generally 2-3 orders of magnitude or more lower than continental measurements (DeMott et al. 2016), as are marine INP active site densities (McCluskey et al. 2018a).

Measurements of SO INPs are sparse, with initial measurements conducted by (Bigg 1973; 1990), and the remainder comprised of data from several cruises, one aircraft campaign, and one study at the Australian Antarctic Division's (AAD) Macquarie Island station, all in the last decade (Kremser et al. 2021; McCluskey et al. 2018c; McFarquhar et al. 2021; Miyakawa et al. 2023; Schmale et al. 2019; Tatzelt et al. 2022; Welti et al. 2020). Many of the measurements were also limited to the surface and to INPs active at temperatures of -15 or -20 °C due to either instrumental constraints or a particular focus on warmer mixed phase clouds (Welti et al. 2020). All of the measurements from the 1980s onwards are at the lower bound of those reported from

other ocean regions (DeMott et al. 2016; Welti et al. 2020). There is now a consensus, supported by the observed low INP numbers, its remote location, and modeling studies (Burrows et al. 2013; McCluskey et al. 2019; Vergara-Temprado et al. 2017), that the SO INP population in the marine boundary layer is dominated by sea spray aerosol (SSA) and distinct from that found in the Northern Hemisphere. This is unlike the northern high latitudes, where mineral dust has been shown to dominate over locally sourced marine INPs in regions such as the Canadian Arctic (Irish et al. 2019).

3.2 METHODS

3.2.1 Southern Ocean Measurement campaigns

Measurements presented in this study were collected during the Southern Ocean Cloud Radiation Aerosol Transport Experimental Study (SOCRATES, hereafter SOC) aircraft campaign and the second Clouds, Aerosols, Precipitation, Radiation and atmospherIc Composition Over the southeRN ocean (CAPRICORN-2, hereafter CAP-2) ship campaign. Both campaigns were conducted simultaneously during Austral summer (January-March) 2018, based out of Hobart, Tasmania and are fully described in McFarquhar et al. (2021). SOC measurements utilized the NSF/NCAR G-V aircraft (UCAR/NCAR - Earth Observing Laboratory 2005) and collected cloud microphysical and aerosol observations within the marine boundary layer (MBL) and up to the free troposphere as far south as 62°S. CAP-2 collected complementary MBL measurements aboard the RV *Investigator* (voyage IN2018_V01), an Australian Government research platform operated by the Commonwealth Science and Industrial Research Organisation (CSIRO). A map indicating the locations of the 15 SOC research flights and the CAP-2 track are given in Fig. B.1. The SOCRATES campaign is noteworthy for collecting the first in situ observations of INPs in and above cloud in this region.

3.2.2 Aerosol Measurements

The collection and analysis of particle size distribution measurements during CAP-2 and SOC were fully described in (Moore et al. 2022) and will only be briefly covered here. Integrated particle number, surface area, and volume concentrations are used as normalization metrics and inputs to parameterizations for estimating INP concentrations, as discussed in Sec. 3.3.2. Measurements of single particle composition during SOC using offline elemental analysis (Twohy et al. 2021) are similarly used as parameterization inputs (Sec. 3.3.4).

3.2.2.1 CAPRICORN-2 Aerosol Size Distributions

Particle size distributions were generated by merging observations from a TSI Scanning Mobility Particle Sizer (TSI, SMPS 3080; 15-660 nm) and a TSI Aerodynamic Particle Sizer (TSI, APS 3320; 500 nm – 20 μm) averaged over 30-min intervals. Silica gel diffusion driers were used to dry particle streams to below the efflorescence relative humidity (ERH) of sea salt (45-48%; Tang et al. 1997) and the resulting particle data are described as "dry" throughout this manuscript. SMPS and APS sizes were converted from their native mobility and aerodynamic diameters, respectively, to volume equivalent diameters prior to merging (Moore et al. 2022). Ship exhaust and waste incineration represent the largest sources of particle contamination for aerosol measurements on the RV *Investigator* and were excluded from the data set using a time series of predicted exhaust influence on measurements following Humphries et al. (2019). Theoretical particle transmission efficiency calculations (Moore et al. 2022) were applied to merged size distributions to correct for primarily supermicron particle losses inside the RV *Investigator* aerosol sampling inlet. Distributions were cut off at 5 μm dry diameter, as above this size the theoretical transmission efficiency drops below 40% and the correction becomes highly uncertain. Three-four lognormal modes were fit to the resulting merged distributions following Quinn et al. (2017) and Modini et al. (2015), and primary marine aerosol (PMA) estimated as the sum of the third and fourth (if applicable) coarse modes (Moore et al. 2022). Integrated particle number, surface area, and volume concentrations were then calculated for each total distribution and the PMA modes, assuming spherical particles. Comparison of total integrated

quantities with those for particles <5 μm from the G-V measurements (see Sec. 3.2.2.2), which were obtained from wing-mounted instruments with minimal or no inlet losses, were used to derive additional corrections for losses not accounted for in the CAP-2 inlet modeling. These corrections were applied to all CAP-2 integrated aerosol measurements presented here. Due to a lack of available nephelometer data for CAP-2, theoretical scattering distributions at 450 nm, 525 nm, and 635 nm were estimated for each size distribution using Mie theory, using a refractive index of n=1.5 (Tang et al. 1997) and assuming spherical particles (Moore et al. 2022). Ångström exponents (å) were then calculated for each wavelength pair from the integrated scattering coefficients. Blue/red å≤0.8 was found to work well as a tracer for aerosol size distributions dominated by primary marine aerosol during CAP-2 (Moore et al. 2022), which will be discussed further in Sec. 3.3.1.

3.2.2.2 SOCRATES Aerosol Size Distributions

Average aerosol distributions were generated by merging observations from a wing-mounted ultra-high sensitivity aerosol spectrometer (Droplet Measurement Technologies, UHSAS; 0.06 – 1.0 μm) and a wing-mounted cloud droplet probe (Droplet Measurement Technologies, CDP; 1-50 μm; Lance et al. 2010). For some distributions, primarily in the MBL, measurements of supermicron particles from the Giant Nucleus Impactor (GNI; Jensen et al. 2020) were also available. UHSAS distributions were considered to represent dry particles due to the use of deicing heaters that lowered the RH in the optical cavity to <40% (Moore et al. 2022; Sanchez et al. 2021b). The GNI technique involves collection of impacted particles onto glass slides, followed by microscopic imaging to calculate the spherical-equivalent dry sizes of collected particles (Jensen et al. 2020). CDP bin sizes were first adjusted following Lance et al. (2010) and then corrected for water uptake using hygroscopic growth factors calculated for sea salt proxies using E-AIM (Clegg et al. 1998; 2021). Following the same method as the CAP-2 observations, after merging the UHSAS, CDP, and GNI data (if available), each distribution was fit with lognormal modes and PMA estimated, although the Aitken mode was ignored in the SOC measurements because the UHSAS doesn't extend to small enough sizes to constrain it.

The distributions presented in Moore et al. (2022) represented averages of ~8-10 min level legs in the lower MBL (150-300 m MSL). Additional level legs above cloud and in the upper troposphere (>5000 m) were identified in this study during INP observation periods (Sec. 3.3.4). For INP observations less than 10 min in duration, level legs up to 10 min were identified where "level legs" were defined as periods with <5% deviation from the midpoint altitude, based on the INP measurement period. For INP observations longer than 10 min in duration, aerosol measurements were averaged over the INP measurement period regardless of altitude variations so that all observed variability was captured in both measurements. To avoid cloud contamination of the aerosol distributions, any points with cloud condensed water >0.01 g m^{-3} were removed prior to averaging. Estimates of cloud condensed water were made with several instruments during SOCRATES; here we define "in-cloud" periods when either the wing-mounted CDP or tunable diode laser hygrometer, which sampled behind a counterflow virtual impactor inside the G-V cabin (CVI; Noone et al. 1988; Twohy et al. 2010) reported cloud condensed water >0.01 g m^{-3}.

Since PMA estimates based on lognormal mode fitting alone are unlikely to be meaningful outside of the MBL, merged distributions for the above cloud and upper troposphere periods were instead generated by first applying a lowpass (smoothing) filter to the average UHSAS, CDP, and GNI (if available) distributions to reduce noise. Then, a smoothing spline was fit to the smoothed distributions, interpolating onto the same logarithmically spaced bins as the lognormal fits to the MBL distributions described in Moore et al. (2022). The merging process was conducted using surface area distributions, since they are more sensitive in the size region between the UHSAS and CDP or GNI. Finally, integrated particle number, surface area, and volume were calculated for each distribution. The same procedure was applied to the MBL periods identified in Moore et al. (2022) and compared to the results of the lognormal fitting to verify both methods produce equivalent results. For both integrated surface area and number concentration of particles larger than 500 nm dry diameter (n500), points cluster around the 1:1 line, with maximum deviations of 57% for aerosol surface area and 67% for n500 (Fig. B.2).

Mie calculations were used to calculate theoretical scattering distributions and Ångström exponents (å) for each merged size distribution, following the same procedure as in Moore et al. (2022).

3.2.2.3 SOCRATES Aerosol Composition Analysis

Particles were collected via impaction onto carbon-coated electron microscope grids during SOCRATES in two dry diameter ranges: 0.1-0.5 µm and 0.5-5 µm, as fully described in Twohy et al. (2021). Collections were made downstream of the CVI inlet in clear air below and above cloud, and of cloud droplet residuals in-cloud. Single-particle size, morphology, and elemental composition were determined with analytical Scanning Transmission Electron Microscopy (STEM) using Energy Dispersive X-ray Spectroscopy (EDS). Particles were then classified into 8 categories, including crustal/dust, sulfur, organic, metals, sea-spray with high sodium, and sea-spray with high sulfur content (Twohy et al. 2021). In this study, the sum of the crustal/dust and metal categories above and below cloud were used as parameterization inputs to estimate INP concentrations (Sec. 3.3.4).

3.2.3 Ice Nucleating Particle observations

Measurements of INPs active in the immersion freezing mode were made in real time with Colorado State University (CSU) Continuous Flow Diffusion Chambers (CFDCs) at temperatures below -25°C, and via offline analyses of aerosol filter samples using the CSU Ice Spectrometer (IS) from -10 to -30°C. Ice crystals that activated within the CFDC were also collected and analyzed by STEM/EDS to assess the composition and size of INP residuals (Twohy et al. 2021).

3.2.3.1 Continuous Flow Diffusion Chamber Measurements

The Continuous Flow Diffusion Chamber (CFDC) is an online instrument used to measure primary INP number concentrations in an aerosol stream (DeMott et al. 2015; Rogers 1988; Rogers et al. 2001). Two concentric, cylindrical walls are coated with ice and thermally

controlled to establish a temperature and humidity gradient between the walls in the upper "growth" region of the chamber, allowing aerosol particles to activate into ice crystals and grow. The HIAPER (CFDC-1H) version of the CFDC used in SOC (Barry et al. 2021b) and a duplicate version used during CAP-2 (McCluskey et al. 2018c) both have total residence times of ~7 s based on their sample volumetric flow rate of 1.5 lpm. Ice crystals are detected optically with an OPC at the base of the chamber and distinguished by size from aerosol or activated cloud droplets. For both SOC and CAP-2, water supersaturated conditions, typically 104-108% RH, were maintained in the growth region, which forces activation of aerosols into cloud droplets prior to ice nucleation, giving results similar to offline immersion freezing techniques (DeMott et al. 2016). Prior to entering the chamber, the aerosol stream is dried to below the frost point, and supermicron aerosols that might interfere with optical detection of ice crystals are removed by passing the aerosol stream through two identical single-jet impactors in series. For SOC, impactors with a 2.4 μm cut size were used; during CAP-2 1.5 μm impactors were used to limit interferences from highly hygroscopic, supermicron sea spray aerosols. Low INP concentrations during both campaigns limited operating temperatures to -25 °C and below, with the majority of measurements collected ~-30 °C. Measurement periods of approximately 10 minutes were alternated with 5-min periods measuring HEPA-filtered air to provide instrument background counts, which vary by operating temperature and environmental conditions. INP concentrations presented here have been background-corrected using adjacent filtered-air periods, as described in (Moore 2020) and (Barry et al. 2021b). Calculation of confidence intervals and assessment of statistical difference between sample and background periods follow (Krishnamoorthy and Lee 2012) and are also detailed in (Moore 2020) and (Barry et al. 2021b). concentrations are reported at standard conditions (STP; 0 °C and 100 kPa).

During CAP-2, the CFDC sampled from the same RV *Investigator* aerosol sampling inlet as the SMPS, APS, and other aerosol instrumentation (Moore et al. 2022). In addition to direct ambient measurements, an aerosol concentrator (MSP Corporation Model 4240) was employed upstream of the CFDC to pre-concentrate ambient aerosol and enhance INP number concen-

trations prior to measurement, as in previous ground-based (Tobo et al. 2013) and ship-board (McCluskey et al. 2018c) studies. The aerosol concentrator inlet was constructed from 1" stainless steel tubing and followed the same path as the main aerosol inlet down the RV *Investigator* foremast and into the aerosol lab at the bow of the ship. INP concentration factors for measurements made with the aerosol concentrator were calculated through comparison to ambient INP measurements made at the same temperature (±2 °C) and within 30 minutes. These concentration factors were used to scale measurements made with the aerosol concentrator to their equivalent ambient concentration. Theoretical particle transmission efficiency calculations for the CFDC ambient and concentrator inlets (Fig. B.3; Brockmann 2011; von der Weiden et al. 2009) indicate >90% for the ambient and >85% transmission efficiency for the concentrator inlet at sizes up to 1.5 μm, and so no particle loss corrections were applied to measured INP concentrations. Unlike the aerosol size distribution measurements (Sec. 3.2.2.1), the CFDC data were not filtered to exclude ship exhaust, as previous measurements have indicated very low IN efficiency of particles emitted from diesel engines (Schill et al. 2016), and inspection of INP concentrations showed no significant differences between adjacent measurements when one was influenced by ship exhaust and the other was not. This is consistent with previous ship-board measurements for temperatures above -26°C (Irish et al. 2019; McCluskey et al. 2018c; Welti et al. 2020).

On the G-V, the CFDC sampled from both the HIAPER modular inlet (HIMIL inlet; Stith et al. 2009) in clear air regions above and below clouds, and from a counterflow virtual impactor (CVI) inlet within clouds (Noone et al. 1988; Twohy et al. 2010) to detect INPs within cloud residuals. Particle transmission efficiencies for the HIMIL inlet have been previously characterized as >94% for submicron particles (Stith et al. 2009), and no corrections were applied to the CFDC data, which has an upper limit of 2.4 μm aerodynamic diameter. CVI transmission efficiencies were modeled by Twohy et al. (2010) using computational fluid dynamics software, and used to correct the in-cloud CVI data presented here for particle enhancements in the inlet. Some measurements in cloud-adjacent regions were also made using the CVI inlet in clear air, with

the counterflow turned off ("total mode"). CVI enhancements in total mode are highly size dependent, and expected to range from ~1.1-3.5 for the particle sizes sampled by the CFDC (Twohy et al. 2016). Since INP sizes during each measurement are unknown, but likely variable (Twohy et al. 2021), no correction has been applied to the total mode CVI measurements from SOCRATES.

3.2.3.2 Ice Spectrometer Measurements

Aerosols were collected onto pre-cleaned 0.2 μm, 47mm track-etched polycarbonate membrane filters (Whatman Nucleopore filters, GE Healthcare Life Sciences) in either pre-sterilized aluminum inline filter housings (Pall) on the G-V, or disposable, sterile, open-faced filter units (Nalgene sterile analytical filter units, Thermo Fisher Scientific) on the RV *Investigator*. During CAP-2, filters were mounted on deck beneath a rain hat for alternating 24 and 48 hr periods at approximately 23 m above sea level. In order to limit ship exhaust contamination, the filter pump was powered with a sector sampler, which provided power to the pump only when the wind speed relative to the ship was between 10 and 80 knots, the ship-relative wind direction was from the forward 90° (relative wind directions greater than 45° and less than 315° were excluded), and the total particle concentrations measured by a CPC were stable and less than 2000 cm^{-3}. On the G-V, filters sampled from the same HIMIL as the CFDC (Sec. 3.2.3.1) above or below cloud. Due to the low INP concentrations, each SOC filter was collected for multiple, approximately level legs at similar altitudes, but different locations throughout a flight. Separate filters were collected in the MBL and above cloud to assess changes in INPs with altitude. Filters where >5% of the collection period was in-cloud based on cloud condensed water measurements (Sec. 3.2.2.2) have been excluded from results presented here. Filters were stored frozen (-80 °C) following collection and during transport (via a liquid nitrogen dry shipper) back to CSU, and at -20 °C thereafter. Blank filters were collected throughout the voyage and during the research flights and processed identically to the samples.

The CSU Ice Spectrometer (IS) was used to measure immersion freezing INP temperature spectra from liquid suspensions of particles collected onto filters during CAP-2 and SOC. The

current version of the IS was described in Hiranuma et al. (2015) and DeMott et al. (2018c). Aliquots of sample suspensions, typically 32 or 48 droplets of 50 μL, were dispensed into sterile 96-well PCR trays (Optimum Ultra, Life Science Products) and then placed into temperature-controlled aluminum blocks and cooled at approximately 0.33 °C min-1. Freezing was detected optically using a CCD camera, with the number and position of frozen droplets (wells) recorded at 1 Hz. The minimum analysis temperature for each sample or blank was determined by comparison with a 0.1 μm-filtered DI water negative control and was typically between -27 and -30 °C. Calculations of INP concentrations in the liquid suspension were made following Vali (1971), which were then converted to concentrations in ambient air, expressed at standard conditions (STP; 0 °C and 100 kPa). Uncertainties are reported as binomial sampling confidence intervals (95%) as in Agresti and Coull (1998). The limit of detection (LOD) was taken as the upper 95% confidence interval for 0 droplets frozen out of a sample, corresponding to 3-4 frozen wells for these filter collections. As a result, samples were considered above the LOD once 4-5 wells had frozen, leading to an upper temperature limit of about -17 °C. Measured concentrations were corrected using the average background number of INPs from 6 (SOC) or 5 (CAP-2) blank filters and are not reported if blank-corrected values fell below zero.

An earlier version of the SOC IS filter dataset was presented in Järvinen et al. (2022) as a comparison to in-cloud measurements of ice crystal number concentrations, and the concentrations were used in McCluskey et al. (2023) and Zhao et al. (2023) to evaluate CAM6 INP predictions (Sec. 3.2.4). Preliminary CAP-2 filter results were shown in McFarquhar et al. (2021), along with previous measurements made in the Southern Ocean. The blank-correction procedure reported here represents an improved statistical methodology from what has been previously reported (e.g. Barry et al. 2021b; DeMott et al. 2018c), providing more accurate 95% confidence intervals on blank-corrected data and improved LOD estimations. The midpoint concentrations are identical to previous methodologies and are directly comparable.

3.2.3.3 INP Size and Composition Analysis

Following the OPC at the outlet of the CFDC chamber is a single-jet impactor with a 50% cut-size of 4 μm aerodynamic diameter, which was used to collect ice crystals that nucleated inside the CFDC chamber during both SOCRATES and CAPRICORN-2 (Barry et al. 2021b; McCluskey et al. 2014). Similarly to the total particle collections during SOC (Sec. 3.2.2.3), the CFDC STEM impactor was fitted with Cu grids (coated with formvar and C), and the collected ice crystal residuals were analyzed with STEM/EDS to determine residual size, morphology, and composition (Twohy et al. 2021). In this study, only the size measurements of INPs will be discussed. Six samples from CAP-2 and four samples from SOC were collected, with collection temperatures that ranged from -27 to -32 °C and n=87 total particles analyzed; the collection locations are shown in Twohy et al. (2021) Fig. 3.1. Since all the CAP-2 and the majority of the SOC INPs were collected in the MBL, the overall sample is expected to be dominated by particles from the MBL.

Indirect inference of INP sizes was also possible based on the INP concentration factors calculated from CAP-2 ambient CFDC measurements versus those made using the aerosol concentrator (Sec. 3.2.3.1). The aerosol concentrator primarily acts on particles >0.5 μm diameter, with a concentration factor that is highly size dependent up to ~1 μm aerodynamic diameter (Tobo et al. 2013). For particles 0.5-1 μm aerodynamic diameter, the measured INP concentration factor thus provides indirect evidence of INP size. Due to the very low INP concentrations present over the Southern Ocean MBL (Fig. 3.1), measurements of INP concentration factor were limited to ≤-25 °C, and predominantly ~-30 °C. Concentration factors of the aerosol concentrator as a function of particle diameter were derived from sequential measurements of ambient aerosol particles with and without the aerosol concentrator upstream of an Aerodynamic Particle Sizer (TSI, APS 3321) for particles between 500 nm and 20 μm aerodynamic diameter. They are shown in Fig. B.4, where the particle sizes have been converted from aerodynamic to physical dry diameter, using the APS diameter correction factor derived for CAP-2 particle measurements (Moore et al. 2022).

3.2.4 SOCRATES CAM6 Model Simulations

A simulation of aerosols during SOCRATES was conducted with the atmospheric component of CESM2 (Community Earth System Model version 2), CAM6 (Community Atmosphere Model version 6), as described and presented in McCluskey et al. (2023). The CAM6 simulation used the standard 32 vertical levels (surface to 3 hPa), a 30-min time step with 10-min microphysical sub-step, and horizontal resolution of 0.9° latitude by 1.25° longitude. It was performed using a "nudged", or specified dynamics, configuration, with winds and temperatures from the MERRA2 reanalysis product with a 24-hr relaxation timescale (Gettelman et al. 2020). For comparison to the in situ observations, CAM6 output were at 1-min resolution and co-located with the measurements using the G-V position and altitude to determine the nearest model gridbox. For co-locations with the IS measurements, model data were averaged along the G-V track during the filter collection period.

CESM2 uses the 2-moment modal aerosol model MAM4 (Liu et al. 2016), which includes six aerosol species: sea salt, mineral dust, black carbon (BC), primary organic matter (POM), sulfate, and secondary organic aerosol (SOA). Aerosols are emitted into 4 modes with contributions that vary by aerosol type, with a fixed modal width and a modal diameter that evolves during the simulations. Inorganic sea spray fluxes are estimated based on whitecap area as a function of wind speed (Monahan and Muircheartaigh 1980) and sea surface temperature in two size ranges: 0.02 to 2.8 μm (Mårtensson et al. 2003) and 2.8-10 μm (Monahan et al. 1986). Mineral dust fluxes are based on wind speed and soil aridity (Zender et al. 2003), and both mineral dust and sea salt emissions are interactive with model meteorology. The remaining aerosol species (BC, POM, sulfate, and SOA) are emitted based on CMIP6 emission inventories (Gettelman et al. 2019). In this analysis, only out of cloud (ambient/interstitial) aerosol was used, and similarly to the observations (Sec. 3.2.2), aerosol surface area concentrations were calculated from the simulated number size distributions assuming spherical particles.

McCluskey et al. (2019; 2023) concluded the best approach for predicting INP concentrations over the Southern Ocean using CAM and existing parameterizations was to sum the sea

spray INP contribution using the marine organic aerosol parameterization (M18) from McCluskey et al. (2018a) and the mineral dust INP contribution following the DeMott et al. (2015) parameterization (D15). The simulated CAM6 INP concentrations presented in this study use this approach. Simulated sea salt aerosol surface area concentrations and the number concentration of mineral dust particles larger than 500 nm were used as parameterization inputs for M18 and D15, respectively.

3.3 RESULTS AND DISCUSSION

3.3.1 CAPRICORN-2 and SOCRATES Marine Boundary Layer INP observations

The most comprehensive historical measurements of Southern Ocean INPs are those of Bigg (1973; 1990). Since then, measurements of INPs, primarily immersion freezing assays of aerosol filters, have been collected during several campaigns in different regions of the Southern Ocean, and are collated in Welti et al. (2020) and McFarquhar et al. (2021). As previously noted for the CAPRICORN-1 (2016; McCluskey et al. 2018c) and Antarctic Circumnavigation Expedition (ACE, 2016-2017; Schmale et al. 2019; Tatzelt et al. 2022; Welti et al. 2020) campaigns, modern measurements are one to several orders of magnitude lower than the original observations presented in Bigg (1973). During CAP-2, average IS measurements of filters at -20 °C are approximately 2 orders of magnitude lower than those collected during 1969-1972 across all latitudes sampled. Measurements at temperatures above -15 °C from CAP-2 were below the detection limit, which prevents additional direct comparisons. Slightly elevated INP concentrations were observed at -25 °C during CAP-2 at the northern and southern ends of the voyage (not shown), though all latitudinally-averaged values agree within their estimated uncertainties. Future measurements should evaluate this latitudinal variability during seasons other than austral summer.

INP measurements collected in the marine boundary layer from both IS filters and CFDC observations during SOCRATES and CAPRICORN-2 are compiled in Fig. 3.1. As discussed in Sec. 3.2.3.2, the INP filter measurements included in this study represent updated versions of

the datasets, with improved confidence interval and LOD estimates. All panels in Fig. 3.1 show INP observations as a function of temperature; Fig. 3.1a has measured INP concentrations and the remaining panels display INP concentrations normalized by measured aerosol concentration metrics for comparison to model parameterizations, which will be discussed further in Sec. 3.3.2. Normalization of INP concentration with particle number gives activated fraction, N_n (Fig. 3.1b), normalization with particle surface area gives the surface active site density, N_s (Fig. 3.1c), and normalization with particle volume gives the volume active site density, N_v (Fig. 3.1d). The activated fraction presented in this study uses the number concentration of aerosols larger than 500 nm (n500), which has been used in several previous INP model parameterizations (e.g. DeMott et al. 2015; Tobo et al. 2013). While the surface active site density is typically abbreviated as n_s, N_s will be used throughout this manuscript to distinguish it from n500. Best-fit exponential functions (black lines in Fig. 3.1b-d) are given by Equation 3.1:

$$N_x(T) = e^{(a \cdot T + b)} \tag{3.1}$$

where N_x is the activated fraction (N_{n500}), surface active site density (N_s), or volume active site density (N_v), T is temperature (°C), and a and b are fit parameters. Fit parameters and R^2 values for functions shown in Fig. 3.1 are listed in Table B.1. The median-lognormal fitting process suggested by Li et al. (2022) was attempted, but the relatively small number of available measurements at warm temperatures prevented robust estimates of the lognormal fit parameters. instead, regression parameters were calculated with all the available data, using the least absolute residuals method to reduce the impact of extreme values far from the median (e.g. Bassett and Koenker 1978).

Good agreement is seen with previously published INP measurements from the Southern Ocean during the CAPRICORN-1 campaign (McCluskey et al. 2018c, blue shading in Fig. 3.1a,c). Due to the more stringent blank-correction procedure applied to this IS dataset than previous ones (Sec. 3.2.3.2), there is no direct overlap with the warm-temperature results from ACE (Schmale et al. 2019, gold shading in Fig. 3.1a), although they are at the high end of those

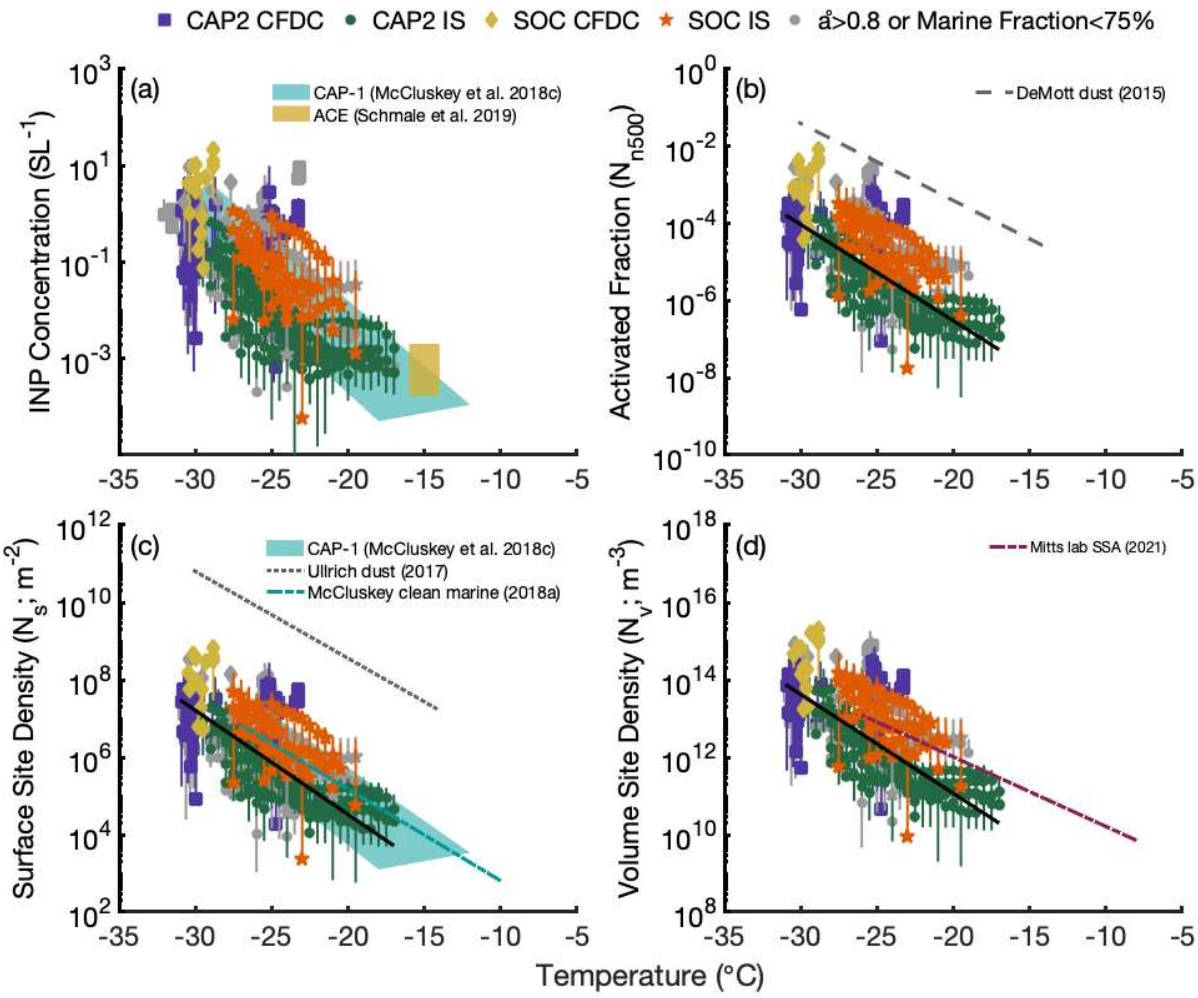

Figure 3.1: INP (a) number concentration, (b) normalized by n500 (N_{n500}), (c) normalized by aerosol surface area (N_s) and (d) normalized by aerosol volume (N_v) temperature spectra during SOC and CAP-2 in the MBL. CAP-2 CFDC (purple squares), CAP-2 filter (green circles), SOC CFDC (gold diamonds), and SOC filter (orange stars) are shown in (a), and in (b-d) when simultaneous aerosol observations were available for normalization. In (a) and (c), the blue shading indicates the range of values observed during CAPRICORN-1 (McCluskey et al. 2018c). The gold shading in (a) shows observations made during the ACE campaign (Schmale et al. 2019). In (b), the grey dashed line shows the DeMott et al. (2015) parameterization for dust based on n500, using the mean n500 value observed during CAP-2. In (c), the grey dotted line indicates the Ullrich et al. (2017) parameterization for dust N_s, and the blue dot-dash line shows the N_s parameterization from McCluskey et al. (2018a) for North Atlantic clean marine air. The dashed magenta line in (d) indicates the Mitts et al. (2021) lab-based parameterization for marine N_v. Non-grey symbols have an å≤0.8 and 5-day back trajectory ocean fraction >75% to identify samples dominated by marine aerosol; grey symbols do not meet at least one of these criteria. Solid black lines in (b-d) indicate the best-fit exponential functions (Eq. 3.1, Table B.1) to the non-grey symbols.

reported for CAPRICORN-1. Additional results from ACE presented in Welti et al. (2020) and Tatzelt et al. (2022) have not been included, as they were not corrected for field blanks, which are a significant fraction of the measured concentrations, particularly at colder temperatures (Tatzelt et al. 2022, Fig. S5 and S8). The lack of blank correction may also explain the higher INP concentrations reported from ACE measurements relative to those from CAPRICORN-1, CAP-2, and SOC, although differences in sampling time and location likely also play a role. Parameterizations for dust INPs based on global INP data and number concentrations of aerosols larger than 500 nm (DeMott et al. 2015) or aerosol surface area concentrations (Ullrich et al. 2017) overpredicted the observations from SOC and CAP-2, corroborating the growing consensus that the majority of boundary layer-INPs in this region are local, and of marine origin (Burrows et al. 2013; McCluskey et al. 2018c; 2019; 2023; Vergara-Temprado et al. 2017; Welti et al. 2020). The N_s-based marine INP parameterization proposed by McCluskey et al. (2018a) using data collected at Mace Head Research Station in Western Ireland is consistent with the exponential best-fit line derived using this dataset between -25 and -27 °C, but has an increasing high bias at warmer temperatures. The more conservative blank-correction procedures used for this study relative to past campaigns (Sec. 3.2.3.2) may have contributed to the lower slope obtained by McCluskey et al. (2018a). Similarly, the Mitts et al. (2021) parameterization for N_v based on laboratory measurements has a lower slope than the fit derived from this dataset, and as a result was found to lie at or above the upper bound of CAP-2 and SOC measurements for temperatures warmer than -20 °C, and above the best fit line at all temperatures.

The role of air-mass history and particle source on INP observations was explored using Ångström exponent (å; Moore et al. 2022) and HYSPLIT (Rolph et al. 2017; Stein et al. 2015) back trajectories. å≤0.8 (Sec. 3.2.2.1) was previously found to work well as a tracer for aerosol size distributions dominated by primary marine aerosol during CAP-2, and was further supported by the degree of marine influence calculated from HYSPLIT back trajectories (Moore et al. 2022). The degree of marine influence was defined as the fraction of a 5-day back-trajectory that passed over the ocean (Sanchez et al. 2021a). Non-grey points in Fig. 3.1 have both å≤0.8 and

a HYSPLIT marine influence >75%; grey points did not meet at least one criterion to be considered marine-dominated. While these metrics worked well to classify SOC and CAP-2 aerosol measurements, there were no discernable differences in INP concentrations or normalized values for marine-dominated periods versus the remaining measurements. Similarly, using primary marine aerosol number, surface area, or volume (Fig. B.5) to normalize INP concentrations produced the same results as using total quantities.

3.3.2 Parameterizing marine INP concentrations

For marine INPs, two parameterizations based on field measurements have been published; one uses aerosol surface area (M18; McCluskey et al. 2018a), and the other SSA organic carbon mass (W15; Wilson et al. 2015) to predict INP concentrations, in addition to activation temperature. The TOC-based parameterization of Wilson et al. (2015) used INP measurements and organic carbon mass concentrations of sea surface microlayer (SML) samples from the Arctic and North Atlantic Oceans to estimate INPs in the organic component of sea spray aerosol. W15 was evaluated in McCluskey et al. (2018a) for North Atlantic marine atmospheric INPs and found to overpredict INP concentrations at -15 and -20 °C by a factor of 4 to 100. Using the same observations, M18 developed an alternative parameterization based on measurements of ambient INPs in SSA at Mace Head, Ireland, which specifically aims to describe organic-coated sea salt particles and not INPs active at warm temperatures, which may be associated with microbes. Both W15 and M18 were evaluated using E3SMv1 (Energy Exascale Earth System Model version 1) simulations of INPs during the March 2016-March 2018 Macquarie Island Cloud Radiation Experiment (MICRE) campaign (Raman et al. 2023). Unlike for the CAPRICORN-1 and SOCRATES campaigns (McCluskey et al. 2019; 2023), W15 produced the best agreement with the MICRE atmospheric INP observations (DeMott et al. 2018a; McFarquhar et al. 2021). However, MICRE observations were also found to be higher than those from open ocean SO measurements, including during ACE (Tatzelt et al. 2022) and the Measurements of Aerosols, Radiation, and Clouds over the Southern Ocean (MARCUS) campaign (DeMott et al. 2018b; McFarquhar

et al. 2021). This discrepancy is likely due to local processes enhancing INP concentrations at Macquarie Island (Raman et al. 2023). Since SOC and CAP-2 measurements are in good agreement with those from CAPRICORN-1, and W15 predicts higher INP concentrations than M18, we adopt the approach of (McCluskey et al. 2019; 2023) and use M18 instead of W15 here. Very recent laboratory experiments suggest that for marine INPs, the active site density may be proportional to particle volume rather than surface area (Mitts et al. 2021), however, field confirmation of this is lacking.

The utility of different normalizations for predicting INP concentrations over the SO are demonstrated in Fig. 3.1. Measurements from CAP-2 and SOC collected in the marine boundary layer were normalized by the number of particles larger than 500 nm (N_{n500}; Fig. 3.1b), aerosol surface area (N_s; Fig. 3.1c) and aerosol volume (N_v; Fig. 3.1d) when simultaneous aerosol measurements were available. While aerosol surface area reduced the spread (in orders of magnitude) of observations the most, none of the normalizations applied here capture the variability in observed INP concentrations. This suggests parameterizations exclusively based on aerosol physical characteristics are only modestly useful in predicting marine INP concentrations, as also concluded by Tatzelt et al. (2022). To further investigate possible INP parameterization inputs, a Spearman's rank correlation analysis was performed between selected environmental variables, aerosol physical characteristics, and concentrations of INPs in binned temperature ranges; the results are shown in Fig. B.6. No strong correlation was found between a single environmental or aerosol metric that applied for every temperature range of INPs, however, moderate but significant correlations ($p<0.05$) were found with both wind speed and aerosol surface area for temperatures colder than -21 °C. Tatzelt et al. (2022) performed a similar analysis between ACE INP concentrations and aerosol number and mass, but did not find any significant relationships between INP and aerosol measurements. However, it should be noted that they did not test for correlations with aerosol surface area, and they only had one INP measurement temperature colder than -21 °C.

SSA concentrations are known to increase with wind speed due to enhanced aerosol formation through wave breaking and bubble bursting (e.g. O'Dowd and de Leeuw 2007). This relationship was also observed for INP concentrations in the MBL during SOC and CAP-2 (Fig. B.7a). INP data used in Fig. B.7 were limited to INPs active at temperatures <-27 °C to reduce the influence of temperature on the observed relationship, since freezing temperature exerts an outsized impact on measured INP concentrations. The wind speed range for the INP measurements shown in Fig. B.7 was 4-23 m s^{-1}, which covers the majority of the observed range in the MBL during CAP-2 (0.1-28 m s^{-1}), though it should be noted measurements were limited to austral summer. Previous research into marine INPs has focused on organic and biological species (DeMott et al. 2016; McCluskey et al. 2018b; Wilson et al. 2015), as soluble salts are not expected to contribute to heterogeneous ice nucleation in the immersion freezing mode, which is the most relevant nucleation mode for low and mixed-phase clouds (e.g. Kanji et al. 2017). Although limited to coastal measurements in the North Atlantic and North Pacific, Gantt et al. (2011) found the organic mass fraction of sea spray aerosol was inversely correlated with wind speed. Taken together, this would predict, if anything, negative correlations between normalized marine INP concentrations and wind speed. However, normalizing the INP concentrations by n500, aerosol surface area, or aerosol volume (Fig. B.7b-d) did not remove the positive wind speed dependence, even though all three aerosol parameters are themselves positively correlated with wind speed (Moore et al. 2022). Figure 3.2 demonstrates that the positive correlation between INP concentration and wind speed extends across the full INP temperature range measured during SOC and CAP-2 and was similarly unaffected by normalization. Together, Fig. B.7 and Fig. 3.2 suggest marine INP emissions are not strictly proportional to SSA production, but instead are enhanced at higher wind speeds through an unknown mechanism. This finding may help explain why parameterizing marine INPs based solely on aerosol physical parameters has not explained as much of the observed variability as for other INP types, particularly dust.

Given the unexpected relationship found between INP concentrations and wind speed, we tested whether adding wind speed as an additional variable improved the marine INP param-

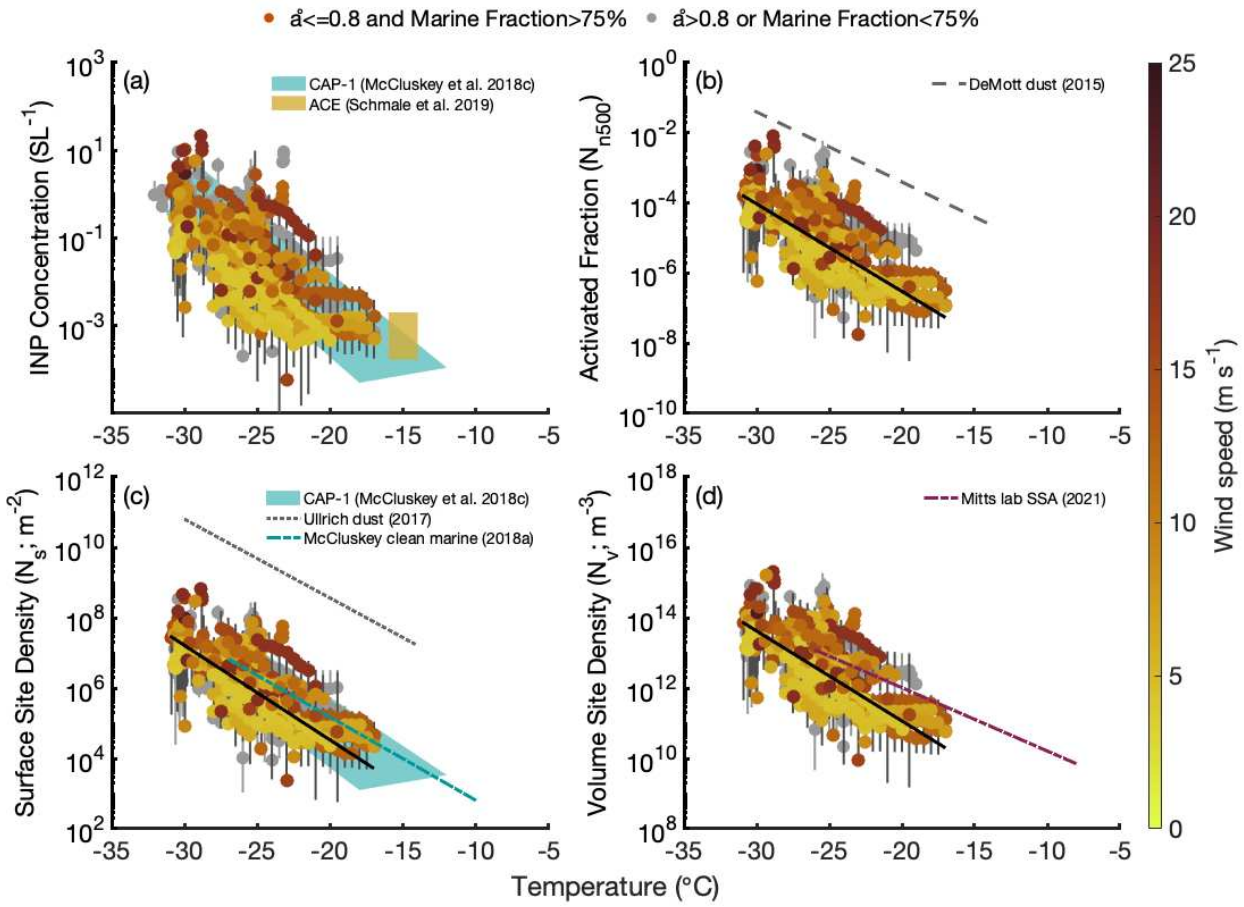

Figure 3.2: INP (a) concentration, (b) N_{n500}, (c) N_s and (d) N_v temperature spectra during SOC and CAP-2 in the MBL. All CFDC and filter measurements are shown as circles and colored by the average wind speed during each measurement period. The shading, parameterizations, best-fit lines, and marine aerosol classification are identical to Fig. 3.1.

eterization developed by McCluskey et al. (2018a). Following the approach of Niemand et al. (2012), N_s for Southern Ocean marine INPs was parameterized using an exponential relationship to activation temperature, with an additional exponential term for wind speed:

$$N_s(T,U) = e^{(a\cdot T+b)} + e^{(c\cdot U+d)} \tag{3.2}$$

where N_s is the surface active site density (m^{-2}), T is temperature (°C), U is wind speed ($m\ s^{-1}$), and a, b, c, and d are fit parameters. CAP-2 and SOC data used to derive the fit parameters were limited to the non-grey points shown in Fig. 3.2, namely, data collected within the marine boundary layer and with å≤0.8 and 5-day back trajectory ocean fraction >75% to isolate marine aerosol. The fit parameters were determined to be: a=-0.66±0.17, b=-3.11±5.11, c=0.51±0.09, and d=6.75±2.03 for this dataset. Modified normalized mean bias (B_n) was reduced from 0.54 to -0.18 by using the best-fit exponential to the SOC and CAP-2 marine boundary layer data instead of the parameterization derived from the North Atlantic (M18), as anticipated by the different slopes seen in Fig. 3.1c. Using wind speed alone to predict N_s does a poor job reproducing the observations, with an increased bias B_n=1.07. Wind speed and temperature together performed the best, with a bias B_n=0.09, supporting its potential utility as a marine INP parameterization (Fig. 3.3).

3.3.3 Southern Ocean Marine INP size

As discussed in Sec. 3.2.3.3, both direct and indirect measurements of INP size were conducted during SOC and CAP-2, based on electron microscopy analysis of ice crystal residuals and INP concentration factors calculated during CAP-2. Measured INP concentration factors during CAP-2 had a maximum value of 37 and a median of 8.3, which are indicated in Fig. B.4 by the grey shading and grey dashed line, respectively. For reference, the average INP concentration factor measured by Tobo et al. (2013) at a forested site in Colorado was 103, suggesting larger INPs were present than over the SO. Comparison with the aerosol concentrator calibration data implies the INPs measured by the CFDC during CAP-2 were dominated by particles

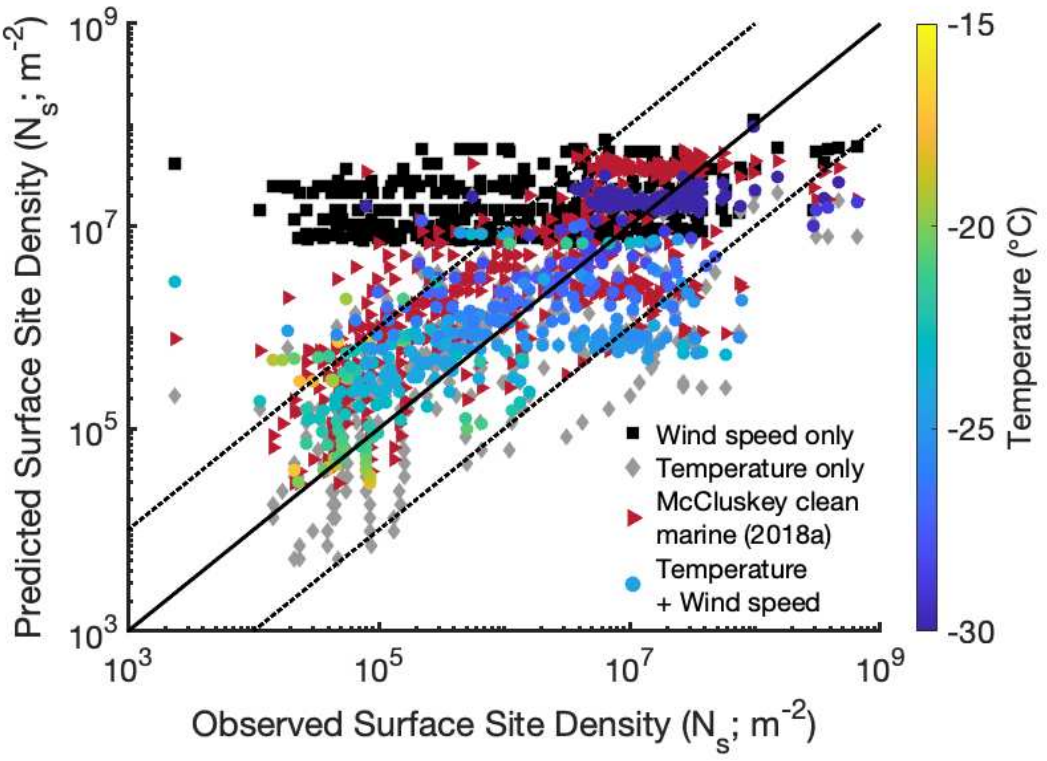

Figure 3.3: Predicted versus observed N_s during CAP-2 and SOC. Data shown are all from the MBL and are limited to observations with å≤0.8 and 5-day back trajectory ocean fraction >75% to isolate marine aerosol. Grey diamonds show a single-exponential fit using only temperature (B_n=-0.18), and black squares only wind speed (B_n=1.07). Non-grey circles show a 2-exponential fit (Eq. 3.2) to both wind speed and temperature and are colored by measurement temperature (B_n=0.09). Red triangles use the N_s parameterization from McCluskey et al. (2018a) for clean marine air (B_n=0.54). The solid black line indicates a 1:1 relationship, and a factor of 10 deviation is shown by the dashed black lines.

<600 nm. CFDC ice crystal residuals collected during CAP-2 and SOC were as small as 0.1 μm; as previously discussed, the maximum size considered was 1.5 μm (Twohy et al. 2021). Ice crystal collections during CAP-2 utilized the aerosol concentrator, so the residual size distribution was corrected for size-dependent enhancements using the calibration data shown in Fig. B.4, as well as for size-dependent losses in the impactors upstream of the CFDC columns (Sec. 3.2.3.1), assuming residuals had the hygroscopicity and density of sea spray aerosols. The corrected median INP residual size was 0.18 μm, which agrees quite well with the 0.3-0.4 μm predicted from the median INP concentration factor measured during CAP-2 (Fig. B.4), given both have large uncertainties. The smaller than expected sizes of Southern Ocean INPs is consistent with the lack of correlation observed by Tatzelt et al. (2022) between ACE INP concentrations and aerosol number or mass, as well as the generally poor or modest relationships found in this study (Sec 3.2; Fig. B.6).

It should be noted that both analyses were limited to particles <1.5 μm due to the CFDC upstream impactors necessary to limit interferences from supermicron SSA in optical detection of ice crystals. Another potential complication is the use of measured concentration factors at relatively cold temperatures (≤-25 °C) to infer the median size of the overall marine INP population. Mason et al. (2016) found supermicron INPs dominated in most of their continental and coastal sites between -15 and -25 °C, and typically measured larger median sizes at warmer temperatures. While biological INPs can be as small as ~10 nm (e.g. Kanji et al. 2017; Pummer et al. 2015; Wilson et al. 2015), many bioaerosols are present in the coarse mode, and typically have warm onset temperatures if active as INPs (e.g. Hoose and Möhler 2012; Kanji et al. 2017). Although the characteristic size distribution or mode size of ambient marine INPs is unknown, good correlation with aerosol surface area (DeMott et al. 2016; McCluskey et al. 2018a), preferential emission in jet drops over film drops (Wang et al. 2017), and recent laboratory studies indicating supermicron marine INPs dominate below -14 °C (Mitts et al. 2021) had suggested the majority of marine INPs are >500 nm, if not larger. However, the excellent agreement between CFDC measurements, which sampled INPs <1.5 μm (CAP-2) or <2.5 μm (SOC), and the IS

filter measurements, which captured larger particles, suggest the CFDCs were collecting most available INPs during CAP-2 and SOC (Fig. 3.1, 3.5). Future studies of size dependent INP concentrations in remote marine environments are needed to comprehensively assess the size distribution of marine INPs.

3.3.4 Altitude dependence

While modeling studies (Burrows et al. 2013; McCluskey et al. 2019; 2023; Vergara-Temprado et al. 2017) have provided insights into the expected vertical distribution of INPs in this region, SOCRATES measurements represent the first in situ observations in and above cloud to validate these results. Although temporally variable, the studies cited predict an increasing influence of mineral dust with height on average. Simulations of the CAPRICORN-1 field campaign (McCluskey et al. 2019) also suggested INP concentrations at -25 °C would decrease with height through the boundary layer and up to 3-4 km, then increase at higher altitudes. Some evidence supporting this structure is seen in Fig. 3.4a, which shows the CAP-2 and SOC INP concentrations as a function of altitude. A minimum in mean INP concentrations colder than -27 °C was seen between 2-4 km, with higher values in the MBL and around 6 km. The very limited observations above 6 km did not support the continued increase in INP concentrations with height predicted by McCluskey et al. (2019). When normalized by aerosol concentrations, N_{n500}, N_s and N_v were consistently higher above cloud and in the upper troposphere (>5000 m) than in the marine boundary layer, particularly N_{n500}. This finding is consistent with modeling results predicting different sources of INPs below and above-cloud. It also agrees with TEM measurements of single particles collected during SOCRATES flights, which found significantly increased abundances of crustal and metal particles >0.5 μm above cloud versus in-cloud or in the MBL (Twohy et al. 2021). Above cloud and upper tropospheric N_{n500} were consistent with the DeMott et al. (2015) parameterization for dust (Fig. B.8b), but N_s values were still 1-2 orders of magnitude lower than the Ullrich et al. (2017) dust parameterization (Fig. B.8c). This

discrepancy between the effectiveness of dust aerosol number- and surface area-based parameterizations has been reported previously for this region (McCluskey et al. 2019; 2023).

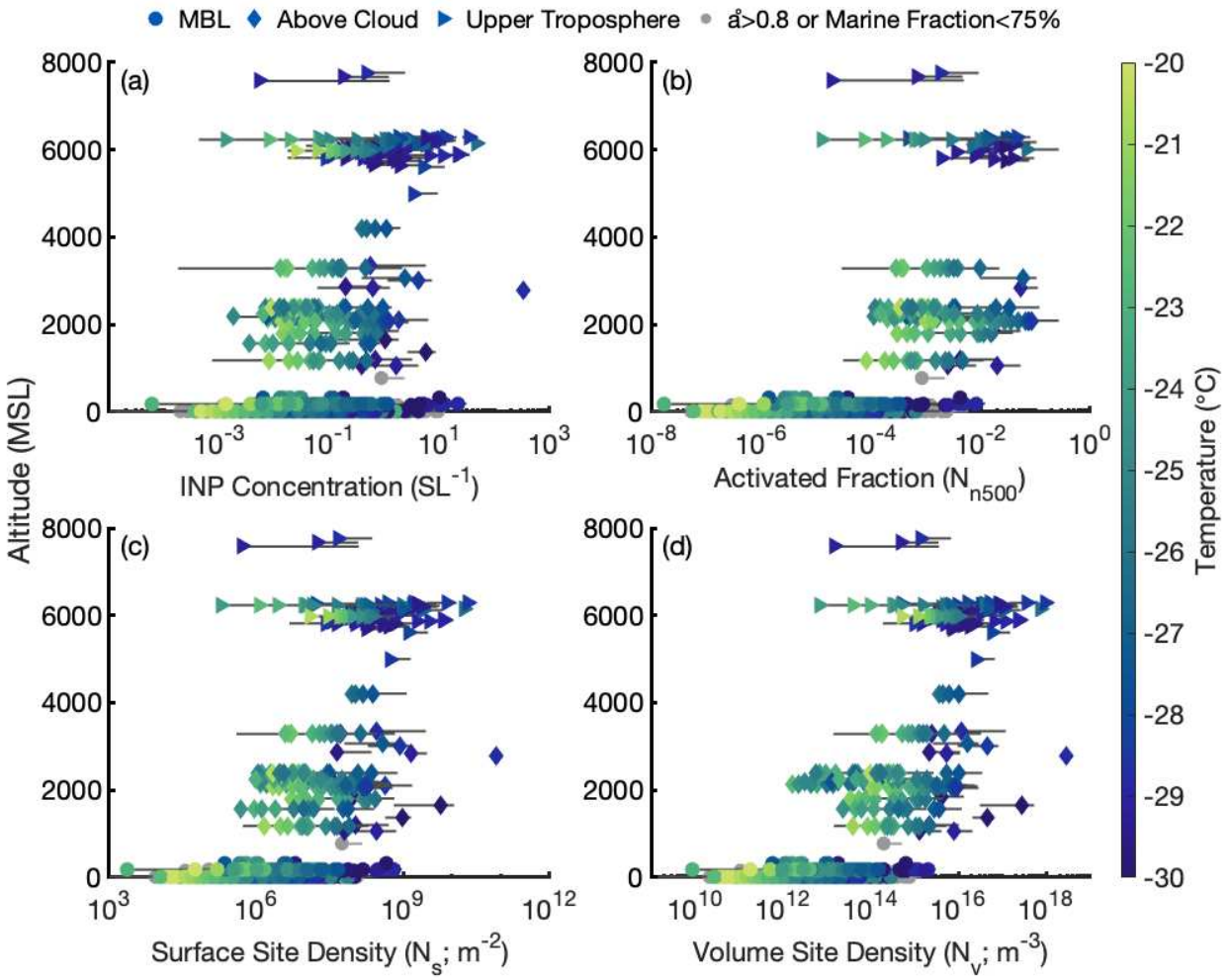

Figure 3.4: INP (a) concentration, (b) N_{n500}, (c) N_s and (d) N_v during SOC and CAP-2 as a function of altitude. Data in the MBL shown as circles, above cloud as diamonds, and upper troposphere (>5000 m) data as triangles. Non-grey symbols for the MBL data (circles) have å≤0.8 and 5-day back trajectory ocean fraction >75% to isolate marine aerosol; grey symbols do not meet at least one of these criteria. All symbols are colored by measurement temperature.

About half of the SOC research flights collected paired filter samples, with one in the MBL and one above cloud. Examples from RF05 (1/25-1/26/18) and RF14 (2/21-2/22/18) are shown in Fig. 3.5, along with SOC CFDC data separated into MBL and above-cloud measurements, in-cloud data on the CVI, and simulated CAM6 INP concentrations (Sec. 3.2.4) co-located with the

SOC observations (McCluskey et al. 2023). When available, CAP-2 CFDC data during G-V overpasses of the RV *Investigator* are also shown for comparison. Due to the very different speeds traveled by the ship and aircraft, measurements were counted as overpasses if they occurred within 30 minutes of each other, and the G-V was within 150 km of the RV *Investigator* during the measurement. Within uncertainty, the MBL and above-cloud measurements agreed for both flights shown here (Fig. 3.5a-b), as well as the in-cloud observations, which was typical for all of the flights with paired filters. When normalized by n500 (Fig. 3.5c-d) or aerosol surface area (Fig. 3.5e-f), some separation between the MBL and above-cloud measurements occurred for most flights with available data, with the largest separation for N_{n500}. Both the McCluskey et al. (2018a) clean marine parameterization and the exponential fit derived in this study predict MBL N_s well on a flight-by-flight basis, while the dust-specific parameterization of Ullrich et al. (2017) uniformly overpredicts N_s, as seen throughout this work.

Simulated total INP concentrations from CAM6 have variable agreement with the co-located SOCRATES IS and CFDC measurements. As described in Sec. 3.2.4, CAM6 INP concentrations are the sum of the sea spray INP contribution, based on simulated SSA surface area using M18, and the dust INP contribution, using the number of simulated mineral dust particles larger than 500 nm and the DeMott et al. (2015) parameterization. Overall, the agreement is better for observations in the MBL, while simulated above-cloud INP concentrations are biased low, although there is significant variation among flights. The low bias of CAM6 above-cloud values relative to observations is typically reduced when considering N_s (Fig. 3.5e-f) instead of INP concentrations (Fig. 3.5a-b). This suggests that in addition to the surface level biases in aerosol surface area, low biases in accumulation mode aerosol aloft, and large uncertainties in particle composition aloft observed by McCluskey et al. (2023), there may also be a low bias in simulated aerosol surface area above cloud, which is partially compensating for the underestimation of INPs in CAM6.

Fig. 3.5a-b and 3.5c-d include two lines indicating the DeMott et al. (2015) INP parameterization for dust. Since D15 is specific to dust INPs but there were not continuous size-

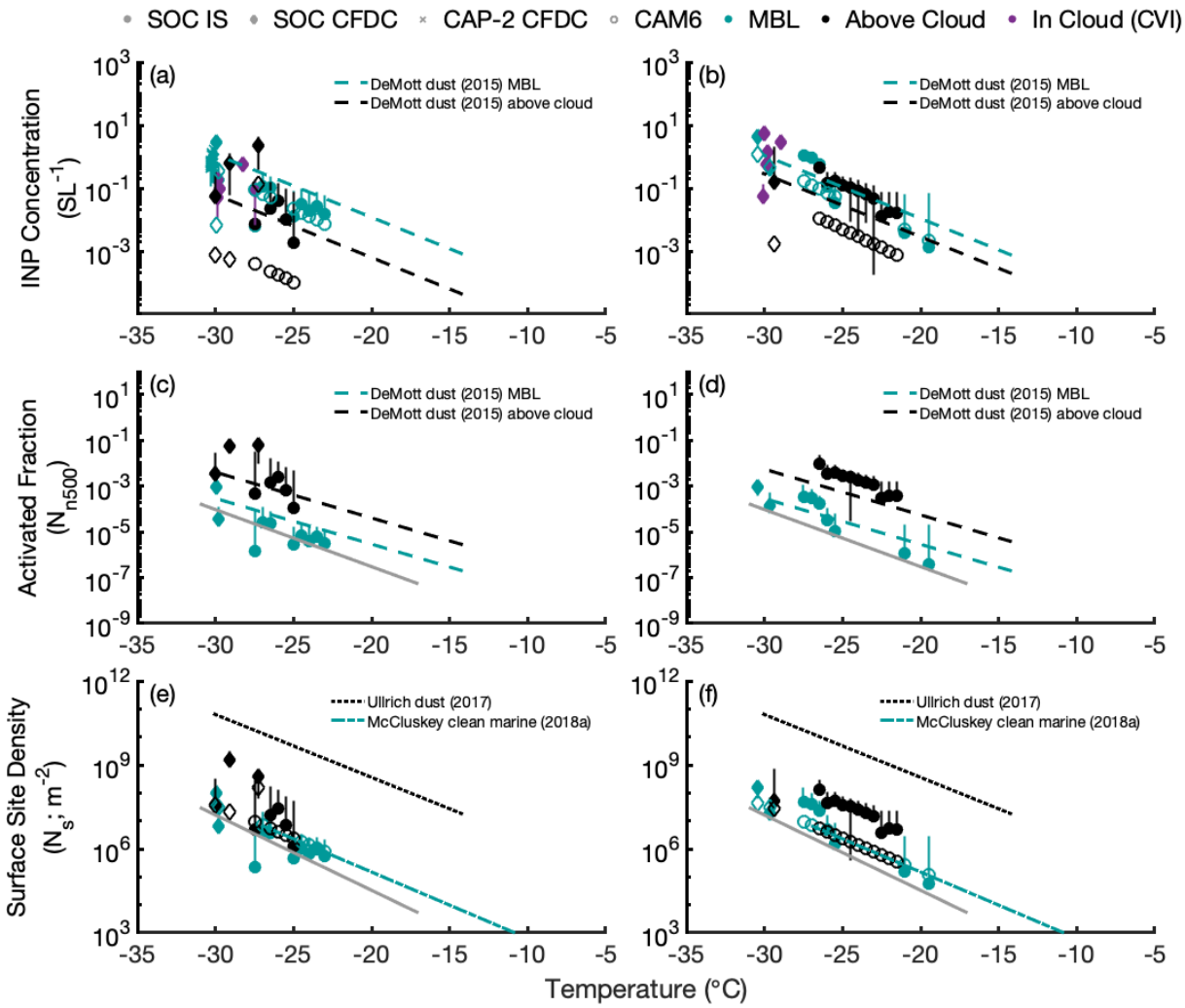

Figure 3.5: INP (a-b) concentration, (c-d) N_{n500}, and (e-f) N_s temperature spectra for SOCRATES flight RF05 (1/25-1/26/18) on the left and RF14 (2/21-2/22/18) on the right. Data in the MBL are shown as light blue symbols, and measurements above cloud in black. SOC filter measurements are circles, SOC CFDC are diamonds, simultaneous CAP-2 CFDC measurements are crosses (if available), and simulated CAM6 INP concentrations are open symbols (panels (a-b) and (e-f) only). If available, SOC CFDC observations in-cloud on the CVI are shown as purple diamonds in panels (a-b). In panels (a-b) and (c-d), the blue and black dashed lines indicate the DeMott et al. (2015) parameterization for dust based on n500 in the MBL and above cloud, respectively. In (e-f), the black dotted line indicates the Ullrich et al. (2017) parameterization for dust N_s, and the light blue dot-dash line shows the N_s parameterization from McCluskey et al. (2018a) for clean marine air. Solid grey lines in (c-d) and (e-f) indicate the best-fit exponential functions to all the MBL data with non-grey symbols (Same as Figure 3.1).

resolved measurements of dust concentration, the required dust n500 inputs were estimated using STEM measurements of aerosol composition averaged over SOC (Sec. 3.2.2.3; Twohy et al. 2021). The total n500 values measured during each SOC filter collection were scaled using the average fraction of particles >0.5 μm that were categorized as crustal or metal types during SOC (0.5 for above-cloud and 0.02 for MBL) to provide an estimate of dust n500. The dashed blue and black lines in Fig. 3.5a-b indicate the dust INP concentrations predicted by D15. Fig. 3.5c-d shows D15 normalized by the total n500 measured during each flight, to provide a fair comparison to the SOC INP measurements, and thus represents the predicted N_{n500} if all the INPs present were dust, but SSA contributes to n500. Excellent agreement was seen between both parameterization estimates and their respective filters when normalized by total n500 (Fig. 3.5c-d). More variable agreement was seen for absolute INP concentration estimates (Fig. 3.5a-b), though most agree with the measurements within uncertainty. In addition to a low bias relative to the SOC observations, CAM6 typically underpredicts INP concentrations relative to D15, especially above cloud (Fig. 3.5a-b). Although not explored in McCluskey et al. (2023), this is consistent with the underprediction of dust concentrations observed in E3SMv1 (Raman et al. 2023), as well as an increasing contribution of dust to INP concentrations with height.

While this exercise does not provide direct evidence of the INP types present during SOC, it does support the results shown in Fig. 3.4 and Fig. B.8 that different types of INPs dominate at different heights. Furthermore, if the average amount of dust measured by STEM during SOC was present uniformly across the SO, D15-estimated dust INPs would be sufficient to account for all or nearly all INPs measured, at all heights. This finding emphasizes the vast differences in nucleation efficiency or site density between marine INPs and dust, and shows how even small amounts of long-range transported dust can significantly influence SO cloud properties, as also noted by McCluskey et al. (2023).

3.4 SUMMARY

The Southern Ocean Cloud Radiation Aerosol Transport Experimental Study (SOCRATES) aircraft campaign, the second Clouds, Aerosols, Precipitation, Radiation and atmospherIc Composition Over the southeRN ocean (CAPRICORN-2) ship campaign, and affiliated projects in 2017-2018 were motivated by a lack of observations and understanding of cloud, aerosol, precipitation, and radiative processes and interactions in the Southern Ocean region (McFarquhar et al. 2021). This study presents measurements of INPs collected over the Southern Ocean in austral summer 2018, along with comparisons to CAM6 model simulations. Simultaneous aircraft and ship campaigns provided the first vertical distribution measurements of INPs in the region, including the first in situ observations in and above cloud. Our results confirm recent findings from the ACE (Schmale et al. 2019; Tatzelt et al. 2022; Welti et al. 2020) and CAPRICORN-1 (McCluskey et al. 2018c) campaigns that INP concentrations in the SO marine boundary layer are lower at all latitudes than measurements made by Bigg (1973)in the late 1960s and early 1970s. The good agreement between CAP-2 CFDC data and SOC measurements during overpasses (Fig. 3.5) shows promise for future campaigns that might employ a similar multi-platform approach to understand vertical profiles of aerosols and INPs.

Modeling studies (Burrows et al. 2013; McCluskey et al. 2019; 2023; Vergara-Temprado et al. 2017) predicted marine INPs would dominate at low altitudes in the SO, with an increasing influence of mineral dust INPs with height. Paired MBL and above cloud measurements from SOC support this hypothesis (Fig. 3.5). Below- and above-cloud INP concentrations typically agree within uncertainty, however, higher ice nucleation efficiency was found above cloud, consistent with significantly enhanced dust concentrations observed in above cloud single-particle composition measurements (Twohy et al. 2021). The outsized impact dust INPs can have on SO cloud properties is also demonstrated in Fig. 3.5. Due to the vastly higher nucleation efficiency of mineral dust compared to marine INPs, dust INP concentrations predicted by the D15 parameterization were sufficient to account for almost all INPs measured, both in the MBL and at higher altitudes. However, this was based on bulk aerosol composition measurements

and would require the average SOC dust n500 fraction to be present uniformly over the SO. As a result, the D15 predictions in Fig. 3.5 can only be interpreted as a broad verification of the relatively low nucleation efficiency of marine INPs, which still likely dominate primary ice nucleation in the SO MBL.

Both direct measurements of collected INP residuals and indirect inferences from enhancement factors measured using an aerosol concentrator suggest INPs in the MBL, at least those in the sub-2.5 μm range, are dominated by particles <500 nm. Small INP sizes are consistent with the minimal correlations observed between ACE INP concentrations and aerosol number or mass (Tatzelt et al. 2022), as well as the only modest relationships found in this study between INP concentrations and environmental or aerosol metrics (Fig. B.6). However, both aerosol surface area and wind speed exhibited moderate correlations ($p<0.05$) for INP concentrations <-21 °C during SOC and CAP-2. Surprisingly, the correlation with wind speed remained after normalizing the INP concentrations by n500, aerosol surface area, or aerosol volume, suggesting marine INP emissions are not strictly proportional to SSA production (Fig. 3.2, Fig. B.7). Following the approach of Niemand et al. (2012), a new parameterization for marine INPs is proposed, which includes wind speed in addition to activation temperature, and has reduced bias when compared to the existing parameterization of McCluskey et al. (2018a). This parameterization captures the observed mean behavior well, but there is still significant unexplained variability in INP concentrations remaining (Fig. 3.1, 3.3). One of the assumptions underlying the Niemand et al. (2012) and M18 approach is that the active site density is constant, or equivalently, the number of INPs per aerosol surface area is fixed. Marine INPs appear to violate this assumption, and wind speed, among other factors, plays a role in how INPs are distributed with aerosol surface area in the remote SO MBL.

4. Wind-driven Emission of Marine Ice Nucleating Particles in the Scripps Ocean-Atmosphere Research Simulator (SOARS)

4.1 INTRODUCTION

Sea spray aerosols (SSA) are marine-derived particles comprised of mixtures of inorganic salts and organic compounds, with the exact composition and mixing state varying based on particle size, production mechanism, and the underlying biology and geochemistry of the source seawater (e.g. Lewis and Schwartz 2004; O'Dowd and de Leeuw 2007; de Leeuw et al. 2011; Cochran et al. 2017). Along with mineral and soil dusts, SSA dominates atmospheric aerosol mass, and contributes ~30% to globally-averaged total aerosol optical depth (AOD) (O'Dowd and de Leeuw 2007; Bellouin et al. 2013). Primary marine aerosol (PMA) are generated through wind stress at the ocean surface, either through the direct tearing of breaking wave crests (spume drops) or as a result of bubble bursting (film and jet drops) following air entrainment during wave breaking (Lewis and Schwartz 2004; O'Dowd and de Leeuw 2007; Deike et al. 2022). Oxidation of dimethyl sulfide (DMS) and other biogenic volatile organic compounds (BVOCs) emitted from the ocean can lead to the condensation of gas-phase species and formation of secondary marine aerosol (SMA) (Lewis and Schwartz 2004; Quinn et al. 2017; Naik et al. 2021). Given their ubiquity in the atmosphere, SSA are an important contributor to both the magnitude and uncertainty of aerosol radiative forcing (Carslaw et al. 2013; 2017; Andreae 2007; Forster et al. 2021).

The indirect radiative impact of both PMA and SMA through their role as cloud condensation nuclei (CCN) has received considerable attention from observational, laboratory, and modeling studies (e.g. Andreae 2007; Quinn et al. 2017; Pierce and Adams 2006; Modini et al. 2015; Mayer et al. 2020; McCoy et al. 2015a; Heinze et al. 2019; Grythe et al. 2014; Gryspeerdt et al. 2023). Spurred by observations in remote ocean regions and laboratory mesocosm studies (Rosinski et al. 1987; Bigg 1973; 1990; Knopf et al. 2011; DeMott et al. 2016), the contribu-

tion of marine aerosols to the ice nucleating particle (INP) budget, and thus indirectly to cloud phase, has become an increasing focus in recent years (e.g. Burrows et al. 2013; McCluskey et al. 2018a;b;c; 2019; 2023; Schmale et al. 2019; Wilson et al. 2015; Tatzelt et al. 2022; Irish et al. 2017; 2019; Alpert et al. 2022; Steinke et al. 2022; Raman et al. 2023; Mitts et al. 2021; Welti et al. 2018; 2020; Hartmann et al. 2020; 2021; Zhao et al. 2021; Vergara-Temprado et al. 2017; 2018; Raatikainen et al. 2022; Miyakawa et al. 2023; Lin et al. 2022; Kawana et al. 2023; Ickes et al. 2020; Huang et al. 2018; Creamean et al. 2019). INPs are critical in initiating cloud glaciation at temperatures warmer than ~-36 °C and thus exert a large influence on cloud properties related to phase, such as lifetime, precipitation formation, and radiative forcing (e.g. Kanji et al. 2017). Additionally, mixed-phase clouds, which contain both liquid and ice, play major roles in determining cloud feedbacks (McCoy et al. 2015b; 2016), global cloud radiative properties (Cesana and Storelvmo 2017), and equilibrium climate sensitivity (Zelinka et al. 2020; Bjordal et al. 2020), and are especially sensitive to aerosols in clean conditions, such as over the ocean.

Measurements of ice nucleation in marine environments were first made in the late 1950s and 1960s (see Ickes et al. 2020, Table 1). Since then, a few studies have suggested whole phytoplankton cells or marine bacteria may be the ice nucleating components of SSA (Knopf et al. 2011; Beall et al. 2021; Fall and Schnell 1985; Wilbourn et al. 2020). However, the majority of studies indicate marine macromolecules, phytoplankton exudates, or other biogenic, organic species are the ice nucleating components based on their generally small size (<0.2 μm) and relationship with biological activity (Wilson et al. 2015; Rosinski et al. 1987; DeMott et al. 2016; Irish et al. 2017; Schnell and Vali 1976; Knopf et al. 2011; Ladino et al. 2016; Alpert et al. 2022; McCluskey et al. 2018b; Wang et al. 2015a). Based on laboratory and mesocosm experiments, several studies have also inferred different components may be active at different temperatures, as well as at different times throughout the onset and decay of phytoplankton blooms (McCluskey et al. 2018b; DeMott et al. 2016; Ickes et al. 2020). In addition to the small and ubiquitous marine organic INPs, a second category of more intermittent, larger, and heat sensitive marine INPs that are active at warmer temperatures has been identified (McCluskey et al. 2018b; Ickes et al.

2020; Hartmann et al. 2020; van Pinxteren et al. 2020). These may be associated with microbes or cellular debris, but have not been definitively identified. Very recent laboratory studies have pointed to the importance of supermicron SSA as a marine INP (Mitts et al. 2021), however, no assessment of the atmospheric transport of such particles was conducted and ambient observations have yet to confirm this.

INP concentrations in remote marine regions are generally several orders of magnitude lower than those in continental areas (DeMott et al. 2016; McCluskey et al. 2018a; Tatzelt et al. 2022; Welti et al. 2020). Based on normalization by particle number or surface area, marine INPs are also significantly less efficient at nucleating ice than species such as mineral or soil dusts (Kanji et al. 2017; DeMott et al. 2016; McCluskey et al. 2018a). Despite this, in remote areas such as the Southern Ocean, marine INPs are hypothesized to be the dominant contribution to the INP budget due to the lack of continental influence (Burrows et al. 2013; Vergara-Temprado et al. 2017; 2018; McCluskey et al. 2019), and may dominate seasonally or intermittently in other regions such as the high Arctic (Ickes et al. 2020; Huang et al. 2018; Creamean et al. 2019; Hartmann et al. 2020; 2021). Atmospheric concentrations of the small, organic marine INP type were parameterized using observations from Mace Head in the North Atlantic (McCluskey et al. 2018a), and subsequent implementation in CAM5 (Community Atmosphere Model version 5) and CAM6 (version 6) compared well to observations made in the Southern Ocean (McCluskey et al. 2019; 2023). Other recent modeling work has focused on the intermittent, high temperature marine INPs (Steinke et al. 2022), or freezing kinetics of background SSA particles (Alpert et al. 2022). Despite these efforts, the fundamental processes controlling the emission of marine INPs from the sea surface to the atmosphere remain largely unknown.

Significantly more is known about the factors influencing the production of sea spray, although there is still huge variability in simulated SSA fluxes among models, especially in polar regions (de Leeuw et al. 2011; Lapere et al. 2023; Deike et al. 2022; Grythe et al. 2014). Numerous parameterizations for sea spray size distribution functions have been proposed (e.g. Monahan and Muircheartaigh 1980; Monahan et al. 1986; de Leeuw et al. 2011; Lewis and Schwartz 2004;

Gong 2003; Mårtensson et al. 2003; Meskhidze et al. 2013; Ovadnevaite et al. 2014; Grythe et al. 2014; Sofiev et al. 2011; Jaeglé et al. 2011; Salter et al. 2015), with the choice influencing not only emitted SSA number and mass, but also the simulated radiative budget and aerosol-cloud interactions once implemented in models (Johnson et al. 2020; McCoy et al. 2015a; Grythe et al. 2014; Barthel et al. 2019). Although wind speed is the dominant influence on SSA production (Lewis and Schwartz 2004; O'Dowd and de Leeuw 2007; de Leeuw et al. 2011), other factors including sea surface temperature (Mårtensson et al. 2003; Sellegri et al. 2006; Salter et al. 2014; 2015; Forestieri et al. 2018; Liu et al. 2021; Saliba et al. 2019; Sellegri et al. 2006; 2023; Barthel et al. 2019; Jaeglé et al. 2011; Zábori et al. 2012; Ovadnevaite et al. 2014; Schwier et al. 2017; Christiansen et al. 2019; Zinke et al. 2022; Hartery et al. 2020), salinity (Mårtensson et al. 2003; Zábori et al. 2012; Nilsson et al. 2021; May et al. 2016; Ovadnevaite et al. 2014; Zinke et al. 2022), and seawater biology and chemistry (O'Dowd et al. 2004; Sellegri et al. 2006; Fuentes et al. 2010; Wang et al. 2015a; McCoy et al. 2015a; Schwier et al. 2017; Burrows et al. 2018; Saliba et al. 2019; Christiansen et al. 2019; Sellegri et al. 2023) have also been shown to influence production. Conflicting and sometimes contradictory results for the magnitude and even sign of the impact of each of these variables has been observed in laboratory and field measurements, which has not aided evaluation of the numerous available SSA source parameterizations.

The new Scripps Ocean-Atmosphere Research Simulator (SOARS) wind-wave channel at the Scripps Institution of Oceanography was designed to tackle some of these outstanding questions about the production and atmospheric impacts of SSA. This study focuses on first results from the SOARS channel during the CHaracterizing Atmosphere-Ocean parameters in SOARS (CHAOS) mesocosm campaign, conducted for two months in 2022. The overarching goal of CHAOS was to understand and reduce uncertainty in two factors known to affect SSA production: sea surface temperature (SST) and wind speed. Improvements over previous wave channel experiments (Prather et al. 2013; Wang et al. 2015a; Sauer et al. 2022) include the ability to initiate wave breaking through wind stress, increasing atmospheric relevance. This study will

touch on SSA production in SOARS, but primarily address the role of wind speed in emissions of marine INPs, which have not previously been characterized through controlled experiments.

4.2 METHODS

4.2.1 Production of Sea Spray Aerosols in SOARS

Measurements described in this study were collected during the CHaracterizing Atmosphere-Ocean parameters in SOARS (CHAOS) study, which was conducted during July-August 2022. SSA were produced in the new Scripps Ocean-Atmosphere Research Simulator (SOARS) wind-wave channel at the Scripps Institution of Oceanography (SIO), which is shown schematically in Figure C.1. The SOARS channel is 2.5 m wide, 2.5 m tall, and 36 m in length, with a nominal water volume of 103,680 L when filled. This is approximately 9 times the water volume of the glass wave channel described in Sauer et al. (2022), which was used during the preceding SeaSCAPE campaign. Waves are generated with a paddle driven by a TEFC (Totally Enclosed, Fan-Cooled) electric motor, up to a maximum height of 1.2 m. In contrast to the glass channel, wave breaking is driven by air flow generated from wind turbines at the front of the SOARS channel and recirculated through the sealed headspace and return vents. A submerged polycarbonate ramp, or "beach", at the end of the channel dissipates residual wave energy and reduces interference at the main wave breaking location, about halfway down the channel. At low wind speeds, HEPA filters and other user-selectable filters (i.e. activated charcoal) can be lowered in-line with the air stream in the recirculation vents to remove particles and organic compounds. A "tent" constructed of plastic sheeting was built around the paddle during CHAOS to minimize particle or VOC contamination of the SOARS headspace through paddle motion. HEPA filters with fans blowing through them maintained positive pressure inside the tent.

Water to fill the SOARS channel is sourced from the Pacific Ocean at the nearby Scripps Pier. Seawater is pumped up from the end of the pier, roughly filtered with an aluminum screen to remove large detritus, and then travels the length of the pier in a gravity flume (Sauer et al. 2022).

Unlike SeaSCAPE, the water volume required to fill the SOARS channel necessitated using the same plumbing and holding tanks as the nearby Birch Aquarium and other SIO labs instead of pumping water directly out of the gravity flume and transporting by truck to the channel. At the pier entrance, seawater is fed into a large settling tank and then filtered through high capacity sand filters prior to being pumped into several large holding tanks, before finally being gravity-fed to labs and other facilities. The SOARS channel is filled using either gravity or adjustable-speed water pumps (typically ~90 gal min^{-1}) and optionally passed through additional filters and/or UV-sterilized. During CHAOS, seawater was not filtered or UV-sterilized, and the channel was gravity-filled without pumps. Two separate fills of the SOARS channel were conducted during CHAOS: July 9-August 12, 2022 and August 13-September 8, 2022. Water temperature can be controlled between -1.6 and 30 °C, and air temperature between -15 and 30 °C. Neither were controlled during CHAOS, and were instead allowed to vary according to the ambient temperature. The channel contains built-in sensors at several locations for measuring air and water temperature, atmospheric CO_2 concentration, and water salinity and turbidity. Since the entire SOARS channel is indoors, there are 2 optional lighting mechanisms. 6 solar tubes centered on the middle 1/3 of the channel can provide up to 10% of ambient light, which penetrates the full depth of the channel. 40000 W of PAR LEDs can provide supplemental lighting during night or stormy conditions. Neither were utilized during CHAOS, as no intentional biological growth was stimulated.

The SOARS paddle can be programmed to generate wave packets of variable wavelength and amplitude. During CHAOS, two wave packets were superimposed to form 5 wave crests, of which 2 break; this pattern was repeated for the duration of each sampling period. Prior to each sampling period, the headspace air was filtered at a low wind speed to remove particles. Then the wind turbines were set to generate the desired wind speed, and the paddle started to create waves. Occasionally, the wind turbines were run without the paddle, which can generate SSA at high enough wind speeds. The wind turbine RPM setpoints were calibrated using a sonic anemometer installed inside the channel with no waves generated. Wind speeds were mea-

sured at 0.6 m above the water surface and extrapolated to a value at 10 m (U_{10}) following Hsu et al. (1994). White cap coverage was calculated from still images collected at high resolution for every measured wind speed. For each wave packet amplitude, there is a single wind turbine setpoint which generates a white cap fraction representative of open-ocean conditions, based on the relationship described in Monahan and Muircheartaigh (1980). During CHAOS, the wave packed amplitude was fixed at 1.3, which yields an open-ocean equivalent white cap coverage at a wind turbine setpoint of 1550 rpm, corresponding to an extrapolated U_{10} of 18.5 m s^{-1}. Measurements collected during CHAOS were made at wind turbine speeds of 850, 1200, 1300, 1400, 1600, and 1800 rpm, which correspond to U_{10} of 9.89, 14.19, 15.42, 16.64, 19.10, and 21.55 m s^{-1}. Measurements made at 1600 rpm (19.10 m s^{-1}) are considered to represent open-ocean breaking wave conditions, through comparison with Monahan and Muircheartaigh (1980). For all other wind speeds measured during CHAOS, the fixed wave amplitude meant the white cap coverage is not comparable to open-ocean conditions and only the relative influence of wind speed alone can be assessed.

4.2.2 Ice Nucleating Particle Measurements

Ice nucleating particle measurements were conducted at all wind speeds. A Colorado State University (CSU) Continuous Flow Diffusion Chamber (CFDC; Section 4.2.2.1) was used to capture online measurements at high temporal resolution (~15 min), and aerosol filter samples were collected and subsequently analyzed with the CSU Ice Spectrometer (IS; Section 4.2.2.2) to provide INP temperature spectra down to -30 °C. Chemical pre-treatments of aerosol filter suspensions allowed INPs produced in SOARS to be classified by broad composition (Section 4.2.2.3), and Atomic Force Microscopy was used to assess INP morphology and phase state (Section 4.2.2.4). Water samples were collected daily from SOARS and seawater ice nucleating entity (INE) temperature spectra were also measured using the IS, as a complement to the aerosol results (Section 4.2.2.2). CFDC measurements (Section 4.2.2.1) presented here exclude the first 15 minutes of each sampling period to allow particle concentrations to reach an approx-

imate steady-state. IS filters (Section 4.2.2.2) were started ~15 min into each sampling period for the same reason.

4.2.2.1 Continuous Flow Diffusion Chamber

Real-time measurements of INP concentration were collected using a CSU Continuous Flow Diffusion Chamber (CFDC), a vertically oriented, ice-thermal diffusion chamber (DeMott et al. 2015; Rogers 1988; Rogers et al. 2001). The HIAPER (CFDC-1H) version of the CFDC used during CHAOS has been previously described in detail and will only be briefly discussed here (e.g. McCluskey et al. 2018c; Moore 2020; DeMott et al. 2023; Moore et al. 2023). Prior to entering the top of the CFDC chamber, the sample aerosol stream drawn from SOARS was dried to below the frost point with diffusion driers, then passed through two sequential single-jet impactors (50% aerodynamic diameter cut size D_{50}=2.4 μm) to remove large aerosols. Within the chamber, particles are first exposed to near steady state humidity and temperature conditions conducive to the activation of cloud droplets and ice crystals, followed by a water-subsaturated region to evaporate haze and cloud droplets back to aerosol sizes. Ice crystals are then detected optically at the base of the chamber using an optical particle counter (OPC) and distinguished by size from aerosols and any remaining cloud droplets (Barry et al. 2021b). The upper region of the chamber was held under water supersaturated conditions (typically 104% to 108%) for this campaign to emphasize the immersion freezing mode of ice nucleation and give comparable results to offline techniques (DeMott et al. 2016; 2017; 2018c; Barry et al. 2021b).

The aerosol lamina temperature was held at -25 °C or -30 °C during CHAOS to maximize the instrumental signal to noise ratio and accommodate limited sampling durations at each wind speed. Paired measurements of the sample air stream (10 min) and HEPA-filtered air (5 min) were used to quantify instrument noise (DeMott et al. 2017). All measurements presented here have been corrected for CFDC background using adjacent filtered-air periods, as in Moore (2020) and Barry et al. (2021b). This correction is achieved using a Poisson model incorporating the detection rates of INPs during ambient and filtered-air measurements. Confidence intervals on INP concentrations and statistical differences between sample and filtered-air periods are

assessed at the same time as the background correction, and follow Krishnamoorthy and Lee (2012). All concentrations are converted to standard conditions to allow for direct comparisons between measurements at varying temperatures (STP; 0 °C and 100 kPa).

Nucleated ice crystals were collected for offline analysis following the OPC at the base of the CFDC chamber and analyzed using Atomic Force Microscopy to ascertain differences in INP morphology and phase state with wind speed (Section 4.2.2.4). Ice crystals were collected onto substrates using a single-jet impactor with a 50% cut-size of 4 μm aerodynamic diameter (Barry et al. 2021b; McCluskey et al. 2014).

4.2.2.2 Ice Spectrometer Measurements

Aerosols produced in SOARS were collected onto pre-cleaned 0.2 μm pore size, 47 mm diameter track-etched polycarbonate membrane filters (Whatman Nucleopore) in pre-sterilized aluminum inline filter housings (Pall), using the protocols described in Barry et al. (2021a). Filter samples represent approximately PM_{10} collections, although significant vibrations and vertical movement of the sampling inlet was observed at higher wind speeds, with unknown effects on particle line losses. Sample flow rates were held at ~5 std lpm (slpm) and the sample stream passed through a silica gel diffusion drier prior to particle collection to prevent saturation/wetting of the filters. Filter collection volumes ranged from 182 to 855 std L, with the higher volumes representing longer sampling durations at lower wind speeds to increase particle mass. Blank filters were collected regularly by installing filters in housings and connecting to the same tubing used for SSA sampling, without airflow. Seawater was sampled from either the rear end of the SOARS channel (beach) or underneath the aerosol sampling manifold, approximately halfway up the water column, using a peristaltic pump and silicone tubing to minimize cell rupture for biological measurements. Filters and seawater were either analyzed immediately or stored frozen (-20 °C) prior to analysis.

Offline measurements of INP and INE immersion freezing temperature spectra were made using the CSU Ice Spectrometer (IS), which has been comprehensively described in its present form elsewhere (Hiranuma et al. 2015; DeMott et al. 2018c; Hill et al. 2023). Aerosol filters were

re-suspended in 8 mL of 0.1 μm filtered DI water, then 50 μL aliquots of either seawater or aerosol suspensions were dispensed into sterile 96-well PCR trays (Optimum Ultra, Life Science Products). Dilutions of each sample were used to extend the measurement temperature range; these were made in 0.1 μm filtered DI water for aerosol filter suspensions and 0.1 μm filtered artificial seawater (NeoMarine, Brightwell Aquatics) for seawater samples. The trays were then placed into temperature-controlled aluminum blocks inside the IS, and cooled at ~0.33 °C min^{-1}. Freezing events were detected optically from CCD camera images collected at 1Hz. A 0.1 μm filtered DI water or artificial seawater negative control was included with each IS measurement and used to correct sample results for INPs present in the water used for resuspension and dilution. INP concentrations in the aerosol suspensions or seawater were calculated following Vali (1971), then converted to concentrations in SOARS headspace air for aerosol filters (reported at STP; 0 °C and 100 kPa). Confidence intervals were derived following Agresti and Coull (1998), and the LOD determined as in Moore et al. (2023). The average background number of INPs from the collected blank filters (4) were used to adjust filter sample concentrations; measurements are not reported if blank-corrected values fell below zero (Moore et al. 2023). Temperature spectra of seawater samples have been adjusted by +2 °C to account for freezing point depression due to salinity.

4.2.2.3 Chemical Composition of INPs in the Ice Spectrometer

Inferences about INP composition are possible using chemical pre-treatments of aerosol filter suspensions or seawater prior to analysis with the IS. Heat treatments are used to assess the contribution of biological INPs to a total sample population (Hill et al. 2016; Suski et al. 2018), as INPs produced by fungi and bacteria are often proteinaceous (Pummer et al. 2015) and denatured by heating. Aliquots of either re-suspended particles from aerosol filters or seawater were immersed in boiling water for 20 min before being cooled to room temperature and then analyzed with the IS as normal (Section 4.2.2.2). The difference between the pre- and post-heat treated sample represents the biological INP contribution. The proportion of refractory, typically mineral, INPs are identified through oxidation experiments that remove organic material

(Hill et al. 2016; McCluskey et al. 2018a). Sample aliquots are digested for 20 min with 10% hydrogen peroxide while immersed in boiling water, with two UVB fluorescent bulbs (Exo Terra) illuminating the samples to generate hydroxyl radicals. After cooling, catalase (MP Biomedicals, PN 100429) is added to remove any excess hydrogen peroxide and prevent unknown but otherwise significant freezing point depression (Hill et al. 2016). The INP temperature spectrum remaining after oxidation is inferred to be the mineral (or other inorganic) component, and the difference between pre-and post-oxidation spectra corresponds to organic INPs.

4.2.2.4 Single Particle Atomic Force Microscopy of INPs

INPs collected in the CFDC were deposited onto hydrophobically coated (Rain-X) silicon substrates (Ted Pella, Inc.) and stored in clean Petri dishes inside a laminar flow hood (Nu-Aire, Inc., NU-425-400) at ambient temperature (20-25 °C) and pressure prior to analysis (Kaluarachchi et al. 2022a;b; Lee et al. 2020). Samples collected at four wind speeds (~10, 17, 19, and 22 m s^{-1}) were analyzed to assess the distribution of physicochemical properties under varied wind stress. A molecular force probe 3D AFM (Asylum Research, Santa Barbara, CA) was used to image individual INPs at ambient temperature (20-25°C) and pressure, as described in prior studies (Lee et al. 2020; Ray et al. 2019). A custom humidity cell was used to control RH between 20% and 60%. Prior to AFM measurements at a particular RH, samples were allowed to equilibrate for at least 10 minutes to ensure thermodynamic equilibrium with the surrounding water vapor (Lee et al. 2020; 2017; Madawala et al. 2021). Silicon nitride AFM tips (MikroMasch, model CSC37, tip radius of curvature ~10 nm, nominal spring constant 0.5-0.9 N m^{-1}) were used for AFM imaging and force spectroscopy measurements (Lee et al. 2017; Madawala et al. 2021). AFM AC (intermittent contact) imaging mode was used to collect 3D height images of individual INPs to determine their morphology, and to quantify their volume-equivalent diameter, as described previously (Ray et al. 2019; Kaluarachchi et al. 2022b). For morphological analysis, approximately 50 individual particles were studied for each sample, with volume-equivalent diameters ranging from 0.05 – 1.0 μm. Particles were classified into six main types: rounded,

core-shell, prism-like, rod, aggregate and irregular. Example images of particles at 20% RH in each category are shown in Figure C.4.

Organic particle phase state was identified for samples at 20% and 60% RH, as in previous studies (Lee et al. 2017; 2020). These RH values were selected as benchmarks based on previous phase state studies on sucrose that showed solid-to-semisolid and semisolid-to-liquid phase transitions at ~20% and 60% RH, respectively (Lee et al. 2017; Ray et al. 2019; Madawala et al. 2021). Briefly, AFM force spectroscopy (i.e., force plots), was performed on individual core-shell particles at a particular RH by probing within the shell region of each particle. At least five force plots were collected for each individual particle at both 20% and 60% RH, with a maximum force of 20 nN and scan rate of 1 Hz. The viscoelastic response distance (VRD) and relative indentation depth (RID), or ratio of the indentation depth to the particle height, were then quantified, which can be related to the viscosity of the material (Lee et al. 2020; Kaluarachchi et al. 2022a). A previously reported framework based on VRD and RID measurements was then utilized to identify the phase state of each particle at 20% and 60% RH (Lee et al. 2017). A total of 5, 19, 12 and 13 individual core-shell particles were studied for the ~10, 17, 19 and 22 m s^{-1} wind speed conditions, respectively (Table C.1).

Since the total number of individual particles that can be realistically studied with AFM is somewhat limited, a probability distribution analysis to assess the statistical significance of the AFM results was employed (Kaluarachchi et al. 2022b; Cappa et al. 2021; 2022). Briefly, the probability distribution curves associated with the likelihood of sampling one of the six particle morphology types, or one of the three phase states, were generated using a Markov chain Monte Carlo method for a “true” population of 10,000 particles. The resulting distributions were fit with Gaussians to provide standard deviation estimates for both morphology and phase state measurements.

4.2.3 Aerosol Size Distribution Measurements

While several dedicated instruments were used to measure aerosol size distributions during CHAOS, the results are not yet available. Instead, data from the OPC at the base of the CFDC chamber was used here to provide aerosol concentrations and size distributions for particles larger than ~300 nm. CFDC operation requires the incoming air stream to be dried to below the frost point at the given measurement temperature (typically -25 °C or -30 °C), so aerosols enter the CFDC at dry sizes. However, particles will deliquesce, and some will activate into cloud droplets under the water supersaturated conditions present in the top section of the CFDC chamber. Any particles not activated into ice crystals will evaporate in the water-subsaturated region at the bottom of the chamber (Section 4.2.2.1), which is held at ice saturation. Following Murphy and Koop (2005), the saturation vapor pressures with respect to ice and water were calculated during each period based on the measurement temperature, as well as the resulting RH. Dry particle sizes were estimated assuming spherical, sea salt particles with a hygroscopic growth factor (HGF) of 1.7 for the 70-75% RH range calculated (Zieger et al. 2017). The CFDC OPC was calibrated against polystyrene latex spheres (PSLs) and glass beads of known sizes and refractive indices, and size distributions calculated assuming a refractive index of n=1.5 for sea salt (Tang et al. 1997). Particle surface area and volume distributions were calculated for each number distribution assuming particle sphericity, as were number concentrations of particles larger than 500 nm dry diameter (N_{500}).

4.3 RESULTS AND DISCUSSION

4.3.1 SSA and INP production at Varying Wind Speeds

Measurements of both SSA and INPs were made at 6 U_{10} wind speed equivalents (9.89, 14.19, 15.42, 16.64, 19.10, and 21.55 m s^{-1}) during CHAOS. Normalized histograms of integrated particle number, number >500 nm diameter (n500), surface area, and volume concentrations are shown in Figure 4.1 for all measured wind speeds. As expected from numerous previous measurements (e.g. Lewis and Schwartz 2004; O'Dowd and de Leeuw 2007; de Leeuw et al. 2011),

particle concentrations generally increased with wind speed in the SOARS channel. However, wide distributions with significant overlap were observed in the intermediate wind speeds of ~15-19 m s^{-1}. This variability occurred for measurements collected both days or weeks apart and on the same day, if wind speeds were repeated, and the source is unknown. Particle concentrations reported for the Southern Ocean (Moore et al. 2022) in a similar wind speed range (0-25 m s^{-1}) did not display this clear multimodal behavior, although wind speeds likely varied during measurement periods. A previous study of wind profiles in a wind-wave tank (Vollestad and Jensen 2021) found that while the horizontal wind speed displayed the expected, approximately logarithmic profile, secondary flows due to the confined channel were found to impact the observed vertical velocity structure. Modification of the near-surface wind and turbulence due to the presence of waves has been observed in wind-wave tanks (Zavadsky and Shemer 2012; Villefer et al. 2021) and in models (Chen et al. 2019), and varies with the fetch (Lamont-Smith and Waseda 2008), as well as the presence of swell in addition to wind-waves (Villefer et al. 2021). As a result, the extrapolated U_{10} values should be treated as approximations. Variation in secondary flow structure is a possible explanation for some of the variability seen in particle concentrations at the same nominal wind speed during CHAOS.

The range of observed values for particle number, surface area, and volume were also much larger during CHAOS than CAP-2, by factors of ~3.3, ~26, and ~5, respectively. At least some of these differences are likely a result of the differences in time scale and fetch, with open ocean measurements closer to steady state, and integrated over a larger area. The enhancement in particle number is underestimated here, since the CFDC OPC can only measure particles >~300 nm, while particles as small as 25 nm contributed to measured concentrations in Moore et al. (2022). Preliminary size distribution measurements (not shown) suggest the size distribution shape and mode size is similar across wind speeds in SOARS, with enhanced supermicron particle production at higher wind speeds. At wind speeds below 18.5 m s^{-1}, the fixed 1.3 amplitude waves generated by the SOARS paddle led to higher whitecap coverages than would be anticipated in the open ocean, and for the highest 21.55 m s^{-1}, whitecap coverage was lower than

open ocean values (Monahan and Muircheartaigh 1980). This likely led to an overestimation of particle production at low wind speeds and underestimation at the highest; as a result, the range reported here may be too small and consequently even higher relative to ambient measurements. Additional tests are currently underway to study particle production when the wave amplitude is varied along with the wind speed to match open ocean whitecap fractions, which may reduce some of the large observed variability in particle production at some wind speeds during CHAOS.

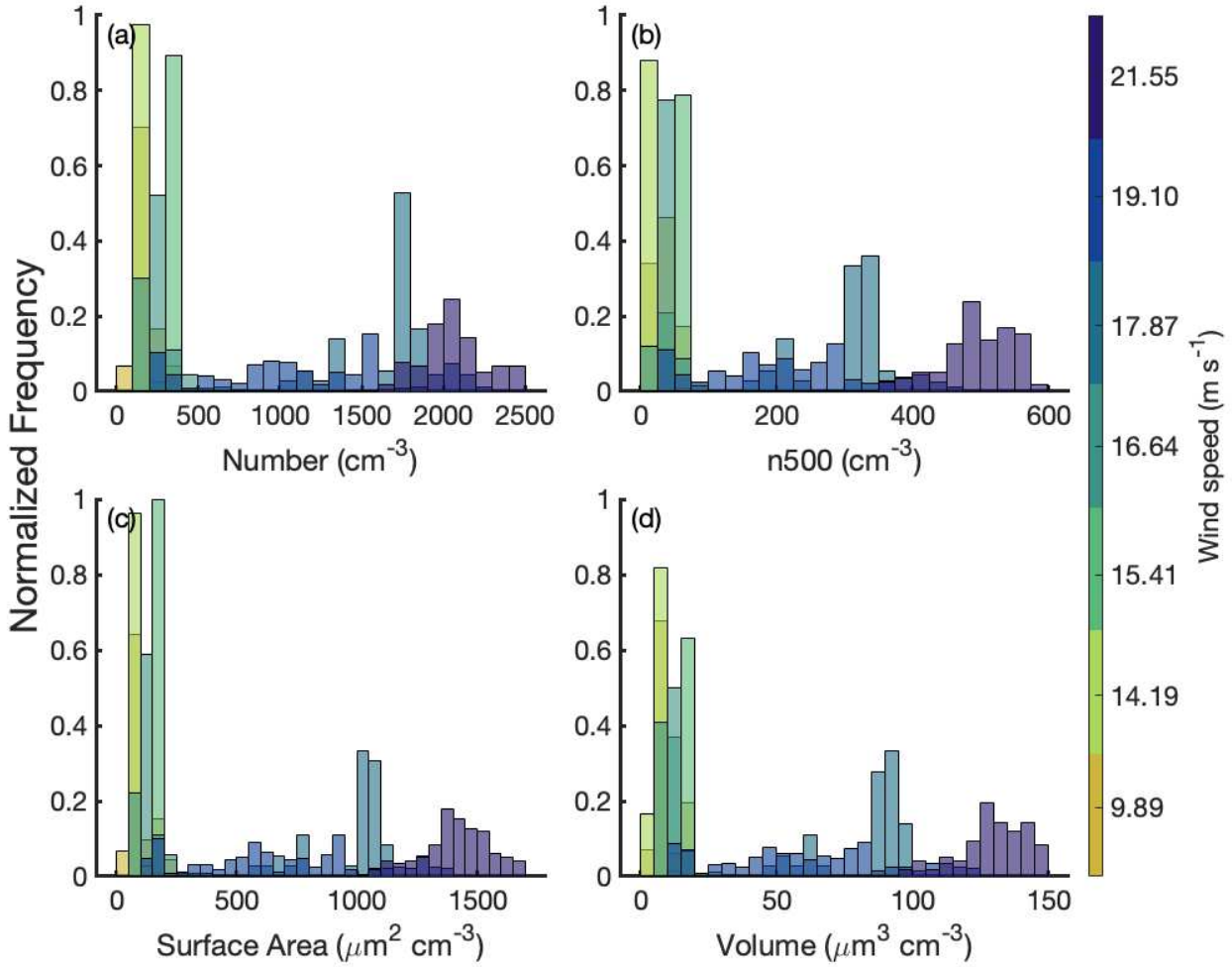

Figure 4.1: Normalized frequency distributions of particle (a) number, (b) number >500 nm diameter (n500), (c) surface area, and (d) volume concentrations at each measured wind speed during CHAOS.

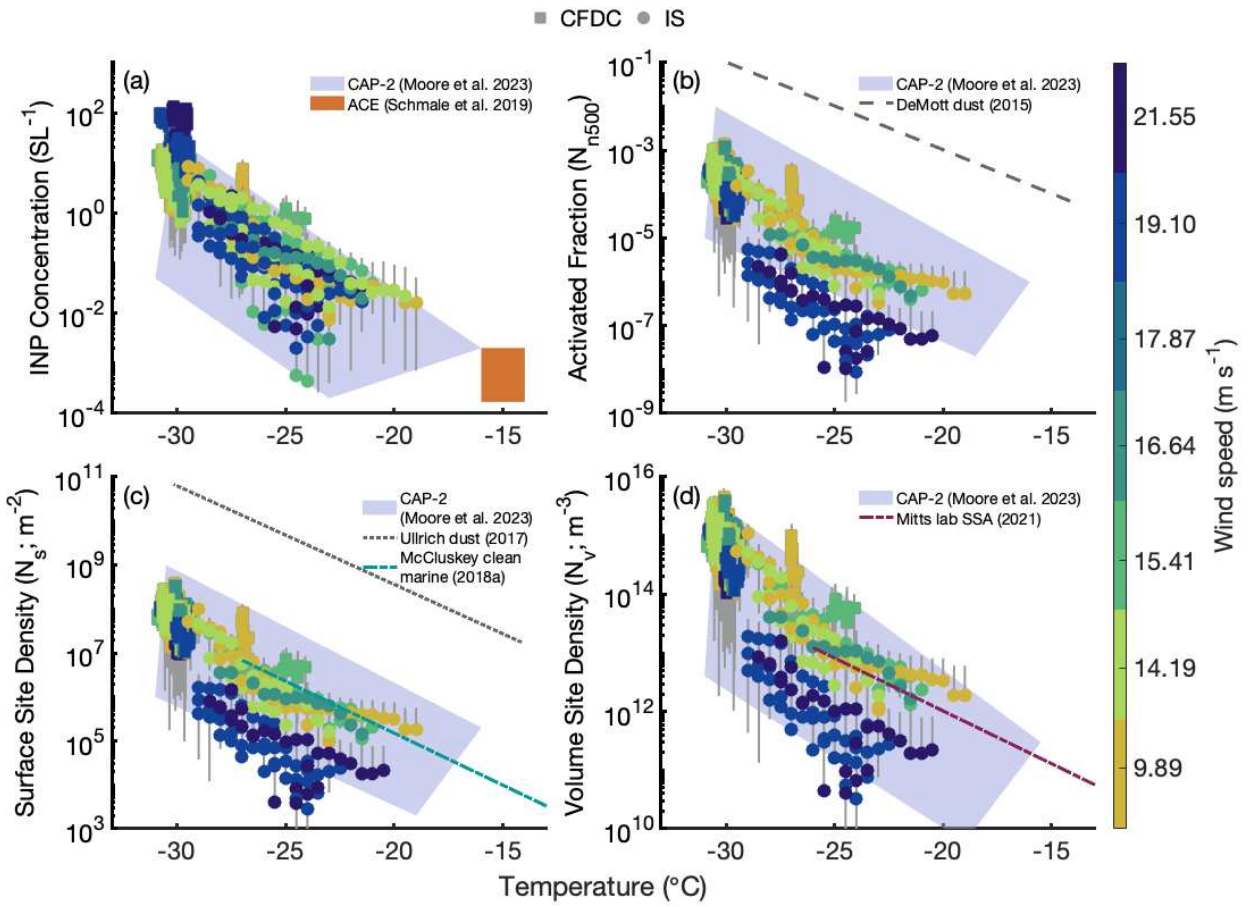

Figure 4.2: INP (a) number concentration, (b) normalized by n500 (N_{n500}), (c) normalized by aerosol surface area (N_s) and (d) normalized by aerosol volume (N_v) temperature spectra during CHAOS. CFDC measurements are indicated by squares and IS filter observations by circles; both are colored by the wind speed during each measurement period. The purple shading in each panel indicates the range of each value observed during CAPRICORN-2 (Moore et al. 2023). The orange shading in (a) shows observations made during the ACE campaign (Schmale et al. 2019). In (b), the grey dashed line shows the DeMott et al. (2015) parameterization for dust based on n500, using the median n500 value measured during 19.10 m s^{-1} wind speed periods. In (c), the grey dotted line indicates the Ullrich et al. (2017) parameterization for dust N_s, and the blue dot-dash line shows the N_s parameterization from McCluskey et al. (2018a) for North Atlantic clean marine air. The dashed magenta line in (d) indicates the Mitts et al. (2021) lab-based parameterization for marine N_v.

A summary of the INP results from CHAOS, along with relevant model parameterizations, are displayed in Figure 4.2, which shows INP measurements from the CFDC (Section 4.2.2.1) and IS filters (Section 4.2.2.2) as a function of temperature. Similar observations made in the Southern Ocean marine boundary layer during the Southern Ocean Cloud Radiation Aerosol Transport Experimental Study (SOCRATES, hereafter SOC) aircraft campaign and the second Clouds, Aerosols, Precipitation, Radiation and atmospherIc Composition Over the southeRN ocean (CAPRICORN-2, hereafter CAP-2) ship campaign are shown in each panel in the light purple shading (Moore et al. 2023). Figure 4.2a shows measured INP concentrations, while the other panels show different normalizations commonly used in models (Figure 4.2b-c) or suggested for marine INPs (Figure 4.2d). Figure 4.2b displays INP concentrations normalized by n500 (N_{n500}), which has been used previously for dust (DeMott et al. 2015) and biological INPs (Tobo et al. 2013) due to observed relationships with supermicron aerosol. Figure 4.2c is normalized by aerosol surface area, which has been widely used for multiple INP types, including marine INPs (Niemand et al. 2012; Ullrich et al. 2017; McCluskey et al. 2018a). Normalization by aerosol volume was suggested by Mitts et al. (2021) for marine INPs on the basis of laboratory experiments, but measurements from the Southern Ocean (Moore et al. 2023) did not support a similar relationship for ambient data.

INP concentrations and normalized values are roughly consistent with CAP-2 and SOC measurements (Figure 4.2), which themselves agreed well with previous observations from the Southern Ocean and mid-latitude North Atlantic (Moore et al. 2023; Schmale et al. 2019; McCluskey et al. 2018c; Tatzelt et al. 2022). INP concentrations during CHAOS were on the high end of Southern Ocean values, especially at the coldest temperatures (~-30 °C) and wind speeds above 18 m s^{-1}. A lack of overlap in measurement temperature between CHAOS and the Southern Ocean observations of Schmale et al. (2019) (ACE campaign) prevents direct comparison, but ACE measurements are also higher than other reported values for the same region (Moore et al. 2023; McCluskey et al. 2018c) and as a result more similar to the CHAOS data (Figure 4.2a). As anticipated, the DeMott et al. (2015) n500-based parameterization (Figure 4.2b) and Ullrich

et al. (2017) N_s parameterization (Figure 4.2c) for dust INPs overestimate CHAOS values by ~2 orders of magnitude. N_{n500} and N_s during CHAOS are at the low end of Southern Ocean observations (Figure 4.2b-c), although interestingly, the N_v normalization has an almost identical range as the CAP-2 values (Moore et al. 2023). This suggests a different shape to the particle size distribution in the SOARS channel than the Southern Ocean MBL, since all of the aerosol concentrations are enhanced in SOARS relative to ambient measurements (Figure 4.1), but only N_v has the same range as ambient observations. It is likely that loss mechanisms such as dry and wet deposition are lower in SOARS, where the aerosol was sampled from 0.6 m above the water surface, compared to the CAP-2 measurements, where the aerosol inlet intake was 18.4 m above sea level. This may alter the measured particle size distributions in SOARS, especially at larger sizes most relevant to calculation of aerosol volume. Similarly to the CAP-2 results (Moore et al. 2023), the Mitts et al. (2021) N_v parameterization has a lower slope than the CHAOS dataset, and is near the upper bound of measured values at all temperatures.

CFDC concentrations generally increase with wind speed, while variability is reduced following normalization by aerosol concentrations, as expected if INPs are emitted proportionally to SSA (Figure 4.2). However, it is clear from the time series of CFDC data presented in Figure C.2 that on some days, INP concentrations were the same at all wind speeds (8/17/22), or the same up to a wind speed threshold of ~18 m s^{-1} (8/9/22, 8/18-8/19/22). Other days did not sample enough wind speeds to assess this variation. INP concentrations measured from the aerosol filters did not have a clear relationship with wind speed (Figure 4.2a). This difference may be due to the different averaging times of the CFDC (~5 minutes) versus the IS filters (2-3 hr), or the different inlet orientations or locations. The CFDC sampled ~2 m upstream of the filters, with a vertically oriented inlet, whereas the IS filters used a horizontal inlet facing into the wind. The consistently higher values measured by the CFDC suggest particle losses in the IS filter inlet may have influenced the measurements, and/or particles >2.5 μm were not the dominant INP size.

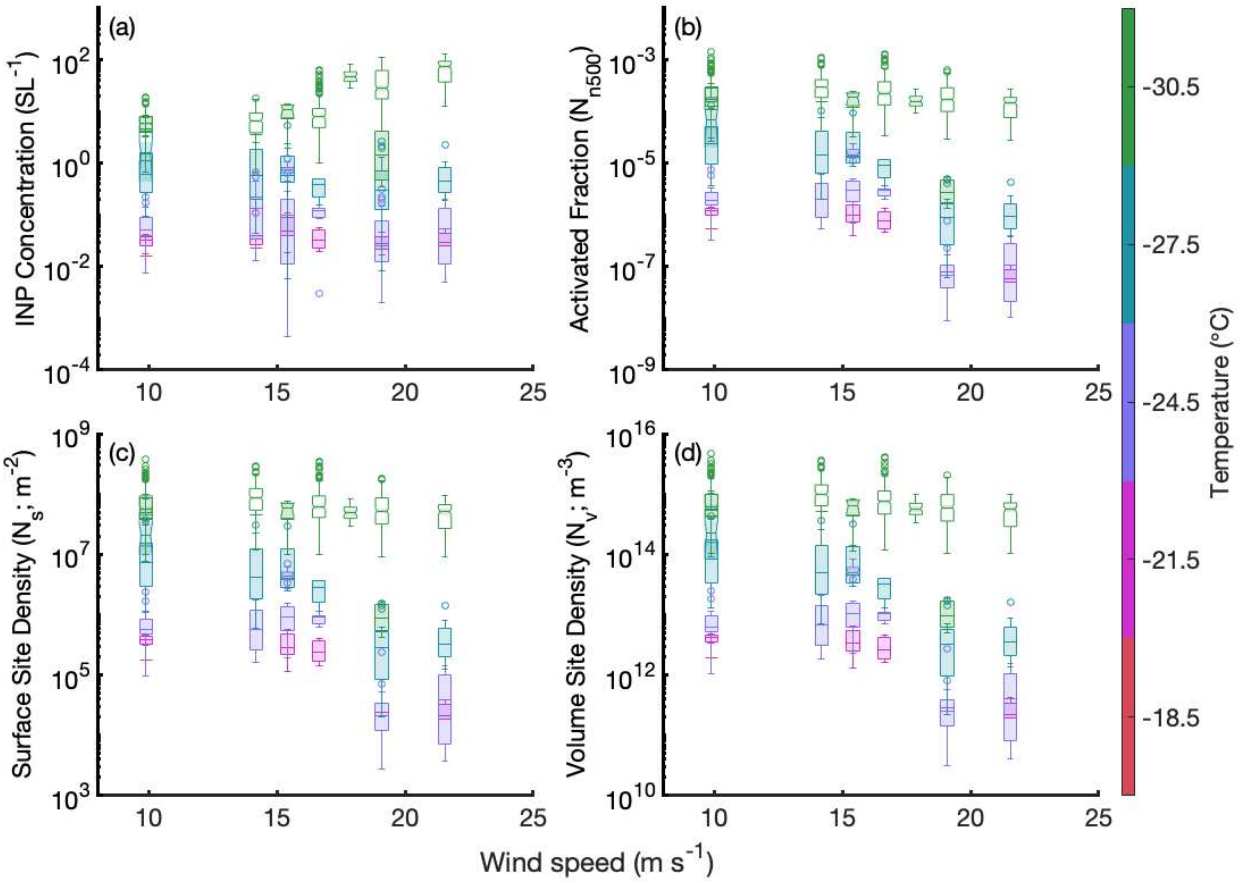

Figure 4.3: Box plots of observed (a) INP concentration, (b) N_{n500}, (c) N_s and (d) N_v as a function of wind speed during CHAOS. Observations are separated into 3 °C temperature bins (indicated by color), with CFDC measurements shown as open boxes and IS filter data as shaded boxes.

Normalized INP concentrations for both instruments generally decreased with increasing wind speed, especially above ~18 m s^{-1}, although decreases were more modest for the CFDC than the IS. This can be seen more clearly in Figure 4.3, which displays the same data from Figure 4.2 as a function of wind speed in 3 °C temperature bins, with CFDC and IS filter ranges indicated by box plots. Also clear in Figure 4.3 is the inter-sample variability observed during CHAOS for samples collected at similar wind speeds and temperatures. INP concentrations in the Southern Ocean MBL were found to increase with wind speed, and to retain the same wind speed dependence after normalization by aerosol number, surface area, and volume (Moore et al. 2023). The opposite relationship was observed during CHAOS, and further suggests particle losses in SOARS are lower than for typical ambient measurements due to the proximity of the sampling inlet to the water surface. Thus, the results from CHAOS may be more representative of interfacial fluxes rather than marine boundary layer or cloud-base values. As previously discussed in relation to measured particle concentrations, the fixed 1.3 amplitude wave height used during CHAOS may also be obscuring the true INP-wind speed relationships, which requires further measurements with co-varying wave amplitude and wind speed to resolve. Seawater INE concentrations were stable throughout CHAOS (Figure C.3) and agree well with previous measurements from the Scripps Pier, as well as the North Indian Ocean (Beall et al. 2022) and mid-Atlantic (Gong et al. 2020), and are higher than observations from the Southern Ocean (McCluskey et al. 2018c) or Barents Sea (Hartmann et al. 2021) by 1-2 orders of magnitude. The INE stability across multiple fills of the SOARS channel and over time with the same water indicates the observed INP-wind speed relationships were driven by wind and wave breaking rather than biological activity in this experiment.

4.3.2 INP Composition and Phase State Changes under Increasing Wind Speeds

The fractional composition of INPs (Section 4.2.2.3) as a function of wind speed is shown in Figure 4.4 for three temperature ranges: -19 to -23 °C, -23 to -26 °C, and -26 to -29 °C. Collected INPs were largely unaffected by heat treatments, although modest reductions at temperatures

<-23 °C were observed for a few samples at low wind speeds (~10 m s^{-1}). On several days, especially at the end of the second water fill (8/16/22-8/19/22), heat treatments led to increased INP concentrations over the untreated filters, which is uncommon but was observed by McCluskey et al. (2018b) during a laboratory-simulated phytoplankton bloom grown in a Marine Aerosol Reference Tank (MART; Stokes et al. 2013). This was suggested to be a result of lysis of microbial cells upon heating, releasing IN-active material, or the dissolution and redistribution of organic material between particles, leading to a net increase in the number of particles with IN-active organic material. This contrasts with results also presented in McCluskey et al. (2018b) for a phytoplankton bloom grown in the SIO glass channel during the IMPACTS (Investigation into Marine Particle Chemistry and Transfer Science) campaign (Wang et al. 2015a), where larger proportions of biological INPs were inferred to be released in response to increased seawater biological activity.

At low wind speeds (<15 m s^{-1}), especially early in the campaign, heat-stable organic INPs were the dominant INP type, corresponding to the DOC-INP type described in McCluskey et al. (2018b). This is in accordance with a number of laboratory (McCluskey et al. 2018b) and field (Wilson et al. 2015; Rosinski et al. 1987; Ladino et al. 2016; Alpert et al. 2022) measurements, although other studies have inferred the dominance of proteinaceous or heat-labile material (Irish et al. 2017; Knopf et al. 2011; Wang et al. 2015a). By contrast, at higher wind speeds, inorganic or refractory INPs were the dominant type observed. At wind speeds >15 m s^{-1}, nearly all peroxide-treated filter samples had higher INP concentrations than the untreated samples, and many of these corresponded to the heat-treated samples with enhanced INP concentrations described above. All of the samples with enhanced concentrations following peroxide digestion (inorganic fractional composition >1 in Figure 4.4) had a characteristic shape to their temperature spectra, an example of which is shown in Figure 4.4d. In contrast to the typical log-linear marine INP spectra (DeMott et al. 2016), dramatic increases are seen in peroxide-treated results at warm temperatures, which flatten out ~-23 °C and meet or approach the untreated spectra around -27 °C. This is reminiscent of INP temperature spectra identified as biological (Hill

et al. 2016; Suski et al. 2018), which have large warm temperature INP populations which are reduced to log-linear spectra following heating and/or peroxide digestion, only inverted. This has not been reported before for marine INPs, but is hypothesized to be the result of enhanced release of large particles at high wind speeds in SOARS, which may contain multiple INPs. The production of spume droplets through the tearing of wave crests, which produces particles predominantly >10 μm and is increasingly active for wind speeds exceeding ~9 m s^{-1} (Monahan et al. 1986; Sofiev et al. 2011), is the most likely mechanism consistent with the observed wind speed dependence. The atmospheric lifetime of such particles is very short, which may explain why this has not been observed in ambient measurements or laboratory studies with low wind speeds. Organic material in seawater, including carbohydrates, lipids, and proteins, are well known to self-assemble into microgels which can range in size from <10 nm (single macromolecule) to μm-sized colloidal gels (Chin et al. 1998; Verdugo 2012). INPs could be trapped in this gel matrix, emitted as large spume drops, and then released following the breakdown of the organic material during peroxide digestion. If so, the composition of the INPs themselves cannot be inferred from these results, since they could be either inorganic contaminants (dust) which are stable against peroxide digestion, or heat-stable organics which the 20-min digestion used here is not long enough to both release from their gel matrix and break down.

Additional information about the composition of INPs produced in SOARS was provided by AFM analysis of submicron ice crystal residuals collected in the CFDC (Section 4.2.2.4). Six particle categories were identified based on 3D height images of particles collected at 4 wind speeds (~10, 17, 19, and 22 m s^{-1}): rounded, core-shell, prism-like, rod, aggregate and irregular (Figure C.4). These are similar to the categories identified for ice crystal residuals during SeaSCAPE (DeMott et al. 2023), except rod and irregular particles were not identified in the glass channel. Some of the particles in these classes are morphologically similar to known contaminants from the SOARS channel itself, and will not be further discussed here. Rod and prism-like particles did not display a clear relationship with wind speed (Figure 4.5). Rounded particles had relatively higher abundances at low wind speeds (<18 m s^{-1}), while core-shell particles in-

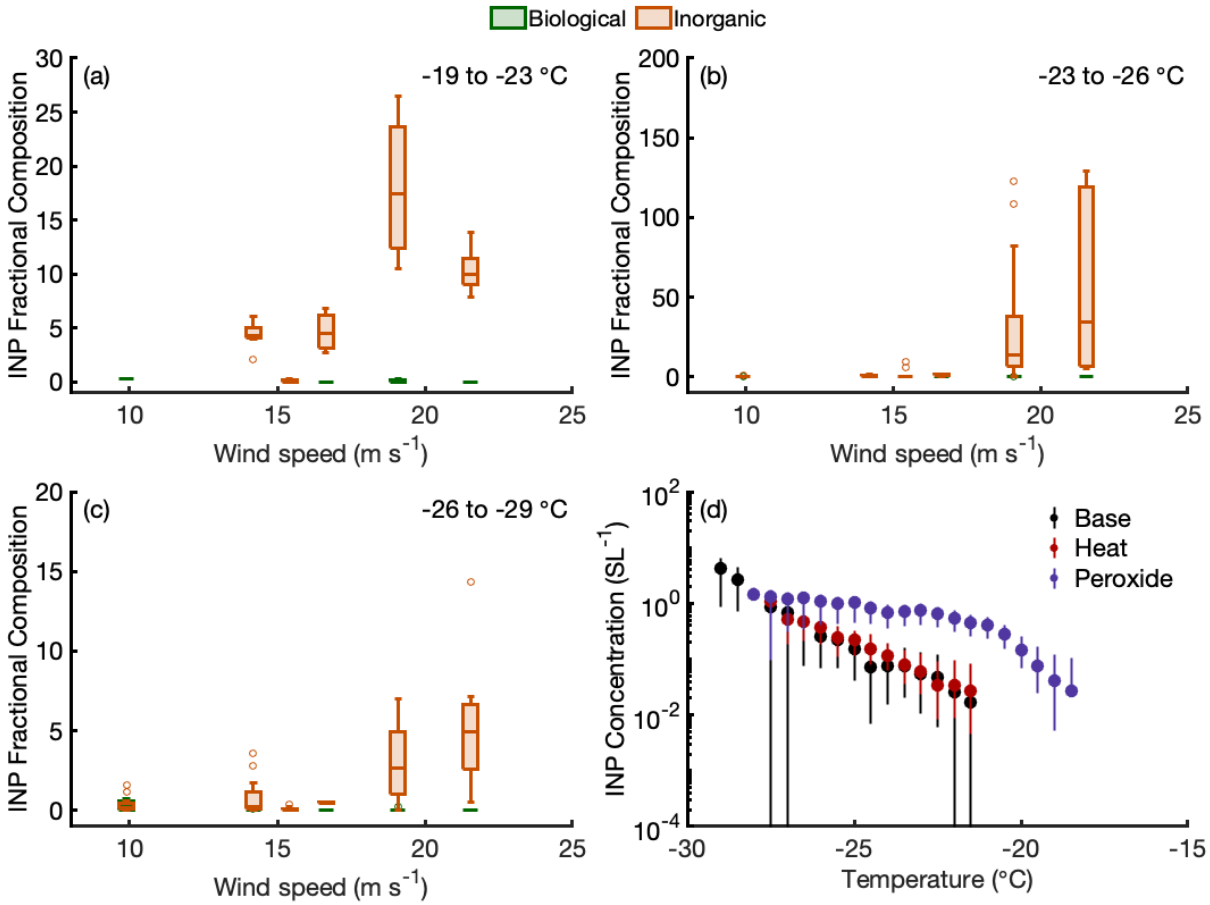

Figure 4.4: Box plots of biological (green) and inorganic (orange) INP fractional composition as a function of wind speed for IS filter measurements at (a) -19 to -23 °C, (b) -23 to -26 °C, and (c) -26 to -29 °C. Panel (d) shows an example IS filter temperature spectra from 8/5/22 (19.10 m s^{-1}), with base measurements in black, heat-treated in red, and peroxide-treated in purple.

creased in relative contribution with increasing wind speeds. Similar collections of SSA produced during CHAOS had identical relationships between relative contributions of core-shell and rounded particles with wind speed as the ice crystal residuals, suggesting the INPs are subsets of all the observed SSA particle morphologies. The SSA particles collected were also analyzed for elemental composition by scanning electron microscopy coupled with energy dispersive X-ray spectroscopy (SEM-EDX) as in Ault et al. (2013) and functional group characterization using atomic force microscopy-Photothermal Infrared spectroscopy (AFM-PTIR) following Or et al. (2018). SEM-EDX indicated rounded SSA particles were organic carbon throughout, while core-shell particles had a cubic NaCl core and organic shell. Rounded particles had more diverse organic functional groups (fatty acids, complex sugars and in some cases traces of sulfates and carbonates), and their composition was similar at both 9.89 and 19.10 m s^{-1}. Core-shell particles were dominated by aliphatic compounds at 9.89 m s^{-1}, with the addition of fatty acids and complex sugars at 19.10 m s^{-1}.

Viscoelastic response distance (VRD), which is related to the viscosity of the material (Lee et al. 2020; Kaluarachchi et al. 2022a), as well as particle phase state (Lee et al. 2017; 2020) was quantified for core-shell ice crystal residuals at 20% and 60% RH (Table C.1). As anticipated due to the hygroscopicity of SSA, the fraction of semisolid shells increased between 20 and 60% RH at all wind speeds. Below 18 m s^{-1}, the shell region of core-shell particles was predominantly solid at 20% RH, while at higher wind speeds, shells were more often semisolid even at low RH. VRD measurements were only possible on semisolid shells, and were similar at both 20% and 60% RH for a given wind speed, but were higher for wind speeds >18 m s^{-1}. The increased abundance of semisolid shells with higher VRD is consistent with lower viscosity and the presence of more oxygenated chemical species in the shell region of core shell particles at higher wind speeds. Interestingly, an increase in VRD was also observed for heterogeneously aged INP core-shell particles during the SeaSCAPE campaign (DeMott et al. 2023).

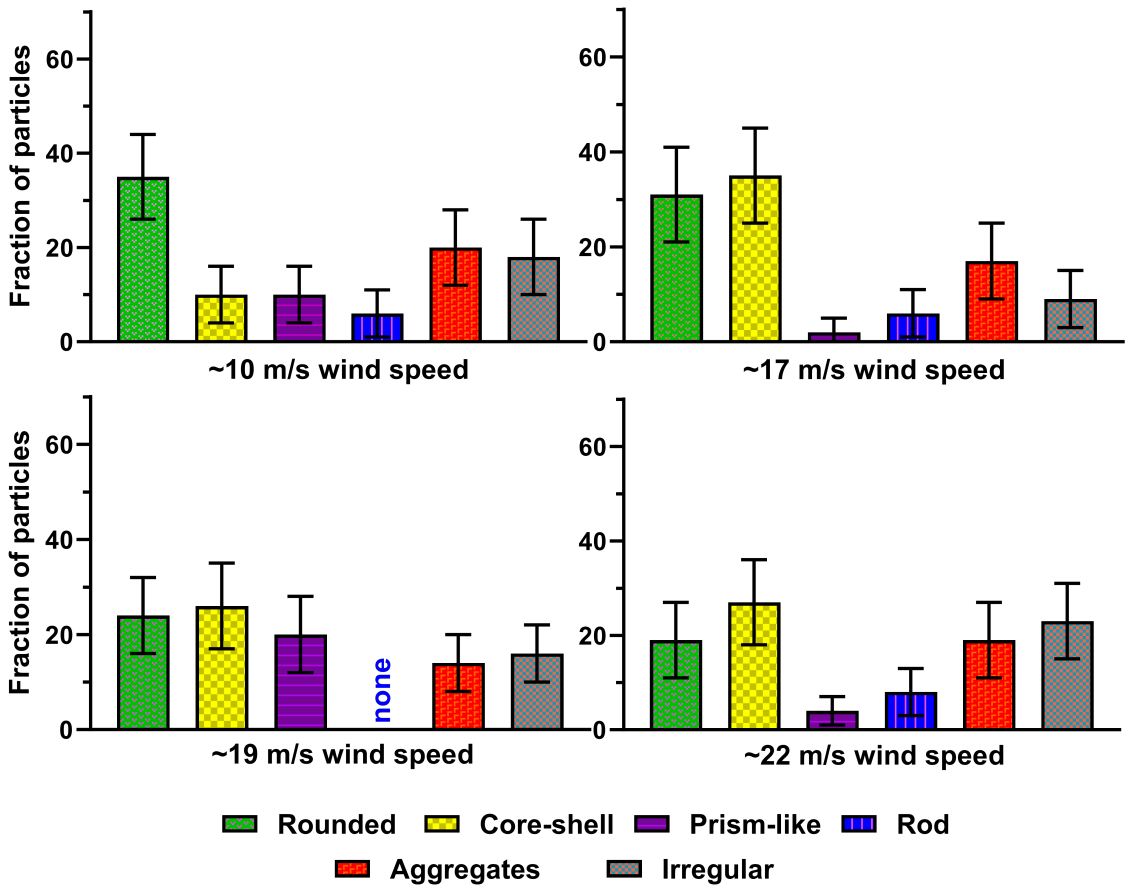

Figure 4.5: Percentage of particles from each morphological category observed during CHAOS at four of the measured wind speeds (~10, 17, 19, and 22 m s^{-1}). For each sample, the individual particles (N = 50 for each sample) characterized were in the volume-equivalent diameter range of 0.05 – 1.0 μm.

4.4 SUMMARY

Initial results from the CHAOS campaign were presented here, which focused on the role of wind speed in the production of SSA and INPs, using the new SOARS wind-wave channel at the Scripps Institution of Oceanography. As expected from numerous field and laboratory measurements, SSA concentrations increased with increasing wind speed (Figure 4.1). Enhanced particle concentrations were observed relative to Southern Ocean MBL measurements in a similar wind speed range (Moore et al. 2022) by factors of ~3.3, ~26, and ~5 for particle number, surface area, and volume, respectively. INP concentrations were broadly consistent with previous measurements from the Southern Ocean (Moore et al. 2023; McCluskey et al. 2018c; Schmale et al. 2019) and North Atlantic (McCluskey et al. 2018a), although atmospheric concentrations were biased high and normalized concentrations biased low relative to ambient results (Figure 4.2). This is likely related to the low sampling height during CHAOS (0.6 m), which may capture more large particles than are typically sampled during ship-board or coastal campaigns where aerosol inlets may be 20+ m above sea level and/or offset from the shore. As a result, measurements from CHAOS likely represent interfacial values and may not be directly comparable to MBL or cloud-base measurements.

INP concentrations also generally increased with wind speed, as was observed in the Southern Ocean MBL (Moore et al. 2023). However, normalized INP concentrations decreased with increasing wind speeds during CHAOS, while the opposite relationship was observed in Moore et al. (2023) for the Southern Ocean (Figure 4.2, Figure 4.3). In addition to the low sampling inlet height and consequently lower particle losses, the fixed 1.3 amplitude wave height used during CHAOS may help explain this discrepancy. Further measurements where wind speed and wave amplitude are both varied to produce white cap fractions representative of open ocean conditions (Monahan and Muircheartaigh 1980) are required to separate these mechanisms. Additionally, the large spread and highly variable particle concentrations observed for both SSA and INPs during CHAOS complicated analysis and should be addressed through detailed estimates of particle losses within the SOARS channel and inlets, and more systematic sampling of

wind speeds than was possible during CHAOS due to time constraints. Seawater INE concentrations during CHAOS were stable and consistent with previous measurements at the SIO pier and in other regions (Beall et al. 2022; Gong et al. 2020; McCluskey et al. 2018c; Hartmann et al. 2021), indicating changes in atmospheric INPs were driven by wind speed and wave-breaking mechanics rather than variations in seawater chemistry or biology (Figure C.3).

Heat-stable organic INPs were the dominant composition at wind speeds below 15 m s^{-1} (Figure 4.4), which corresponds to the DOC-type marine INP described in McCluskey et al. (2018b). A number of field measurements have also identified similar small, heat-stable marine INPs (Wilson et al. 2015; Rosinski et al. 1987; Ladino et al. 2016; Alpert et al. 2022), although a second category of larger and protinaceous (heat-labile) marine INPs has also been observed in both field and laboratory measurements (McCluskey et al. 2018b; Irish et al. 2017; Knopf et al. 2011; Wang et al. 2015a). At high wind speeds, peroxide-treated filter samples almost uniformly had higher INP concentrations than untreated samples (Figure 4.4d), which has not been previously seen for marine INPs. We hypothesize that spume droplet production at higher wind speeds, coupled with the low height of the SOARS sampling inlet, may have allowed for the sampling of larger, aggregate particles containing multiple INPs, which were broken up through peroxide digestion. The composition of INPs emitted in such gels is unknown, since results from CHAOS are consistent with dust or other inorganic contaminants that are unaffected by peroxide digestion, or heat stable organics which are only released from the larger particle and not broken down due to the 20-min digestions performed here. The very short atmospheric lifetime of large (>10 μm) spume droplets may explain why this has not been seen in ambient measurements or laboratory experiments without wind (Wang et al. 2015a; McCluskey et al. 2018b).

AFM 3D height images of collected ice crystal residuals were used to identify 6 dominant particle morphologies, which were similar to residual classifications during SeaSCAPE (DeMott et al. 2023). Rounded particles were the most abundant morphology at wind speeds <18 m s^{-1}, and core-shell particles dominated at higher wind speeds (Figure 4.5). The abundance of core-

shell particles with semisolid shells increased with wind speed, while the viscosity of the shells simultaneously decreased. This is consistent with an increasing contribution of oxygenated chemical species in the shells, which was also noted as an outcome of heterogeneous aging of INPs during SeaSCAPE (DeMott et al. 2023). It is possible the decreased viscosity and more complex chemical composition at high wind speeds is related to the enhancement in INP concentration following peroxide digestions through increased water solubility of the shells, as was observed during SeaSCAPE for aged SSA (Kaluarachchi et al. 2022a).

The CHAOS campaign represents a first attempt at using the new SOARS wind-wave channel to isolate individual factors impacting SSA and INP emissions from seawater. Additional experiments with co-varying wind speed and wave amplitude are ongoing, although only SSA concentrations are being measured. This is intended to generate realistic white cap fractions at all wind speeds and increase comparability with ambient data. Both SSA and INP concentrations measured by the CFDC increased with wind speed during CHAOS, as expected. IS measurements of INP concentration demonstrated a less clear trend with wind speed, which may be due to the use of separate inlets with different particle losses, although this still remains to be verified. The very low sampling height during CHAOS (0.6 m) relative to ambient (several to 20+ m) may have led to decreased losses of large particles, and requires further study before the comparability of such interfacial measurements to ambient marine boundary layer observations can be assessed. A mechanism involving spume droplet production of aggregate particles was proposed to explain the unexpected results of peroxide digestions of IS filters collected at high wind speeds, which requires further observations to evaluate.

5. Sources and Composition of Southern Ocean Ice Nucleating Particles during CAPRICORN-2 and SOCRATES

5.1 INTRODUCTION

Mixed phase clouds, which contain both liquid droplets and ice crystals, occur in the atmosphere between 0°C and ~-38°C. They are ubiquitous in polar regions, particularly at low and mid-levels (e.g. Cesana et al. 2012; McFarquhar et al. 2021; Tan et al. 2016) and have a large influence on Earth's energy budget (Bjordal et al. 2020; Tan et al. 2016; Cesana et al. 2022). Cloud phase, particularly at high latitudes, has been identified as a key component in predicting future equilibrium climate sensitivity (Bjordal et al. 2020) and for improving radiation biases in global models (Cesana et al. 2022; Tan and Storelvmo 2019). The initiation of ice in mixed phase clouds is dependent on aerosols known as ice nucleating particles (INPs), which can have an outsize effect on cloud phase and related climate feedbacks due to their relative scarcity. The size, composition, and surface characteristics of INPs controls the temperature at which they freeze (Kanji et al. 2017; Hoose and Möhler 2012; DeMott et al. 2016). As a result, INPs from different sources vary in ice nucleating efficiency, contributing to regional or seasonal differences in cloud phase, as well as model biases (Vergara-Temprado et al. 2018; Tan et al. 2016; Tan and Storelvmo 2019).

The ice nucleating abilities of mineral and soil dusts have received considerable attention, and in most areas are the dominant INP type due to their generally effective ice nucleating ability and large emission rates (see Kanji et al. 2017, and references therein). Marine INPs have garnered increasing interest after their relatively recent identification as a distinct INP class (see DeMott et al. 2016). The few measurements of INP concentrations in remote marine regions have indicated significantly lower levels than over or near the continents (DeMott et al. 2016; McCluskey et al. 2018a; Tatzelt et al. 2022; Welti et al. 2020; Moore et al. 2023), as well as much lower ice nucleating ability (by 2-3 orders of magnitude) for marine INPs compared

to dust (Kanji et al. 2017; DeMott et al. 2016; McCluskey et al. 2018a). The Southern Ocean (SO) is thought to be the largest area where marine INPs dominate the overall budget, due to the remoteness from land surfaces and persistent strong westerlies that act to isolate the region from continental influences (Burrows et al. 2013; Vergara-Temprado et al. 2017; 2018; McCluskey et al. 2019). Several studies have suggested marine INPs may also dominate in the high Arctic seasonally or intermittently (Ickes et al. 2020; Huang et al. 2018; Creamean et al. 2019; Hartmann et al. 2020; 2021), although other measurements have indicated mineral dust (Irish et al. 2019) or non-locally sourced biological INPs (Porter et al. 2022) were the dominant INP type. Very recently, the potential role of high-latitude dust (HLD) sources (Tobo et al. 2019; Sanchez-Marroquin et al. 2020) or thawing permafrost (Creamean et al. 2020; Barry et al. 2023a) as a source of INPs to the Arctic atmosphere has begun to be explored. However, HLD has not yet been evaluated as a possible missing INP source for the Southern Ocean.

Glaciogenic and other high-latitude dust sources can be regionally or globally significant, but are often overlooked in both observations and compilations of global dust flux estimates, and not accounted for in earth system models (Bullard et al. 2016; Meinander et al. 2022). A combination of global models, trajectory analysis, and limited observations have been used to develop dust budgets for the Southern Ocean and Antarctica (e.g. Neff and Bertler 2015; Li et al. 2008). The primary regions estimated to contribute to atmospheric dust concentrations are South America, particularly Patagonia, and Australia, with New Zealand being identified more recently as a potential source (Neff and Bertler 2015). Antarctic sources are often neglected in such budgets, since they are typically smaller in scale and more sporadic, but the total magnitude is completely unconstrained (Bullard et al. 2016). In addition, the katabatic and föhn winds likely responsible for lofting Antarctic dusts are not usually included in global models due to a lack of parameterizations for these subgrid-scale processes (Bullard et al. 2016). Glacier retreat is anticipated to increase the land area exposed to wind action, as is the switch from marine-terminating to land-terminating glaciers, and as a result, high latitude dust sources are expected to increase in the future (Bullard 2013).

Several Antarctic regions, including the McMurdo dry valleys and nearby McMurdo Ice Sheet, parts of the Antarctic peninsula, and several coastal locations have been identified as dust sources (Kavan et al. 2018; Diaz et al. 2018; Meinander et al. 2022). Brechtel et al. (1998) and Kreidenweis et al. (1998) reported air masses of Antarctic origin had different particle characteristics, including mode sizes and number concentrations, than clean marine air masses sampled at Macquarie Island in the Southern Ocean. Those measurements were limited to submicron particles and did not explicitly measure dust, but still demonstrate that Antarctic outflow may alter the typical SO aerosol population. Measurements of radon-222 have provided additional constraints relevant to aerosol transport in the region (Chambers et al. 2018; Kreidenweis et al. 1998). Radon-222 has an almost exclusively terrestrial source and can be used to infer the degree of continental influence on a measured air mass. Coastal Antarctic and remote SO measurements from Chambers et al. (2018) indicated a mix of marine boundary layer (MBL) synoptic transport from Australia and New Zealand, free tropospheric intrusion events in the vicinity of the polar front, and local Antarctic sources. Simultaneous particle measurements were also used to infer an influence of Antarctic katabatic outflow on SO aerosol properties extending 100-200 km from the coast. Some of the air contained in these events originates from free-tropospheric subsidence over the Antarctic continent (Chambers et al. 2018), and provides a potential mechanism for long range transported particles from continental regions to influence the Southern Ocean MBL. Bhattachan et al. (2015) suggested dust lofted from Taylor Valley in the McMurdo Dry Valleys could be deposited over large swaths of the Southern Ocean on the basis of forward trajectory modeling. An evaluation of simulated surface level dust concentrations against observations determined they are underpredicted at southern high-latitudes (Huneeus et al. 2011). This was briefly discussed in McCluskey et al. (2019), who noted that simulated dust INPs in the Southern Ocean may be underpredicted as a result.

Another potential mechanism for Antarctic influence on SO INPs is direct bioaerosol emissions from the Antarctic continent, similar to the contribution of biogenic INPs from coastal Russia to recent measurements made in the central Arctic (Porter et al. 2022). However, evi-

dence of biological INPs in Antarctica are mixed. INP activity at warm temperatures (>-15°C) has been demonstrated for isolated cultures of Antarctic diatoms and bacteria (Parker et al. 1985), although a more recent survey of Antarctic sea-ice bacteria and one virus concluded none were important for immersion freezing (Junge and Swanson 2008). Christner et al. (2008) analyzed INP concentrations in Antarctic snow samples, and found all the INPs active warmer than -9°C were biological, based on their susceptibility to heating. The ice nucleation activity (INA) of known IN-active *Pseudomonas* strains, including one isolated from Antarctic glacier melt, was explored by Attard et al. (2012). The glacial melt strain had significantly higher INA than mineral dust when normalized by particle surface area, and the INA at moderate supercoolings (~-10°C) was robust against exposure to UV-A radiation, acidification, or joint NO_2/O_3 exposure, indicating it may retain INA during and after atmospheric transport. Recent measurements of DNA diversity over the Southern Ocean found little contribution of Antarctic soil bacteria, despite some sample back-trajectories passing over or near ice-free areas of Antarctica (Uetake et al. 2020). However, the Antarctic soil samples used as a reference were from a single location far from the sampling region, and further study is needed.

The potential of Antarctica to influence Southern Ocean MBL clouds through the emission of INPs is explored in this study using data collected during the Southern Ocean Cloud Radiation Aerosol Transport Experimental Study (SOCRATES) and the second Clouds, Aerosols, Precipitation, Radiation and atmospherIc Composition Over the southeRN ocean (CAPRICORN-2) campaigns in 2018. A combination of ice nucleating particle and aerosol trace metal measurements provide details on particle composition at varying latitudes between Australia and the Antarctic marginal ice zone. The addition of air mass back trajectories and CALIPSO satellite aerosol type classifications assist with interpretation of aerosol and INP sources during these campaigns.

5.2 METHODS

5.2.1 Southern Ocean and Antarctic Measurements

This study utilized atmospheric measurements collected during the 2018 Southern Ocean Cloud Radiation Aerosol Transport Experimental Study (SOCRATES, hereafter SOC) aircraft campaign and the second Clouds, Aerosols, Precipitation, Radiation and atmospherIc Composition Over the southeRN ocean (CAPRICORN-2, hereafter CAP-2) ship campaign. An overview of the campaigns and data are given in McFarquhar et al. (2021), and detailed descriptions of the aerosol size distribution and INP observations used here are presented in Moore et al. (2022) and Moore et al. (2023), respectively. The NSF/NCAR G-V aircraft (UCAR/NCAR - Earth Observing Laboratory 2005) used for SOC was based in Hobart, Tasmania, and made observations of clouds and aerosols from ~150 m ASL to the free troposphere, and from Tasmania down to 62°S. Complementary measurements in the MBL were made on the RV *Investigator* (voyage IN2018_V01), an Australian Government research platform operated by the Commonwealth Science and Industrial Research Organisation (CSIRO), which transited from Hobart to the Antarctic marginal ice zone (66.5 °S) during CAP-2. Antarctic soil samples from the edge of Shackleton Glacier (Diaz et al. 2021; Dragone et al. 2022) were analyzed for INP activity (Section 5.2.2,Section 5.2.2.1) to assess the possibility of Antarctic mineral or soil dusts influencing Southern Ocean INP budgets.

5.2.2 Aerosol and INP Measurements

Aerosol size distribution and INP measurements were obtained on both the RV *Investigator* (CAP-2) and G-V aircraft (SOC), and both data collection and results are described thoroughly in Moore et al. (2022) and Moore et al. (2023). During SOC, aerosol measurements were made using a wing-mounted ultra-high sensitivity aerosol spectrometer (UHSAS, Droplet Measurement Technologies) and cloud droplet probe (CDP, Droplet Measurement Technologies; Lance et al. 2010), as well as physical collection and sizing of impacted supermicron particles (0.7-16 μm dry diameter) using the Giant Nucleus Impactor (GNI; Jensen et al. 2020). Data from all

three instruments were merged into aerosol number size distributions at ~10 minute intervals, to match the length of G-V level legs below and above cloud. Any points with cloud condensed water >0.01 g m^{-3} were removed to avoid cloud contamination of aerosol distributions (Moore et al. 2023). CAP-2 aerosol distributions were constructed by merging measurements from a TSI Scanning Mobility Particle Sizer (TSI, SMPS 3080; 15-660 nm) and a TSI Aerodynamic Particle Sizer (TSI, APS 3320; 500 nm - 20 μm) at 30-minute intervals. Size distributions were filtered to remove ship exhaust, and corrected for particle losses in the aerosol sampling inlet based on theoretical calculations (Moore et al. 2022). Aerosol distributions from both SOC and CAP-2 were integrated to calculate total particle number, and particle surface area and volume concentrations estimated assuming spherical particles. All aerosol distributions and concentrations are reported dry.

Offline analysis of aerosol filter samples using the CSU Ice Spectrometer (IS; Hiranuma et al. 2015; DeMott et al. 2018c) provided INP temperature spectra from -10 to -30°C for both campaigns (Moore et al. 2023). Aerosols were collected onto pre-cleaned 0.2 μm pore-size, 47 mm diameter track-etched polycarbonate membrane filters (Whatman Nucleopore filters, GE Healthcare Life Sciences). During CAP-2, filters were mounted on deck beneath a rain hat at ~23 m above sea level, in disposable, sterile, open-faced filter units (Nalgene sterile analytical filter units, Thermo Fisher Scientific). The filter pump was powered by a sector sampler to limit ship exhaust contamination; power was provided to the pump only when the wind speed relative to the ship was between 10 and 80 knots, the ship-relative wind direction was from the forward 90°, and total particle concentrations were stable and less than 2000 cm^{-3} (Moore et al. 2023). On the G-V, filters were loaded in pre-sterilized aluminum inline filter housings (Pall) and sampled from a HIAPER modular inlet (HIMIL inlet; Stith et al. 2009) in clear air. Filters where >5% of the collection was made in cloud (cloud condensed water >0.01 g m^{-3}) were excluded from analysis. After collection, filters from both CAP-2 and SOC were frozen, then transported back to CSU using a liquid nitrogen dry shipper and stored frozen (-20 °C) until analysis. Particles collected onto filters were resuspended in 0.1 μm filtered DI water and then analyzed in

the IS, as described in Moore et al. (2023). Blank filters were collected during both campaigns and stored and processed identically to the samples. Sample filter INP concentrations were corrected using the average background number of INPs from 6 (SOC) or 5 (CAP-2) blank filters and are not reported if blank-corrected values fell below zero. Antarctic soil and aeolian dust samples were re-suspended in 0.1 μm filtered DI water and analyzed identically to the aerosol filter samples.

5.2.2.1 INP Chemical Composition

In addition to the "base" INP temperature spectra reported in Moore et al. (2023), chemical pre-treatments of collected aerosol filters and Antarctic soil/dust samples prior to IS analysis were used to infer INP composition and assess possible sources. Ice nucleating particles produced by bacteria and fungi are often proteins (Pummer et al. 2015), and heating the sample is a simple way to denature these proteins and infer the contribution of biological INPs to a sample (Hill et al. 2016; Suski et al. 2018). Aliquots of sample re-suspensions are immersed in boiling water for 20 min before cooling to room temperature and analyzing with the IS using standard procedures. The biological INP contribution is then given by the difference between the INP temperature spectra pre- and post-heat treatment. Oxidation experiments are used to selectively destroy organic materials, leaving behind refractory (typically mineral) INPs (Hill et al. 2016; McCluskey et al. 2018a). Sample aliquots are digested with 10% hydrogen peroxide while immersed in boiling water for 20 min. UVB fluorescent bulbs (Exo Terra) are used to illuminate the samples and generate hydroxyl radicals. Any residual hydrogen peroxide is removed after cooling the sample to room temperature through the addition of catalase (MP Biomedicals, PN 100429), which prevents freezing point depression, and the sample is then analyzed on the IS as normal (Hill et al. 2016). The difference between the pre- and post-oxidation INP spectra represents the contribution of organic INPs, and the temperature spectrum remaining after peroxide digestion is inferred to be the mineral (or other inorganic) component.

5.2.2.2 Aerosol Trace Metal Observations

Aerosol trace metal concentrations were measured from particles collected on bulk aerosol filters during CAP-2, as described in Perron (2020) Chapter 4. Thirteen samples were collected on acid washed Whatman 41 (W41) cellulose filters (Morton et al. 2013; Cutter et al. 2017), punched to 47 mm to fit Savillex PFA filter holders compatible with the RV *Investigator* filtration manifold. Particles were sampled from the same aerosol inlet used for the other particle measurements during CAP-2 (Section 5.2.2) and described in Moore et al. (2022). Ambient air was subsampled at ~1 m^3 h^{-1} through conductive Teflon tubing to reduce particle losses, and the filtration manifold was placed in a HEPA-filtered laminar flow hood to minimize contamination. A similar sector sampler to the one used for INP filter collection was utilized to minimize ship exhaust contamination; the filter pump was activated for wind speeds between 8 and 80 km h^{-1} and ship-relative wind directions of 270-90°. Due to low particle concentrations, each filter was collected to reach a minimum of 45 m^3 of air (21-98 hr), rather than the 20 m^3 used for previous Australian coastal measurements (Perron et al. 2020a). Collected filters were folded in half and stored frozen in double sealed plastic bags prior to analysis. Procedural blank filters were loaded into the sampling manifold for 2 min with the pumps off and used to correct sample filters for background due to handling. Aerosol filters were thawed at room temperature and then a three-step leaching protocol was employed to determine the soluble (S_X) and labile (L_X) fractions, as well as total concentration (T_X) of each analyzed trace metal (Perron et al. 2020a;b). The soluble and labile fractions are suggested to represent lower and upper bounds on the bioavailability of each measured species, which has implications for both oceanic primary productivity and the sources of the aerosols (Perron et al. 2020a;b). Trace metal concentrations were measured using Sector Field Inductively Coupled Plasma-Mass Spectrometry (SF-ICP-MS, Thermo Fisher Scientific ELEMENT 2) within 3 days of sample preparation (Bowie et al. 2010). Enrichment factors (EF) for each element were calculated as the mass ratio of a trace metal to aluminum in the aerosol sample (aer), relative to the same ratio in the upper continental crust (UCC), using UCC abundances from McLennan (2001):

$$EF_X = \frac{(X/Al)_{aer}}{(X/Al)_{UCC}} \tag{5.1}$$

where EF_X is the enrichment factor of a trace metal X and Al is the aluminum concentration. EFs can help differentiate particles from different sources (Shelley et al. 2015), with EF>10 indicative of non-mineral sources (Shelley et al. 2017).

5.2.3 CALIOP Lidar Aerosol Sub-type Identification

The Cloud-Aerosol Lidar with Orthogonal Polarization (CALIOP) instrument is an active lidar installed on the joint NASA/CNES (Centre National d'Etudes Spatiales) Cloud-Aerosol Lidar and Infrared Pathfinder Satellite Observation (CALIPSO) satellite (NASA 22). CALIOP produces lidar measurements at 2 wavelengths, 532 and 1064 nm, and the 532 nm signal is further separated into orthogonally polarized components. For this study, the aerosol subtype classification as part of the Level 2 Vertical Feature Mask (VFM) product (Version 4-20) was utilized, which defines six aerosol types: clean continental, clean marine, dust, polluted continental, polluted dust, and smoke (Omar et al. 2009). The CALIOP VFM product has variable resolution at different altitudes. Only VMF features at altitudes <8.2 km were considered here, which has 1/3 km horizontal and 30 m vertical resolution. Each "box" was considered a single sample for statistical purposes, and samples with unidentified aerosol subtypes were ignored. No data affected by low laser energy were included in the analysis, and both day and night data were used to increase sampling statistics (NASA 22). CALIOP VFM data were used to identify the presence of dust, sea spray, and other aerosol types over the Southern Ocean during CAP-2 and SOC. Available VFM data were subset to overlap with the time period and location of the campaigns, and included retrievals between -70 to -30 °S, 110 to 180 °S, and January 1 - February 20, 2018. Data were separated into two altitude ranges: 0-2 km and 2-8.2 km, to approximate the MBL and free troposphere, respectively. Given the narrow swath width (5 km) of CALIOP, overpasses of the RV *Investigator* were considered to have occurred if CALIOP identified dust below 2 km, and the

swath passed within 100 km of the ship. Nine overpasses were identified which fit this criteria, which are listed in Table D.1.

5.2.4 Back Trajectory Calculations

Potential particle sources for INP and trace metal filters collected during CAP-2 were investigated using back trajectories calculated with the Hybrid Single-Particle Lagrangian Integrated Trajectory (HYSPLIT) model (Rolph et al. 2017; Stein et al. 2015). GDAS reanalysis at 0.5° resolution was used as the meteorological input, as in Sanchez et al. (2021b). Backwards trajectory ensembles (10 days) were released at five of the overpass locations identified in Table D.1 (Sample numbers 1, 2, 4, 5, 9), where CALIOP identified dust below 2 km in the proximity of the RV *Investigator*. The back trajectories and frequency of trajectories passing through a given 0.5 x 0.5 ° model grid box are shown in Figure D.5 for each overpass. Neff and Bertler (2015) found 10 day forward trajectories were sufficient for particles from potential dust source regions in Patagonia, Australia, Southern Africa, and New Zealand to reach the Southern Ocean.

5.3 RESULTS AND DISCUSSION

5.3.1 INP composition and aerosol iron solubility

INP concentrations at -26.5 °C measured from aerosol filters during CAP-2, as well as the inorganic INP contribution to the total, are shown in Figure 5.1a overlaid on the path of the RV *Investigator*. This temperature was selected to maximize both the number of available measurements and the possible contribution of mineral dust, which is an increasingly important ice nucleator at lower temperatures (Kanji et al. 2017). Both total concentration and the inorganic fraction are seen to vary with latitude, with northern samples displaying the highest concentrations and generally low inorganic fractions. Filters from the central Southern Ocean have the lowest concentrations but a large inorganic contribution to the INP budget, and filters from near Antarctica have moderate INP concentrations and moderate-high inorganic fractions. Enhancements in INP concentrations near Antarctica were unexpected, as marine (organic) INPs

are thought to dominate the INP budget in this region due to its isolation from continental airmasses (Burrows et al. 2013; Vergara-Temprado et al. 2017; 2018; McCluskey et al. 2019).

A similar pattern was observed by Perron (2020) for aerosol iron (Fe) concentrations, with high values observed near both Australia and Antarctica, and low concentrations between 50 and 60 °S (Figure 5.1b). This was coupled with increased iron solubility in the middle latitudes, which together were used to infer that different aerosol sources dominated in these broad latitude bands (Perron 2020). The solubility of trace element micro-nutrients, including iron, determines the bioavailability of the material and is a key factor influencing marine phytoplankton growth (e.g. Boyd et al. 2000), and may also indicate its source or path through the atmosphere. Atmospheric transport increases iron solubility through a variety of mechanisms, including gravitational settling, photoreduction, and reactions with acidic species (Shi et al. 2012). Low iron concentrations coupled with increased solubility between 50 and 60 °S is indicative of long-range atmospheric transport leading to solubilization of Fe and/or more-soluble Fe sourced from anthropogenic combustion (Liu et al. 2022), and is consistent with the prevailing westerlies and lack of land in the central SO. Enhanced concentrations and reduced Fe solubility south of 60 °S presents more of a puzzle, since it suggests a closer source of dust than the known SO source regions of South America, Australia, and New Zealand (Neff and Bertler 2015; Li et al. 2008; Bullard et al. 2016). We suggest Antarctica may be an intermittent source of dust aerosol to the Southern Ocean MBL, and one that may increase in the future under a warming climate (Bullard 2013; Meinander et al. 2022).

Trace metal enrichment factors (EF; Section 5.2.2.2) using aluminum as the reference crustal material can provide additional information about particle source, with EF<10 indicative of mineral sources (Shelley et al. 2015; 2017). Iron EFs were predominantly less than this threshold (Figure 5.1c) during CAP-2, indicating primarily mineral and soil dust sources, including samples at high latitudes. Three samples between 49 and 63 °S had EF~20, suggesting the iron in the central latitude band was likely from a mixture of dust and anthropogenic particles that had undergone long-range transport (Perron 2020). An abnormally elevated iron EF~120 north of

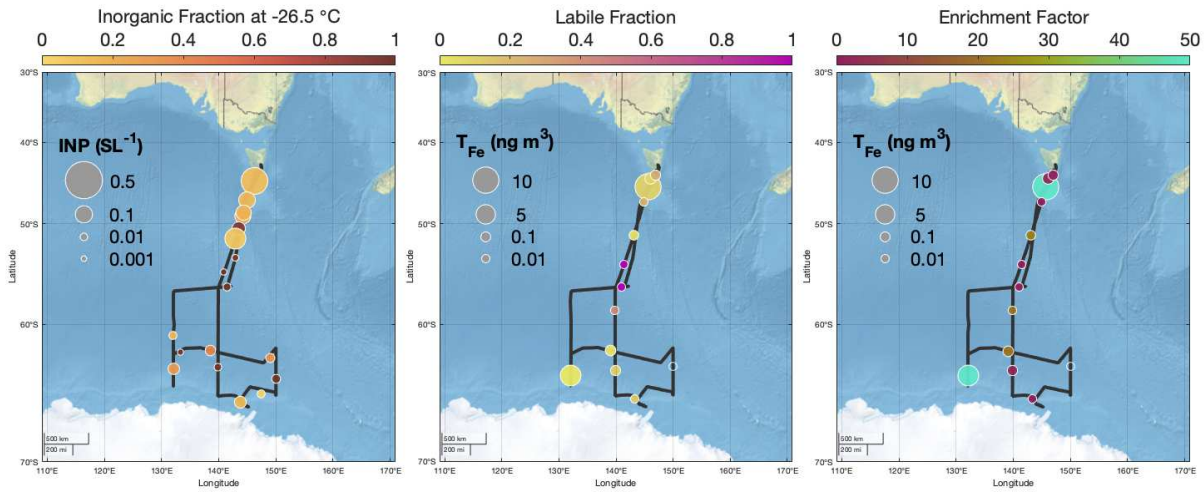

Figure 5.1: INP concentrations at -26.5 °C (a) and aerosol iron concentrations (b-c) overlaid on the track of the RV *Investigator* during CAP-2. Symbols are positioned at the midpoint latitude and longitude of each filter collection. Symbol size reflects total concentration, and color indicates the fractional contribution of inorganic INPs (a), the labile iron fraction (b), or the iron enrichment factor (c).

50 °S probably reflects anthropogenic emissions from Australia, while the iron EF~120 in conjunction with elevated EFs for manganese (Mn) and cobalt (Co) seen at 62.5 °S may be a result of either aerosolization of Fe-rich particles from ice or soil in Antarctica, or perhaps a contribution from anthropogenic emissions from an Antarctic base or vessel. Co-enrichment in Mn and Fe have been reported for sea ice (Lannuzel et al. 2016), snow (Raiswell et al. 2018), and in glacial meltwater (Kim et al. 2015) relative to seawater, but the potential for aerosolization is unknown.

INP concentrations at all measured temperatures (Figure 5.2a) demonstrate the same pattern observed at -26.5 °C (Figure 5.1a), with the highest concentrations north of 52 °S and smaller concentrations in the middle and southern latitude bands. Inorganic INP contributions are uniformly high at temperatures below -23 °C between 52 and 60 °S, consistent with the long-range mineral dust source suggested by the iron solubility and EF (Figure 5.1b-c). At warmer temperatures, the peroxide-treated IS spectra (Section 5.2.2.1) were below the instrument detection limit, and as a result the inorganic contribution could not be inferred. The contribution of biological INPs is highest across all temperatures for samples collected north of 52 °S (Figure 5.2c). Inorganic and biological INP contributions are highly variable south of

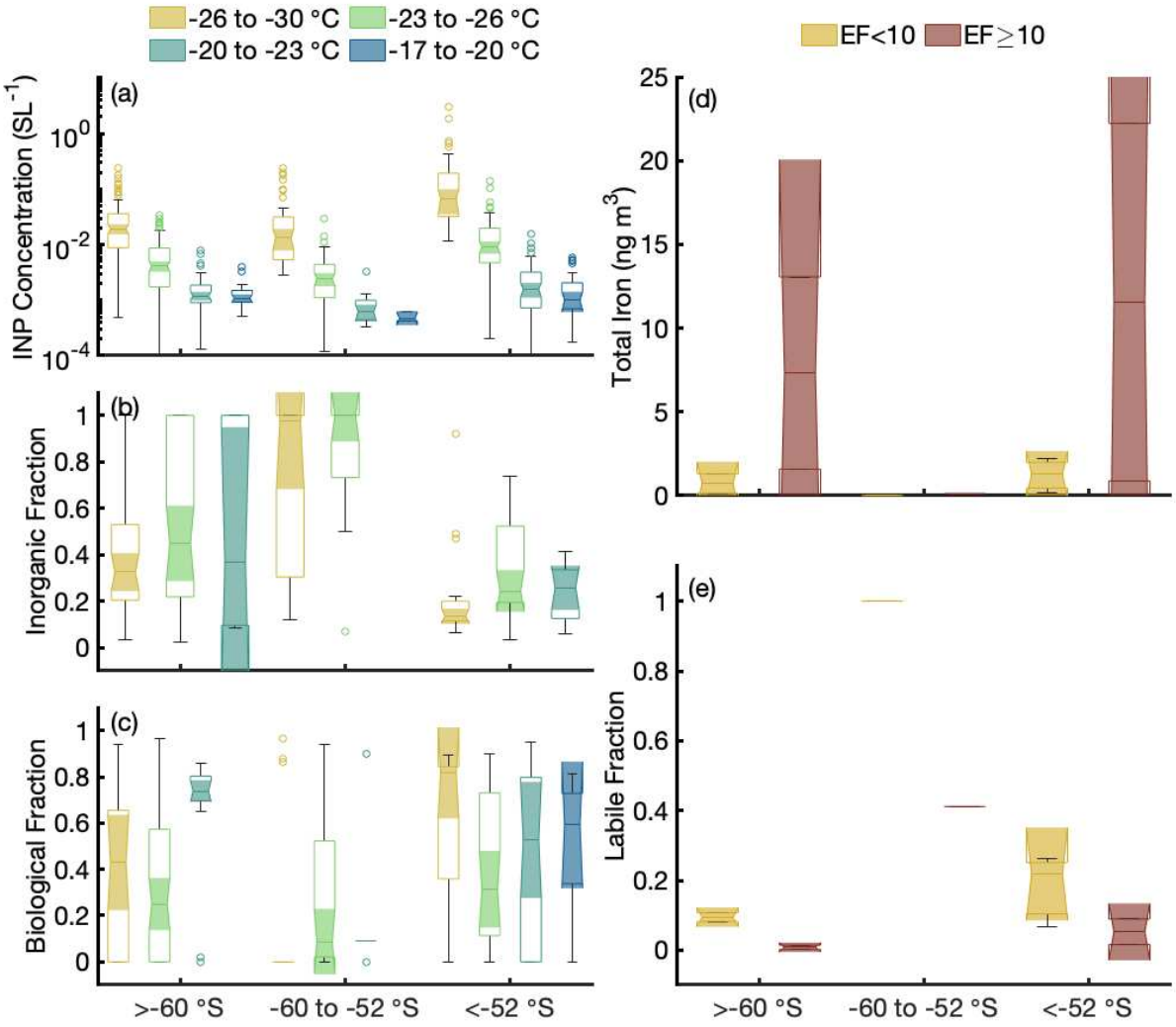

Figure 5.2: Box plots of (a) INP concentration, (b) INP inorganic fraction, and (c) INP biological fraction in the northern (<-52 °S), middle (-60 to -52 °S) and southern (>-60°S) latitude bands. Both concentration and fractional composition are separated into ~3 °C temperature bins, indicated by color. Box plots of (d) aerosol iron and (e) labile iron fraction are shown on the right, separated into the same latitude bands. Box color indicates samples with EF<10 (yellow) and EF≥10 (red).

60 °S, which does not rule out bioaerosol or dust contributions from Antarctica. The inverse relationship between fractional iron solubility and concentration (Figure 5.2d-e) observed for the northern and southern latitude bands has been previously observed and attributed to dry deposition, due to increased solubility of smaller particles with a larger surface area to volume ratio (Chen and Siefert 2004; Baker and Jickells 2006). The enhanced solubility of aerosol iron in the 52-60 °S latitude band is striking in Figure 5.2e, and further corroborates the hypothesis that Fe sources are different for all three latitude bands.

5.3.2 Identification of dust with CALIOP

Aerosol type classifications from the CALIOP vertical feature mask (Section 5.2.3) are shown in Figure D.1, separated into 0-2 km and 2-8.2 km altitude ranges. The relative contributions of sea salt and dust in both height categories are remarkably consistent with measurements of aerosol composition for particles >0.5 μm during SOCRATES (Twohy et al. 2021), given that the CALIOP results were averaged over a much larger domain and time span. Figure 2b of Twohy et al. (2021) is reproduced in Figure D.2 for a direct comparison between the two datasets. Below cloud sea spray and dust fractions were ~85% and ~2% respectively, during SOC, with CALIOP estimations of 68% and 4% for the 0-2 and 2-8.2 km bins. Above cloud (Twohy et al. 2021) observed ~2% sea spray and ~50% dust; CALIOP values are 3% and 41%, respectively. This provides support that 2 km is an appropriate threshold for dividing the MBL and free troposphere during CAP-2. However, it should be noted that the categories used for aerosol type classification varied between Twohy et al. (2021) and the CALIOP VFM product, so exact comparisons would require re-defining the SOC categories to more closely align with CALIOP. The CALIOP dust and clean marine aerosol types are visualized in Figure D.3 as a function of both latitude and altitude. Sea spray fractional contribution maximizes at ~52 °S in the MBL, which is expected based on wind-driven production (e.g. Lewis and Schwartz 2004; O'Dowd and de Leeuw 2007; de Leeuw et al. 2011), and is uniformly low above 2 km. Dust fraction above 2 km steadily increases from ~0.1 at 40 °S to almost 50% at 67 °S. This seems likely to indicate free-

tropospheric subsidence at high southern latitudes as observed by Chambers et al. (2018) using Radon-222, and may indicate dust at high altitudes is representative of long-range transport. Dust at low altitudes has a bimodal distribution, which peaks north of 40 °S and south of 60 °S, although only reaching ~15% of the total aerosol burden in both cases. This result unfortunately cannot be used to distinguish between long-range transport followed by subsidence versus local Antarctic emissions. This is broadly consistent with modeling studies which have predicted marine INPs dominate at low altitudes over the SO, and an increasing influence of mineral dust INPs above cloud (Burrows et al. 2013; McCluskey et al. 2019; 2023; Vergara-Temprado et al. 2017). This was supported by vertically resolved measurements collected during SOC (Moore et al. 2023), although it was noted that even small amounts of mineral dust, such as were observed by CALIOP, can have an outsized impact on cloud properties due to the much higher ice nucleation efficiency of mineral dust compared to marine INPs (Kanji et al. 2017; McCluskey et al. 2018a; Moore et al. 2023).

5.3.3 INP sources

The concentration and frequency of atmospheric dust transport at all latitudes, including in cold climates, is tied to wind. Aeolian sediment transport depends on wind velocity and turbulence, as well as surface characteristics such as roughness and moisture content (Bullard 2013). The wind speed threshold needed to loft dust in northern glaciated regions has been estimated at 5-10 m s^{-1} (Bullard et al. 2016), which typical coastal Antarctic wind speeds reach and exceed (Parish and Bromwich 2007). In addition to the frontal and pressure gradient winds that drive subtropical dust emissions, density and thermal gradient-generated katabatic and föhn winds are important for high latitude dust emission. Such winds typically dissipate within 10-20 km of the ice margin, but are likely the most significant causes of dust lofting in Antarctica (Bullard 2013; Bullard et al. 2016). The threshold wind velocity required for sediment entrainment in Victoria Valley (McMurdo Dry Valleys) was estimated at 5.3 m^{-1} (Speirs et al. 2008), which is lower than in warm desert regions. This is consistent with temperature-dependent changes

in air density that also increase sediment transport rates in cold environments (Wolfe 2022; Mckenna Neuman 2003). Intense and frequent katabatic winds have been observed at sites near the sampling region of CAP-2, including Port Martin along the Antarctic coast and Terra Nova bay (Bromwich 1989; Parish and Bromwich 2007). Although stronger and more persistent in winter, mean Austral summer wind speeds exceed 10 m^{-1} in many coastal areas (Parish and Bromwich 2007), suggesting wind conditions above the dust entrainment threshold occur year-round. Simulated wind field projections indicate small and largely insignificant decreases in wind speed over Antarctica through 2100 (Bintanja et al. 2014), so conditions conducive to dust lofting are likely to only increase in frequency through expansion of ice-free areas as the surface temperature warms.

Measurements of potential Antarctic sources of biological INPs have largely been limited to bacteria and phytoplankton cultures from seawater (Parker et al. 1985), sea-ice or glacial melt (Junge and Swanson 2008; Attard et al. 2012), or analysis of snow samples (Christner et al. 2008). Mixed results were found, with some species identified as IN-active. Uetake et al. (2020) found little contribution of Antarctic soil to DNA diversity over the Southern Ocean during CAP-2, although only one soil sample was used as a reference, and from a location far from the sampling region. A few soil samples from the ice-free edges of Shackleton glacier (Diaz et al. 2021; Dragone et al. 2022) were analyzed for INP activity in this study, and the results are shown in Figure 5.3. Both microbial diversity and soil geochemistry were found to vary strongly with elevation in these soil samples, and two samples were selected for INP analysis from each of the three geochemical zones (lower, middle, upper) identified in Diaz et al. (2021) to span the anticipated range of INP concentrations. INP concentrations decreased with height, along with organic carbon (Diaz et al. 2021) and microbial diversity (Dragone et al. 2022). Samples at the lowest elevations were surprisingly active, with onset temperatures (~-5 °C), concentrations, and spectral shapes similar to the ice-active fungus *Mortierella alpina* (Fröhlich-Nowoisky et al. 2015) and Arctic permafrost (Barry et al. 2023b). Soils from the middle and upper elevations had more log-linear INP temperature spectra, but still reached concentrations of 10^7-10^9 g^{-1} soil at

-30 °C, comparable to the range observed in Alaskan permafrost samples by Barry et al. (2023b). Concentrations at -20 °C ranged from 10^4 g^{-1} for high elevation to 10^9 g^{-1} for low elevation samples. Shackleton Glacier low elevation soils have comparable concentrations to soil samples from natural and agricultural grasslands and forests in central North America (10^7-10^9 g^{-1}) at -20 °C (Hill et al. 2016). At -10 °C, the low elevation samples (10^7-10^8 g^{-1}) are more active than those measured by O'Sullivan et al. (2014) from arable agricultural fields in the UK (10^6 g^{-1}), although the middle and high elevation Shackleton Glacier soils are much less active (<10^4 g^{-1}).

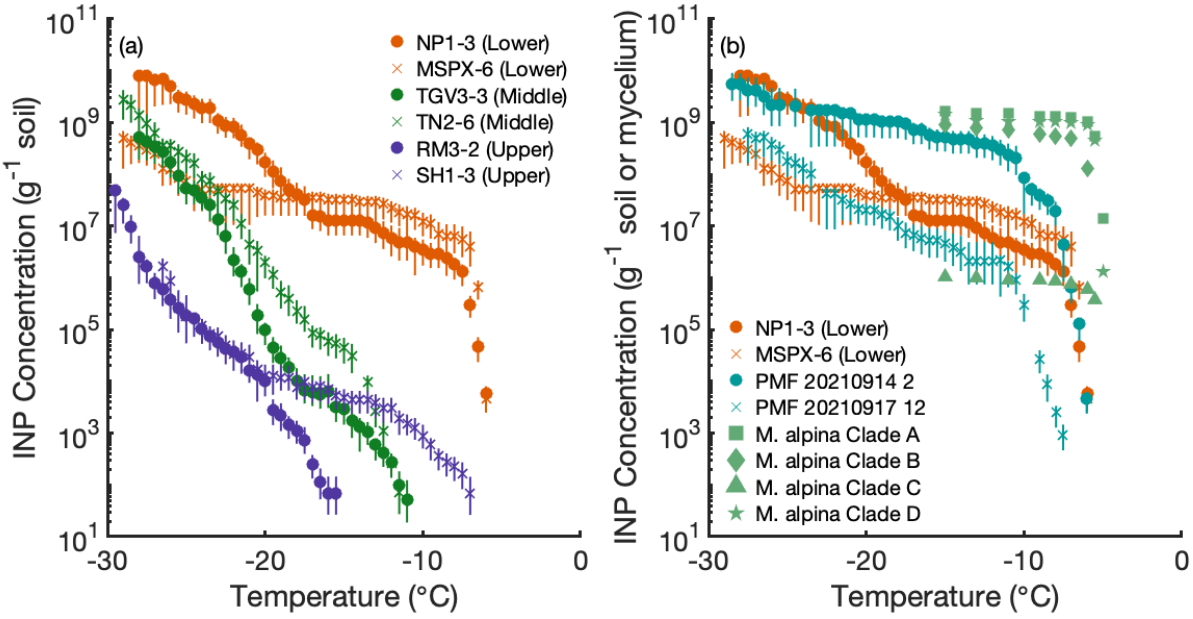

Figure 5.3: INP temperature spectra of six representative soil samples from the lower, middle, and upper regions of Shackleton Glacier (Diaz et al. 2021; Dragone et al. 2022) are shown in (a). The lower elevation samples from Shackleton Glacier are displayed again in (b), along with previously reported spectra from IN-active soil fungus *M. alpina* (Fröhlich-Nowoisky et al. 2015) and recently collected Arctic permafrost cores (Barry et al. 2023b) for reference.

While aerosolization of soil from Shackleton Glacier has not been directly observed, these results suggest the potential for highly active, warm temperature INPs to be emitted from Antarctica, with a likely larger role as the climate warms and further ice-free areas are exposed (Bullard et al. 2016; Meinander et al. 2022). INP concentrations at such temperatures were well below the detection limit for the aerosol samples from CAP-2, so more targeted INP sampling

using a high-volume sampler, ideally coupled with DNA source tracking (i.e. Uetake et al. 2020), would be required to confirm this hypothesis. Significant numbers of INPs active at colder temperatures (<-23 °C) indicate these soils could also be responsible for the inorganic INP contribution seen in the CAP-2 filters at high latitudes (Figure 5.2b).

Back trajectories corresponding to CALIOP identifications of dust in the lower atmosphere (0-2 km) near the RV *Investigator* are shown in Figure D.5 for five of the overpass locations listed in Table D.1 and shown relative to the INP samples in Figure D.4. The two overpasses identified in the northern latitude band (<52 °S; Figure D.5a-b, j-k) are indicative of long-range transport, with potential sources including Southern Africa and Patagonia, and some influence from coastal Antarctic air masses for overpass 9. The remaining 3 locations were all south of 60 °S, and were predominantly influenced by Antarctica, including both the high elevation interior and coastal areas. Trajectory ensembles for overpasses 2 (Figure D.5c-d), 4 (Figure D.5e-f), and 5 (Figure D.5g-h) remained at low elevations for the vast majority of the 10-day back trajectories, and could therefore be consistent with both subsidence of long-range transported particles or local Antarctic emissions. Perron (2020) found similar results for HYSPLIT back trajectories initialized from the midpoint sampling locations of the trace metal filters. Trajectories north of 50 °S were largely influenced by Australian outflow, samples between 50 and 60 °S were dominated by long-range transport, and the southernmost trajectories mainly received Antarctic air masses.

5.4 SUMMARY

Ice nucleating particle concentrations in the remote Southern Ocean marine boundary layer, particularly at high southern latitudes, were anticipated to be dominated by local marine emissions of organic INPs on the basis of modeling studies (Burrows et al. 2013; Vergara-Temprado et al. 2017; 2018; McCluskey et al. 2019) and observed low INP concentrations (McCluskey et al. 2018c; Schmale et al. 2019; Tatzelt et al. 2022; Moore et al. 2023). While INP concentrations were consistent with previous Southern Ocean and North Atlantic observations

(McCluskey et al. 2018a;c) during CAP-2 (Moore et al. 2023), unexpectedly high concentrations near the Antarctic continent prompted analysis of the potential emission of INPs from Antarctica.

Aerosol trace metal measurements and back trajectories suggest particle sources in the Southern Ocean can be divided into three roughly 10 ° latitude bands during the CAP-2 voyage. Aerosol samples collected north of ~50 °S have relatively higher INP and iron concentrations, low-moderate iron solubilities, and were influenced by a mixture of Australian and long-range transported air masses. Samples between ~50 and 60 °S are characterized by the lowest INP and Fe concentrations, but large INP inorganic contributions and high iron solubilities, consistent with long range transport and atmospheric processing of particles, or sources with higher Fe solubility (Liu et al. 2022). Filters collected south of ~60 °S have similar Fe concentrations to the northernmost samples but lower Fe solubility, coupled with moderate INP concentrations and a mix of biological and inorganic INPs. HYSPLIT back trajectories indicate significant Antarctic influence, but cannot distinguish between subsidence of long-range transported particles and local Antarctic emissions. CALIOP was able to identify dust in the lower atmosphere (0-2 km) in the vicinity of the RV *Investigator*, including south of ~60 °S. Surprisingly, the relative contribution of dust below 2 km approaches 15% near Antarctica, but similarly cannot definitively identify the source.

Dust emissions have been observed in several regions of Antarctica, including the Antarctic peninsula, McMurdo dry valleys, McMurdo ice sheet, and several coastal locations (Kavan et al. 2018; Diaz et al. 2018; Meinander et al. 2022), but the seasonality and mass is completely unconstrained. Modeled forward trajectories suggest dust from Taylor valley in the McMurdo dry valleys could reach large areas of the Southern Ocean (Bhattachan et al. 2015), although measurements of sediment on sea ice in McMurdo Sound (Chewings et al. 2014; Atkins and Dunbar 2009) show little influence from the dry valleys. Dust from ice cores at the high elevations is dominated by long range transport from Australia, South America, southern Africa, and New Zealand (e.g. Bullard et al. 2016). However, measurements in coastal areas have shown

accumulation rates over 100 times higher than those recorded at high elevation or in global dust models (Chewings et al. 2014; Winton et al. 2014). Gao et al. (2013) inferred local Antarctic dust sources in coastal East Antarctica on the basis of higher iron concentrations than over the nearby Southern Ocean and the presence of coarse mode Fe only along the coast. At the Talos Dome ice core site in the Ross Sea sector of East Antarctica, Delmonte et al. (2013) found local Victoria Land high-elevation sources contributed to the measured dust deposition.

Taken all together, the high INP and iron concentrations and low Fe solubilities observed in the Southern Ocean south of 60 °S, identifications of dust in the MBL near Antarctica from CALIOP, and back trajectories indicating significant Antarctic influence, we suggest Antarctic coastal or potentially even higher elevation sites (Shackleton Glacier, Victoria Land) are acting as a source of INPs to the Southern Ocean. This is supported by the studies mentioned above, which have observed dust emissions from a variety of Antarctic regions (Kavan et al. 2018; Diaz et al. 2018; Meinander et al. 2022; Gao et al. 2013; Delmonte et al. 2013). Highly active INPs with warm onset temperatures (~-5 °C) were found in low-elevation soils from the ice-free edges of Shackleton Glacier (Diaz et al. 2021; Dragone et al. 2022) and indicate biological INPs could potentially also be emitted from Antarctica. Both biological and dust INPs have the potential to significantly alter Southern Ocean cloud microphysical and radiative properties (Frey and Kay 2017; Kay et al. 2016a; Mace et al. 2020; McFarquhar et al. 2021; Tan et al. 2016; Vergara-Temprado et al. 2018). Such high-latitude INP sources have been observed in Iceland (Sanchez-Marroquin et al. 2020) and Svalbard (Tobo et al. 2019), and are likely to increase in importance as the climate warms (Bullard et al. 2016; Meinander et al. 2022).

6. Conclusions and Future Directions

6.1 RESEARCH SUMMARY

The results presented in this dissertation summarized recent field and mesocosm measurements of sea spray aerosols and ice nucleating particles, and assessed both generation and the atmospheric consequences of such emissions. Low clouds in remote marine environments such as the Southern Ocean are highly sensitive to particle number, size, and composition due to their generally low droplet concentrations. When combined with the ubiquity of cloud cover over the SO (Mace et al. 2020) and high proportion of supercooled liquid water (McFarquhar et al. 2021), the potential for INPs to influence cloud phase and the resulting radiative properties has enormous implications for global climate. The need to better understand cloud-aerosol-precipitation-radiation interactions in the Southern Ocean region motivated two large, international field campaigns in austral summer 2018: the Southern Ocean Cloud Radiation Aerosol Transport Experimental Study (SOCRATES) aircraft campaign, and the second Clouds, Aerosols, Precipitation, Radiation and atmospherIc Composition Over the southeRN ocean (CAPRICORN-2) ship campaign (McFarquhar et al. 2021). Results from these ambient observations were supplemented by measurements from a mesocosm experiment at the new Scripps Ocean-Atmosphere Research Simulator (SOARS) wind-wave channel at the Scripps Institution of Oceanography (CHAOS; CHaracterizing Atmosphere-Ocean parameters in SOARS) to assess the role of wind speed in marine INP production, which had not previously been characterized through controlled experiments.

Chapter 2 (Moore et al. 2022) focused on measurements of sea spray aerosols and the relationship between their physical and optical properties. In particular, two existing parameterizations used to estimate marine aerosol surface area from lidar (Mamouri and Ansmann 2016) and nephelometer (DeMott et al. 2016) measurements were evaluated against in situ observations of aerosol surface area from size distributions collected during SOC and CAP-2. Aerosol

surface area is a key quantity for model evaluation of aerosol fields, as well as influencing light scattering, hygroscopic growth, and reactivity (Lewis and Schwartz 2004; O'Dowd and de Leeuw 2007). In addition, INP model parameterizations often rely on normalizing INP concentrations with a more commonly measured quantity, such as particle number or surface area concentrations (DeMott et al. 2010; 2015; Hoose and Möhler 2012; Kanji et al. 2017; McCluskey et al. 2018a; Niemand et al. 2012; Ullrich et al. 2017). The DeMott et al. (2016) method uses scattering coefficients from a three-channel nephelometer to assign an effective scattering efficiency (Q) for each measured size distribution. This was found to underestimate aerosol surface area during SOC and CAP-2 by a factor of 2 or more if å>1. A new relationship was instead proposed between Q and å, which explains 80% of the variance between Q and å for -0.2<å<2 based on CAP-2 and SOC measurements. å=0.8 was also found to separate size distributions dominated by PMA (å<0.8) from those dominated by secondary biogenic marine aerosol (å>0.8) on the basis of HYSPLIT back trajectories. Over the Southern Ocean, Mamouri and Ansmann (2016)'s method of estimating aerosol number and surface area from lidar backscatter overestimates surface area by a factor of ~3-5, and N_{500} by a factor ~1.5-3 using their 355 nm marine aerosol conversion parameters. This may be a result of the need to filter the AERONET Barbados observations used to generate the MA parameters to remove biomass burning and dust, which are more common in the Caribbean than over the SO (Corona-Núñez et al. 2020; Prospero et al. 2014). New conversion factors between extinction and aerosol surface area or N_{500} were derived using Microtops AOT measurements from CAP-2, reducing overestimates by factors of 4.9 and 2.8 for surface area and N_{500}, respectively, relative to the MA 355 nm marine aerosol parameters.

Chapter 3 (Moore et al. 2023) presented INP measurements from the concurrent SOCRATES and CAPRICORN-2 campaigns, along with comparisons to CAM6 model simulations. Notably, SOC and CAP-2 represent the first vertical distribution measurements of INPs in the Southern Ocean, including the first in situ observations in and above cloud in the region. Excellent agreement was seen between measurements made on the G-V during the few overpasses of the RV *Investigator* when the aircraft was within the marine boundary layer. SOC and CAP-2 results

also confirmed findings from the recent ACE (Schmale et al. 2019; Tatzelt et al. 2022; Welti et al. 2020) and CAPRICORN-1 (McCluskey et al. 2018c) campaigns that SO INP concentrations in the MBL are uniformly lower than those of Bigg (1973). MBL and above cloud INP concentrations from the same SOC flight support the hypothesis suggested by several modeling studies (Burrows et al. 2013; McCluskey et al. 2019; 2023; Vergara-Temprado et al. 2017) that marine INPs dominate at low altitudes, and mineral dust becomes increasingly important with height. Size measurements of collected ice crystal residuals from the CFDC and indirect inferences based on aerosol concentrator enhancement factors suggest MBL INPs are predominantly <500 nm. This was unexpected based on strong relationships with large aerosols observed for other INP types (DeMott et al. 2015; Tobo et al. 2013), but consistent with weak or modest relationships observed between INP concentrations and aerosol number, mass, or surface area during both CAP-2 and ACE (Moore et al. 2023; Tatzelt et al. 2022). Another unforeseen finding was that MBL INP concentrations exhibit a positive relationship with wind speed, even following normalization by aerosol number, surface area, or volume. This suggests another reason surface area-based N_s parameterizations such as McCluskey et al. (2018a) capture mean behavior but not variability in INP temperature spectra is that the active site density is not constant for marine INPs, or at least not after emission to the atmosphere.

Chapter 4 summarizes initial results from the CHAOS campaign, conducted in the new SOARS wind-wave channel at SIO in La Jolla, CA. The aim was to isolate individual factors such as seawater temperature and wind speed that may influence INP emissions and carefully vary them in a controlled laboratory setting. Due to several technical issues, only wind speed variations were accomplished during the CHAOS campaign, but additional measurements of SSA flux variability are ongoing. INP concentrations were broadly consistent with Southern Ocean (Moore et al. 2023; McCluskey et al. 2018c; Schmale et al. 2019) and North Atlantic (McCluskey et al. 2018a) observations, although biased high, and also increased with wind speed, as during CAP-2 (Moore et al. 2023). SSA number, surface area, and volume concentrations were several to a few tens of times larger than was observed for similar wind speeds in the Southern Ocean

MBL (Moore et al. 2022). Normalized INP concentrations were biased low, and also decreased with wind speed (only slightly for CFDC measurements), unlike CAP-2 observations (Moore et al. 2023). Prior to CAP-2, all normalized INP concentrations were anticipated to have no relationship with wind speed, since wind is the primary driver of variability in SSA emissions (Lewis and Schwartz 2004; O'Dowd and de Leeuw 2007; de Leeuw et al. 2011). The discrepancy between CAP-2 and CHAOS may be related to one or a combination of reasons briefly discussed below. First, the low sampling height in SOARS (0.6 m) compared to typical ambient measurements, where inlets may be 20+ m above the ocean surface, likely resulted in decreased particle losses at large sizes. Wave height during CHAOS was fixed at an amplitude of 1.3, meaning only one wind speed (19.10 m s^{-1}) yielded white cap fractions comparable to open ocean conditions (Monahan and Muircheartaigh 1980), with unknown consequences for SSA production. Finally, CAP-2 results may be a reflection of atmospheric processing of particles, where CHAOS measurements were performed on freshly emitted SSA. Regardless of the mechanism(s), measurements from CHAOS likely represent interfacial values and may not be directly comparable to MBL or cloud-base measurements as a result. Unexpectedly, peroxide-treated filter samples collected at wind speeds >19.10 m s^{-1} almost uniformly had significantly higher INP concentrations than untreated samples, especially at warm temperatures, which has not previously been observed. Spume droplet production, which produces particles >10 μm above a wind speed threshold of ~9 m s^{-1} (Monahan et al. 1986; Sofiev et al. 2011) is suggested to be the most likely explanation. Lower losses of large particles in SOARS may have allowed aggregate particles with multiple INPs to be sampled, which were then broken apart during peroxide digestion of the samples. Atomic force microscopy measurements of ice crystal residual viscosity suggests viscosity decreases at higher wind speeds. This may be compatible with the peroxide-treatment results, if decreasing viscosity leads to increased water solubility of the shells, as was observed during SeaSCAPE for aged SSA (Kaluarachchi et al. 2022a).

Chapter 5 expands on the INP measurements presented in Chapter 3, using INP composition, aerosol iron concentrations, back trajectories, and satellite aerosol measurements to

discuss possible sources of INPs to the SO MBL, and some implications for changes under a warming climate. As discussed in Moore et al. (2023), the range of INP concentrations observed during CAP-2 and SOC was consistent with previous measurements (McCluskey et al. 2018a;c; Schmale et al. 2019). However, the observation that INP concentrations increase south of 60 °S relative to those made between 40 and 50 °S precipitated the hypothesis that Antarctica may serve as a source of INP emissions. A combination of back trajectories and aerosol trace metal measurements were used to divide the Southern Ocean into northern (<-52 °S), central (-60 to -52 °S) and southern (>-60°S) latitude bands. Aerosols in the northern band were influenced by a mixture of Australian air masses and long-range transport, and were characterized by high INP and aerosol iron concentrations and moderate iron solubilities. The central band exhibited INP and iron properties consistent with predominantly long range transport and atmospheric processing. In addition to high INP concentrations, filters collected in the southern band had high iron concentrations but low Fe solubility, and back trajectories were dominated by Antarctic air masses. CALIOP aerosol type classification identified dust at low levels (<2 km) near Antarctica during the CAP-2 and SOC campaigns, but could not distinguish between subsidence of long-range transported particles and local Antarctic emissions. But in conjunction with high INP and iron concentrations and low Fe solubilities in this band, as well as Antarctic influence in the back trajectories, it seems probable that Antarctic dust emissions are being lofted to the Southern Ocean and serve as INPs. Although the amount is unconstrained, dust emissions have been observed in several regions of Antarctica (Kavan et al. 2018; Diaz et al. 2018; Meinander et al. 2022), and a modeling study suggested dust from the largest ice-free region could be deposited over large portions of the Southern Ocean (Bhattachan et al. 2015). Observations of iron (Gao et al. 2013) and deposited dust (Delmonte et al. 2013) inferred a local Antarctic contribution at two different coastal areas. Soils from the ice-free edges of Shackleton Glacier (Diaz et al. 2021; Dragone et al. 2022) were tested for INP activity and found to contain high concentrations of INPs with warm onset temperatures (~-5 °C), supporting the potential for Antarctic mineral or soil dust emissions to influence clouds offshore. Sources of high latitude dust are increasing

under a warming climate (Bullard 2013; Bullard et al. 2016; Meinander et al. 2022), so even if this source is not active now, it is likely to become increasingly important in the future.

6.2 CONCLUDING THOUGHTS AND FUTURE WORK

The overarching goal of this dissertation was to assess sources and properties of marine INPs and their role in determining cloud phase and radiative properties in order to improve and evaluate current INP model parameterizations. This was accomplished through observations in the remote Southern Ocean, one of the few remaining pristine aerosol environments (Hamilton et al. 2014), as well as controlled laboratory experiments to isolate individual factors influencing marine INP emission. Aerosol and especially INP observations are limited in the Southern Ocean, even though low and mid-level clouds in this region play a key role in the radiative budget (Bodas-Salcedo et al. 2013; 2016; Kay et al. 2016b; Naud et al. 2014). Recent updates to the microphysical schemes and cloud processes of several CMIP6 models have reduced biases in supercooled liquid water and radiation biases in the SO (Bodas-Salcedo et al. 2019; Gettelman et al. 2020) relative to their precursors, which was needed given the historically poor performance of earth system models and reanalyses in this region (Bodas-Salcedo et al. 2013; 2016; Kay et al. 2016b; Naud et al. 2014). However, these changes are likely responsible for the increased equilibrium climate sensitivities observed in many CMIP6 models over CMIP5 (Zelinka et al. 2020). The cloud phase feedback is a strong contributor to future ECS (Bjordal et al. 2020), meaning it is critical to constrain factors that influence cloud phase, such as INP concentration and efficiency, in order to ensure model simulations include atmospherically representative microphysics and improve predictions of ECS.

The SOCRATES, CAPRICORN-2, and related campaigns in 2017-2018 (McFarquhar et al. 2021) aimed to do just that, and results presented in this dissertation represent small steps forward in improving our understanding of aerosols and aerosol-cloud interactions in the Southern Ocean, and remote marine regions more broadly. Returning to the key questions identified in the Introduction, the advancements made in the preceding chapters will be summarized,

along with suggestions for future work.

Key Questions:

1. **Can marine aerosol surface area be accurately estimated with remote sensing measurements?**

This question was the focus of Chapter 2 (Moore et al. 2022), which started by evaluating existing parameterizations for marine aerosol surface area using nephelometer (DeMott et al. 2016) and lidar (Mamouri and Ansmann 2016) measurements. Neither performed well for Southern Ocean MBL data collected during CAP-2 and SOC, and new parameterizations for estimating marine aerosol surface area and N_{500}, key quantities often used in INP parameterizations (e.g. DeMott et al. 2010; 2015; Tobo et al. 2013; McCluskey et al. 2018a; Niemand et al. 2012; Ullrich et al. 2017) were developed in Moore et al. (2022) for both types of observations. If these new parameterizations are validated against other data sets and found to perform well, it would significantly increase the number of aerosol concentration and surface area observations, since nephelometers and lidars can operate for long periods mostly autonomously once installed and calibrated.

2. **What factors (seawater temperature, wind speed) influence the emission of marine INPs?**

The CHAOS campaign (Chapter 4) represents a first attempt at isolating individual variables influencing marine INP emissions, and provides a comparison to the ambient observations collected during CAP-2 (Chapter 3; Moore et al. 2023). Technical issues with the paddle in the SOARS channel prevented a systematic assessment of the impact of seawater temperature on INP emissions, which will need to be addressed in a future study. As also observed in CAP-2 (Moore et al. 2023), INP concentrations measured in SOARS increased with wind speed, although INP concentrations normalized by particle number, surface area, and volume decreased

with wind speed during CHAOS, whereas the opposite was observed during CAP-2. SSA concentrations measured in SOARS were much larger than Southern Ocean observations, which may reflect differences in production or, most likely, decreased particle losses, especially at larger particle sizes. Although direct flux measurements were not possible due to the time scales of current INP observations, CHAOS results are more representative of interfacial values than the approximately steady-state concentrations measured during CAP-2. As a result, SOARS data may not be directly comparable to ambient MBL or cloud-base measurements.

Several key lessons were learned, which should be incorporated into similar studies in the future. Wind speed and wave amplitude should be co-varied to generate realistic white cap fractions at all wind speeds, to increase confidence in observed wind speed trends. Highly variable particle concentrations at ocean-relevant wind speeds (~15-19 m s^{-1}) were observed, and need to be addressed through both more systematic wind speed sampling and also detailed particle loss measurements or estimates. If possible, co-sampling with the CFDC and IS from the same inlet would provide a more robust comparison between the offline temperature spectra and high resolution point measurements. A mechanism was proposed for spume droplet production of aggregate particles containing multiple INPs, which needs to be assessed through combined measurements of INPs and microgels such as TEP (Verdugo 2012) in subsequent studies using SOARS or a similar wind-wave channel.

3. How can marine INPs be best parameterized in models?

Corroborating the results of Tatzelt et al. (2022) from the ACE campaign, Moore et al. (2023) (Chapter 3) found no strong relationships between INP concentrations and aerosol or meteorological metrics for every INP measurement temperature during CAP-2 and SOC. This is consistent with both direct measurements of ice crystal residual sizes collected in the CFDCs, as well as inferences of INP size based on measured enhancement factors following an aerosol concentrator, which both indicate Southern Ocean MBL INPs are predominantly <500 nm. However, for temperatures <-21 °C, INPs were moderately correlated with both aerosol surface area and

wind speed. A new parameterization for marine INPs was proposed, which includes wind speed in addition to activation temperature, and reduces bias compared to the existing N_s parameterization of McCluskey et al. (2018a). This parameterization captures the observed mean behavior well, but there is still significant unexplained variability in INP concentrations remaining, which will require additional measurements and modeling studies to fully capture. The multi-platform measurement approach used during CAP-2 and SOC exhibited excellent agreement in aerosol and INP concentrations observed during overpasses, and shows promise for future campaigns that may employ a similar tactic to understand vertical profiles of aerosols and INPs.

4. **What are the sources of INPs in the Southern Ocean marine boundary layer, and what are the implications for clouds?**

Vertically resolved INP observations collected during CAP-2 and SOC (Chapter 3; Moore et al. 2023) provides observational confirmation that marine INPs dominate at low altitudes over the Southern Ocean, while the influence of mineral dust increases with height. Below and in-cloud ice nucleation efficiency was found to be lower than above cloud, which is consistent with enhanced dust concentrations in single-particle measurements of aerosol composition above cloud (Twohy et al. 2021). Similarities in ice nucleation efficiency and chemical composition between particles collected in the MBL and cloud residuals indicates they are from the same, primarily oceanic, sources. As also noted by McCluskey et al. (2023), the enormous discrepancy in ice nucleation site density between marine INPs and dust means even small quantities of soil or mineral dusts can have an outsized influence on Southern Ocean low cloud properties. Additional field measurements are required to determine if this occurs seasonally or sporadically due to long-range transport under current atmospheric conditions.

Finally, Chapter 5 proposes Antarctica as a source of both biological and inorganic INPs to the Southern Ocean marine boundary layer through the emission of mineral and soil dusts from ice-free areas. Further field measurements are needed to validate this theory in additional regions around Antarctica, as well as to explore the seasonal variability. Soils collected

from the edges of Shackleton Glacier (Diaz et al. 2021; Dragone et al. 2022) exhibited warm ice activation onset temperatures and high INP concentrations, and represent a possible source of both biological INPs at warm temperatures and inorganic components at colder temperatures. Targeted sampling of warm temperature INPs, which were below the detection limit of CAP-2 aerosol samples, could be accomplished with a high-volume sampler and would help to confirm these findings. DNA source tracking analyses, such as those described in Uetake et al. (2020) for CAP-2, may also aid in source identification if additional Antarctic soil and dust samples are included. Size resolved INP measurements could assist in distinguishing between subsidence following long-range transport versus local Antarctic emissions, as was done in Gao et al. (2013) for aerosol iron. Co-located INP and aeolian dust measurements are also necessary to distinguish between inorganic and biological INP emissions, which may have different sources or seasonality, even if both are released from Antarctica. If verified, the emission of cloud-active particles from Antarctica is likely to increase in importance under a warmer climate, as ice-free areas increase in extent (Bullard et al. 2016; Meinander et al. 2022), with large implications for Southern Ocean cloud phase, radiative feedbacks, and ECS.

Bibliography

Agresti, A. and B. A. Coull, 1998: Approximate Is Better than "Exact" for Interval Estimation of Binomial Proportions. *The American Statistician*, **52 (2)**, 119, doi:10.2307/2685469, 2685469.

Alexander, S. P. and A. Protat, 2018: Cloud Properties Observed From the Surface and by Satellite at the Northern Edge of the Southern Ocean. *Journal of Geophysical Research: Atmospheres*, **123 (1)**, 443–456, doi:10.1002/2017JD026552.

Alexander, S. P. and A. Protat, 2019: Vertical Profiling of Aerosols With a Combined Raman-Elastic Backscatter Lidar in the Remote Southern Ocean Marine Boundary Layer (43–66°S, 132–150°E). *Journal of Geophysical Research: Atmospheres*, **124 (22)**, 12 107–12 125, doi:10.1029/2019JD030628.

Alpert, P. A., et al., 2022: Ice-nucleating agents in sea spray aerosol identified and quantified with a holistic multimodal freezing model. *Science Advances*, **8 (44)**, eabq6842, doi:10.1126/sciadv.abq6842.

Alroe, J., et al., 2020: Marine productivity and synoptic meteorology drive summer-time variability in Southern Ocean aerosols. *Atmospheric Chemistry and Physics*, **20 (13)**, 8047–8062, doi:10.5194/acp-20-8047-2020.

Andreae, M. O., 2007: Aerosols Before Pollution. *Science*, **315 (5808)**, 50–51, doi:10.1126/science.1136529.

Andrews, E., et al., 2019: Overview of the NOAA/ESRL Federated Aerosol Network. *Bulletin of the American Meteorological Society*, **100 (1)**, 123–135, doi:10.1175/BAMS-D-17-0175.1.

Atkins, C. B. and G. B. Dunbar, 2009: Aeolian sediment flux from sea ice into Southern McMurdo Sound, Antarctica. *Global and Planetary Change*, **69 (3)**, 133–141, doi:10.1016/j.gloplacha.2009.04.006.

Attard, E., H. Yang, A.-M. Delort, P. Amato, U. Pöschl, C. Glaux, T. Koop, and C. E. Morris, 2012: Effects of atmospheric conditions on ice nucleation activity of *Pseudomonas*. *Atmospheric Chemistry and Physics*, **12 (22)**, 10 667–10 677, doi:10.5194/acp-12-10667-2012.

Ault, A. P., et al., 2013: Size-Dependent Changes in Sea Spray Aerosol Composition and Properties with Different Seawater Conditions. *Environmental Science & Technology*, **47 (11)**, 5603–5612, doi:10.1021/es400416g.

Baker, A. R. and T. D. Jickells, 2006: Mineral particle size as a control on aerosol iron solubility. *Geophysical Research Letters*, **33 (17)**, doi:10.1029/2006GL026557.

Barry, K. R., T. C. J. Hill, C. Jentzsch, B. F. Moffett, F. Stratmann, and P. J. DeMott, 2021a: Pragmatic protocols for working cleanly when measuring ice nucleating particles. *Atmospheric Research*, **250**, 105 419, doi:10.1016/j.atmosres.2020.105419.

Barry, K. R., T. C. J. Hill, K. A. Moore, T. A. Douglas, S. M. Kreidenweis, P. J. DeMott, and J. M. Creamean, 2023a: Persistence and Potential Atmospheric Ramifications of Ice-Nucleating Particles Released from Thawing Permafrost. *Environmental Science & Technology*, **57 (9)**,

3505–3515, doi:10.1021/acs.est.2c06530.

Barry, K. R., T. C. J. Hill, M. Nieto-Caballero, T. A. Douglas, S. M. Kreidenweis, P. J. DeMott, and J. M. Creamean, 2023b: Active thermokarst regions contain rich sources of ice nucleating particles. *EGUsphere*, 1–19, doi:10.5194/egusphere-2023-1208.

Barry, K. R., et al., 2021b: Observations of Ice Nucleating Particles in the Free Troposphere From Western US Wildfires. *Journal of Geophysical Research: Atmospheres*, **126 (3)**, e2020JD033 752, doi:10.1029/2020JD033752.

Barthel, S., I. Tegen, and R. Wolke, 2019: Do new sea spray aerosol source functions improve the results of a regional aerosol model? *Atmospheric Environment*, **198**, 265–278, doi:10.1016/j.atmosenv.2018.10.016.

Bassett, G. and R. Koenker, 1978: Asymptotic Theory of Least Absolute Error Regression. *Journal of the American Statistical Association*, **73 (363)**, 618–622, doi:10.1080/01621459.1978.10480065.

Beall, C. M., et al., 2021: Cultivable halotolerant ice-nucleating bacteria and fungi in coastal precipitation. *Atmospheric Chemistry and Physics*, **21 (11)**, 9031–9045, doi:10.5194/acp-21-9031-2021.

Beall, C. M., et al., 2022: Ice-nucleating particles near two major dust source regions. *Atmospheric Chemistry and Physics*, **22 (18)**, 12 607–12 627, doi:10.5194/acp-22-12607-2022.

Bellouin, N., J. Quaas, J.-J. Morcrette, and O. Boucher, 2013: Estimates of aerosol radiative forcing from the MACC re-analysis. *Atmospheric Chemistry and Physics*, **13 (4)**, 2045–2062, doi:10.5194/acp-13-2045-2013.

Bhattachan, A., L. Wang, M. F. Miller, K. J. Licht, and P. D'Odorico, 2015: Antarctica's Dry Valleys: A potential source of soluble iron to the Southern Ocean? *Geophysical Research Letters*, **42 (6)**, 1912–1918, doi:10.1002/2015GL063419.

Bi, L., W. Lin, Z. Wang, X. Tang, X. Zhang, and B. Yi, 2018: Optical Modeling of Sea Salt Aerosols: The Effects of Nonsphericity and Inhomogeneity. *Journal of Geophysical Research: Atmospheres*, **123 (1)**, 543–558, doi:10.1002/2017JD027869.

Bigg, E., 1990: Long-term trends in ice nucleus concentrations. *Atmospheric Research*, **25 (5)**, 409–415, doi:10.1016/0169-8095(90)90025-8.

Bigg, E. K., 1973: Ice Nucleus Concentrations in Remote Areas. *Journal of the Atmospheric Sciences*, **30 (6)**, 1153–1157, doi:10.1175/1520-0469(1973)030<1153:INCIRA>2.0.CO;2.

Bintanja, R., C. Severijns, R. Haarsma, and W. Hazeleger, 2014: The future of Antarctica's surface winds simulated by a high-resolution global climate model: 2. Drivers of 21st century changes. *Journal of Geophysical Research: Atmospheres*, **119 (12)**, 7160–7178, doi:10.1002/2013JD020848.

Bjordal, J., T. Storelvmo, K. Alterskjær, and T. Carlsen, 2020: Equilibrium climate sensitivity above 5 °C plausible due to state-dependent cloud feedback. *Nature Geoscience*, **13 (11)**,

718–721, doi:10.1038/s41561-020-00649-1.

Bodas-Salcedo, A., P. G. Hill, K. Furtado, K. D. Williams, P. R. Field, J. C. Manners, P. Hyder, and S. Kato, 2016: Large Contribution of Supercooled Liquid Clouds to the Solar Radiation Budget of the Southern Ocean. *Journal of Climate*, **29 (11)**, 4213–4228, doi:10.1175/JCLI-D-15-0564.1.

Bodas-Salcedo, A., J. P. Mulcahy, T. Andrews, K. D. Williams, M. A. Ringer, P. R. Field, and G. S. Elsaesser, 2019: Strong Dependence of Atmospheric Feedbacks on Mixed-Phase Microphysics and Aerosol-Cloud Interactions in HadGEM3. *Journal of Advances in Modeling Earth Systems*, **11 (6)**, 1735–1758, doi:10.1029/2019MS001688.

Bodas-Salcedo, A., et al., 2013: Origins of the Solar Radiation Biases over the Southern Ocean in CFMIP2 Models. *Journal of Climate*, **27 (1)**, 41–56, doi:10.1175/JCLI-D-13-00169.1.

Bowie, A. R., A. T. Townsend, D. Lannuzel, T. A. Remenyi, and P. van der Merwe, 2010: Modern sampling and analytical methods for the determination of trace elements in marine particulate material using magnetic sector inductively coupled plasma–mass spectrometry. *Analytica Chimica Acta*, **676 (1)**, 15–27, doi:10.1016/j.aca.2010.07.037.

Boyd, P. W., et al., 2000: A mesoscale phytoplankton bloom in the polar Southern Ocean stimulated by iron fertilization. *Nature*, **407 (6805)**, 695–702, doi:10.1038/35037500.

Brechtel, F. J., S. M. Kreidenweis, and H. B. Swan, 1998: Air mass characteristics, aerosol particle number concentrations, and number size distributions at Macquarie Island during the First

Aerosol Characterization Experiment (ACE 1). *Journal of Geophysical Research: Atmospheres*, **103 (D13)**, 16 351–16 367, doi:10.1029/97JD03014.

Brockmann, J. E., 2011: Aerosol Transport in Sampling Lines and Inlets. *Aerosol Measurement*, John Wiley & Sons, Ltd, 68–105, doi:10.1002/9781118001684.ch6.

Bromwich, D. H., 1989: An Extraordinary Katabatic Wind Regime at Terra Nova Bay, Antarctica. *Monthly Weather Review*, **117 (3)**, 688–695, doi:10.1175/1520-0493(1989)117<0688:AEKWRA>2.0.CO;2.

Bromwich, D. H., et al., 2012: Tropospheric clouds in Antarctica. *Reviews of Geophysics*, **50 (1)**, doi:10.1029/2011RG000363.

Bullard, J. E., 2013: Contemporary glacigenic inputs to the dust cycle. *Earth Surface Processes and Landforms*, **38 (1)**, 71–89, doi:10.1002/esp.3315.

Bullard, J. E., et al., 2016: High-latitude dust in the Earth system. *Reviews of Geophysics*, **54 (2)**, 447–485, doi:10.1002/2016RG000518.

Burrows, S. M., C. Hoose, U. Pöschl, and M. G. Lawrence, 2013: Ice nuclei in marine air: Biogenic particles or dust? *Atmospheric Chemistry and Physics*, **13 (1)**, 245–267, doi:10.5194/acp-13-245-2013.

Burrows, S. M., et al., 2018: OCEANFILMS sea-spray organic aerosol emissions – Part 1: Implementation and impacts on clouds. *Atmospheric Chemistry and Physics Discussions*,

1–27, doi:10.5194/acp-2018-70.

Cappa, C. D., S. Asadi, S. Barreda, A. S. Wexler, N. M. Bouvier, and W. D. Ristenpart, 2021: Expiratory aerosol particle escape from surgical masks due to imperfect sealing. *Scientific Reports*, **11 (1)**, 12 110, doi:10.1038/s41598-021-91487-7.

Cappa, C. D., W. D. Ristenpart, S. Barreda, N. M. Bouvier, E. Levintal, A. S. Wexler, and S. A. Roman, 2022: A highly efficient cloth facemask design. *Aerosol Science and Technology*, **56 (1)**, 12–28, doi:10.1080/02786826.2021.1962795.

Carrico, C. M., P. Kus, M. J. Rood, P. K. Quinn, and T. S. Bates, 2003: Mixtures of pollution, dust, sea salt, and volcanic aerosol during ACE-Asia: Radiative properties as a function of relative humidity. *Journal of Geophysical Research: Atmospheres*, **108 (D23)**, doi:10.1029/2003JD003405.

Carslaw, K. S., H. Gordon, D. S. Hamilton, J. S. Johnson, L. A. Regayre, M. Yoshioka, and K. J. Pringle, 2017: Aerosols in the Pre-industrial Atmosphere. *Current Climate Change Reports*, **3 (1)**, 1–15, doi:10.1007/s40641-017-0061-2.

Carslaw, K. S., et al., 2013: Large contribution of natural aerosols to uncertainty in indirect forcing. *Nature*, **503 (7474)**, 67–71, doi:10.1038/nature12674.

Ceppi, P., Y.-T. Hwang, D. M. W. Frierson, and D. L. Hartmann, 2012: Southern Hemisphere jet latitude biases in CMIP5 models linked to shortwave cloud forcing. *Geophysical Research*

Letters, **39 (19)**, doi:10.1029/2012GL053115.

Ceppi, P., M. D. Zelinka, and D. L. Hartmann, 2014: The response of the Southern Hemispheric eddy-driven jet to future changes in shortwave radiation in CMIP5. *Geophysical Research Letters*, **41 (9)**, 3244–3250, doi:10.1002/2014GL060043.

Cesana, G., J. E. Kay, H. Chepfer, J. M. English, and G. de Boer, 2012: Ubiquitous low-level liquid-containing Arctic clouds: New observations and climate model constraints from CALIPSO-GOCCP. *Geophysical Research Letters*, **39 (20)**, doi:10.1029/2012GL053385.

Cesana, G. and T. Storelvmo, 2017: Improving climate projections by understanding how cloud phase affects radiation. *Journal of Geophysical Research: Atmospheres*, **122 (8)**, 4594–4599, doi:10.1002/2017JD026927.

Cesana, G. V., T. Khadir, H. Chepfer, and M. Chiriaco, 2022: Southern Ocean Solar Reflection Biases in CMIP6 Models Linked to Cloud Phase and Vertical Structure Representations. *Geophysical Research Letters*, **49 (22)**, e2022GL099 777, doi:10.1029/2022GL099777.

Chambers, S. D., et al., 2018: Characterizing Atmospheric Transport Pathways to Antarctica and the Remote Southern Ocean Using Radon-222. *Frontiers in Earth Science*, **6**, doi:10.3389/feart.2018.00190.

Chen, S., F. Qiao, W. Jiang, J. Guo, and D. Dai, 2019: Impact of Surface Waves on Wind Stress under Low to Moderate Wind Conditions. *Journal of Physical Oceanography*, **49 (8)**, 2017–2028,

doi:10.1175/JPO-D-18-0266.1.

Chen, Y. and R. L. Siefert, 2004: Seasonal and spatial distributions and dry deposition fluxes of atmospheric total and labile iron over the tropical and subtropical North Atlantic Ocean. *Journal of Geophysical Research: Atmospheres*, **109 (D9)**, doi:10.1029/2003JD003958.

Chewings, J. M., C. B. Atkins, G. B. Dunbar, and N. R. Golledge, 2014: Aeolian sediment transport and deposition in a modern high-latitude glacial marine environment. *Sedimentology*, **61 (6)**, 1535–1557, doi:10.1111/sed.12108.

Chin, W.-C., M. V. Orellana, and P. Verdugo, 1998: Spontaneous assembly of marine dissolved organic matter into polymer gels. *Nature*, **391 (6667)**, 568–572, doi:10.1038/35345.

Christiansen, S., M. E. Salter, E. Gorokhova, Q. T. Nguyen, and M. Bilde, 2019: Sea Spray Aerosol Formation: Laboratory Results on the Role of Air Entrainment, Water Temperature, and Phytoplankton Biomass. *Environmental Science & Technology*, **53 (22)**, 13 107–13 116, doi:10.1021/acs.est.9b04078.

Christner, B. C., R. Cai, C. E. Morris, K. S. McCarter, C. M. Foreman, M. L. Skidmore, S. N. Montross, and D. C. Sands, 2008: Geographic, seasonal, and precipitation chemistry influence on the abundance and activity of biological ice nucleators in rain and snow. *Proceedings of the National Academy of Sciences*, **105 (48)**, 18 854–18 859, doi:10.1073/pnas.0809816105.

Chubb, T. H., J. B. Jensen, S. T. Siems, and M. J. Manton, 2013: In situ observations of supercooled liquid clouds over the Southern Ocean during the HIAPER Pole-to-Pole Observation

campaigns. *Geophysical Research Letters*, **40 (19)**, 5280–5285, doi:10.1002/grl.50986.

Clegg, S. L., P. Brimblecombe, and A. S. Wexler, 1998: Thermodynamic Model of the System H+-NH4+-Na+-SO42--NO3--Cl--H2O at 298.15 K. *The Journal of Physical Chemistry A*, **102 (12)**, 2155–2171, doi:10.1021/jp973043j.

Clegg, S. L., P. Brimblecombe, and A. S. Wexler, 2021: E-AIM Home Page. http://www.aim.env.uea.ac.uk/aim/aim.php.

Cochran, R. E., O. S. Ryder, V. H. Grassian, and K. A. Prather, 2017: Sea Spray Aerosol: The Chemical Link between the Oceans, Atmosphere, and Climate. *Accounts of Chemical Research*, **50 (3)**, 599–604, doi:10.1021/acs.accounts.6b00603.

Corona-Núñez, R. O., F. Li, and J. E. Campo, 2020: Fires Represent an Important Source of Carbon Emissions in Mexico. *Global Biogeochemical Cycles*, **34 (12)**, e2020GB006 815, doi:10.1029/2020GB006815.

Creamean, J. M., T. C. J. Hill, P. J. DeMott, J. Uetake, S. Kreidenweis, and T. A. Douglas, 2020: Thawing permafrost: An overlooked source of seeds for Arctic cloud formation. *Environmental Research Letters*, **15 (8)**, 084 022, doi:10.1088/1748-9326/ab87d3.

Creamean, J. M., et al., 2019: Ice Nucleating Particles Carried From Below a Phytoplankton Bloom to the Arctic Atmosphere. *Geophysical Research Letters*, **46 (14)**, 8572–8581, doi:10.1029/2019GL083039.

Cutter, G., K. Casciotti, P. Croot, W. Geibert, L.-E. Heimbürger, M. Lohan, H. Planquette, and T. van de Flierdt, 2017: Sampling and Sample-handling Protocols for GEOTRACES Cruises. Version 3, August 2017. Report, GEOTRACES International Project Office. doi: 10.25607/OBP-2.

de Leeuw, G., E. L. Andreas, M. D. Anguelova, C. W. Fairall, E. R. Lewis, C. O'Dowd, M. Schulz, and S. E. Schwartz, 2011: Production flux of sea spray aerosol. *Reviews of Geophysics*, **49 (2)**, doi:10.1029/2010RG000349.

DeCarlo, P. F., J. G. Slowik, D. R. Worsnop, P. Davidovits, and J. L. Jimenez, 2004: Particle Morphology and Density Characterization by Combined Mobility and Aerodynamic Diameter Measurements. Part 1: Theory. *Aerosol Science and Technology*, **38 (12)**, 1185–1205, doi:10.1080/027868290903907.

Deike, L., B. G. Reichl, and F. Paulot, 2022: A Mechanistic Sea Spray Generation Function Based on the Sea State and the Physics of Bubble Bursting. *AGU Advances*, **3 (6)**, e2022AV000 750, doi:10.1029/2022AV000750.

Delmonte, B., et al., 2013: Modern and Holocene aeolian dust variability from Talos Dome (Northern Victoria Land) to the interior of the Antarctic ice sheet. *Quaternary Science Reviews*, **64**, 76–89, doi:10.1016/j.quascirev.2012.11.033.

DeMott, P. J., T. C. Hill, R. Marchand, and S. Alexander, 2018a: Macquarie Island Cloud and Radiation Experiment (MICRE) Ice Nucleating Particle Measurements Field Campaign Report. Tech. Rep. DOE/SC-ARM-18-030, ARM user facility, Pacific Northwest National Laboratory,

Richland, WA.

DeMott, P. J., T. C. Hill, and G. McFarquhar, 2018b: Measurements of Aerosols, Radiation, and Clouds over the Southern Ocean (MARCUS) Ice Nucleating Particle Measurements Field Campaign Report. Tech. Rep. DOE/SC-ARM-18-031, ARM user facility, Pacific Northwest National Laboratory, Richland, WA.

DeMott, P. J., et al., 2010: Predicting global atmospheric ice nuclei distributions and their impacts on climate. *Proceedings of the National Academy of Sciences*, **107 (25)**, 11 217–11 222, doi:10.1073/pnas.0910818107.

DeMott, P. J., et al., 2015: Integrating laboratory and field data to quantify the immersion freezing ice nucleation activity of mineral dust particles. *Atmospheric Chemistry and Physics*, **15 (1)**, 393–409, doi:10.5194/acp-15-393-2015.

DeMott, P. J., et al., 2016: Sea spray aerosol as a unique source of ice nucleating particles. *Proceedings of the National Academy of Sciences*, **113 (21)**, 5797–5803, doi:10.1073/pnas.1514034112.

DeMott, P. J., et al., 2017: Comparative measurements of ambient atmospheric concentrations of ice nucleating particles using multiple immersion freezing methods and a continuous flow diffusion chamber. *Atmospheric Chemistry and Physics*, **17 (18)**, 11 227–11 245, doi:10.5194/acp-17-11227-2017.

DeMott, P. J., et al., 2018c: The Fifth International Workshop on Ice Nucleation phase 2 (FIN-02): Laboratory intercomparison of ice nucleation measurements. *Atmospheric Measurement Techniques*, **11 (11)**, 6231–6257, doi:10.5194/amt-11-6231-2018.

DeMott, P. J., et al., 2023: Atmospheric Oxidation Impact on Sea Spray Produced Ice Nucleating Particles. *Environmental Science*.

Diaz, M. A., et al., 2018: Aeolian Material Transport and Its Role in Landscape Connectivity in the McMurdo Dry Valleys, Antarctica. *Journal of Geophysical Research: Earth Surface*, **123 (12)**, 3323–3337, doi:10.1029/2017JF004589.

Diaz, M. A., et al., 2021: Geochemical zones and environmental gradients for soils from the central Transantarctic Mountains, Antarctica. *Biogeosciences*, **18 (5)**, 1629–1644, doi:10.5194/bg-18-1629-2021.

Dragone, N. B., et al., 2022: Elevational Constraints on the Composition and Genomic Attributes of Microbial Communities in Antarctic Soils. *mSystems*, **7 (1)**, e01 330–21, doi:10.1128/msystems.01330-21.

Fall, R. and R. Schnell, 1985: Association of an ice-nucleating pseudomonad with cultures of the marine dinoflagellate, Heterocapsa niei. *Journal of Marine Research*, **43 (1)**.

Fernald, F. G., 1984: Analysis of atmospheric lidar observations: Some comments. *Applied Optics*, **23 (5)**, 652–653, doi:10.1364/AO.23.000652.

Forestieri, S. D., K. A. Moore, R. M. Borrero, A. Wang, M. D. Stokes, and C. D. Cappa, 2018: Temperature and Composition Dependence of Sea Spray Aerosol Production. *Geophysical Research Letters*, **45 (14)**, 7218–7225, doi:10.1029/2018GL078193.

Forster, P., et al., 2021: The Earth's energy budget, climate feedbacks, and climate sensitivity. *Climate Change 2021: The Physical Science Basis. Contribution of Working Group I to the Sixth Assessment Report of the Intergovernmental Panel on Climate Change*, V. Masson-Delmotte, P. Zhai, A. Pirani, S. L. Connors, C. Péan, S. Berger, N. Caud, Y. Chen, L. Goldfarb, M. I. Gomis, M. Huang, K. Leitzell, E. Lonnoy, J. B. R. Matthews, T. K. Maycock, T. Waterfield, Ö. Yelekçi, R. Yu, and B. Zhou, Eds., Cambridge University Press, Cambridge, United Kingdom and New York, NY, USA, 923–1054, doi:10.1017/9781009157896.001.

Fossum, K. N., et al., 2018: Summertime Primary and Secondary Contributions to Southern Ocean Cloud Condensation Nuclei. *Scientific Reports*, **8 (1)**, 13 844, doi:10.1038/s41598-018-32047-4.

Frey, W. R. and J. E. Kay, 2017: The influence of extratropical cloud phase and amount feedbacks on climate sensitivity. *Climate Dynamics*, **50 (7)**, 3097–3116, doi:10.1007/s00382-017-3796-5.

Fröhlich-Nowoisky, J., T. C. J. Hill, B. G. Pummer, P. Yordanova, G. D. Franc, and U. Pöschl, 2015: Ice nucleation activity in the widespread soil fungus *Mortierella alpina*. *Biogeosciences*, **12 (4)**, 1057–1071, doi:10.5194/bg-12-1057-2015.

Fuentes, E., H. Coe, D. Green, G. de Leeuw, and G. McFiggans, 2010: On the impacts of phytoplankton-derived organic matter on the properties of the primary marine aerosol

– Part 1: Source fluxes. *Atmospheric Chemistry and Physics*, **10 (19)**, 9295–9317, doi: 10.5194/acp-10-9295-2010.

Gantt, B., N. Meskhidze, M. C. Facchini, M. Rinaldi, D. Ceburnis, and C. D. O'Dowd, 2011: Wind speed dependent size-resolved parameterization for the organic mass fraction of sea spray aerosol. *Atmospheric Chemistry and Physics*, **11 (16)**, 8777–8790, doi: 10.5194/acp-11-8777-2011.

Gao, Y., G. Xu, J. Zhan, J. Zhang, W. Li, Q. Lin, L. Chen, and H. Lin, 2013: Spatial and particle size distributions of atmospheric dissolvable iron in aerosols and its input to the Southern Ocean and coastal East Antarctica. *Journal of Geophysical Research: Atmospheres*, **118 (22)**, 12,634–12,648, doi:10.1002/2013JD020367.

Garcia, E., T. C. J. Hill, A. J. Prenni, P. J. DeMott, G. D. Franc, and S. M. Kreidenweis, 2012: Biogenic ice nuclei in boundary layer air over two U.S. High Plains agricultural regions. *Journal of Geophysical Research: Atmospheres*, **117 (D18)**, doi:10.1029/2012JD018343.

Gettelman, A., et al., 2019: The Whole Atmosphere Community Climate Model Version 6 (WACCM6). *Journal of Geophysical Research: Atmospheres*, **124 (23)**, 12 380–12 403, doi: 10.1029/2019JD030943.

Gettelman, A., et al., 2020: Simulating Observations of Southern Ocean Clouds and Implications for Climate. *Journal of Geophysical Research: Atmospheres*, **125 (21)**, e2020JD032 619, doi:10.1029/2020JD032619.

Ginoux, P., J. M. Prospero, T. E. Gill, N. C. Hsu, and M. Zhao, 2012: Global-scale attribution of anthropogenic and natural dust sources and their emission rates based on MODIS Deep Blue aerosol products. *Reviews of Geophysics*, **50 (3)**, doi:10.1029/2012RG000388.

Gong, S. L., 2003: A parameterization of sea-salt aerosol source function for sub- and super-micron particles. *Global Biogeochemical Cycles*, **17 (4)**, doi:10.1029/2003GB002079.

Gong, X., et al., 2020: Characterization of aerosol particles at Cabo Verde close to sea level and at the cloud level – Part 2: Ice-nucleating particles in air, cloud and seawater. *Atmospheric Chemistry and Physics*, **20 (3)**, 1451–1468, doi:10.5194/acp-20-1451-2020.

Gryspeerdt, E., A. C. Povey, R. G. Grainger, O. Hasekamp, N. C. Hsu, J. P. Mulcahy, A. M. Sayer, and A. Sorooshian, 2023: Uncertainty in aerosol–cloud radiative forcing is driven by clean conditions. *Atmospheric Chemistry and Physics*, **23 (7)**, 4115–4122, doi:10.5194/acp-23-4115-2023.

Grythe, H., J. Ström, R. Krejci, P. Quinn, and A. Stohl, 2014: A review of sea-spray aerosol source functions using a large global set of sea salt aerosol concentration measurements. *Atmospheric Chemistry and Physics*, **14 (3)**, 1277–1297, doi:10.5194/acp-14-1277-2014.

Hamilton, D. S., L. A. Lee, K. J. Pringle, C. L. Reddington, D. V. Spracklen, and K. S. Carslaw, 2014: Occurrence of pristine aerosol environments on a polluted planet. *Proceedings of the National Academy of Sciences*, **111 (52)**, 18 466–18 471, doi:10.1073/pnas.1415440111.

Hartery, S., D. Toohey, L. Revell, K. Sellegri, P. Kuma, M. Harvey, and A. J. McDonald, 2020: Constraining the Surface Flux of Sea Spray Particles From the Southern Ocean. *Journal of*

Geophysical Research: Atmospheres, **125 (4)**, e2019JD032 026, doi:10.1029/2019JD032026.

Hartmann, M., et al., 2020: Wintertime Airborne Measurements of Ice Nucleating Particles in the High Arctic: A Hint to a Marine, Biogenic Source for Ice Nucleating Particles. *Geophysical Research Letters*, **47 (13)**, e2020GL087 770, doi:10.1029/2020GL087770.

Hartmann, M., et al., 2021: Terrestrial or marine – indications towards the origin of ice-nucleating particles during melt season in the European Arctic up to 83.7° N. *Atmospheric Chemistry and Physics*, **21 (15)**, 11 613–11 636, doi:10.5194/acp-21-11613-2021.

Heinze, C., et al., 2019: ESD Reviews: Climate feedbacks in the Earth system and prospects for their evaluation. *Earth System Dynamics*, **10 (3)**, 379–452, doi:10.5194/esd-10-379-2019.

Hill, T. C. J., P. J. DeMott, Y. Tobo, J. Fröhlich-Nowoisky, B. F. Moffett, G. D. Franc, and S. M. Kreidenweis, 2016: Sources of organic ice nucleating particles in soils. *Atmospheric Chemistry and Physics*, **16 (11)**, 7195–7211, doi:10.5194/acp-16-7195-2016.

Hill, T. C. J., et al., 2023: Resolving the controls over the production and emission of ice-nucleating particles in sea spray. *Environmental Science: Atmospheres*, **3 (6)**, 970–990, doi:10.1039/D2EA00154C.

Hiranuma, N., et al., 2015: A comprehensive laboratory study on the immersion freezing behavior of illite NX particles: A comparison of 17 ice nucleation measurement techniques. *Atmospheric Chemistry and Physics*, **15 (5)**, 2489–2518, doi:10.5194/acp-15-2489-2015.

Hoose, C. and O. Möhler, 2012: Heterogeneous ice nucleation on atmospheric aerosols: A review of results from laboratory experiments. *Atmospheric Chemistry and Physics*, **12 (20)**, 9817–9854, doi:10.5194/acp-12-9817-2012.

Hsu, S. A., E. A. Meindl, and D. B. Gilhousen, 1994: Determining the Power-Law Wind-Profile Exponent under Near-Neutral Stability Conditions at Sea. *Journal of Applied Meteorology and Climatology*, **33 (6)**, 757–765, doi:10.1175/1520-0450(1994)033<0757:DTPLWP>2.0.CO;2.

Huang, W. T. K., L. Ickes, I. Tegen, M. Rinaldi, D. Ceburnis, and U. Lohmann, 2018: Global relevance of marine organic aerosol as ice nucleating particles. *Atmospheric Chemistry and Physics*, **18 (15)**, 11 423–11 445, doi:10.5194/acp-18-11423-2018.

Huang, Y., S. T. Siems, M. J. Manton, A. Protat, and J. Delanoë, 2012: A study on the low-altitude clouds over the Southern Ocean using the DARDAR-MASK. *Journal of Geophysical Research: Atmospheres*, **117 (D18)**, doi:10.1029/2012JD017800.

Humphries, R. S., A. R. Klekociuk, R. Schofield, M. Keywood, J. Ward, and S. R. Wilson, 2016: Unexpectedly high ultrafine aerosol concentrations above East Antarctic sea ice. *Atmospheric Chemistry and Physics*, **16 (4)**, 2185–2206, doi:10.5194/acp-16-2185-2016.

Humphries, R. S., I. M. McRobert, W. A. Ponsonby, J. P. Ward, M. D. Keywood, Z. M. Loh, P. B. Krummel, and J. Harnwell, 2019: Identification of platform exhaust on the RV *Investigator*. *Atmospheric Measurement Techniques*, **12 (6)**, 3019–3038, doi:10.5194/amt-12-3019-2019.

Humphries, R. S., et al., 2015: Boundary layer new particle formation over East Antarctic sea ice – possible Hg-driven nucleation? *Atmospheric Chemistry and Physics*, **15 (23)**, 13 339–13 364, doi:10.5194/acp-15-13339-2015.

Humphries, R. S., et al., 2021: Southern Ocean latitudinal gradients of Cloud Condensation Nuclei. *Atmospheric Chemistry and Physics Discussions*, 1–35, doi:10.5194/acp-2020-1246.

Huneeus, N., et al., 2011: Global dust model intercomparison in AeroCom phase I. *Atmospheric Chemistry and Physics*, **11 (15)**, 7781–7816, doi:10.5194/acp-11-7781-2011.

Hwang, Y.-T. and D. M. W. Frierson, 2013: Link between the double-Intertropical Convergence Zone problem and cloud biases over the Southern Ocean. *Proceedings of the National Academy of Sciences*, **110 (13)**, 4935–4940, doi:10.1073/pnas.1213302110.

Ickes, L., et al., 2020: The ice-nucleating activity of Arctic sea surface microlayer samples and marine algal cultures. *Atmospheric Chemistry and Physics*, **20 (18)**, 11 089–11 117, doi:10.5194/acp-20-11089-2020.

Irish, V. E., et al., 2017: Ice-nucleating particles in Canadian Arctic sea-surface microlayer and bulk seawater. *Atmospheric Chemistry and Physics*, **17 (17)**, 10 583–10 595, doi:10.5194/acp-17-10583-2017.

Irish, V. E., et al., 2019: Ice nucleating particles in the marine boundary layer in the Canadian Arctic during summer 2014. *Atmospheric Chemistry and Physics*, **19 (2)**, 1027–1039, doi:

10.5194/acp-19-1027-2019.

Jaeglé, L., P. K. Quinn, T. S. Bates, B. Alexander, and J.-T. Lin, 2011: Global distribution of sea salt aerosols: New constraints from in situ and remote sensing observations. *Atmospheric Chemistry and Physics*, **11 (7)**, 3137–3157, doi:10.5194/acp-11-3137-2011.

Järvinen, E., et al., 2022: Evidence for Secondary Ice Production in Southern Ocean Maritime Boundary Layer Clouds. *Journal of Geophysical Research: Atmospheres*, **127 (16)**, e2021JD036 411, doi:10.1029/2021JD036411.

Jensen, J. B., S. P. Beaton, J. L. Stith, K. Schwenz, M. Colón-Robles, R. M. Rauber, and J. Gras, 2020: The Giant Nucleus Impactor (GNI)—A System for the Impaction and Automated Optical Sizing of Giant Aerosol Particles with Emphasis on Sea Salt. Part I: Basic Instrument and Algorithms. *Journal of Atmospheric and Oceanic Technology*, **37 (9)**, 1551–1569, doi:10.1175/JTECH-D-19-0109.1.

Johnson, J. S., et al., 2020: Robust observational constraint of uncertain aerosol processes and emissions in a climate model and the effect on aerosol radiative forcing. *Atmospheric Chemistry and Physics*, **20 (15)**, 9491–9524, doi:10.5194/acp-20-9491-2020.

Jokinen, T., et al., 2018: Ion-induced sulfuric acid–ammonia nucleation drives particle formation in coastal Antarctica. *Science Advances*, **4 (11)**, eaat9744, doi:10.1126/sciadv.aat9744.

Jung, J., et al., 2020: Characteristics of methanesulfonic acid, non-sea-salt sulfate and organic carbon aerosols over the Amundsen Sea, Antarctica. *Atmospheric Chemistry and Physics*,

20 (9), 5405–5424, doi:10.5194/acp-20-5405-2020.

Junge, K. and B. D. Swanson, 2008: High-resolution ice nucleation spectra of sea-ice bacteria: Implications for cloud formation and life in frozen environments. *Biogeosciences*, **5 (3)**, 865–873, doi:10.5194/bg-5-865-2008.

Kaluarachchi, C. P., et al., 2022a: Effects of Atmospheric Aging Processes on Nascent Sea Spray Aerosol Physicochemical Properties. *ACS Earth and Space Chemistry*, **6 (11)**, 2732–2744, doi:10.1021/acsearthspacechem.2c00258.

Kaluarachchi, C. P., et al., 2022b: Size-Dependent Morphology, Composition, Phase State, and Water Uptake of Nascent Submicrometer Sea Spray Aerosols during a Phytoplankton Bloom. *ACS Earth and Space Chemistry*, **6 (1)**, 116–130, doi:10.1021/acsearthspacechem.1c00306.

Kanji, Z. A., L. A. Ladino, H. Wex, Y. Boose, M. Burkert-Kohn, D. J. Cziczo, and M. Krämer, 2017: Overview of Ice Nucleating Particles. *Meteorological Monographs*, **58**, 1.1–1.33, doi:10.1175/AMSMONOGRAPHS-D-16-0006.1.

Kavan, J., P. Dagsson-Waldhauserova, J. B. Renard, K. Láska, and K. Ambrožová, 2018: Aerosol Concentrations in Relationship to Local Atmospheric Conditions on James Ross Island, Antarctica. *Frontiers in Earth Science*, **6**, doi:10.3389/feart.2018.00207.

Kawana, K., F. Taketani, K. Matsumoto, T. Miyakawa, Y. Tobo, Y. Iwamoto, A. Ito, and Y. Kanaya, 2023: Roles of marine biota in the formation of atmospheric bioaerosols, cloud condensation nuclei, and ice-nucleating particles over the North Pacific Ocean, Bering Sea, and Arctic

Ocean. *Atmospheric Chemistry and Physics Discussions*, 1–42, doi:10.5194/acp-2023-39.

Kay, J. E., L. Bourdages, N. B. Miller, A. Morrison, V. Yettella, H. Chepfer, and B. Eaton, 2016a: Evaluating and improving cloud phase in the Community Atmosphere Model version 5 using spaceborne lidar observations. *Journal of Geophysical Research: Atmospheres*, **121 (8)**, 4162–4176, doi:10.1002/2015JD024699.

Kay, J. E., C. Wall, V. Yettella, B. Medeiros, C. Hannay, P. Caldwell, and C. Bitz, 2016b: Global Climate Impacts of Fixing the Southern Ocean Shortwave Radiation Bias in the Community Earth System Model (CESM). *Journal of Climate*, **29 (12)**, 4617–4636, doi: 10.1175/JCLI-D-15-0358.1.

Kiehl, J. T., 2007: Twentieth century climate model response and climate sensitivity. *Geophysical Research Letters*, **34 (22)**, doi:10.1029/2007GL031383.

Kim, I., G. Kim, and E. J. Choy, 2015: The significant inputs of trace elements and rare earth elements from melting glaciers in Antarctic coastal waters. *Polar Research*, doi: 10.3402/polar.v34.24289.

Knopf, D. A., P. A. Alpert, B. Wang, and J. Y. Aller, 2011: Stimulation of ice nucleation by marine diatoms. *Nature Geoscience*, **4 (2)**, 88–90, doi:10.1038/ngeo1037.

Kok, J. F., E. J. R. Parteli, T. I. Michaels, and D. B. Karam, 2012: The physics of wind-blown sand and dust. *Reports on Progress in Physics*, **75 (10)**, 106 901, doi:

10.1088/0034-4885/75/10/106901.

Kok, J. F., T. Storelvmo, V. A. Karydis, A. A. Adebiyi, N. M. Mahowald, A. T. Evan, C. He, and D. M. Leung, 2023: Mineral dust aerosol impacts on global climate and climate change. *Nature Reviews Earth & Environment*, **4 (2)**, 71–86, doi:10.1038/s43017-022-00379-5.

Korolev, A., et al., 2017: Mixed-Phase Clouds: Progress and Challenges. *Meteorological Monographs*, **58 (1)**, 5.1–5.50, doi:10.1175/AMSMONOGRAPHS-D-17-0001.1.

Kreidenweis, S. M., L. M. McInnes, and F. J. Brechtel, 1998: Observations of aerosol volatility and elemental composition at Macquarie Island during the First Aerosol Characterization Experiment (ACE 1). *Journal of Geophysical Research: Atmospheres*, **103 (D13)**, 16 511–16 524, doi:10.1029/98JD00800.

Kremser, S., et al., 2021: Southern Ocean cloud and aerosol data: A compilation of measurements from the 2018 Southern Ocean Ross Sea Marine Ecosystems and Environment voyage. *Earth System Science Data*, **13 (7)**, 3115–3153, doi:10.5194/essd-13-3115-2021.

Krishnamoorthy, K. and M. Lee, 2012: New approximate confidence intervals for the difference between two Poisson means and comparison. *Journal of Statistical Computation and Simulation*, **83 (12)**, 2232–2243, doi:10.1080/00949655.2012.686616.

Kupc, A., C. Williamson, N. L. Wagner, M. Richardson, and C. A. Brock, 2018: Modification, calibration, and performance of the Ultra-High Sensitivity Aerosol Spectrometer for particle size distribution and volatility measurements during the Atmospheric Tomography Mission

(ATom) airborne campaign. *Atmospheric Measurement Techniques*, **11 (1)**, 369–383, doi: 10.5194/amt-11-369-2018.

Ladino, L. A., et al., 2016: Addressing the ice nucleating abilities of marine aerosol: A combination of deposition mode laboratory and field measurements. *Atmospheric Environment*, **132**, 1–10, doi:10.1016/j.atmosenv.2016.02.028.

Lamont-Smith, T. and T. Waseda, 2008: Wind Wave Growth at Short Fetch. *Journal of Physical Oceanography*, **38 (7)**, 1597–1606, doi:10.1175/2007JPO3712.1.

Lance, S., C. A. Brock, D. Rogers, and J. A. Gordon, 2010: Water droplet calibration of the Cloud Droplet Probe (CDP) and in-flight performance in liquid, ice and mixed-phase clouds during ARCPAC. *Atmospheric Measurement Techniques*, **3 (6)**, 1683–1706, doi: 10.5194/amt-3-1683-2010.

Lannuzel, D., M. Vancoppenolle, P. van der Merwe, J. de Jong, K. Meiners, M. Grotti, J. Nishioka, and V. Schoemann, 2016: Iron in sea ice: Review and new insights. *Elementa: Science of the Anthropocene*, **4**, 000 130, doi:10.12952/journal.elementa.000130.

Lapere, R., et al., 2023: The Representation of Sea Salt Aerosols and Their Role in Polar Climate Within CMIP6. *Journal of Geophysical Research: Atmospheres*, **128 (6)**, e2022JD038 235, doi:10.1029/2022JD038235.

Lee, H. D., K. K. Ray, and A. V. Tivanski, 2017: Solid, Semisolid, and Liquid Phase States of Individual Submicrometer Particles Directly Probed Using Atomic Force Microscopy. *Analytical*

Chemistry, **89 (23)**, 12 720–12 726, doi:10.1021/acs.analchem.7b02755.

Lee, H. D., et al., 2020: Organic Enrichment, Physical Phase State, and Surface Tension Depression of Nascent Core–Shell Sea Spray Aerosols during Two Phytoplankton Blooms. *ACS Earth and Space Chemistry*, **4 (4)**, 650–660, doi:10.1021/acsearthspacechem.0c00032.

Lewis, E. R. and S. E. Schwartz, 2004: *Sea Salt Aerosol Production: Mechanisms, Methods, Measurements and Models—A Critical Review*, Geophysical Monograph, Vol. 152. American Geophysical Union, Washington, DC.

Li, F., P. Ginoux, and V. Ramaswamy, 2008: Distribution, transport, and deposition of mineral dust in the Southern Ocean and Antarctica: Contribution of major sources. *Journal of Geophysical Research: Atmospheres*, **113 (D10)**, doi:10.1029/2007JD009190.

Li, G., J. Wieder, J. T. Pasquier, J. Henneberger, and Z. A. Kanji, 2022: Predicting atmospheric background number concentration of ice-nucleating particles in the Arctic. *Atmospheric Chemistry and Physics*, **22 (21)**, 14 441–14 454, doi:10.5194/acp-22-14441-2022.

Lin, Y., et al., 2022: Modeling impacts of ice-nucleating particles from marine aerosols on mixed-phase orographic clouds during 2015 ACAPEX field campaign. *Atmospheric Chemistry and Physics*, **22 (10)**, 6749–6771, doi:10.5194/acp-22-6749-2022.

Liu, M., H. Matsui, D. S. Hamilton, K. D. Lamb, S. D. Rathod, J. P. Schwarz, and N. M. Mahowald, 2022: The underappreciated role of anthropogenic sources in atmospheric soluble

iron flux to the Southern Ocean. *npj Climate and Atmospheric Science*, **5 (1)**, 1–9, doi: 10.1038/s41612-022-00250-w.

Liu, S., et al., 2021: Sea spray aerosol concentration modulated by sea surface temperature. *Proceedings of the National Academy of Sciences*, **118 (9)**, doi:10.1073/pnas.2020583118.

Liu, X., P.-L. Ma, H. Wang, S. Tilmes, B. Singh, R. C. Easter, S. J. Ghan, and P. J. Rasch, 2016: Description and evaluation of a new four-mode version of the Modal Aerosol Module (MAM4) within version 5.3 of the Community Atmosphere Model. *Geoscientific Model Development*, **9 (2)**, 505–522, doi:10.5194/gmd-9-505-2016.

Mace, G. G., Q. Zhang, M. Vaughan, R. Marchand, G. Stephens, C. Trepte, and D. Winker, 2009: A description of hydrometeor layer occurrence statistics derived from the first year of merged Cloudsat and CALIPSO data. *Journal of Geophysical Research: Atmospheres*, **114 (D8)**, doi:10.1029/2007JD009755.

Mace, G. G., et al., 2020: Southern Ocean Cloud Properties Derived from CAPRICORN and MARCUS Data. *Journal of Geophysical Research: Atmospheres*, e2020JD033368, doi: 10.1029/2020JD033368.

Madawala, C. K., H. D. Lee, C. P. Kaluarachchi, and A. V. Tivanski, 2021: Probing the Water Uptake and Phase State of Individual Sucrose Nanoparticles Using Atomic Force Microscopy. *ACS Earth and Space Chemistry*, **5 (10)**, 2612–2620, doi:10.1021/acsearthspacechem.1c00101.

Mamouri, R.-E. and A. Ansmann, 2015: Estimated desert-dust ice nuclei profiles from polarization lidar: Methodology and case studies. *Atmospheric Chemistry and Physics*, **15 (6)**, 3463–3477, doi:10.5194/acp-15-3463-2015.

Mamouri, R.-E. and A. Ansmann, 2016: Potential of polarization lidar to provide profiles of CCN- and INP-relevant aerosol parameters. *Atmospheric Chemistry and Physics*, **16 (9)**, 5905–5931, doi:10.5194/acp-16-5905-2016.

Marchand, R., 2020: Macquarie Island Cloud and Radiation Experiment (MICRE) Final Report. White Paper.

Maring, H., D. L. Savoie, M. A. Izaguirre, L. Custals, and J. S. Reid, 2003: Mineral dust aerosol size distribution change during atmospheric transport. *Journal of Geophysical Research: Atmospheres*, **108 (D19)**, doi:10.1029/2002JD002536.

Mårtensson, E. M., E. D. Nilsson, G. de Leeuw, L. H. Cohen, and H.-C. Hansson, 2003: Laboratory simulations and parameterization of the primary marine aerosol production. *Journal of Geophysical Research: Atmospheres*, **108 (D9)**, doi:10.1029/2002JD002263.

Mason, R. H., et al., 2016: Size-resolved measurements of ice-nucleating particles at six locations in North America and one in Europe. *Atmospheric Chemistry and Physics*, **16 (3)**, 1637–1651, doi:10.5194/acp-16-1637-2016.

May, N. W., J. L. Axson, A. Watson, K. A. Pratt, and A. P. Ault, 2016: Lake spray aerosol generation: A method for producing representative particles from freshwater wave breaking. *Atmospheric*

Measurement Techniques, **9 (9)**, 4311–4325, doi:10.5194/amt-9-4311-2016.

Mayer, K. J., X. Wang, M. V. Santander, B. A. Mitts, J. S. Sauer, C. M. Sultana, C. D. Cappa, and K. A. Prather, 2020: Secondary Marine Aerosol Plays a Dominant Role over Primary Sea Spray Aerosol in Cloud Formation. *ACS Central Science*, **6 (12)**, 2259–2266, doi:10.1021/acscentsci.0c00793.

McCluskey, C. S., P. J. DeMott, P.-L. Ma, and S. M. Burrows, 2019: Numerical Representations of Marine Ice-Nucleating Particles in Remote Marine Environments Evaluated Against Observations. *Geophysical Research Letters*, **46 (13)**, 7838–7847, doi:10.1029/2018GL081861.

McCluskey, C. S., et al., 2014: Characteristics of atmospheric ice nucleating particles associated with biomass burning in the US: Prescribed burns and wildfires. *Journal of Geophysical Research: Atmospheres*, **119 (17)**, 10 458–10 470, doi:10.1002/2014JD021980.

McCluskey, C. S., et al., 2018a: Marine and Terrestrial Organic Ice-Nucleating Particles in Pristine Marine to Continentally Influenced Northeast Atlantic Air Masses. *Journal of Geophysical Research: Atmospheres*, **123 (11)**, 6196–6212, doi:10.1029/2017JD028033.

McCluskey, C. S., et al., 2018b: A Mesocosm Double Feature: Insights into the Chemical Makeup of Marine Ice Nucleating Particles. *Journal of the Atmospheric Sciences*, **75 (7)**, 2405–2423, doi:10.1175/JAS-D-17-0155.1.

McCluskey, C. S., et al., 2018c: Observations of Ice Nucleating Particles Over Southern Ocean Waters. *Geophysical Research Letters*, **45 (21)**, 11,989–11,997, doi:10.1029/2018GL079981.

McCluskey, C. S., et al., 2023: Simulating Southern Ocean Aerosol and Ice Nucleating Particles in the Community Earth System Model Version 2. *Journal of Geophysical Research: Atmospheres*, **n/a (n/a)**, e2022JD036 955, doi:10.1029/2022JD036955.

McCoy, D. T., S. M. Burrows, R. Wood, D. P. Grosvenor, S. M. Elliott, P.-L. Ma, P. J. Rasch, and D. L. Hartmann, 2015a: Natural aerosols explain seasonal and spatial patterns of Southern Ocean cloud albedo. *Science Advances*, **1 (6)**, doi:10.1126/sciadv.1500157.

McCoy, D. T., D. L. Hartmann, M. D. Zelinka, P. Ceppi, and D. P. Grosvenor, 2015b: Mixed-phase cloud physics and Southern Ocean cloud feedback in climate models. *Journal of Geophysical Research: Atmospheres*, **120 (18)**, 9539–9554, doi:10.1002/2015JD023603.

McCoy, D. T., I. Tan, D. L. Hartmann, M. D. Zelinka, and T. Storelvmo, 2016: On the relationships among cloud cover, mixed-phase partitioning, and planetary albedo in GCMs. *Journal of Advances in Modeling Earth Systems*, **8 (2)**, 650–668, doi:10.1002/2015MS000589.

McFarquhar, G. M., et al., 2021: Observations of Clouds, Aerosols, Precipitation, and Surface Radiation over the Southern Ocean: An Overview of CAPRICORN, MARCUS, MICRE, and SOCRATES. *Bulletin of the American Meteorological Society*, **102 (4)**, E894–E928, doi:10.1175/BAMS-D-20-0132.1.

Mckenna Neuman, C., 2003: Effects of Temperature and Humidity upon the Entrainment of Sedimentary Particles by Wind. *Boundary-Layer Meteorology*, **108 (1)**, 61–89, doi: 10.1023/A:1023035201953.

McLennan, S. M., 2001: Relationships between the trace element composition of sedimentary rocks and upper continental crust. *Geochemistry, Geophysics, Geosystems*, **2 (4)**, doi:10.1029/2000GC000109.

Meinander, O., et al., 2022: Newly identified climatically and environmentally significant high-latitude dust sources. *Atmospheric Chemistry and Physics*, **22 (17)**, 11 889–11 930, doi:10.5194/acp-22-11889-2022.

Meskhidze, N., et al., 2013: Production mechanisms, number concentration, size distribution, chemical composition, and optical properties of sea spray aerosols. *Atmospheric Science Letters*, **14 (4)**, 207–213, doi:10.1002/asl2.441.

Mitts, B. A., X. Wang, D. D. Lucero, C. M. Beall, G. B. Deane, P. J. DeMott, and K. A. Prather, 2021: Importance of Supermicron Ice Nucleating Particles in Nascent Sea Spray. *Geophysical Research Letters*, **48 (3)**, e2020GL089 633, doi:10.1029/2020GL089633.

Miyakawa, T., F. Taketani, Y. Tobo, K. Matsumoto, M. Yoshizue, M. Takigawa, and Y. Kanaya, 2023: Measurements of Aerosol Particle Size Distributions and INPs Over the Southern Ocean in the Late Austral Summer of 2017 on Board the R/V Mirai: Importance of the Marine Boundary Layer Structure. *Earth and Space Science*, **10 (3)**, e2022EA002 736, doi: 10.1029/2022EA002736.

Modini, R. L., et al., 2015: Primary marine aerosol-cloud interactions off the coast of California. *Journal of Geophysical Research: Atmospheres*, **120 (9)**, 4282–4303, doi: 10.1002/2014JD022963.

Monahan, E. C. and I. Muircheartaigh, 1980: Optimal Power-Law Description of Oceanic Whitecap Coverage Dependence on Wind Speed. *Journal of Physical Oceanography*, **10 (12)**, 2094–2099, doi:10.1175/1520-0485(1980)010<2094:OPLDOO>2.0.CO;2.

Monahan, E. C., D. E. Spiel, and K. L. Davidson, 1986: A Model of Marine Aerosol Generation Via Whitecaps and Wave Disruption. *Oceanic Whitecaps: And Their Role in Air-Sea Exchange Processes*, E. C. Monahan and G. M. Niocaill, Eds., Springer Netherlands, Dordrecht, Oceanographic Sciences Library, 167–174, doi:10.1007/978-94-009-4668-2_16.

Moore, K. A., 2020: Constraining marine ice nucleating particle parameterizations in atmospheric models using observations from the Southern Ocean. MS Thesis, Colorado State University, https://mountainscholar.org/handle/10217/208435.

Moore, K. A., et al., 2022: Estimation of Sea Spray Aerosol Surface Area Over the Southern Ocean Using Scattering Measurements. *Journal of Geophysical Research: Atmospheres*, **127 (22)**, e2022JD037 009, doi:10.1029/2022JD037009.

Moore, K. A., et al., 2023: Characterizing Ice Nucleating Particles over the Southern Ocean using Simultaneous Aircraft and Ship Observations. *ESS Open Archive*, doi: 10.22541/essoar.168889890.00880378/v1.

Moore, R. H., et al., 2021: Sizing response of the Ultra-High Sensitivity Aerosol Spectrometer (UHSAS) and Laser Aerosol Spectrometer (LAS) to changes in submicron aerosol composition and refractive index. *Atmospheric Measurement Techniques*, **14 (6)**, 4517–4542, doi:10.5194/amt-14-4517-2021.

Morrison, A. E., S. T. Siems, and M. J. Manton, 2011: A Three-Year Climatology of Cloud-Top Phase over the Southern Ocean and North Pacific. *Journal of Climate*, **24 (9)**, 2405–2418, doi:10.1175/2010JCLI3842.1.

Morton, P. L., et al., 2013: Methods for the sampling and analysis of marine aerosols: Results from the 2008 GEOTRACES aerosol intercalibration experiment. *Limnology and Oceanography: Methods*, **11 (2)**, 62–78, doi:10.4319/lom.2013.11.62.

Mulcahy, J. P., C. D. O'Dowd, and S. G. Jennings, 2009: Aerosol optical depth in clean marine and continental northeast Atlantic air. *Journal of Geophysical Research*, **114 (D20)**, D20 204, doi:10.1029/2009JD011992.

Murphy, D. M. and T. Koop, 2005: Review of the vapour pressures of ice and supercooled water for atmospheric applications. *Quarterly Journal of the Royal Meteorological Society*, **131 (608)**, 1539–1565, doi:10.1256/qj.04.94.

Naik, V., et al., 2021: Short-lived climate forcers. *Climate Change 2021: The Physical Science Basis. Contribution of Working Group I to the Sixth Assessment Report of the Intergovernmental Panel on Climate Change*, V. Masson-Delmotte, P. Zhai, A. Pirani, S. L. Connors, C. Péan, S. Berger, N. Caud, Y. Chen, L. Goldfarb, M. I. Gomis, M. Huang, K. Leitzell, E. Lonnoy, J. B. R. Matthews, T. K. Maycock, T. Waterfield, Ö. Yelekçi, R. Yu, and B. Zhou, Eds.,

Cambridge University Press, Cambridge, United Kingdom and New York, NY, USA, 817–922, doi:10.1017/9781009157896.001.

NASA, 22: NASA - Cloud-Aerosol Lidar and Infrared Pathfinder Satellite Observations. David Winker, https://www-calipso.larc.nasa.gov/resources/calipso_users_guide/essential_reading/index.php.

Naud, C. M., J. F. Booth, and A. D. D. Genio, 2014: Evaluation of ERA-Interim and MERRA Cloudiness in the Southern Ocean. *Journal of Climate*, **27 (5)**, 2109–2124, doi: 10.1175/JCLI-D-13-00432.1.

Neff, P. D. and N. A. N. Bertler, 2015: Trajectory modeling of modern dust transport to the Southern Ocean and Antarctica. *Journal of Geophysical Research: Atmospheres*, **120 (18)**, 9303–9322, doi:10.1002/2015JD023304.

Niemand, M., et al., 2012: A Particle-Surface-Area-Based Parameterization of Immersion Freezing on Desert Dust Particles. *Journal of the Atmospheric Sciences*, **69 (10)**, 3077–3092, doi:10.1175/JAS-D-11-0249.1.

Nilsson, E. D., K. A. H. Hultin, E. M. Mårtensson, P. Markuszewski, K. Rosman, and R. Krejci, 2021: Baltic Sea Spray Emissions: In Situ Eddy Covariance Fluxes vs. Simulated Tank Sea Spray. *Atmosphere*, **12 (2)**, 274, doi:10.3390/atmos12020274.

Nilsson, E. D., Ü. Rannik, E. Swietlicki, C. Leck, P. P. Aalto, J. Zhou, and M. Norman, 2001: Turbulent aerosol fluxes over the Arctic Ocean: 2. Wind-driven sources from the sea. *Journal*

of Geophysical Research: Atmospheres, **106 (D23)**, 32 139–32 154, doi:10.1029/2000JD900747.

Noone, K. J., J. A. Ogren, J. Heintzenberg, R. J. Charlson, and D. S. Covert, 1988: Design and Calibration of a Counterflow Virtual Impactor for Sampling of Atmospheric Fog and Cloud Droplets. *Aerosol Science and Technology*, **8 (3)**, 235–244, doi:10.1080/02786828808959186.

O'Dowd, C. D. and G. de Leeuw, 2007: Marine aerosol production: A review of the current knowledge. *Philosophical Transactions of the Royal Society A: Mathematical, Physical and Engineering Sciences*, **365 (1856)**, 1753–1774, doi:10.1098/rsta.2007.2043.

O'Dowd, C. D., M. H. Smith, I. E. Consterdine, and J. A. Lowe, 1997: Marine aerosol, sea-salt, and the marine sulphur cycle: A short review. *Atmospheric Environment*, **31 (1)**, 73–80, doi:10.1016/S1352-2310(96)00106-9.

O'Dowd, C. D., et al., 2004: Biogenically driven organic contribution to marine aerosol. *Nature*, **431 (7009)**, 676–680, doi:10.1038/nature02959.

Omar, A. H., et al., 2009: The CALIPSO Automated Aerosol Classification and Lidar Ratio Selection Algorithm. *Journal of Atmospheric and Oceanic Technology*, **26 (10)**, 1994–2014, doi:10.1175/2009JTECHA1231.1.

Or, V. W., A. D. Estillore, A. V. Tivanski, and V. H. Grassian, 2018: Lab on a tip: Atomic force microscopy – photothermal infrared spectroscopy of atmospherically relevant organic/inorganic aerosol particles in the nanometer to micrometer size range. *Analyst*,

143 (12), 2765–2774, doi:10.1039/C8AN00171E.

O'Sullivan, D., et al., 2014: Ice nucleation by fertile soil dusts: Relative importance of mineral and biogenic components. *Atmospheric Chemistry and Physics*, **14 (4)**, 1853–1867, doi:10.5194/acp-14-1853-2014.

Ovadnevaite, J., A. Manders, G. de Leeuw, D. Ceburnis, C. Monahan, A.-I. Partanen, H. Korhonen, and C. D. O'Dowd, 2014: A sea spray aerosol flux parameterization encapsulating wave state. *Atmospheric Chemistry and Physics*, **14 (4)**, 1837–1852, doi:10.5194/acp-14-1837-2014.

Parish, T. R. and D. H. Bromwich, 2007: Reexamination of the Near-Surface Airflow over the Antarctic Continent and Implications on Atmospheric Circulations at High Southern Latitudes. *Monthly Weather Review*, **135 (5)**, 1961–1973, doi:10.1175/MWR3374.1.

Parker, L. V., C. W. Sullivan, T. W. Forest, and S. F. Ackley, 1985: Ice nucleation activity of antarctic marine microorganisms. *Antarctic Journal*, **20**, 126–127.

Perlwitz, J. P., C. P. García-Pando, and R. L. Miller, 2015: Predicting the mineral composition of dust aerosols – Part 1: Representing key processes. *Atmospheric Chemistry and Physics*, **15 (20)**, 11 593–11 627, doi:10.5194/acp-15-11593-2015.

Perron, M. M. G., 2020: Natural iron fertilisation of oceans around Australia : Linking terrestrial aerosols to ocean biogeochemistry. Thesis, University Of Tasmania, doi:10.25959/100.00035207.

Perron, M. M. G., B. C. Proemse, M. Strzelec, M. Gault-Ringold, P. W. Boyd, E. S. Rodriguez, B. Paull, and A. R. Bowie, 2020a: Origin, transport and deposition of aerosol iron to Australian coastal waters. *Atmospheric Environment*, **228**, 117 432, doi:10.1016/j.atmosenv.2020.117432.

Perron, M. M. G., M. Strzelec, M. Gault-Ringold, B. C. Proemse, P. W. Boyd, and A. R. Bowie, 2020b: Assessment of leaching protocols to determine the solubility of trace metals in aerosols. *Talanta*, **208**, 120 377, doi:10.1016/j.talanta.2019.120377.

Pierce, J. R. and P. J. Adams, 2006: Global evaluation of CCN formation by direct emission of sea salt and growth of ultrafine sea salt. *Journal of Geophysical Research: Atmospheres*, **111 (D6)**, doi:10.1029/2005JD006186.

Porter, G. C. E., et al., 2022: Highly Active Ice-Nucleating Particles at the Summer North Pole. *Journal of Geophysical Research: Atmospheres*, **127 (6)**, e2021JD036 059, doi:10.1029/2021JD036059.

Prather, K. A., et al., 2013: Bringing the ocean into the laboratory to probe the chemical complexity of sea spray aerosol. *Proceedings of the National Academy of Sciences*, **110 (19)**, 7550–7555, doi:10.1073/pnas.1300262110.

Prospero, J. M., F.-X. Collard, J. Molinié, and A. Jeannot, 2014: Characterizing the annual cycle of African dust transport to the Caribbean Basin and South America and its impact on the environment and air quality. *Global Biogeochemical Cycles*, **28 (7)**, 757–773, doi:10.1002/2013GB004802.

Pruppacher, H. R. and J. D. Klett, 2010: *Microphysics of Clouds and Precipitation*. 2d ed., Atmospheric and Oceanographic Sciences Library, Springer Netherlands, doi: 10.1007/978-0-306-48100-0.

Pummer, B. G., et al., 2015: Ice nucleation by water-soluble macromolecules. *Atmospheric Chemistry and Physics*, **15 (8)**, 4077–4091, doi:10.5194/acp-15-4077-2015.

Quinn, P. K., D. J. Coffman, J. E. Johnson, L. M. Upchurch, and T. S. Bates, 2017: Small fraction of marine cloud condensation nuclei made up of sea spray aerosol. *Nature Geoscience*, **10 (9)**, 674–679, doi:10.1038/ngeo3003.

Quinn, P. K., D. J. Coffman, V. N. Kapustin, T. S. Bates, and D. S. Covert, 1998: Aerosol optical properties in the marine boundary layer during the First Aerosol Characterization Experiment (ACE 1) and the underlying chemical and physical aerosol properties. *Journal of Geophysical Research: Atmospheres*, **103 (D13)**, 16 547–16 563, doi:10.1029/97JD02345.

Raatikainen, T., M. Prank, J. Ahola, H. Kokkola, J. Tonttila, and S. Romakkaniemi, 2022: The effect of marine ice-nucleating particles on mixed-phase clouds. *Atmospheric Chemistry and Physics*, **22 (6)**, 3763–3778, doi:10.5194/acp-22-3763-2022.

Raiswell, R., J. Hawkings, A. Elsenousy, R. Death, M. Tranter, and J. Wadham, 2018: Iron in Glacial Systems: Speciation, Reactivity, Freezing Behavior, and Alteration During Transport. *Frontiers in Earth Science*, **6**.

Raman, A., et al., 2023: Long-term variability in immersion-mode marine ice-nucleating particles from climate model simulations and observations. *Atmospheric Chemistry and Physics*, **23 (10)**, 5735–5762, doi:10.5194/acp-23-5735-2023.

Ray, K. K., H. D. Lee, M. A. J. Gutierrez, F. J. Chang, and A. V. Tivanski, 2019: Correlating 3D Morphology, Phase State, and Viscoelastic Properties of Individual Substrate-Deposited Particles. *Analytical Chemistry*, **91 (12)**, 7621–7630, doi:10.1021/acs.analchem.9b00333.

Rintoul, S. R., 2007: Rapid freshening of Antarctic Bottom Water formed in the Indian and Pacific oceans. *Geophysical Research Letters*, **34 (6)**, doi:10.1029/2006GL028550.

Rogers, D. C., 1988: Development of a continuous flow thermal gradient diffusion chamber for ice nucleation studies. *Atmospheric Research*, **22 (2)**, 149–181, doi:10.1016/0169-8095(88)90005-1.

Rogers, D. C., P. J. DeMott, S. M. Kreidenweis, and Y. Chen, 2001: A Continuous-Flow Diffusion Chamber for Airborne Measurements of Ice Nuclei. *Journal of Atmospheric and Oceanic Technology*, **18**, 17.

Rolph, G., A. Stein, and B. Stunder, 2017: Real-time Environmental Applications and Display sYstem: READY. *Environmental Modelling & Software*, **95**, 210–228, doi:10.1016/j.envsoft.2017.06.025.

Rosenfeld, D., et al., 2013: The common occurrence of highly supercooled drizzle and rain near the coastal regions of the western United States. *Journal of Geophysical Research:*

Atmospheres, **118 (17)**, 9819–9833, doi:10.1002/jgrd.50529.

Rosinski, J., P. L. Haagenson, C. T. Nagamoto, and F. Parungo, 1987: Nature of ice-forming nuclei in marine air masses. *Journal of Aerosol Science*, **18 (3)**, 291–309, doi:10.1016/0021-8502(87)90024-3.

Saliba, G., et al., 2019: Factors driving the seasonal and hourly variability of sea-spray aerosol number in the North Atlantic. *Proceedings of the National Academy of Sciences*, **116 (41)**, 20 309–20 314, doi:10.1073/pnas.1907574116.

Saliba, G., et al., 2021: Organic composition of three different size ranges of aerosol particles over the Southern Ocean. *Aerosol Science and Technology*, **55 (3)**, 268–288, doi:10.1080/02786826.2020.1845296.

Salter, M. E., E. D. Nilsson, A. Butcher, and M. Bilde, 2014: On the seawater temperature dependence of the sea spray aerosol generated by a continuous plunging jet. *Journal of Geophysical Research: Atmospheres*, **119 (14)**, 9052–9072, doi:10.1002/2013JD021376.

Salter, M. E., P. Zieger, J. C. Acosta Navarro, H. Grythe, A. Kirkevåg, B. Rosati, I. Riipinen, and E. D. Nilsson, 2015: An empirically derived inorganic sea spray source function incorporating sea surface temperature. *Atmospheric Chemistry and Physics*, **15 (19)**, 11 047–11 066, doi:10.5194/acp-15-11047-2015.

Sanchez, K. J., et al., 2021a: Linking marine phytoplankton emissions, meteorological processes, and downwind particle properties with FLEXPART. *Atmospheric Chemistry and*

Physics, **21 (2)**, 831–851, doi:10.5194/acp-21-831-2021.

Sanchez, K. J., et al., 2021b: Measurement report: Cloud processes and the transport of biological emissions affect southern ocean particle and cloud condensation nuclei concentrations. *Atmospheric Chemistry and Physics*, **21 (5)**, 3427–3446, doi:10.5194/acp-21-3427-2021.

Sanchez-Marroquin, A., et al., 2020: Iceland is an episodic source of atmospheric ice-nucleating particles relevant for mixed-phase clouds. *Science Advances*, **6 (26)**, eaba8137, doi:10.1126/sciadv.aba8137.

Sauer, J. S., et al., 2022: The Sea Spray Chemistry and Particle Evolution study (SeaSCAPE): Overview and experimental methods. *Environmental Science: Processes & Impacts*, **24 (2)**, 290–315, doi:10.1039/D1EM00260K.

Schill, G. P., et al., 2016: Ice-nucleating particle emissions from photochemically aged diesel and biodiesel exhaust. *Geophysical Research Letters*, **43 (10)**, 5524–5531, doi:10.1002/2016GL069529.

Schmale, J., et al., 2019: Overview of the Antarctic Circumnavigation Expedition: Study of Preindustrial-like Aerosols and Their Climate Effects (ACE-SPACE). *Bulletin of the American Meteorological Society*, **100 (11)**, 2260–2283, doi:10.1175/BAMS-D-18-0187.1.

Schnell, R. C. and G. Vali, 1976: Biogenic Ice Nuclei: Part I. Terrestrial and Marine Sources. *Journal of the Atmospheric Sciences*, **33 (8)**, 1554–1564, doi:10.1175/1520-0469(1976)033<1554:

BINPIT>2.0.CO;2.

Schwier, A. N., et al., 2017: Primary marine aerosol physical flux and chemical composition during a nutrient enrichment experiment in mesocosms in the Mediterranean Sea. *Atmospheric Chemistry and Physics*, **17 (23)**, 14 645–14 660, doi:10.5194/acp-17-14645-2017.

Seinfeld, J. H. and S. N. Pandis, 2016: *Atmospheric Chemistry and Physics: From Air Pollution to Climate Change*. John Wiley & Sons.

Sellegri, K., C. D. O'Dowd, Y. J. Yoon, S. G. Jennings, and G. de Leeuw, 2006: Surfactants and submicron sea spray generation. *Journal of Geophysical Research: Atmospheres*, **111 (D22)**, doi:10.1029/2005JD006658.

Sellegri, K., et al., 2023: Quantified effect of seawater biogeochemistry on the temperature dependence of sea spray aerosol fluxes. *Atmospheric Chemistry and Physics*, **23 (20)**, 12 949–12 964, doi:10.5194/acp-23-12949-2023.

Shelley, R. U., P. L. Morton, and W. M. Landing, 2015: Elemental ratios and enrichment factors in aerosols from the US-GEOTRACES North Atlantic transects. *Deep Sea Research Part II: Topical Studies in Oceanography*, **116**, 262–272, doi:10.1016/j.dsr2.2014.12.005.

Shelley, R. U., et al., 2017: Quantification of trace element atmospheric deposition fluxes to the Atlantic Ocean (>40°N; GEOVIDE, GEOTRACES GA01) during spring 2014. *Deep Sea Research Part I: Oceanographic Research Papers*, **119**, 34–49, doi:10.1016/j.dsr.2016.11.010.

Shi, Z., M. D. Krom, T. D. Jickells, S. Bonneville, K. S. Carslaw, N. Mihalopoulos, A. R. Baker, and L. G. Benning, 2012: Impacts on iron solubility in the mineral dust by processes in the source region and the atmosphere: A review. *Aeolian Research*, **5**, 21–42, doi: 10.1016/j.aeolia.2012.03.001.

Smirnov, A., et al., 2009: Maritime Aerosol Network as a component of Aerosol Robotic Network. *Journal of Geophysical Research: Atmospheres*, **114 (D6)**, doi:10.1029/2008JD011257.

Sofiev, M., J. Soares, M. Prank, G. de Leeuw, and J. Kukkonen, 2011: A regional-to-global model of emission and transport of sea salt particles in the atmosphere. *Journal of Geophysical Research: Atmospheres*, **116 (D21)**, doi:10.1029/2010JD014713.

SouthWest Sciences, I. S. and UCAR/NCAR-Earth Observing Laboratory, 2008: Vertical Cavity Surface-Emitting Laser (VCSEL) Hygrometer. *UCAR/NCAR - Earth Observing Laboratory*, doi:10.5065/D6PV6HDM.

Speirs, J. C., H. A. McGowan, and D. T. Neil, 2008: Meteorological controls on sand transport and dune morphology in a polar-desert: Victoria Valley, Antarctica. *Earth Surface Processes and Landforms*, **33 (12)**, 1875–1891, doi:10.1002/esp.1739.

Stein, A. F., R. R. Draxler, G. D. Rolph, B. J. B. Stunder, M. D. Cohen, and F. Ngan, 2015: NOAA's HYSPLIT Atmospheric Transport and Dispersion Modeling System. *Bulletin of the American Meteorological Society*, **96 (12)**, 2059–2077, doi:10.1175/BAMS-D-14-00110.1.

Steinke, I., P. J. DeMott, G. B. Deane, T. C. J. Hill, M. Maltrud, A. Raman, and S. M. Burrows, 2022: A numerical framework for simulating the atmospheric variability of supermicron marine biogenic ice nucleating particles. *Atmospheric Chemistry and Physics*, **22 (2)**, 847–859, doi:10.5194/acp-22-847-2022.

Stith, J. L., et al., 2009: An overview of aircraft observations from the Pacific Dust Experiment campaign. *Journal of Geophysical Research: Atmospheres*, **114 (D5)**, doi: 10.1029/2008JD010924.

Stokes, M. D., G. B. Deane, K. Prather, T. H. Bertram, M. J. Ruppel, O. S. Ryder, J. M. Brady, and D. Zhao, 2013: A Marine Aerosol Reference Tank system as a breaking wave analogue for the production of foam and sea-spray aerosols. *Atmospheric Measurement Techniques*, **6 (4)**, 1085–1094, doi:10.5194/amt-6-1085-2013.

Strapp, J. W., W. R. Leaitch, and P. S. K. Liu, 1992: Hydrated and Dried Aerosol-Size-Distribution Measurements from the Particle Measuring Systems FSSP-300 Probe and the Deiced PCASP-100X Probe. *Journal of Atmospheric and Oceanic Technology*, **9 (5)**, 548–555, doi: 10.1175/1520-0426(1992)009<0548:HADASD>2.0.CO;2.

Suski, K. J., T. C. J. Hill, E. J. T. Levin, A. Miller, P. J. DeMott, and S. M. Kreidenweis, 2018: Agricultural harvesting emissions of ice-nucleating particles. *Atmospheric Chemistry and Physics*, **18 (18)**, 13 755–13 771, doi:10.5194/acp-18-13755-2018.

Tan, I. and T. Storelvmo, 2019: Evidence of Strong Contributions From Mixed-Phase Clouds to Arctic Climate Change. *Geophysical Research Letters*, **46 (5)**, 2894–2902, doi:

10.1029/2018GL081871.

Tan, I., T. Storelvmo, and M. D. Zelinka, 2016: Observational constraints on mixed-phase clouds imply higher climate sensitivity. *Science*, **352 (6282)**, 224–227, doi:10.1126/science.aad5300.

Tang, I. N., A. C. Tridico, and K. H. Fung, 1997: Thermodynamic and optical properties of sea salt aerosols. *Journal of Geophysical Research: Atmospheres*, **102 (D19)**, 23 269–23 275, doi:10.1029/97JD01806.

Tatzelt, C., et al., 2022: Circum-Antarctic abundance and properties of CCN and INPs. *Atmospheric Chemistry and Physics*, **22 (14)**, 9721–9745, doi:10.5194/acp-22-9721-2022.

Testa, B., et al., 2021: Ice Nucleating Particle Connections to Regional Argentinian Land Surface Emissions and Weather During the Cloud, Aerosol, and Complex Terrain Interactions Experiment. *Journal of Geophysical Research: Atmospheres*, **126 (23)**, e2021JD035 186, doi:10.1029/2021JD035186.

Tobo, Y., et al., 2013: Biological aerosol particles as a key determinant of ice nuclei populations in a forest ecosystem. *Journal of Geophysical Research: Atmospheres*, **118 (17)**, 10,100–10,110, doi:10.1002/jgrd.50801.

Tobo, Y., et al., 2019: Glacially sourced dust as a potentially significant source of ice nucleating particles. *Nature Geoscience*, **12 (4)**, 253–258, doi:10.1038/s41561-019-0314-x.

Trenberth, K. E. and J. T. Fasullo, 2010: Simulation of Present-Day and Twenty-First-Century Energy Budgets of the Southern Oceans. *Journal of Climate*, **23 (2)**, 440–454, doi:10.1175/2009JCLI3152.1.

Truong, S. C. H., Y. Huang, F. Lang, M. Messmer, I. Simmonds, S. T. Siems, and M. J. Manton, 2020: A Climatology of the Marine Atmospheric Boundary Layer Over the Southern Ocean From Four Field Campaigns During 2016–2018. *Journal of Geophysical Research: Atmospheres*, **125 (20)**, e2020JD033 214, doi:10.1029/2020JD033214.

Twohy, C. H., et al., 2010: Relationships of Biomass-Burning Aerosols to Ice in Orographic Wave Clouds. *Journal of the Atmospheric Sciences*, **67 (8)**, 2437–2450, doi:10.1175/2010JAS3310.1.

Twohy, C. H., et al., 2016: Abundance of fluorescent biological aerosol particles at temperatures conducive to the formation of mixed-phase and cirrus clouds. *Atmospheric Chemistry and Physics*, **16 (13)**, 8205–8225, doi:10.5194/acp-16-8205-2016.

Twohy, C. H., et al., 2021: Cloud-Nucleating Particles Over the Southern Ocean in a Changing Climate. *Earth's Future*, **9 (3)**, e2020EF001 673, doi:10.1029/2020EF001673.

UCAR/NCAR - Earth Observing Laboratory, 2005: NSF/NCAR GV HIAPER Aircraft. Tech. rep., UCAR/NCAR- Earth Observing Laboratory, https://doi.org/10.5065/D6DR2SJP.

Uetake, J., T. C. J. Hill, K. A. Moore, P. J. DeMott, A. Protat, and S. M. Kreidenweis, 2020: Airborne bacteria confirm the pristine nature of the Southern Ocean boundary layer. *Proceedings of*

the National Academy of Sciences, doi:10.1073/pnas.2000134117.

Ullrich, R., et al., 2017: A New Ice Nucleation Active Site Parameterization for Desert Dust and Soot. *Journal of the Atmospheric Sciences*, **74 (3)**, 699–717, doi:10.1175/JAS-D-16-0074.1.

Vali, G., 1971: Quantitative Evaluation of Experimental Results on the Heterogeneous Freezing Nucleation of Supercooled Liquids. *Journal of the Atmospheric Sciences*, **28 (3)**, 402–409, doi:10.1175/1520-0469(1971)028<0402:QEOERA>2.0.CO;2.

van Pinxteren, M., et al., 2020: Marine organic matter in the remote environment of the Cape Verde islands – an introduction and overview to the MarParCloud campaign. *Atmospheric Chemistry and Physics*, **20 (11)**, 6921–6951, doi:10.5194/acp-20-6921-2020.

Verdugo, P., 2012: Marine Microgels. *Annual Review of Marine Science*, **4 (1)**, 375–400, doi:10.1146/annurev-marine-120709-142759.

Vergara-Temprado, J., et al., 2017: Contribution of feldspar and marine organic aerosols to global ice nucleating particle concentrations. *Atmospheric Chemistry and Physics*, **17 (5)**, 3637–3658, doi:10.5194/acp-17-3637-2017.

Vergara-Temprado, J., et al., 2018: Strong control of Southern Ocean cloud reflectivity by ice-nucleating particles. *Proceedings of the National Academy of Sciences*, **115 (11)**, 2687–2692, doi:10.1073/pnas.1721627115.

Villefer, A., M. Benoit, D. Violeau, C. Luneau, and H. Branger, 2021: Influence of Following, Regular, and Irregular Long Waves on Wind-Wave Growth with Fetch: An Experimental Study. *Journal of Physical Oceanography*, **51 (11)**, 3435–3448, doi:10.1175/JPO-D-21-0050.1.

Vollestad, P. and A. Jensen, 2021: Modification of Airflow Structure Due to Wave Breaking on a Submerged Topography. *Boundary-Layer Meteorology*, **180 (3)**, 507–526, doi:10.1007/s10546-021-00631-3.

Vömel, H. and W. Brown, 2018: SOCRATES -2018 Radiosonde Data Quality Report, UCAR/NCAR - Earth Observing Laboratory. Tech. rep., UCAR/NCAR- Earth Observing Laboratory, https://doi.org/10.5065/D69P30HG.

von der Weiden, S.-L., F. Drewnick, and S. Borrmann, 2009: Particle Loss Calculator – a new software tool for the assessment of the performance of aerosol inlet systems. *Atmospheric Measurement Techniques*, **2 (2)**, 479–494, doi:10.5194/amt-2-479-2009.

Wang, X., et al., 2015a: Microbial Control of Sea Spray Aerosol Composition: A Tale of Two Blooms. *ACS Central Science*, **1 (3)**, 124–131, doi:10.1021/acscentsci.5b00148.

Wang, X., et al., 2017: The role of jet and film drops in controlling the mixing state of submicron sea spray aerosol particles. *Proceedings of the National Academy of Sciences*, **114 (27)**, 6978–6983, doi:10.1073/pnas.1702420114.

Wang, Z., S. T. Siems, D. Belusic, M. J. Manton, and Y. Huang, 2015b: A Climatology of the Precipitation over the Southern Ocean as Observed at Macquarie Island. *Journal of Applied*

Meteorology and Climatology, **54 (12)**, 2321–2337, doi:10.1175/JAMC-D-14-0211.1.

Webb, A. L., M. A. van Leeuwe, D. den Os, M. P. Meredith, H. J. Venables, and J. Stefels, 2019: Extreme spikes in DMS flux double estimates of biogenic sulfur export from the Antarctic coastal zone to the atmosphere. *Scientific Reports*, **9 (1)**, 2233, doi:10.1038/s41598-019-38714-4.

Welti, A., K. Müller, Z. L. Fleming, and F. Stratmann, 2018: Concentration and variability of ice nuclei in the subtropical maritime boundary layer. *Atmospheric Chemistry and Physics*, **18 (8)**, 5307–5320, doi:10.5194/acp-18-5307-2018.

Welti, A., et al., 2020: Ship-based measurements of ice nuclei concentrations over the Arctic, Atlantic, Pacific and Southern oceans. *Atmospheric Chemistry and Physics*, **20 (23)**, 15 191–15 206, doi:10.5194/acp-20-15191-2020.

Wilbourn, E. K., et al., 2020: Ice Nucleation by Marine Aerosols Over the North Atlantic Ocean in Late Spring. *Journal of Geophysical Research: Atmospheres*, **125 (4)**, e2019JD030 913, doi:10.1029/2019JD030913.

Wilson, T. W., et al., 2015: A marine biogenic source of atmospheric ice-nucleating particles. *Nature*, **525 (7568)**, 234–238, doi:10.1038/nature14986.

Winton, V. H. L., G. B. Dunbar, N. a. N. Bertler, M.-A. Millet, B. Delmonte, C. B. Atkins, J. M. Chewings, and P. Andersson, 2014: The contribution of aeolian sand and dust to iron fertilization of phytoplankton blooms in southwestern Ross Sea, Antarctica. *Global Biogeochemical*

Cycles, **28 (4)**, 423–436, doi:10.1002/2013GB004574.

Wolfe, S. A., 2022: 7.08 - Cold-Climate Aeolian Environments. *Treatise on Geomorphology (Second Edition)*, J. J. F. Shroder, Ed., Academic Press, Oxford, 195–219, doi:10.1016/B978-0-12-818234-5.00036-5.

Yu, F. and G. Luo, 2010: Oceanic Dimethyl Sulfide Emission and New Particle Formation around the Coast of Antarctica: A Modeling Study of Seasonal Variations and Comparison with Measurements. *Atmosphere*, **1 (1)**, 34–50, doi:10.3390/atmos1010034.

Zábori, J., M. Matisāns, R. Krejci, E. D. Nilsson, and J. Ström, 2012: Artificial primary marine aerosol production: A laboratory study with varying water temperature, salinity, and succinic acid concentration. *Atmospheric Chemistry and Physics*, **12 (22)**, 10 709–10 724, doi:10.5194/acp-12-10709-2012.

Zavadsky, A. and L. Shemer, 2012: Characterization of turbulent airflow over evolving water-waves in a wind-wave tank. *Journal of Geophysical Research: Oceans*, **117 (C11)**, doi:10.1029/2011JC007790.

Zelinka, M. D., T. A. Myers, D. T. McCoy, S. Po-Chedley, P. M. Caldwell, P. Ceppi, S. A. Klein, and K. E. Taylor, 2020: Causes of Higher Climate Sensitivity in CMIP6 Models. *Geophysical Research Letters*, **47 (1)**, e2019GL085 782, doi:10.1029/2019GL085782.

Zender, C. S., H. Bian, and D. Newman, 2003: Mineral Dust Entrainment and Deposition (DEAD) model: Description and 1990s dust climatology. *Journal of Geophysical Research:*

Atmospheres, **108 (D14)**, doi:10.1029/2002JD002775.

Zhao, X., X. Liu, S. M. Burrows, and Y. Shi, 2021: Effects of marine organic aerosols as sources of immersion-mode ice-nucleating particles on high-latitude mixed-phase clouds. *Atmospheric Chemistry and Physics*, **21 (4)**, 2305–2327, doi:10.5194/acp-21-2305-2021.

Zhao, X., et al., 2023: Important Ice Processes Are Missed by the Community Earth System Model in Southern Ocean Mixed-Phase Clouds: Bridging SOCRATES Observations to Model Developments. *Journal of Geophysical Research: Atmospheres*, **128 (4)**, e2022JD037 513, doi:10.1029/2022JD037513.

Zheng, C. W., J. Pan, and C. Y. Li, 2016: Global oceanic wind speed trends. *Ocean & Coastal Management*, **129**, 15–24, doi:10.1016/j.ocecoaman.2016.05.001.

Zieger, P., et al., 2017: Revising the hygroscopicity of inorganic sea salt particles. *Nature Communications*, **8 (1)**, 15 883, doi:10.1038/ncomms15883.

Zinke, J., E. D. Nilsson, P. Zieger, and M. E. Salter, 2022: The Effect of Seawater Salinity and Seawater Temperature on Sea Salt Aerosol Production. *Journal of Geophysical Research: Atmospheres*, **127 (16)**, e2021JD036 005, doi:10.1029/2021JD036005.

Zondlo, M. A., M. E. Paige, S. M. Massick, and J. A. Silver, 2010: Vertical cavity laser hygrometer for the National Science Foundation Gulfstream-V aircraft. *Journal of Geophysical Research: Atmospheres*, **115 (D20)**, doi:10.1029/2010JD014445.

A. Chapter 2 Supporting Information

A.1 INTRODUCTION

This supporting information contains figures that provide additional details about inlet loss modeling and correction during CAPRICORN-2 (Fig. A.1), CAP-2 size distributions analyzed but not presented elsewhere in the text (Fig. A.2), and estimation of >5 μm particles not captured during CAP-2 due to poor inlet transmission efficiency of large supermicron particles (Fig. A.3). Also included are figures that support the results discussed in the main text, including frequency distributions of CAP-2 and SOCRATES integrated particle concentrations (Fig. A.4), the relationship between PMA mode diameter, wind speed, and SST during CAP-2 (Fig. A.5), particle concentrations as a function of latitude (Fig. A.6), frequency distributions of Ångström exponent (å) calculated from the CAP-2 size distributions using Mie theory (Fig. A.7), frequency distributions of RV *Investigator* latitude and wind speed for particles with å≤0.8 and å>0.8 (Fig. A.8), the relationship between PMA fraction and Ångström exponent (Fig. A.9), AERONET inversion data during the MICRE campaign to test the Mamouri and Ansmann (2016) aerosol SA retrieval algorithm over the Southern Ocean (Fig. A.10-A.11), correlations between aerosol surface area and AOT during CAP-2 (Fig. A.12), and a timeline (Fig. A.13) and frequency distributions (Fig. A.14) of measured and estimated aerosol surface area during CAP-2. Finally, this supporting information includes tables that compare key values and results from the text. These include a summary of the parameters used to estimate dry marine aerosol surface area from aerosol light scattering (Q_{green}) and lidar extinction ($c_{s,m}/4$), and to estimate N_{500} from lidar extinction ($C_{1000,m}$) (Table A.1), the limits applied to mode diameter and width during log-normal fitting of CAP-2 and SOC size distributions (Table A.2), the wind speed dependent PMA production fits derived here for SOC and CAP-2 (Table A.3), and a summary of the å and AOT values for marine aerosol observations, including this work (Table A.4).

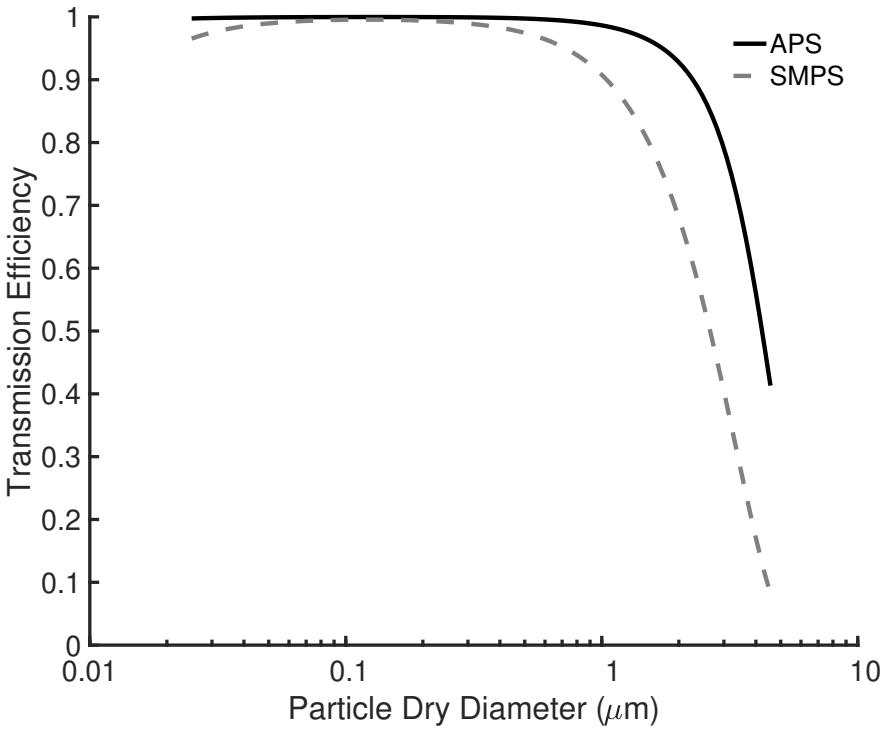

Figure A.1: Estimated particle transmission efficiency for the RV *Investigator* aerosol inlet for particles reaching either the SMPS or APS instrument inlets during CAP-2, based on the different inlet geometries. These theoretical calculations used the von der Weiden et al. (2009) Particle Loss Calculator and Paul Baron's Aerocalc spreadsheet (Brockmann 2011). A constant aspiration angle of 0° and a wind velocity of 10 m s^{-1}, which is the average for the CAP-2 campaign, were assumed. Calculations were performed for the whole inlet in aerodynamic diameter, with a particle density ρ_p=1, and were afterwards corrected for expected particle density, water uptake and shape factor, as in Section 2.3.3.

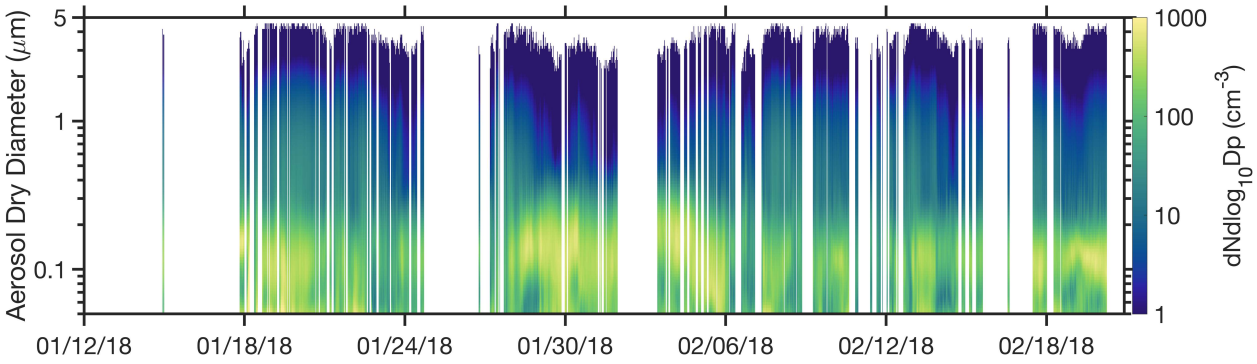

Figure A.2: Merged aerosol number distributions for CAP-2, shown as a contour map of $dNdlog_{10}Dp$ in cm^{-3}.

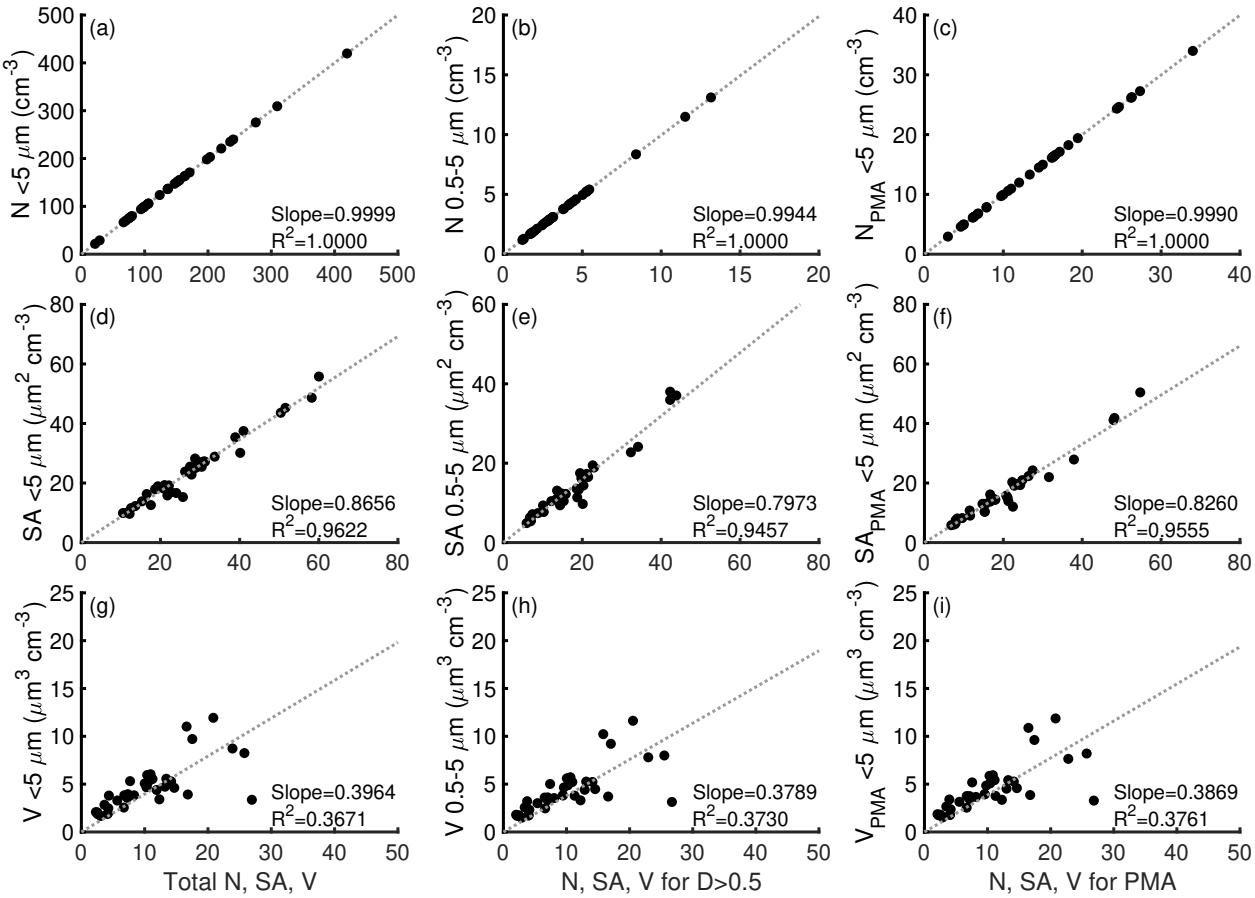

Figure A.3: Estimation of CAP2- inlet and line losses of particles with dry diameters (D) >5 μm for particle a-c) number (N), d-f) surface area (SA), and g-i) volume (V) concentrations from SOC MBL passes. Panels a,d,g) have concentrations of particles with D<5 μm against the total concentrations, b,e,h) have concentrations of particles with 0.5<D<5 μm against D>0.5 μm and c,f,i) have concentrations of PMA with D<5 μm against total PMA. Best-fit linear correlations are shown in each panel in the grey dashed lines, with the slope and R^2 reported on the figure.

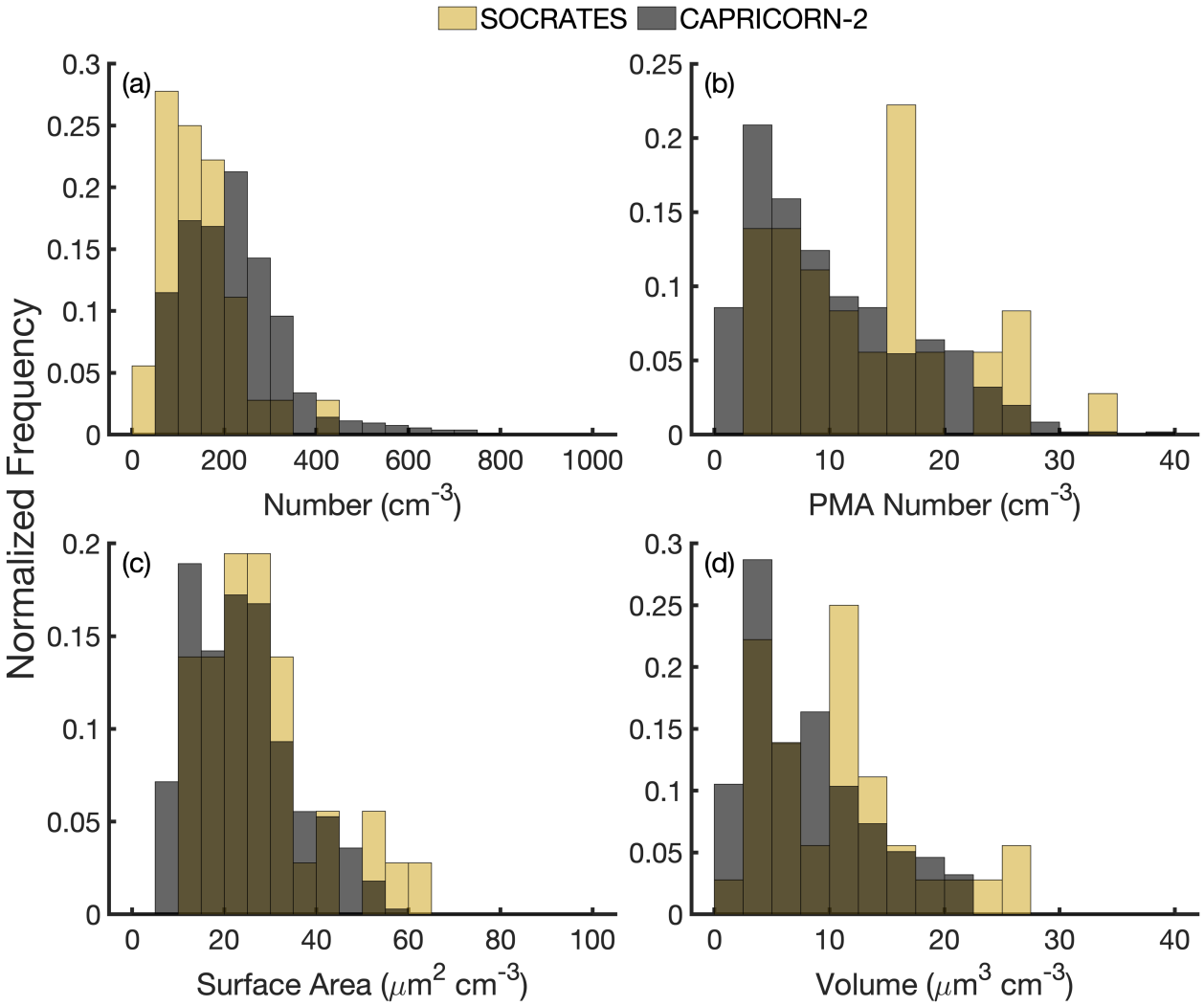

Figure A.4: Normalized frequency distributions of particle (a) number, (b) PMA number, (c) surface area, and (d) volume concentrations. CAP-2 data are shown in black and SOC MBL data in gold.

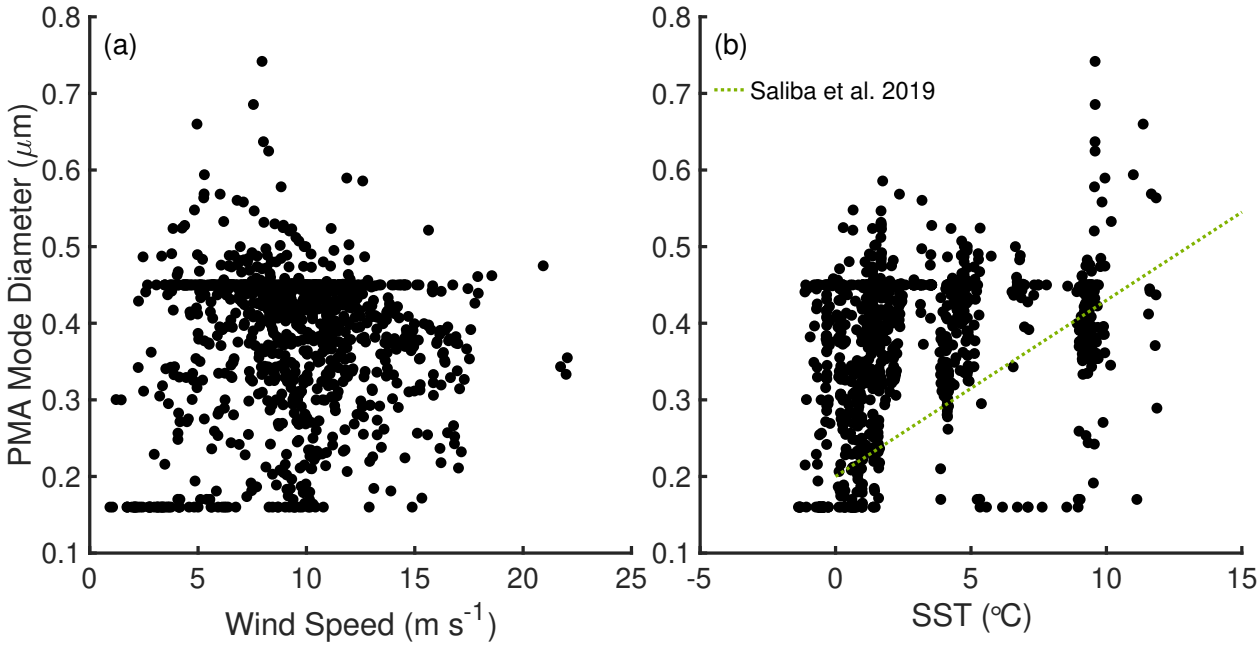

Figure A.5: CAP-2 PMA mode diameter as a function of (a) wind speed and b (SST) measured onboard the RV *Investigator* . The green curve in (b) is the PMA mode diameter fit from Saliba et al. (2019).

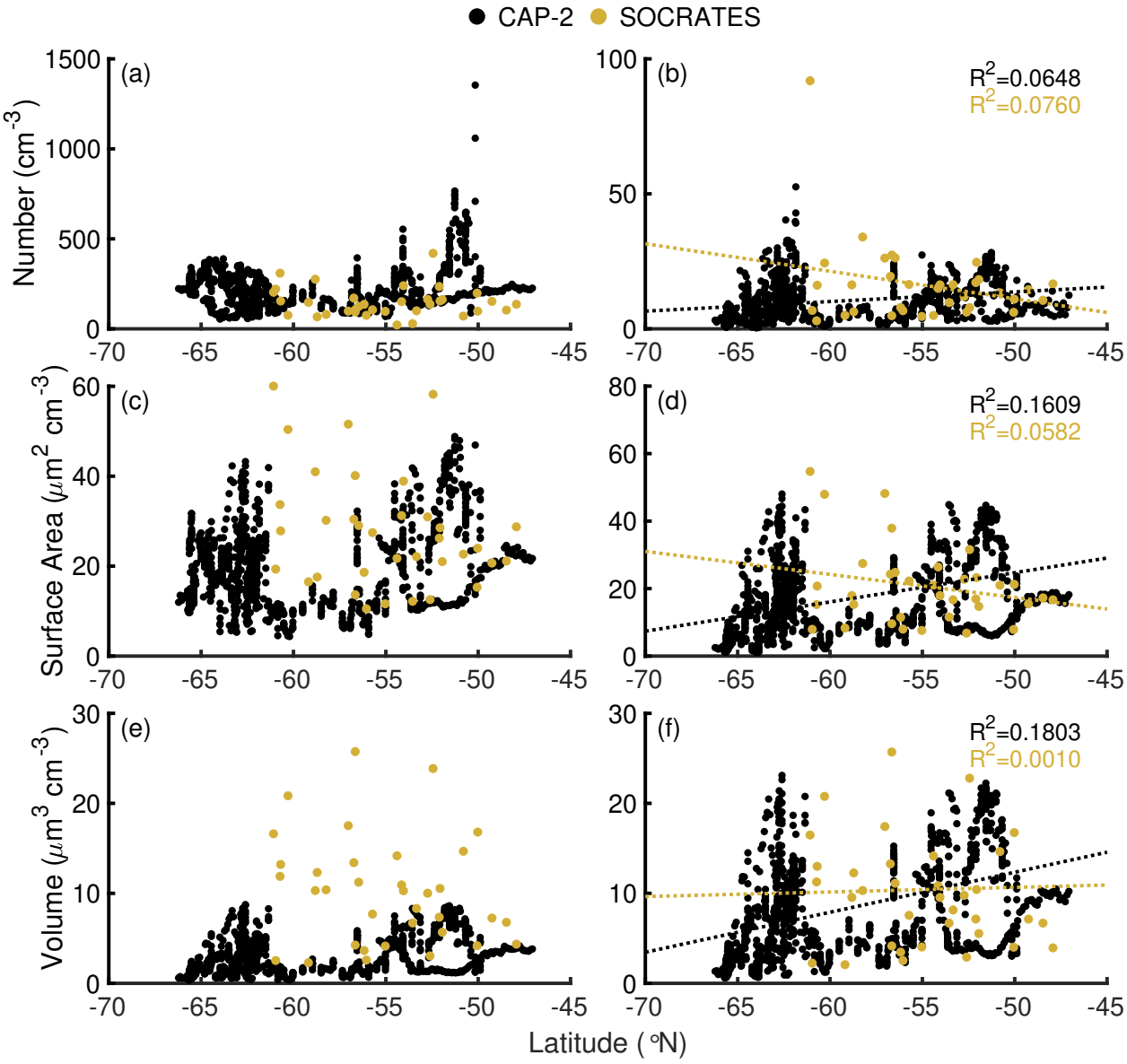

Figure A.6: Particle a-b) number, c-d) surface area, and e-f) volume concentrations versus latitude. Panels a,c,e) have total concentrations and b,d,f) show PMA concentrations and best fit linear functions (dashed lines). CAP-2 data are in black, and data for the SOC G-V marine boundary layer passes in gold.

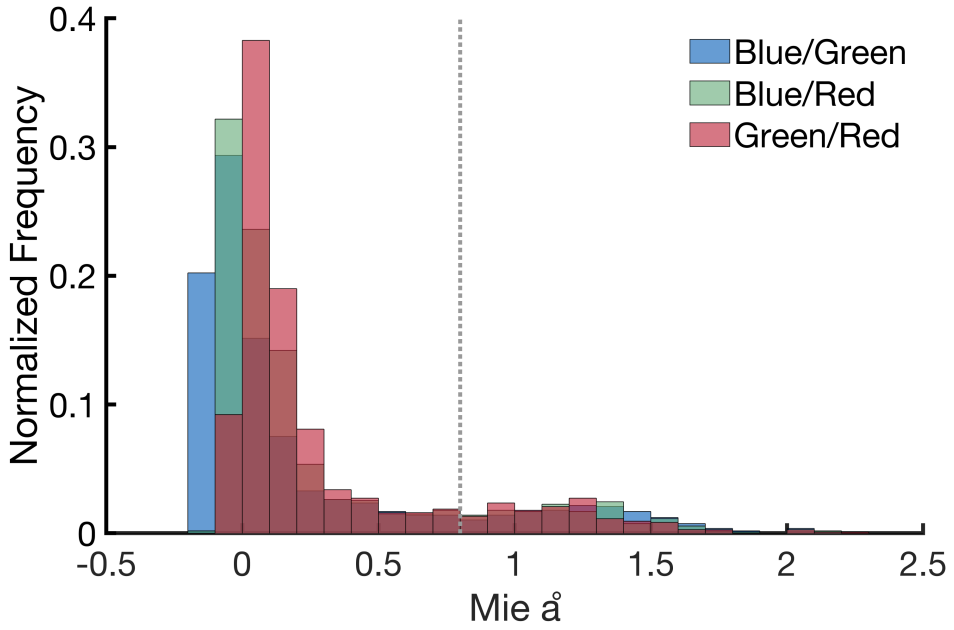

Figure A.7: Normalized frequency distributions of Ångström exponent calculated from the CAP-2 size distributions using Mie theory. Blue bars are for the blue/green å (450nm, 525 nm), green bars show blue/red å (450nm, 635 nm), and red bars are the green/red å (525 nm, 635 nm). The dashed line at å=0.8 represents the proposed cutoff for distributions dominated by primary marine aerosol.

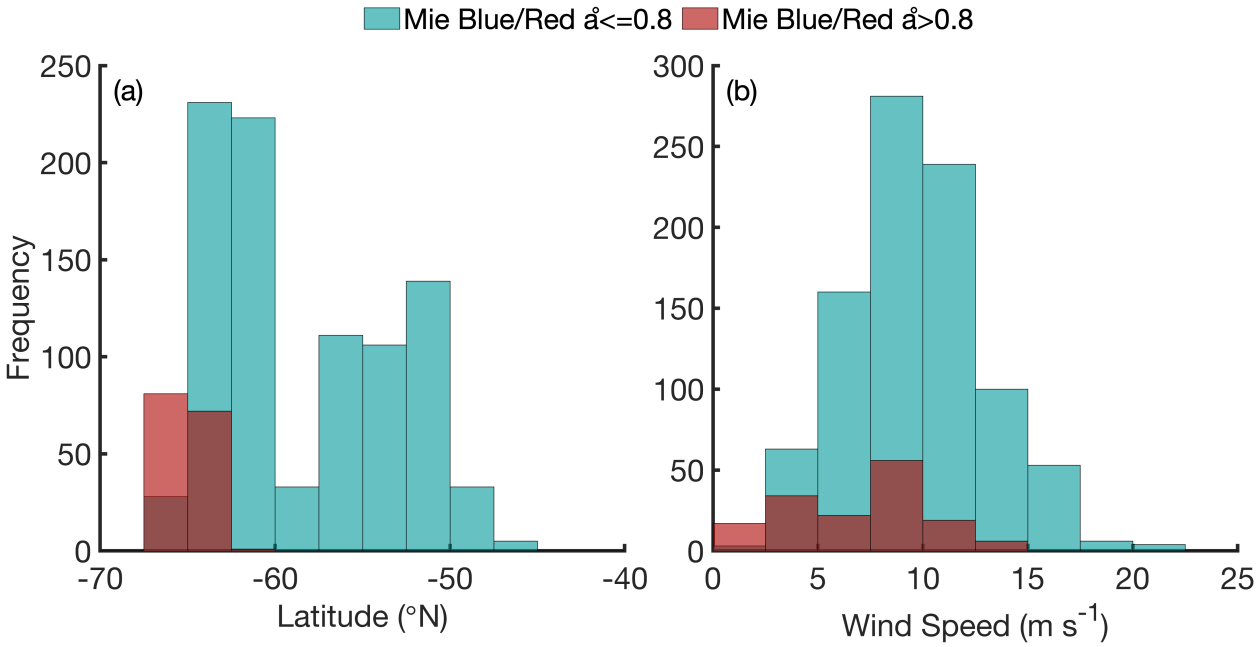

Figure A.8: Frequency distributions of RV *Investigator* (a) latitude during CAP-2 in 5° bins and (b) wind speed in 5 m s^{-1} bins. Histograms were calculated separately for distributions with blue/red å≤0.8 (blue bars) and å>0.8 (red bars).

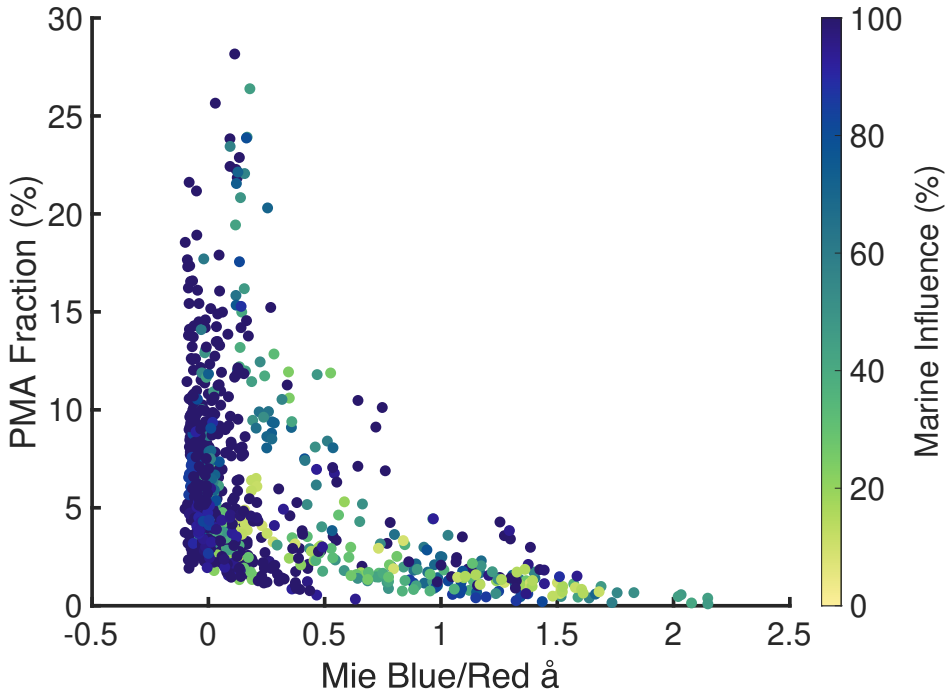

Figure A.9: Relationship between the fraction of integrated particle number attributed to PMA and calculated blue/red å for the CAP-2 size distributions. Points are colored by the degree of marine influence, defined as the fraction of a 5-day back trajectory that passed over the ocean (Sanchez et al. 2021b;a).

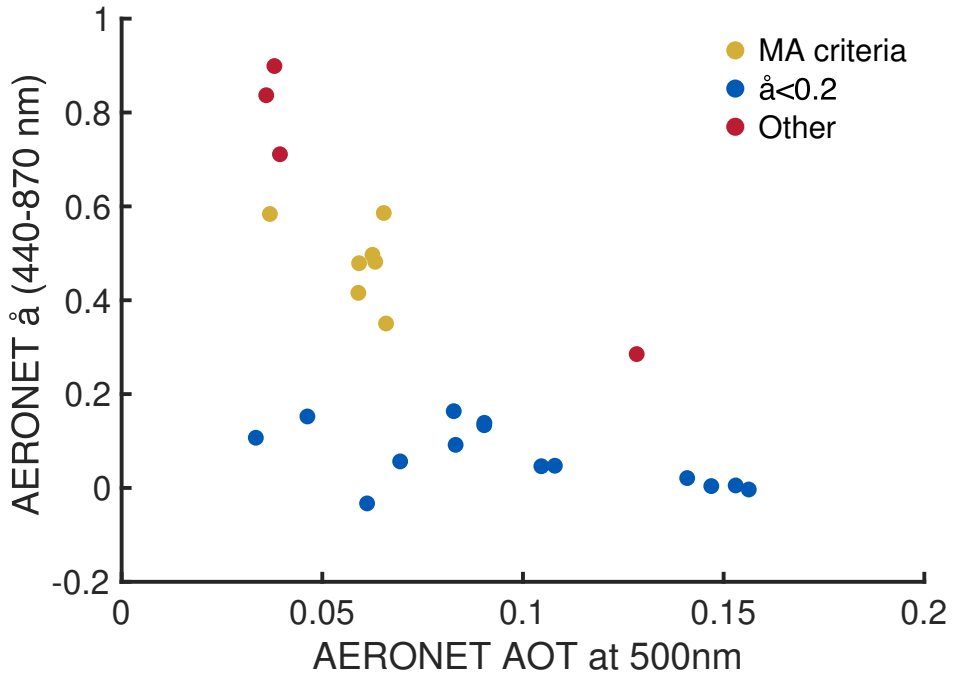

Figure A.10: AERONET Level 2.0 Version 3 inversion data during MICRE, showing the total å (440nm, 870nm) and AOT interpolated to 500 nm. Yellow points are those meeting the criterion applied by Mamouri and Ansmann (2016) for isolating Ragged Point marine data, as described in Sec. 2.2.2. Dark blue points are those with å<0.2, expected to be dominated by coarse mode aerosol. Red points are data outside of these two classifications.

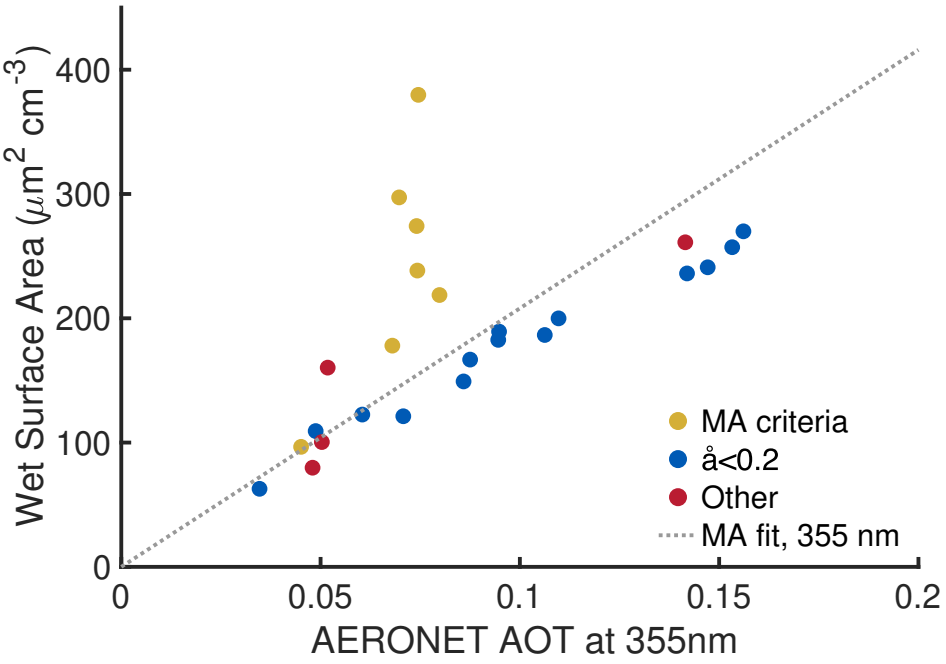

Figure A.11: Column wet aerosol surface areas derived from MICRE AERONET inversions and AERONET AOT interpolated to 355 nm. The dashed line is the marine aerosol fit for 355 nm data from Mamouri and Ansmann (2016). Yellow points are those meeting the criterion applied by MA for isolating Ragged Point marine data, as described in Sec 2.2. Dark blue points are those with å<0.2, expected to be dominated by coarse mode aerosol. Red points are data outside of these two classifications.

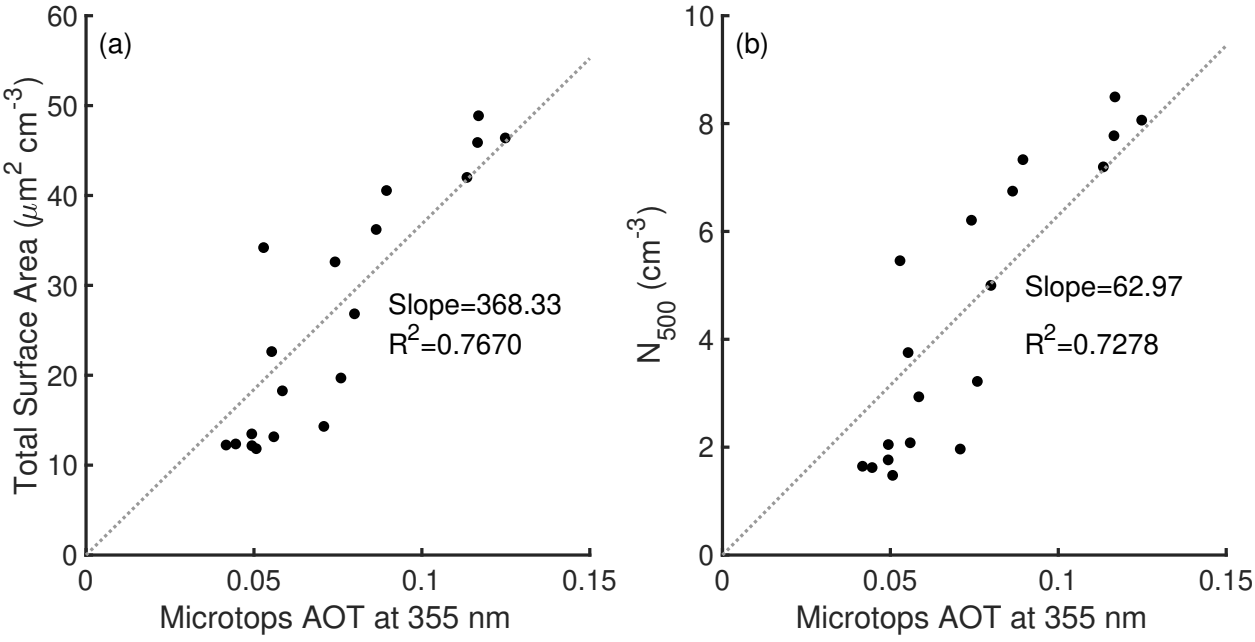

Figure A.12: Correlations of AOT at 355 nm from the MAN Microtops measurements during CAP-2 with (a) total aerosol surface area and (b) N_{500} from merged aerosol size distributions (Sec. 2.2.3.3).

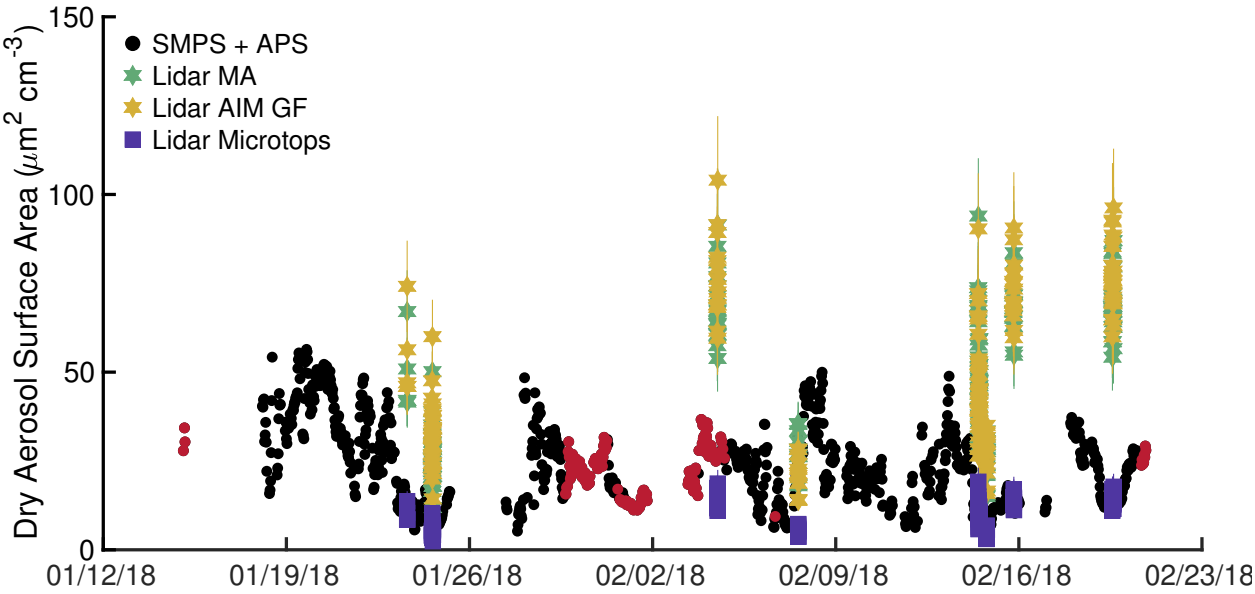

Figure A.13: Timeline of total aerosol surface area during CAP-2 from the SMPS+APS size distributions (black and red), those estimated from the lidar at 300 m using the Mamouri and Ansmann (2016) parameters (green), using the MA method but adjusting the assumed HGF based on the ambient RH (gold), and using the MA method but conversion parameters derived from the CAP-2 Microtops data (purple). The SMPS+APS data shown in red were excluded from the correlation analysis in Fig. 2.9 to isolate PMA.

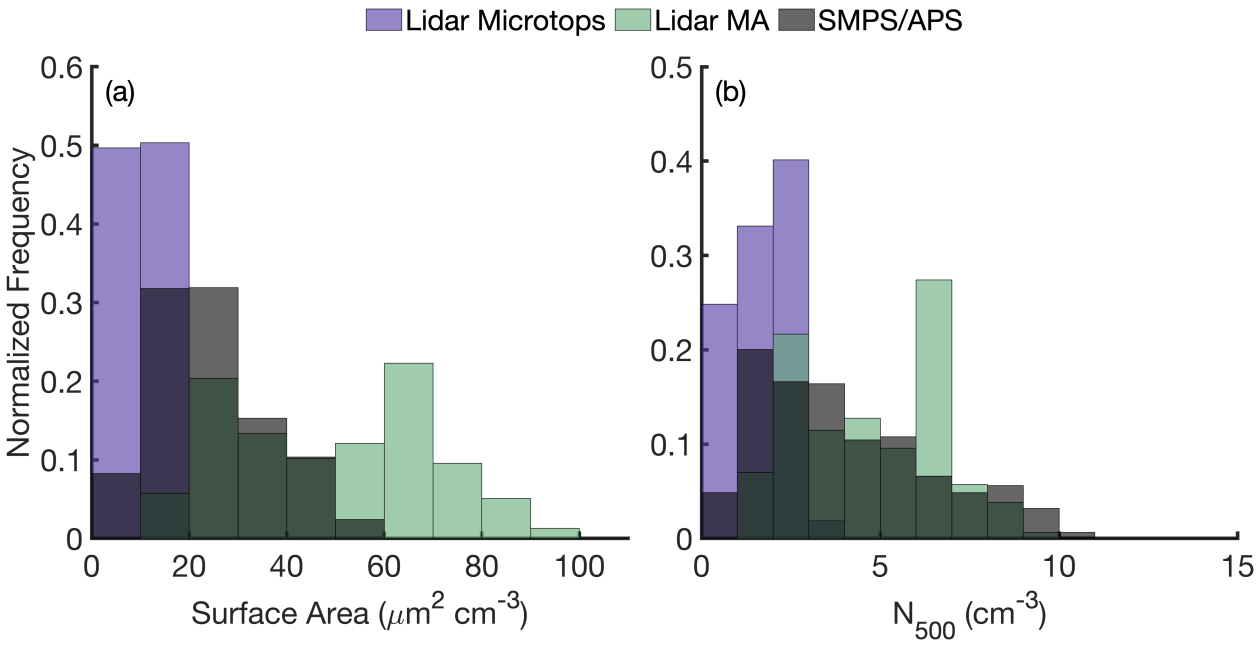

Figure A.14: Normalized frequency distributions of particle (a) surface area and (b) number concentrations for dry diameters >500 nm during CAP-2 from the aerosol size distributions and lidar at 300 m using the Mamouri and Ansmann (2016) method. Data using the MA parameters are shown in green, those using the MA method with conversion parameters derived from the CAP-2 Microtops in purple, and the SMPS+APS data is shown in black.

Table A.1: Summary of parameters used to estimate dry marine aerosol surface area from aerosol light scattering (Q_{green}) and lidar extinction ($c_{s,m}/4$), and to estimate N_{500} from lidar extinction ($C_{1000,m}$).

	D16 (ambient)	å fit (dry; this work)	MA	Microtops (this work)
Q_{green}	å<1: Q=2 å>1: Q=3	$2.15*e^{(-0.80*å)}$		
$\frac{c_{s,m}}{4}$ at 355 nm (μm^2 cm^{-3} Mm)			0.52±0.09	0.106±0.022
$C_{1000,m}$ at 355 nm (cm^{-3} Mm)			0.05±0.01	0.0182±0.0036

Note. The MA conversion parameters adjusted for ambient surface RH during CAP-2 are not listed here, as they varied for each measurement; they differed from the MA parameters by 4-22%. The D16 method accounts for ambient RF by applying a correction to the SA calculated using Eq. 2.4 and the å thresholds listed here, while the å fit presented in this work is for dry scattering measurements.

Table A.2: Limits applied to mode diameter and widths during lognormal fitting of aerosol size distributions.

	Mode 1	Mode 2	Mode 3	Mode 4
Minimum diameter (μm)	0.01	0.06	0.17	0.3
Maximum diameter (μm)	0.1	0.3	0.45	N/A
Minimum geometric standard deviation (width)	0.8	0.8	1	2
Maximum geometric standard deviation (width)	2	2	3	4

Note. Initial CAP-2 3-mode fit was modes 1-3, with mode 4 added if needed to match supermicron particle observations. SOC 2-mode fit used modes 2-3, with mode 4 only added if necessary to reproduce observations.

Table A.3: Wind speed dependent PMA production fits for CAP-2 and SOC.

	CAPRICORN-2 Fit	CAPRICORN-2 R^2	SOCRATES Fit	SOCRATES R^2
Number (cm^{-3})	$0.5298(U_{18}^{1.316})$	0.4276	$1.61(U_{18}^{0.8668})$	0.0936
Surface area (μm2 cm^{-3})	$1.41(U_{18}^{1.101})$	0.3568	$1.149(U_{18}^{1.085})$	0.3850
Volume (μm3 cm^{-3})	$0.8386(U_{18}^{1.02})$	0.3219	$0.1487(U_{18}^{1.582})$	0.6044

Table A.4: Summary of å and AOT values for marine aerosol observations, including this work.

Study	å	$AOT_{500\ nm}$
Andrews et al. (2019)[a]	CPT[b]: 0.2 – 0.8 CPR[c]: 0.2 – 0.6 SMO[d]: 0-0.3	
Carrico et al. (2003)	0.16±0.60	
Mulcahy et al. (2009)	-0.2 – 1.6	0.14±0.06
This study	0.07 - 0.58	0.036 - 0.127
MA marine criteria	0.25<å<0.6	<0.07

Note. The criteria used in Mamouri and Ansmann (2016) to select marine observations are included for comparison. [a]Measurements from NOAA Federated Aerosol Network (FAN) sites. [b]Cape Point, South Africa. [c]Cape San Juan, Puerto Rico. [d]NOAA American Samoa baseline observatory.

B. Chapter 3 Supporting Information

B.1 INTRODUCTION

This supporting information contains additional figures and tables to clarify details and support the conclusions in the main text. Figure B.1 indicates the location of the CAPRICORN-2 (CAP-2) and SOCRATES (SOC) campaigns and the locations of measurements discussed in the text. Figure B.2 provides a comparison between methods to estimate aerosol surface area and the number of particles larger than 0.5 μm (Moore et al. 2022). Figure B.3 provides additional details about inlet loss modeling and correction during CAPRICORN-2, and Figure B.4 shows calibration data for the aerosol concentrator used during CAP-2 (Sec. 3.2.3.1, 3.2.3.3). Figure B.5 replicates Fig. 3.1, but using primary marine aerosol concentrations instead of total quantities to normalize the ice nucleating particle (INP) data. Figure B.6 is a visual representation of the Spearman's correlation analysis discussed in Sec. 3.3.2. Figure B.7 indicates the relationship between INP concentrations at temperatures <-27 °C and wind speed for CAP-2 and SOC measurements in the marine boundary layer. Figure B.8 is an alternative way to visualize the vertically resolved INP measurements shown in Fig. 3.4, with measurements separated into altitude categories and observations shown as a function of temperature explicitly. Table B.1 lists the exponential fit parameters (Eq. 3.1) for the best-fit functions shown in Fig. 3.1, 3.2, 3.5, B.5, and B.8.

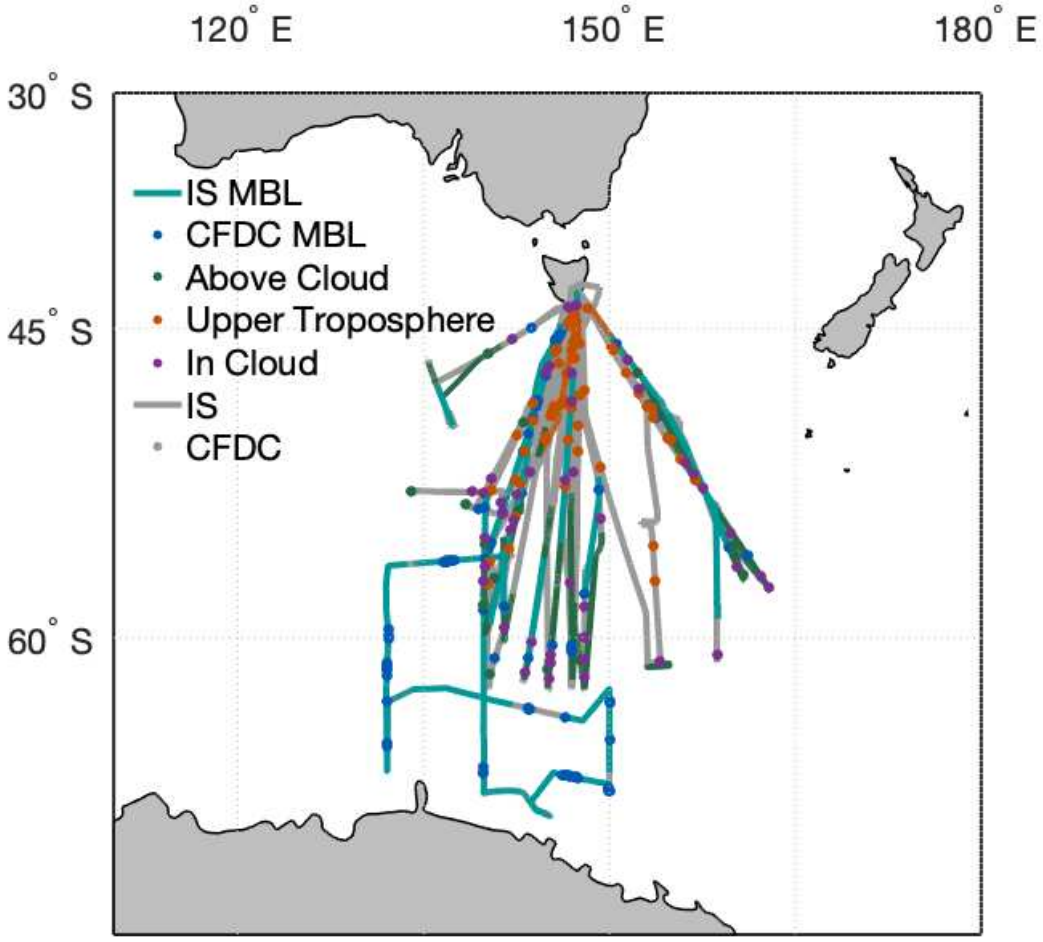

Figure B.1: Tracks of the RV *Investigator* (CAP-2) and NSF/NCAR G-V (SOC) are shown in grey. Locations of IS filter sample collections are shown as colored lines and CFDC measurement positions as circles. MBL measurements are in blue (light blue IS, dark blue CFDC), above cloud in green, upper troposphere (>5000 m) in orange, and in cloud (CFDC only) in purple.

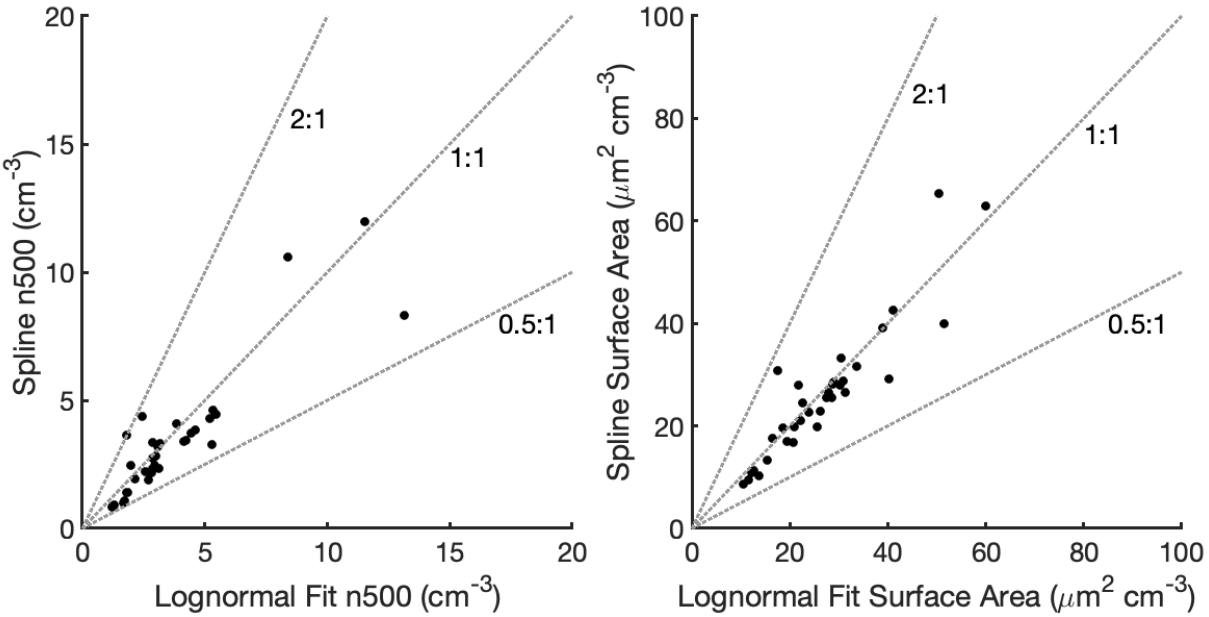

Figure B.2: Comparison of SOC MBL (a) n500 and (b) dry aerosol surface area estimated from size distributions merged through lognormal fitting (Moore et al. 2022) with those merged using a smoothing spline.

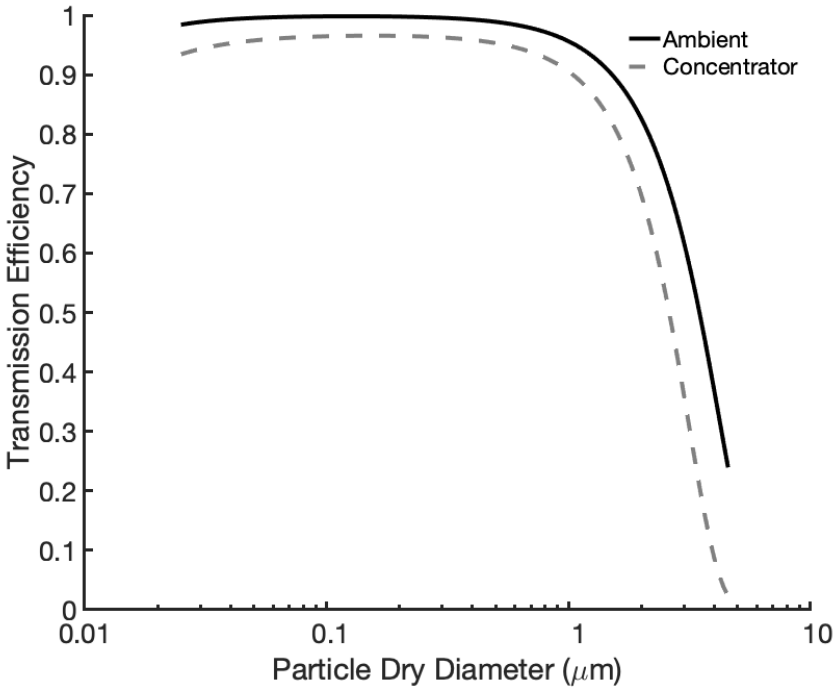

Figure B.3: Estimated particle transmission efficiency for the CFDC sampling on the RV *Investigator* from either the ambient aerosol inlet (solid black line) or the aerosol concentrator (dashed grey line). These theoretical calculations used the von der Weiden et al. (2009) Particle Loss Calculator and Paul Baron's Aerocalc spreadsheet (Brockmann 2011), with the sampling configuration and inputs described in Moore et al. (2022).

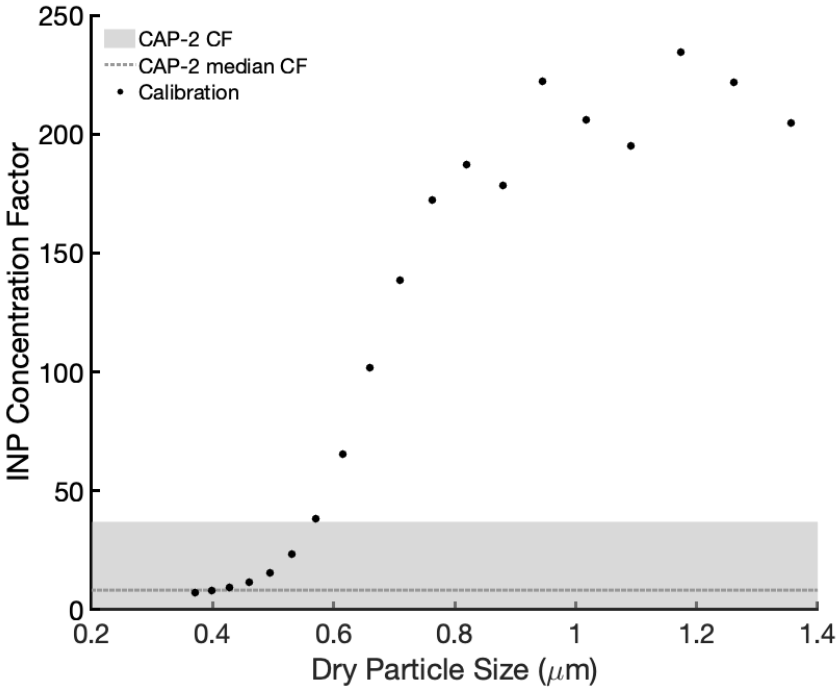

Figure B.4: Concentration factor for the aerosol concentrator used during CAP-2 as a function of particle size (black dots). The grey shaded region indicates the range of INP concentration factors measured during CAP-2, and the dashed grey line indicates the project median value.

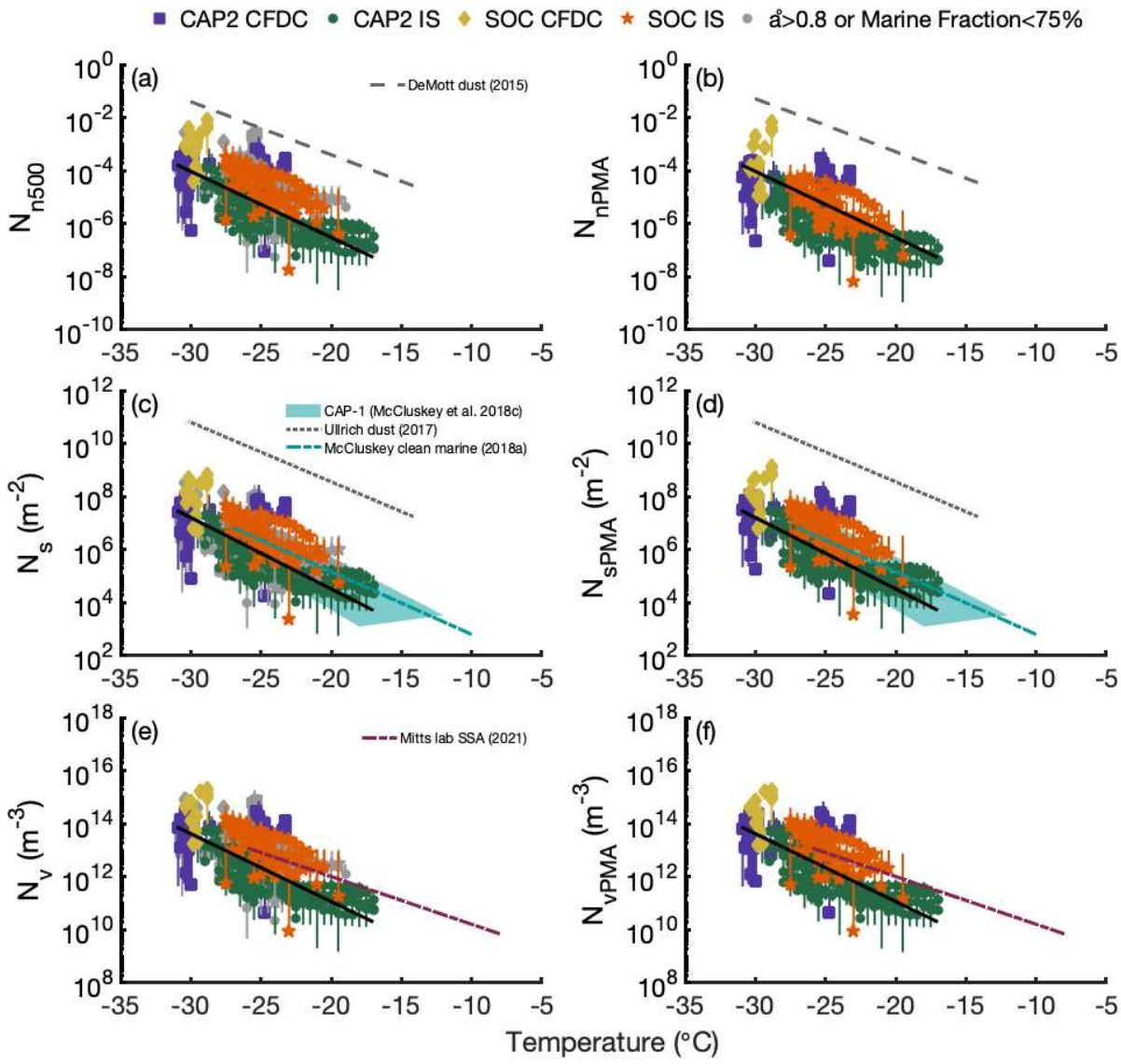

Figure B.5: Panels (a), (c), (e) are the same as Figure 3.1 (b-d). (b), (d), and (f) show the same normalizations of INP concentration, but use PMA fits (Moore et al. 2022) to aerosol data for normalizations, instead of total distribution values. Data in (b), (d), and (f) only include observations with å≤0.8 and 5-day back trajectory ocean fraction >75%. Grey symbols in (a), (c), (e) grey symbols do not meet at least one of these criteria. The best-fit exponential functions (solid black lines) in (a), (c), (e) are replicated in (b), (d), (f).

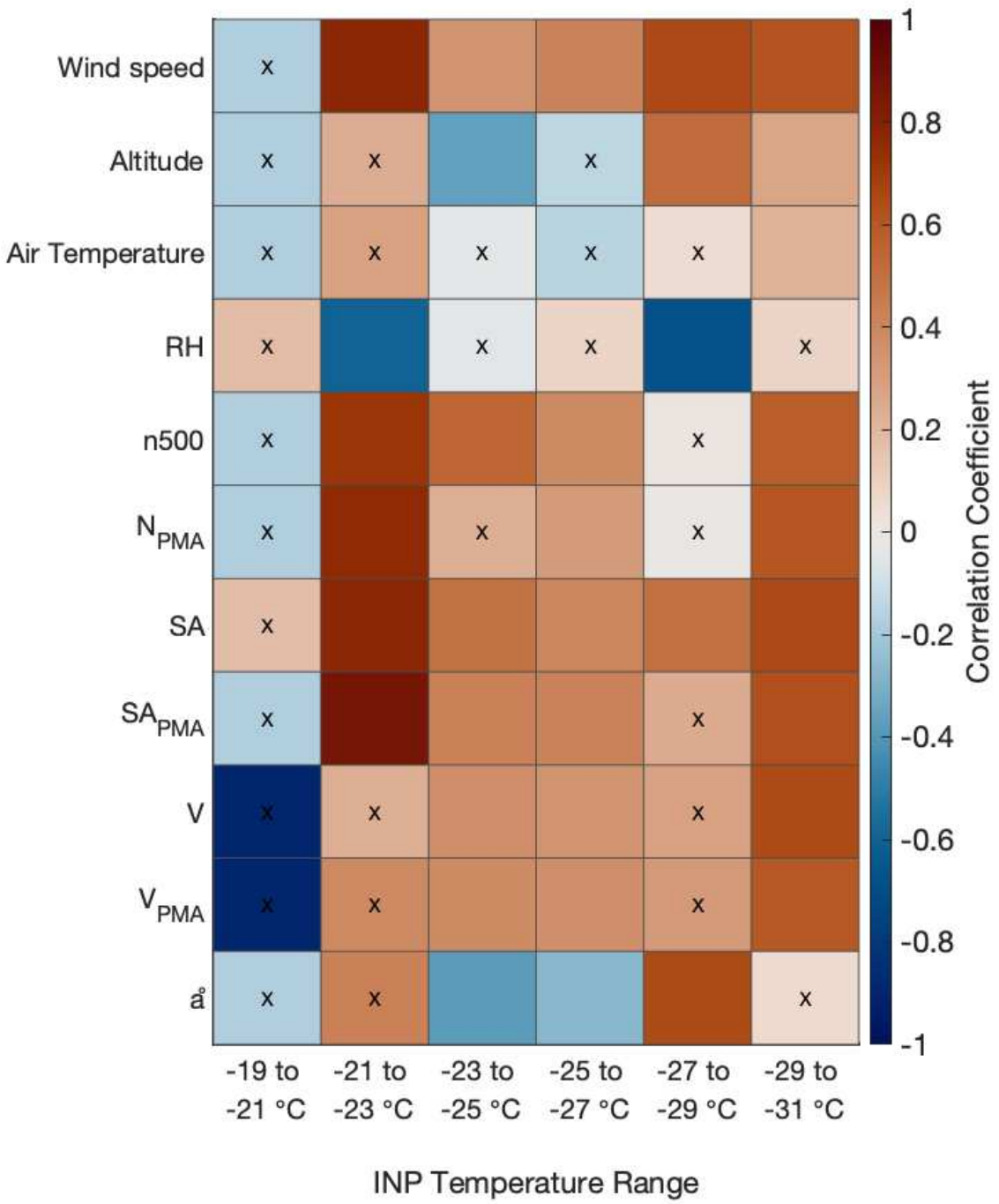

Figure B.6: Spearman's rank correlation between environmental variables, aerosol metrics, and concentrations of INPs in multiple temperature ranges. Correlation coefficient indicated by color; boxes without crosses represent a significant relation ($p<0.05$). Aerosol metrics tested include the number concentration of particles larger than 500 nm (n500), number concentration of primary marine aerosol (N_{PMA}), total aerosol and PMA surface area concentration (SA and SA_{PMA}, respectively), total aerosol and PMA volume concentration (V and V_{PMA}, respectively), and Ångström exponent (å; 450/635 nm wavelength pair). environmental variables include wind speed, measurement altitude, and air temperature.

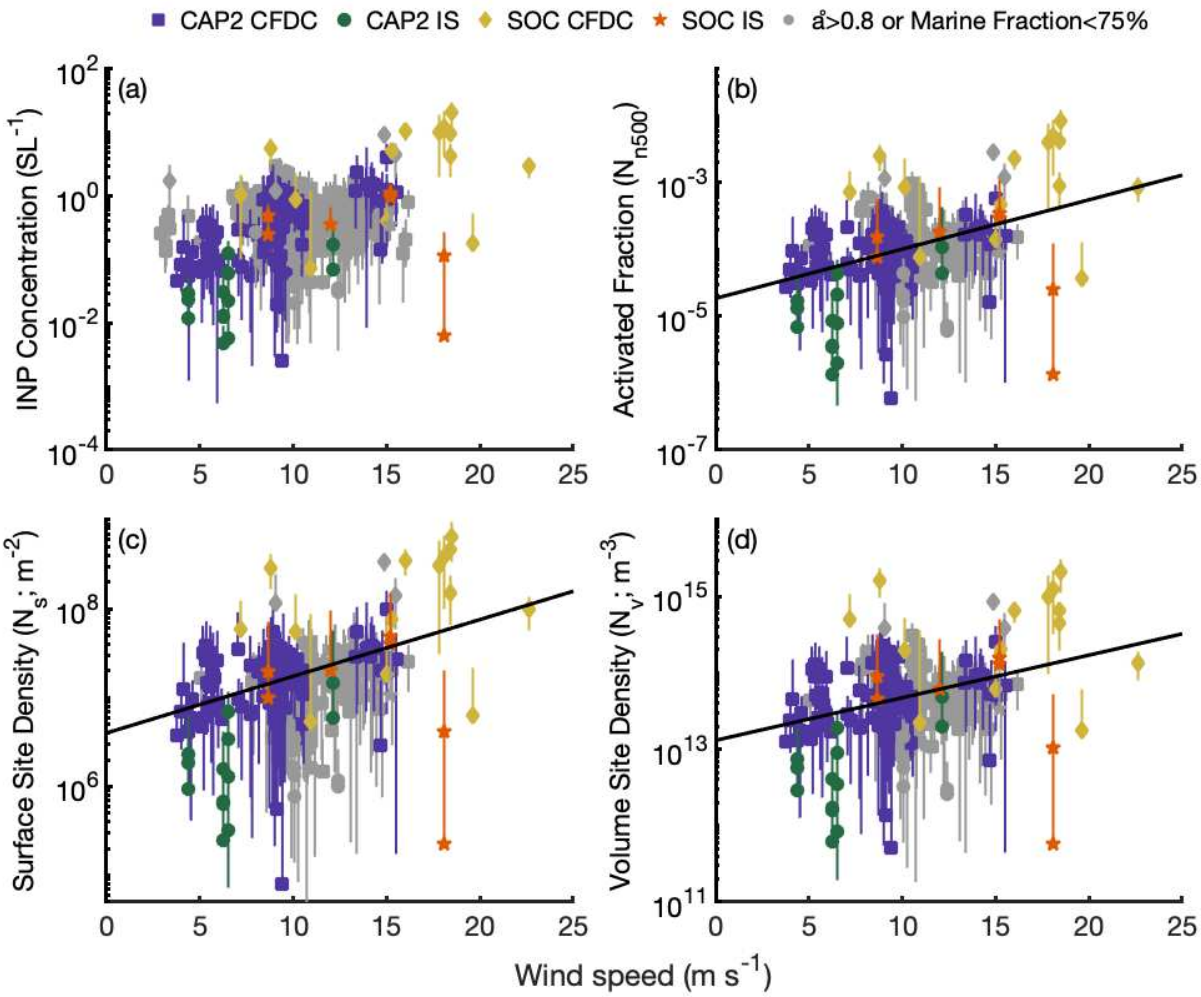

Figure B.7: Relationships between (a) INP concentration, (b) N_{n500}, (c) N_s and (d) N_v and average wind speed during each respective measurement period. INP measurements are limited to <-27 °C to reduce the effect of activation temperature. CAP-2 CFDC (purple squares), CAP-2 filter (green circles), SOC CFDC (gold diamonds), and SOC filter (orange stars) are shown in (a), and in (b-d) when simultaneous aerosol observations were available for normalization. Non-grey symbols have å≤0.8 and 5-day back trajectory ocean fraction >75% to isolate marine aerosol; CAP-2 IS filters were additionally required to have a wind speed variance <0.06 due to their long integration times. Grey symbols do not meet at least one of these criteria. Solid black lines in (b-d) indicate the best-fit exponential functions to all the non-grey symbols (R^2 for all fits=0.98).

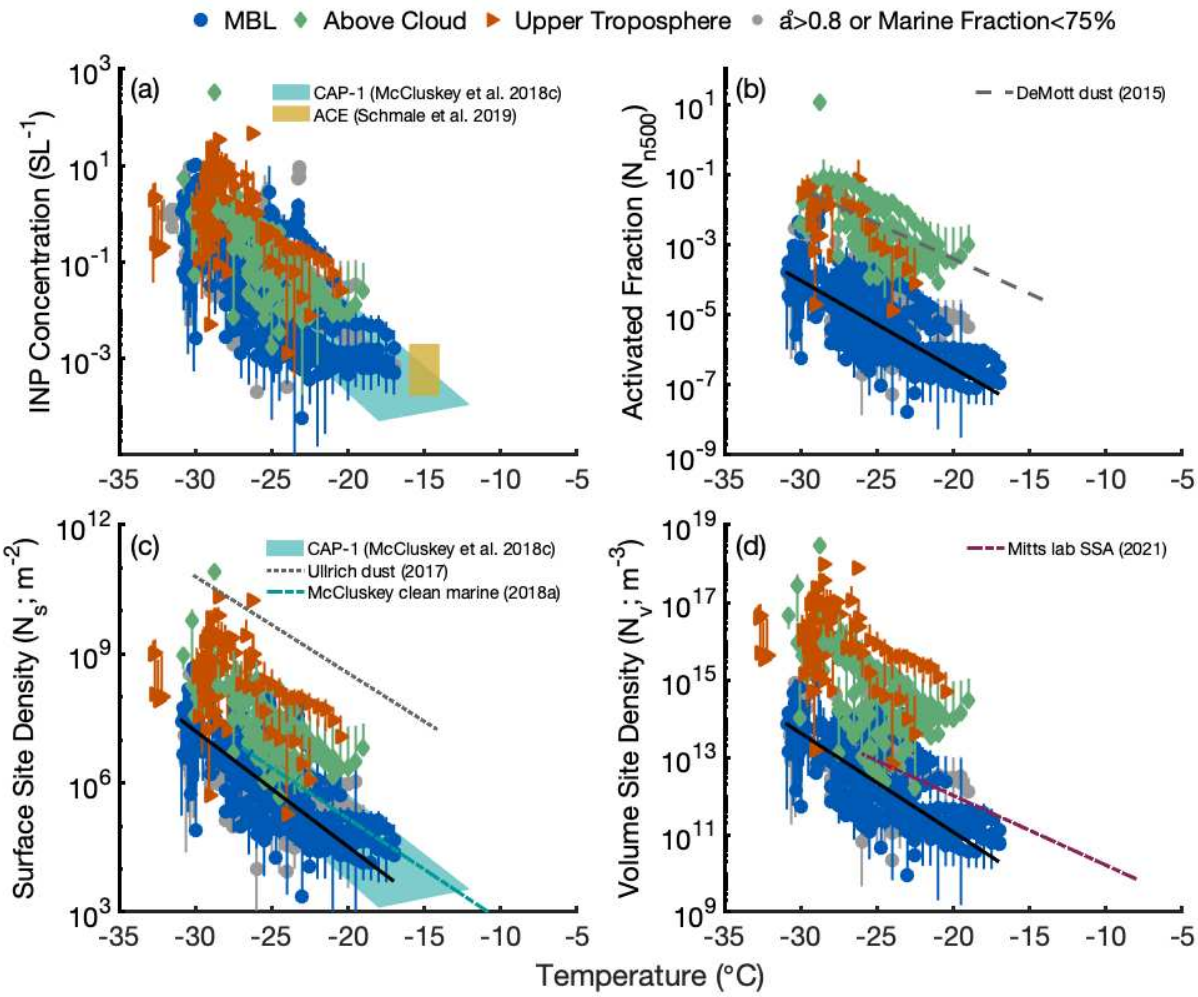

Figure B.8: INP (a) concentration, (b) N_{n500}, (c) N_s and (d) N_v temperature spectra during SOC and CAP-2 for different vertical regions. Data in the MBL shown as dark blue circles, above cloud as light green diamonds, and upper troposphere (>5000 m) data as orange triangles. The shading, parameterizations, best-fit lines, and marine aerosol classification are identical to Fig. 3.1.

Table B.1: Exponential fit parameters for MBL INP activated fraction (N_{n500}), surface active site density (N_s), and volume active site density (N_v) as a function of temperature. Functional form is given in Eq. 3.1.

Normalization	a ($°C^{-1}$)	b	R^2
N_{n500}	-0.57	-26.5	0.99
N_s (m^{-2})	-0.62	-1.97	0.99
N_v (m^{-3})	-0.59	13.7	0.99

C. Chapter 4 Supporting Information

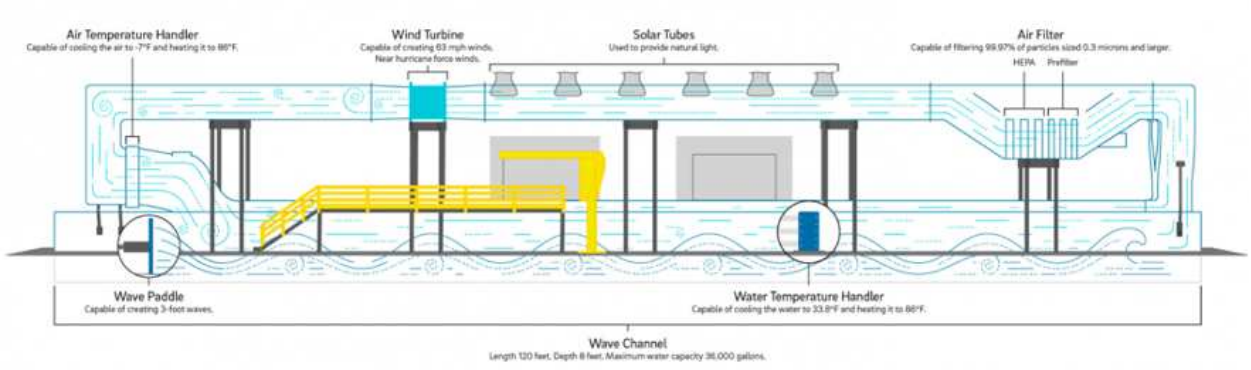

Figure C.1: Schematic of the Scripps Ocean-Atmosphere Research Simulator (SOARS) wind-wave channel at the Scripps Institution of Oceanography showing key features relevant for SSA production and seawater biology.

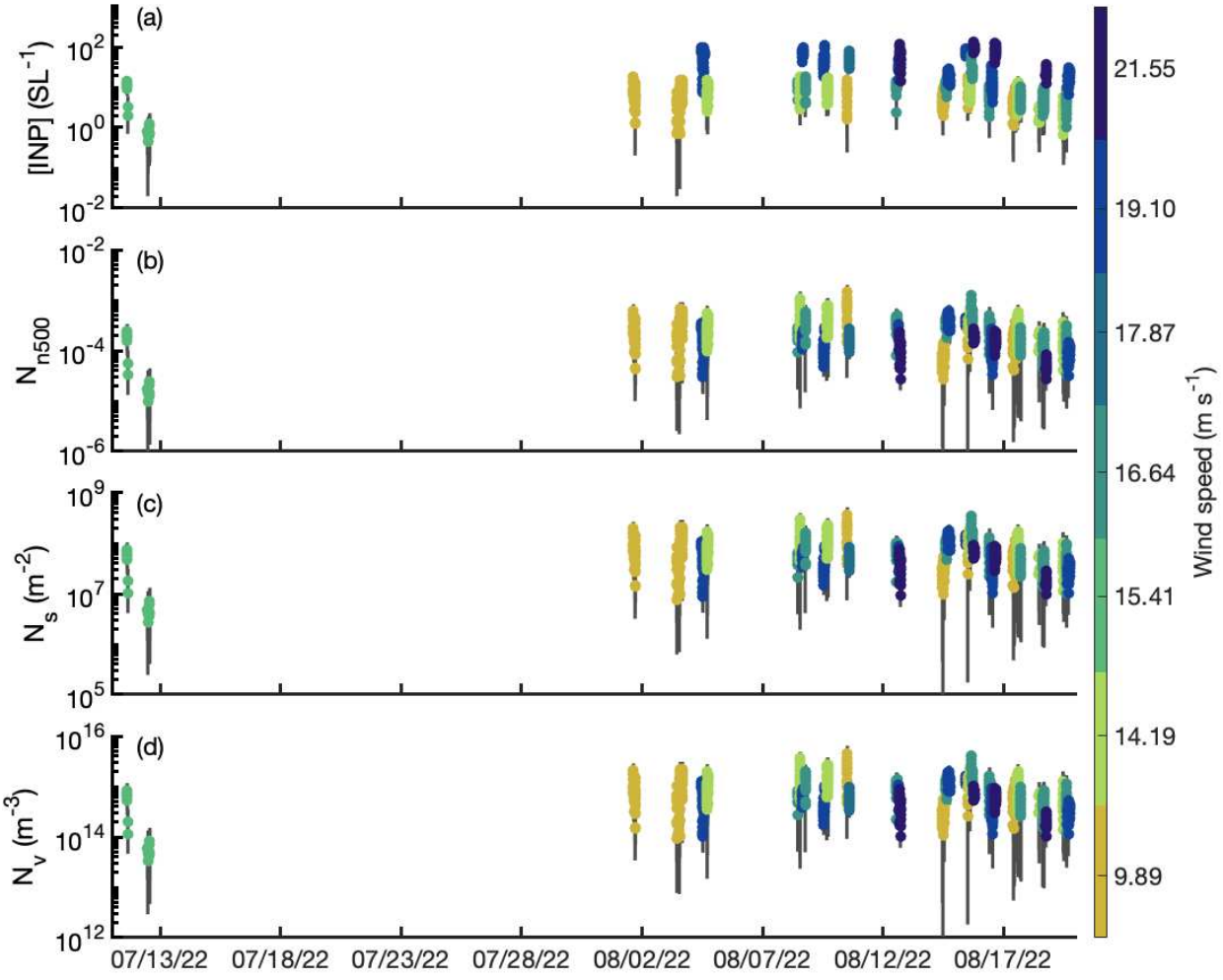

Figure C.2: Time series of CFDC INP (a) number concentration, (b) normalized by n500 (N_{n500}), (c) normalized by aerosol surface area (N_s) and (d) normalized by aerosol volume (N_v) during CHAOS. Observations are colored by the wind speed during each measurement period.

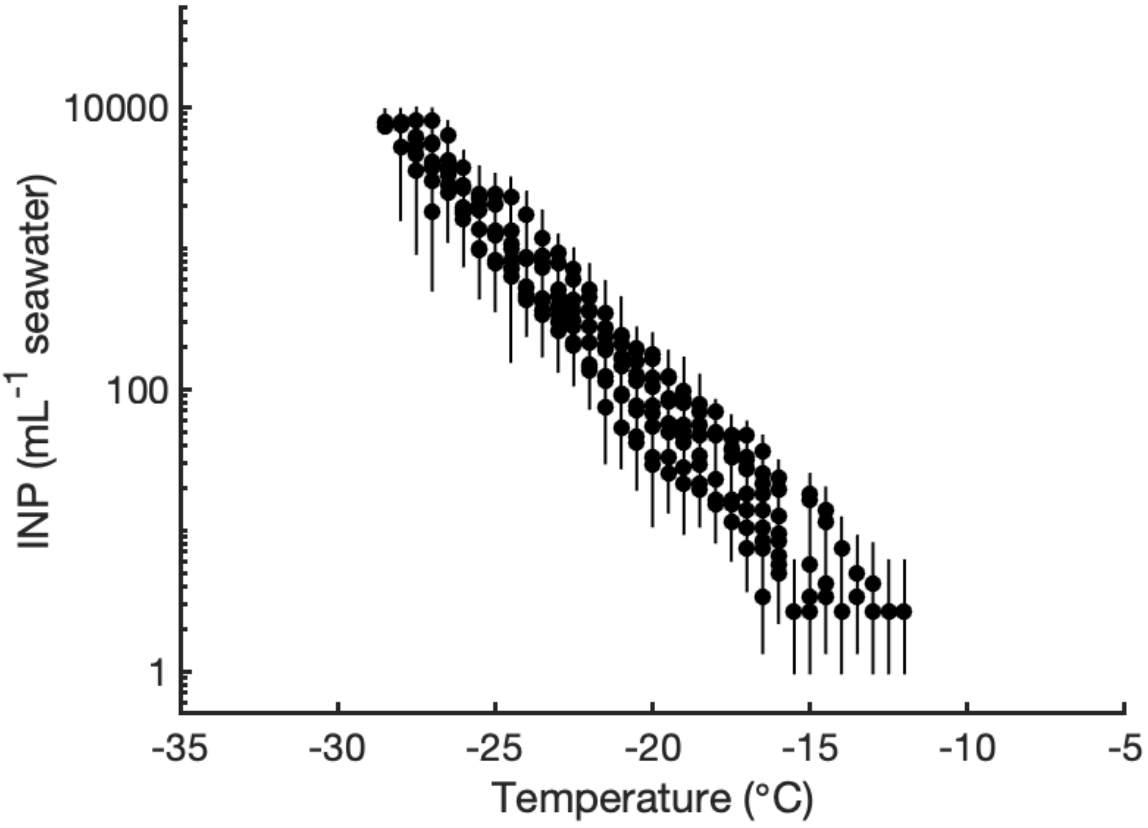

Figure C.3: Seawater INP temperature spectra during CHAOS.

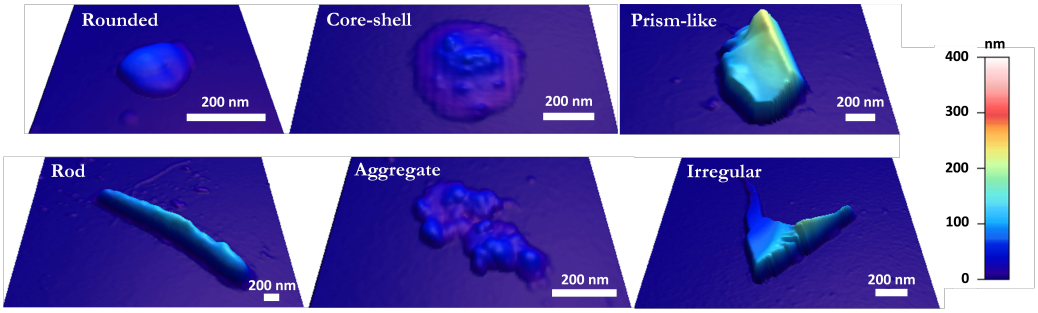

Figure C.4: Selected illustrative AFM 3D-height images of six main particle morphological categories (rounded, core-shell, prism-like, rod, aggregate and irregular) identified for four wind speeds of ~10, 17, 19, and 22 m s^{-1}. Images were all collected at 20% RH.

Table C.1: Summary of the average (± one standard deviation) percentage of core-shell INPs with solid, semisolid, and liquid shells emitted at different wind speeds (~10, 17, 19 and 22 m s^{-1}), as well as the average and range of viscoelastic response distances (VRD) measured for particles with semisolid shells. Measurements were made at 20% and 60% RH.

Wind speed ($m\ s^{-1}$)	RH (%)	Solid (%)	Semisolid (%)	Liquid (%)	VRD* (nm)	VRD range* (nm)
10	20	60 ± 24	0	40 ± 26	N/A	N/A
	60	0	60 ± 26	40 ± 27	0.6 ± 0.1	0.5 – 0.7
17	20	95 ± 1	5 ± 1	0	0.6 ± 0.0	0.6
	60	47 ± 16	53 ± 16	0	0.8 ± 0.4	0.5 – 1.5
19	20	50 ± 24	42 ± 23	8 ± 1	2.7 ± 1.9	0.7 – 4.4
	60	14 ± 1	71 ± 22	14 ± 1	2.8 ± 2.3	0.8 – 5.4
22	20	46 ± 18	46 ± 18	8 ± 1	1.5 ± 1.2	0.5 – 3.6
	60	0	71 ± 21	29 ± 10	1.8 ± 1.6	0.5 – 3.8

*Data reported only for core-shell particles with organic coatings classified as semisolid

D. Chapter 5 Supporting Information

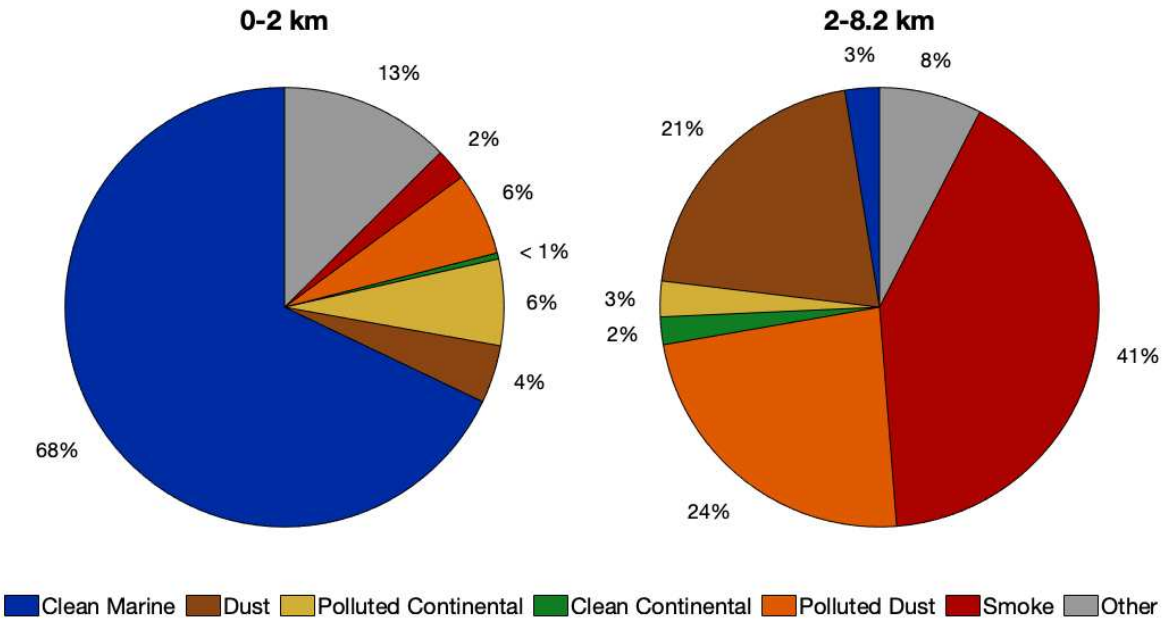

Figure D.1: Frequency of aerosol categories observed by CALIOP in two altitude ranges: 0-2 km and 2-8.2 km during the SOC and CAP-2 campaigns.

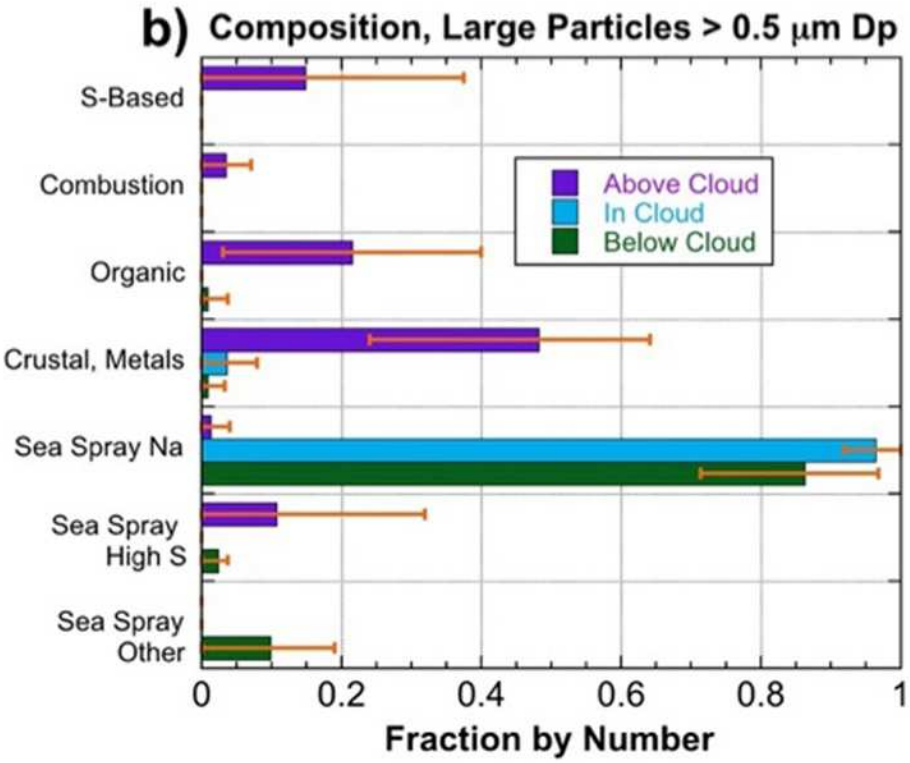

Figure D.2: Fractional particle composition of 0.5-5 μm particles observed during SOCRATES, reproduced with no changes from Twohy et al. (2021) Fig. 2b. Colored bars indicate the mean of all below cloud (green), cloud droplet residual (blue) and above cloud (purple) samples collected throughout all flights. Orange bars indicate the range observed for individual samples (n=6 below cloud; n=3 in-cloud; n=3 above cloud). A total of 364 particles were analyzed in the large size range. License available here: https://creativecommons.org/licenses/by-nc/4.0.

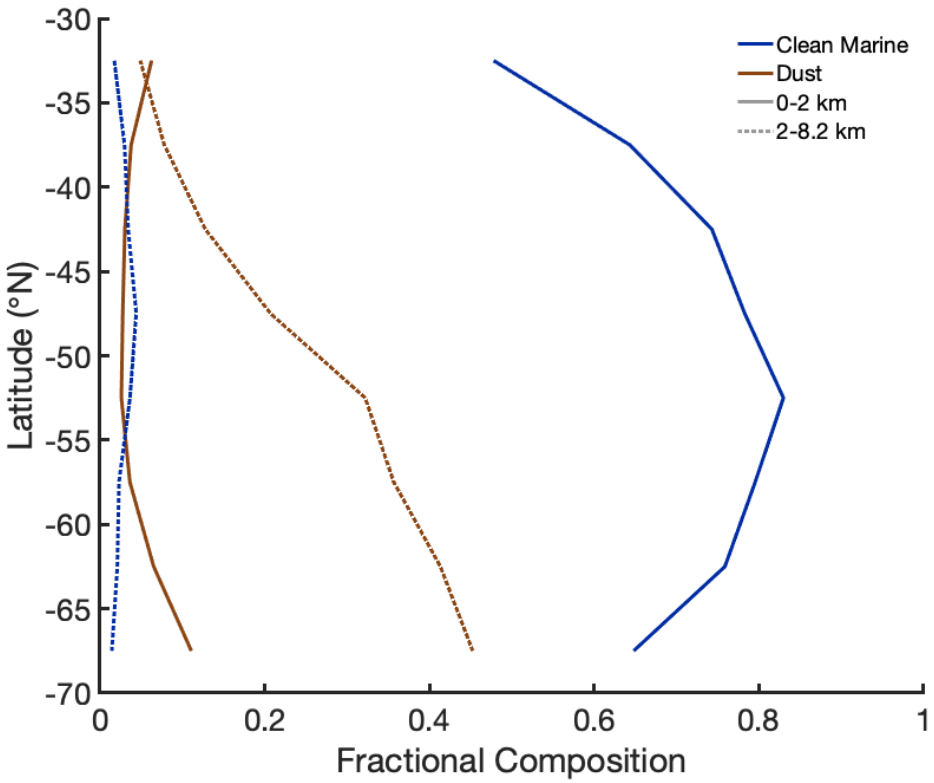

Figure D.3: Fraction of CALIOP aerosol observations identified to be dust or clean marine aerosol types during SOC and CAP-2 as a function of latitude, and separated into 0-2 km and 2-8.2 km altitude ranges.

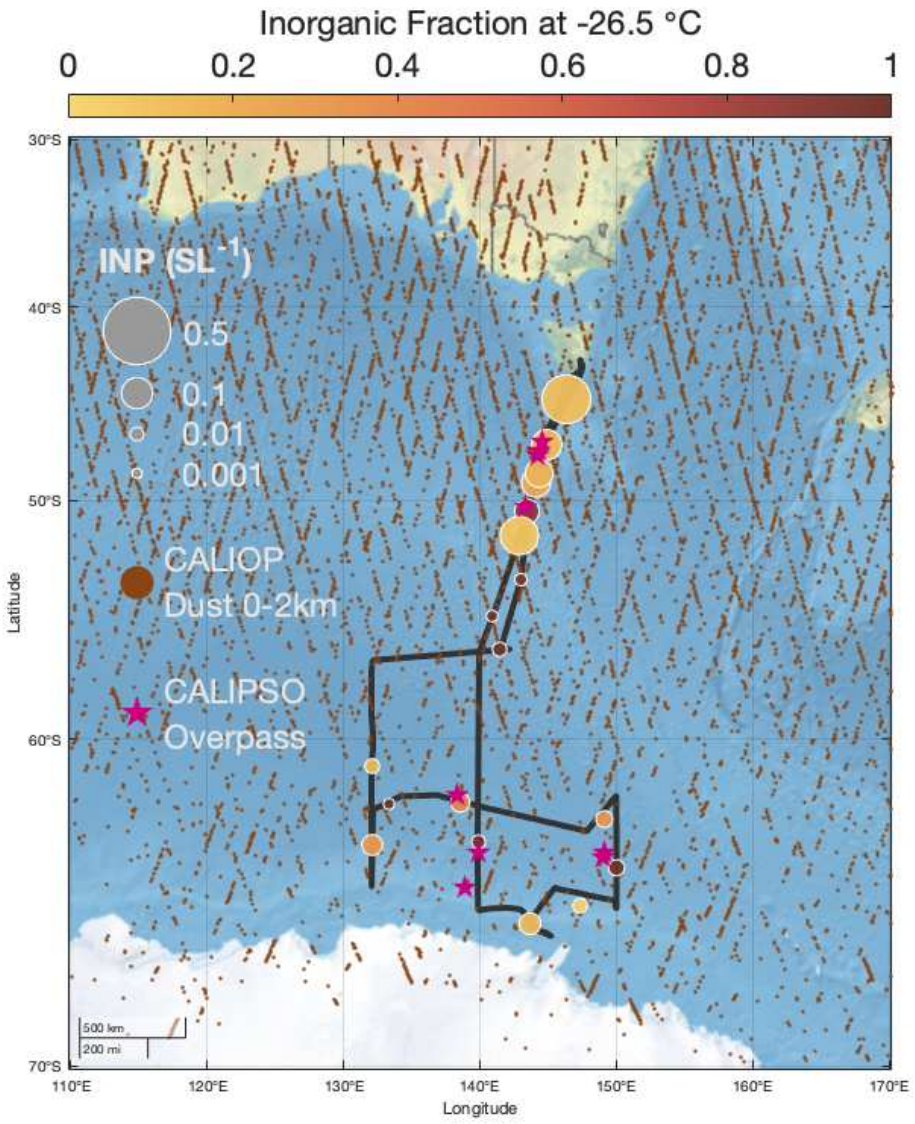

Figure D.4: The same map of INP concentration and inorganic fraction at -26.5 °C during CAP-2 as Figure 5.1a, but with CALIOP dust identifications <2 km shown as brown dots, and the locations of the overpasses listed in Table D.1 shown as magenta stars.

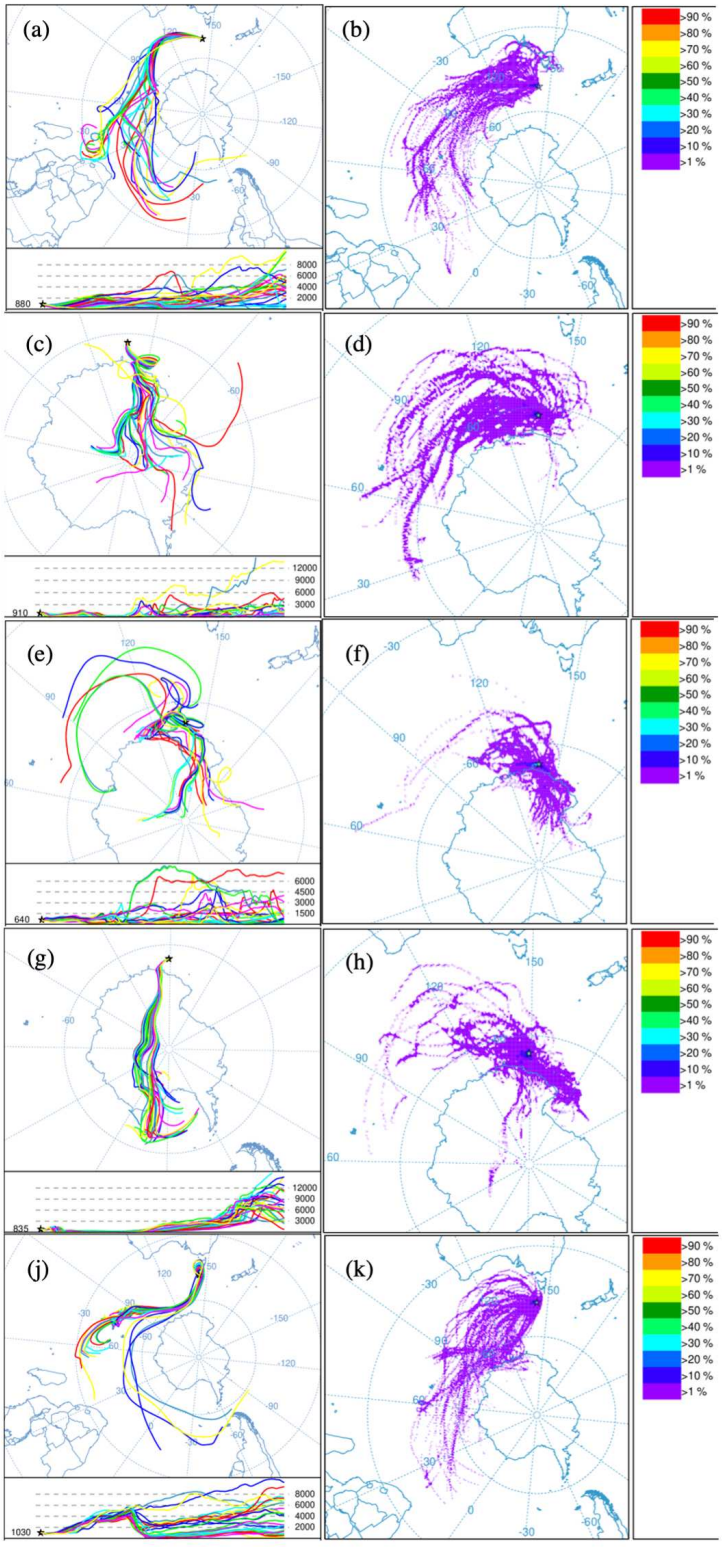

Figure D.5: HYSPLIT ensemble back trajectories (10 days) are shown on the left, in panels (a), (c), (e), (g), and (j). On the right, in (b), (d), (f), (h), and (k), trajectory frequencies are shown (color indicates % of trajectories passing through a given 0.5 x 0.5 ° model grid box). Back trajectories were initialized at the times and locations listed in Table D.1, sample numbers 1 (a-b), 2 (c-d), 4 (e-f), 5 (g-h), and 9 (j-k).

Table D.1: CALIOP overpasses of the RV *Investigator* where dust was identified below 2 km.

Sample Number	Time	Latitude (°)	Longitude (°)	Altitude (m)	Distance from RV *Investigator* (km)
1	01/19/18 15:31	-50.3073	143.3154	0.880	84.5026
2	01/28/18 15:29	-61.9692	138.3055	0.910	82.0708
3	01/30/18 15:17	-63.8883	139.8566	0.715	36.5272
4	01/30/18 15:17	-64.9887	138.8834	0.640	96.9861
5	02/05/18 14:40	-63.8931	149.1095	0.835	62.1004
6	02/05/18 14:40	-64.0627	148.9644	0.925	80.8098
7	02/20/18 15:31	-47.1654	144.5223	0.940	6.0836
8	02/20/18 15:31	-47.6063	144.3513	0.970	45.1344
9	02/20/18 15:31	-47.8257	144.2652	1.030	70.3772